Ministry of Education and Science of the Russian Federation
Saint Petersburg National Research University of Information
Technologies, Mechanics, and Optics

NANOSYSTEMS:

PHYSICS, CHEMISTRY, MATHEMATICS

2017, volume 8(4)

Наносистемы: физика, химия, математика

2017, том 8, № 4

NANOSYSTEMS:

PHYSICS, CHEMISTRY, MATHEMATICS

ADVISORY BOARD MEMBERS

Chairman: V.N. Vasiliev *(St. Petersburg, Russia),*
V.M. Buznik *(Moscow, Russia)*; V.M. Ievlev *(Voronezh, Russia),* P.S. Kop'ev*(St. Petersburg, Russia),* N.F. Morozov *(St. Petersburg, Russia),* V.N. Parmon *(Novosibirsk, Russia),* A.I. Rusanov *(St. Petersburg, Russia),*

EDITORIAL BOARD

Editor-in-Chief: I.Yu. Popov *(St. Petersburg, Russia)*

Section Co-Editors:
Physics – V.M. Uzdin *(St. Petersburg, Russia),*
Chemistry, material science –V.V. Gusarov *(St. Petersburg, Russia),*
Mathematics – I.Yu. Popov *(St. Petersburg, Russia).*

Editorial Board Members:
V.M. Adamyan *(Odessa, Ukraine)*; O.V. Al'myasheva *(St. Petersburg, Russia)*; A.P. Alodjants *(Vladimir, Russia)*; S. Bechta *(Stockholm, Sweden)*; J. Behrndt *(Graz, Austria)*; M.B. Belonenko *(Volgograd, Russia)*; V.G. Bespalov *(St. Petersburg, Russia)*; J. Brasche *(Clausthal, Germany)*; A. Chatterjee (*Hyderabad, India)*; S.A. Chivilikhin *(St. Petersburg, Russia)*; A.V. Chizhov *(Dubna, Russia)*; A.N. Enyashin *(Ekaterinburg, Russia),* P.P. Fedorov *(Moscow, Russia)*; E.A. Gudilin *(Moscow, Russia)*; V.K. Ivanov *(Moscow, Russia),* H. Jónsson *(Reykjavik, Iceland)*; A.A. Kiselev *(Madison, USA)*; Yu.S. Kivshar *(Canberra, Australia)*; S.A. Kozlov *(St. Petersburg, Russia)*; P.A. Kurasov *(Stockholm, Sweden)*; A.V. Lukashin *(Moscow, Russia)*; V.A. Margulis *(Saransk, Russia)*; I.V. Melikhov *(Moscow, Russia)*; G.P. Miroshnichenko *(St. Petersburg, Russia)*; I.Ya. Mittova *(Voronezh, Russia)*; H. Neidhardt *(Berlin, Germany)*; V.V. Pankov *(Minsk, Belagus)*; K. Pankrashkin *(Orsay, France)*; A.V. Ragulya *(Kiev, Ukraine)*; V. Rajendran *(Tamil Nadu, India)*; A.A. Rempel *(Ekaterinburg, Russia)*; V.Ya. Rudyak *(Novosibirsk, Russia)*; D Shoikhet *(Karmiel, Israel)*; P Stovicek *(Prague, Czech Republic)*; V.M. Talanov *(Novocherkassk, Russia)*; A.Ya. Vul' *(St. Petersburg, Russia)*; A.V. Yakimansky (*St. Petersburg, Russia*), V.A. Zagrebnov *(Marseille, France).*

Editors:
I.V. Blinova; A.I. Popov; A.I. Trifanov; E.S. Trifanova *(St. Petersburg, Russia),*
R. Simoneaux *(Philadelphia, Pennsylvania, USA).*

Address: University ITMO, Kronverkskiy pr., 49, St. Petersburg 197101, Russia.
Phone: +7(812)232-67-65, **Journal site:** http://nanojournal.ifmo.ru/,
E-mail: popov1955@gmail.com

AIM AND SCOPE

The scope of the journal includes all areas of nano-sciences. Papers devoted to basic problems of physics, chemistry, material science and mathematics inspired by nanosystems investigations are welcomed. Both theoretical and experimental works concerning the properties and behavior of nanosystems, problems of its creation and application, mathematical methods of nanosystem studies are considered.

The journal publishes scientific reviews (up to 30 journal pages), research papers (up to 15 pages) and letters (up to 5 pages). All manuscripts are peer-reviewed. Authors are informed about the referee opinion and the Editorial decision.

CONTENT

MATHEMATICS

PHYSICS

CHEMISTRY AND MATERIAL SCIENCE

NANOSYSTEMS: PHYSICS, CHEMISTRY, MATHEMATICS, 2017, 8 (4), P. 413–419

The loaded parabolic-hyperbolic equation and its relation to non-local problems

U. I. Baltaeva

National University of Uzbekistan named after Mirzo Ulugbek
Differential equations and Mathematical physics, 100174, Tashkent, Uzbekistan

umida_baltayeva@mail.ru

DOI 10.17586/2220-8054-2017-8-4-413-419

In this present paper, unique solvability is proved for the boundary value problems for the loaded differential equations associated with non-local boundary value problems, for the classical partial differential equations.

Keywords: parabolic-hyperbolic type equations, non-local problems, loaded equation, boundary value problems, gluing condition, integral equation.

Received: 25 July 2017

Revised: 3 August 2017

1. Introduction

Research on equations of parabolic-hyperbolic and hyperbolic-elliptic types has been conducted heavily. Since, there are both theoretical and practical uses for their applications, especially in the development of principal parts of partial differential equations. Moreover, in recent years it has become increasingly important to investigate a new class of equations, known as loaded equations, as a direct result of issues with the optimal control of the agro-economical system, long-term forecasting and regulation of groundwater levels and soil moisture [1–4].

Basic questions on the theory of boundary value problems for partial differential equations still exist, and are equivalent to that of the boundary value problems for loaded differential equations. However, the existence of the loaded part operator A does not often make it possible to directly apply the known theory of boundary value problems, for the classical partial differential equations. In view of this, searching for the solutions of loaded differential equation using preassigned classes, it may be possible to reduce to them to new problems, for non-loaded equations(see [4–6]).

At the same time, mixed type equations appear in some problems of nanophysics and are present in some micro- and nanoflow models. Particularly, parabolic-hyperbolic equations are considered in some models of spinodal decomposition (so-called hyperbolic diffusion, see, e.g. [7, 8]), and also described flow in thin viscous layers subjected to ultrasonic acoustic field [9].

The present work is devoted to the formulation and investigation of the boundary value problems for a loaded equation of the mixed parabolic hyperbolic type:

$$\frac{\partial}{\partial x}(Lu) = \mu\sum_{i=1}^{n} a_i(x) D_{0x}^{\alpha_i}[u_y(x,0) - u(x,0)], \tag{1}$$

where

$$Lu \equiv u_{xx} - \frac{1-\mathrm{sgn}y}{2}u_{yy} - \frac{1+\mathrm{sgn}y}{2}u_y - \lambda u\,,$$

$$D_{0x}^{\alpha_i} f(x) = \begin{cases} \dfrac{1}{\Gamma(-\alpha_i)}\displaystyle\int\limits_0^x \dfrac{f(t)dt}{(x-t)^{1+\alpha_i}}, & \alpha_i < 0, \\ \dfrac{d}{dx} D_{0x}^{\alpha_i - 1} f(x), & 0 < \alpha_i < 1, \end{cases}$$

integro-differential operator [4]. $D_{0x}^{-\alpha_i} D_{0x}^{\alpha_i} f \equiv D_{0x}^{0} f \equiv f(x)$. We assume, that $\alpha_n < \alpha_{n-1} < \ldots < \alpha_1 = \alpha < 1$ and coefficients $a_i = a_i(x) \in C^1[0,1] \cap C^3\,(0,1)$, λ, μ are given real parameters, and $\lambda > 0$.

Furthermore, we will discuss how the boundary value problem for the loaded differential equation is associated with non-local boundary value problems, for classical partial differential equations. In our investigations, we have formulated first-kind boundary value problems (such as the Tricomi problems) for the linearly loaded, integro-differential equation of the third order, with mixed operators.

2. First kind of boundary value problems for a loaded equation of the mixed type

Let $\Omega_1 \subset R^2$ be a domain bounded by the segments AB, BB_0, AA_0, A_0B_0 of straight lines $y=0$, $x=1$, $x=0$, $y=h$, respectively when $y>0$. Ω_2 is a characteristic triangle bounded by the segment AB the axis OX and two characteristics:

$$AC : x+y=0, \quad BC : x-y=1,$$

of equation (1) for $y<0$.

Let us introduce the following notation:

$$I=\{(x,y) : 0<x<1, \;\; y=0\}, \quad \Omega=\Omega_1\cup\Omega_2\cup I.$$

Problem 2.1. Find a regular solution $u(x,y)$ equation (1) in Ω, which has continuous derivatives $u_x(u_y)$, up to $AA_0 \cup AB \cup AC\,(AB\cup AC)$, and satisfies the boundary value conditions:

$$u(0,y)=\varphi_1(y), \;\; u(1,y)=\varphi_2(y), \;\; u_x(0,y)=\varphi_3(y), \;\; 0\le y\le h, \tag{2}$$

$$u(x,-x)=\psi_1(x), \quad \left.\frac{\partial u(x,y)}{\partial n}\right|_{y=-x}=\psi_2(x), \quad 0\le x\le \frac{1}{2}, \tag{3}$$

and the gluing conditions:

$$u_y\left(x,+0\right)=u_y\left(x,-0\right), \;\; (x,0)\in I,$$

where $\varphi_1(y)$, $\varphi_2(y)$, $\varphi_3(y)$, $\psi_1(x)$ and $\psi_2(x)$ are the given functions.

Problem 2.2. Find a regular solution $u(x,y)$ equation (1) in Ω, which has continuous derivatives $u_x(u_y)$, up to $AA_0 \cup AB\cup BC$ $(AB\cup BC)$, and satisfies the boundary value conditions (2),

$$u(x,x-1)=\tilde{\psi}_1(x), \quad \left.\frac{\partial u(x,y)}{\partial n}\right|_{y=x-1}=\tilde{\psi}_2(x), \quad \frac{1}{2}\le x\le 1, \tag{4}$$

and the gluing condition:

$$u_y\left(x,+0\right)=u_y\left(x,-0\right), \;\; (x,0)\in I,$$

where $\tilde{\psi}_1(x)$ and $\tilde{\psi}_2(x)$ are the given functions.

We note that physical characteristic problems may reduce to equations which include, some composed operator in the loaded part. The unique solvability of the analogs of the Tricomi for the loaded differential equations was investigated in [5, 10], for which the loaded part contains the imputation or imputation operators of the unknown function.

An important aspect of the investigation of the boundary value problems, is shown by the following theorem. The following theorem holds.

Theorem 2.1. Any regular solution of equation (1) (when $y\ne 0$) is represented in the form:

$$u(x,y)=z(x,y)+w(x), \tag{5}$$

where $z(x,y)$ is a solution to the equation:

$$\frac{\partial}{\partial x}\left(z_{xx}-\frac{1-\mathrm{sgn}y}{2}z_{yy}-\frac{1+\mathrm{sgn}y}{2}z_y-\lambda z\right)=0, \tag{6}$$

$w(x)$ is a solution of the following ordinary differential equation:

$$w^{'''}(x)-\lambda w^{'}(x)-\mu\sum_{i=1}^{n}a_iD_{0x}^{\alpha_i(x)}w(x)=\mu\sum_{i=1}^{n}a_i(x)D_{0x}^{\alpha_i}[z_y(x,0)-z(x,0)]. \tag{7}$$

Proof of Theorem 2.1.

Let $u(x,y)$, represented by formula (5), be the solution of equation (1) for $y<0$. Then, substituting:

$$\frac{\partial}{\partial x}\left(u_{xx}-u_{yy}-\lambda u\right)-\mu\sum_{i=1}^{n}a_i(x)D_{0x}^{\alpha_i}[u_y(x,0)-u(x,0)]=\frac{\partial}{\partial x}\left(z_{xx}-z_{yy}-\lambda z\right)+$$
$$+w'''(x)-\lambda w'(x)-\mu\sum_{i=1}^{n}a_i(x)D_{0x}^{\alpha_i}w(x)-\mu\sum_{i=1}^{n}a_i(x)D_{0x}^{\alpha_i}[z_y(x,0)-z(x,0)]=0,$$

satisfies equation (1) for $y<0$.

Then, vice versa, let $u(x,y)$ be a regular solution to equation (1), and $w(x)$ be a certain solution:

$$w'''(x)-\lambda w'(x)-\mu\sum_{i=1}^{n}a_i(x)D_{0x}^{\alpha_i}w(x)=\mu\sum_{i=1}^{n}a_i(x)D_{0x}^{\alpha_i}[u_y(x,0)-u(x,0)]. \tag{8}$$

Let us prove the validity of the relation (5). Manifestly, the function:

$$u(x,y)=z(x,y)+\frac{\mu}{\lambda}\int_0^x(\cosh\sqrt{\lambda}(x-t)-1)\sum_{i=1}^{n}a_i(x)D_{0t}^{\alpha_i}[u_y(t,0)-u(t,0)]dt,$$

is a solution to equation (1), where $z(x,y)$ is a solution to equation (6), and the function:

$$u(x,y)=-\frac{\mu}{\lambda}\int_0^x(1-\cosh\sqrt{\lambda}(x-t))\sum_{i=1}^{n}a_i(t)D_{0t}^{\alpha_i}[u_y(t,0)-u(t,0)]dt,$$

is a partial solution to equation (1). Hence, (1) highlights the validity of the representation (5), i.e. $u(x,y)=z(x,y)+w(x)$.

It follows from the latter representation that $u(x,0)=z(x,0)+w(x)$. Then, (8) provides:

$$w'''(x)-\lambda w'(x)-\mu\sum_{i=1}^{n}a_i(x)D_{0x}^{\alpha_i}w(x)-\mu\sum_{i=1}^{n}a_i(x)D_{0x}^{\alpha_i}[z_y(x,0)-z(x,0)]=0,$$

and the function $z(x,y)=u(x,y)-w(x)$, satisfies equation (6) for $y<0$.

Analogously proved in the case for $y<0$. Theorem 2.1 is proved.

Now, invoking that the function $ae^{\sqrt{\lambda}x}+be^{-\sqrt{\lambda}x}+c$ satisfies equation (6), we can assume without loss of generality that:

$$w(0)=w'(0)=w''(0)=0, \tag{9}$$

when studying Problem 2.1 and Problem 2.2.

Let us solve the Cauchy problem for equation (7) with the conditions (9), with respect to $w(x)$. Assuming that:

$$\widetilde{f}(x)=\mu\sum_{i=1}^{n}a_i(x)D_{0x}^{\alpha_i}w(x)+\mu\sum_{i=1}^{n}a_i(x)D_{0x}^{\alpha_i}\left[z_y(x,0)-z(x,0)\right],$$

we write equation (7) in the form:

$$\omega(x)=\frac{1}{\lambda}\int_0^x\left(\cosh\sqrt{\lambda}(x-t)-1\right)\widetilde{f}(t)dt.$$

The last equality with respect to designation and after some transformation becomes:

$$\omega(x)-\mu\int_0^x K(x,t)\omega(t)dt=F(x),\quad 0\le x\le 1, \tag{10}$$

where

$$K(x,t)=\frac{1}{\Gamma(-\alpha_i)}\int_0^x A_i(t)(t-s)^{-1-\alpha_i}\left(\cosh\sqrt{\lambda}(x-t)-1\right)dt,\quad \alpha_i<0, \tag{11}$$

$$K(x,t)=\frac{1}{\lambda\Gamma(1-\alpha_i)}\int_s^x\frac{\partial}{\partial t}\left[A_i(t)(t-s)^{-\alpha_i}\left(\cosh\sqrt{\lambda}(x-t)-1\right)\right]dt,\ 0<\alpha_i<1, \tag{12}$$

$$F(x)=\frac{\mu}{\lambda}\int_0^x\left(\cosh\sqrt{\lambda}(x-t)-1\right)\sum_{i=1}^{n}a_i(t)D_{0x}^{\alpha_i}[z_y(t,0)-z(t,0)]dt. \tag{13}$$

The recurring index $i=1,2,...n$, implies summation. Therefore, solving the next equation with respect to [11], we have a solution to the Cauchy problem for equation (7) with the conditions (9):

$$\omega(x)=\int_0^x P(x,t)\sum_{i=1}^{n}a_i(t)D_{0x}^{\alpha_i}[z_y(t,0)-z(t,0)]dt, \tag{14}$$

where

$$P(x,t)=\frac{\mu}{\lambda}\left\{\cosh\sqrt{\lambda}(x-t)-1+\mu\int\limits_{t}^{x}\Big(\cosh\sqrt{\lambda}(s-t)-1\Big)R(x,s;\mu)ds\right\}. \tag{15}$$

$R(x,s;\mu)$ is the resolvent of the kernel $K(x,t)$, when studying Problem 2.1 and Problem 2.2. Thus, by virtue of the representation (5), equation (1) Problem 2.1 and Problem 2.2, in view of (9), are all reduced to the following Problem NP_1 and Problem NP_2 for equation (6).

We investigate the following problems:

Problem NP_1. To find a regular solution to equation (6) in the domains Ω_1 and Ω_2, which has continuous derivatives $u_x(u_y)$, up to $AA_0\cup AC\,(AC)$, and satisfies the boundary conditions:

$$z(0,y)=\varphi_1(y),\ z(0,y)=\varphi_2(y)-w(1),\quad 0\le y\le h, \tag{16}$$

$$z_x(0,y)=\varphi_3(y),\quad 0\le y\le h, \tag{17}$$

$$z(x,-x)=\psi_1(x)-\int\limits_0^x P(x,t)\sum_{i=1}^n a_i(t)D_{0x}^{\alpha_i}[z_y(t,0)-z(t,0)]dt,\ 0\le x\le\frac{1}{2}, \tag{18}$$

$$\frac{\partial z(x,-x)}{\partial n}=\psi_2(x)-\frac{1}{\sqrt{2}}\int\limits_0^x P'_x(x,t)\sum_{i=1}^n a_i(t)D_{0x}^{\alpha_i}[z_y(t,0)-z(t,0)]dt,\ 0\le x\le\frac{1}{2}, \tag{19}$$

and the gluing condition:

$$z_y\left(x,+0\right)=z_y\left(x,-0\right),\ \ (x,0)\in I,$$

where $\varphi_1(y),\ \varphi_2(y),\varphi_3(y),\psi_1(x)$ and $\psi_2(x)$ are given functions, such that $\varphi_1(0)=\psi_1(0)$.

Problem NP_2. To find a regular solution of equation (6) in the domains Ω_1 and Ω_2, has continuous derivatives $u_x(u_y)$, up to $AA_0\cup BC\,(BC)$, and satisfies the boundary conditions (16), (17),

$$z(x,x-1)=\tilde{\psi}_1(x)-\int\limits_0^x P(x,t)\sum_{i=1}^n a_i(t)D_{0x}^{\alpha_i}[z_y(t,0)-z(t,0)]dt,\ \frac{1}{2}\le x\le 1, \tag{20}$$

$$\frac{\partial z(x,x-1)}{\partial n}=\tilde{\psi}_2(x)-\frac{1}{\sqrt{2}}\int\limits_0^x P'_x(x,t)\sum_{i=1}^n a_i(t)D_{0x}^{\alpha_i}[z_y(t,0)-z(t,0)]dt,\ \frac{1}{2}\le x\le 1, \tag{21}$$

and the gluing condition:

$$z_y\left(x,+0\right)=z_y\left(x,-0\right),\ \ (x,0)\in I,$$

where $\tilde{\psi}_1(x)$ and $\tilde{\psi}_2(x)$ are given functions, such that $\varphi_2(0)=\tilde{\psi}_1(1)$.

Since Problem 2.1 and Problem 2.2 were reduced to the equivalent non-local Problems NP_1 and NP_2 for the third order mixed type equation (6), we may conclude that Problems 2.1 and 2.2 have a unique solutions, as a direct result of the unique solvability of the non-local problem. The early 1970's marked the beginning of the systematic study of the third and higher order, mixed and mixed composite type PDEs; which contain parabolic-hyperbolic, hyperbolic-elliptic and elliptic-parabolic operators in the main part. This subject has been studied extensively and has been developed by numerous mathematicians [12–14], due to, the increasing popularity of its connection with non-local problems, and the appearance of these PDEs in mathematical models for various problems which possess physical traits. For instance, while studying problems of moisture transfer in soils, heat transfer in heterogeneous media, diffusion of thermal neutrons in inhibitors, simulation of various biological processes, phenomena etc [6, 15–18].

The following theorems hold.

Theorem 2.2. If $\lambda>0$ and $\varphi_1(0)=\psi_1(0)$,

$$\varphi_j(y)\in C^1[0,h],\ (j=1,2),\ \varphi_3(y)\in C[0,h]\cap C^1(0,h),$$

$$\psi_1(x)\in C^1\left[0,1/2\right]\cap C^3\left(0,1/2\right),\ \psi_2(x)\in C\left[0,1/2\right]\cap C^2\left(0,1/2\right),$$

then there exists a unique solution to the Problem 2.1 in the domain Ω.

Theorem 2.3. If $\lambda > 0$ and $\varphi_2(0) = \tilde{\psi}_1(1)$,

$$\varphi_j(y) \in C^1[0,h],\ (j=1,2),\ \varphi_3(y) \in C[0,h] \cap C^1(0,h),$$

$$\tilde{\psi}_1(x) \in C^1[1/2,1] \cap C^3\left(1/2,1\right),\ \ \tilde{\psi}_2(x) \in C[1/2,1] \cap C^2\left(1/2,1\right),$$

then there exists a unique solution to the Problem 2.2 in the domain Ω.

3. Existence of solution to Problem 2.1

Let us introduce the notation:

$$u(x,\pm 0) = \tau(x),\ u_y(x,\pm 0) = \nu(x),$$

now with regards (5) and gluing conditions, we get:

$$z(x,\pm 0) = \tau(x) - \omega(x),\quad 0 \le x \le 1, \tag{22}$$

$$\left.\frac{\partial z(x,y)}{\partial y}\right|_{y=\pm 0} = \nu(x),\quad 0 < x < 1. \tag{23}$$

A solution of the Darboux problem for the equation (6) with the boundary value conditions (18), (19) and (22) in the domain Ω_2 can be represented as:

$$\begin{gathered} z(x,y) = \tau^*(x+y) + \psi_1^*\left(\frac{x-y}{2}\right) - \psi_1^*\left(\frac{x+y}{2}\right) - \\ -\lambda y \int_0^{x+y} \tau^*(t)\bar{I}_1\left[\sqrt{\lambda(x-y-t)(x+y-t)}\right]dt + \sqrt{\lambda}\int_0^{y} \sin\sqrt{\lambda}\,(y-t)\,\psi_1^*(-t)dt+ \\ +\sqrt{2}\int_0^{y} \cos\sqrt{\lambda}(y-t)\psi_2^*(-t)dt + \lambda \int_0^{\frac{x-y}{2}} g_1\left(x-y,x+y,t\right)\psi_1^*(t)dt- \\ -\lambda \int_0^{\frac{x+y}{2}} g_1\left(x+y,x-y,t\right)\psi_1^*(t)dt + \sqrt{2}\int_0^{\frac{x-y}{2}} g_2\left(x-y,x+y,t\right)\psi_2^*(t)dt- \\ -\sqrt{2}\int_0^{\frac{x-y}{2}} g_2\left(x+y,x-y,t\right)\psi_2^*(t)dt-\sqrt{\frac{2}{\lambda}}\psi_2^*(0)\Big\{\sin\sqrt{\lambda}\left(\frac{x-y}{2}\right) - \\ -\sin\sqrt{\lambda}\left(\frac{x+y}{2}\right) + \sin\sqrt{\lambda}y + \lambda(x+y)\int_0^{\frac{x-y}{2}} \bar{I}_1\left[\sqrt{\lambda(x+y)(x-y-2t)}\right]\sin\sqrt{\lambda}tdt- \\ -\lambda(x-y)\int_0^{\frac{x+y}{2}} \bar{I}_1\left[\sqrt{\lambda(x-y)(x+y-2t)}\right]\sin\sqrt{\lambda}\,tdt\Big\}, \end{gathered} \tag{24}$$

where

$$g_1(x,y,t) = \frac{1}{\sqrt{\lambda}}\sin\sqrt{\lambda}\left(t-\frac{x}{2}\right) + y\bar{I}_1\left[\sqrt{\lambda y(x-2t)}\right] + \sqrt{\lambda}y\int_t^{x/2} \sin\sqrt{\lambda}(t-s)\bar{I}_1\left[\sqrt{\lambda y(x-2s)}\right]ds, \tag{25}$$

$$g_2(x,y,t) = \cos\sqrt{\lambda}\left(t-\frac{x}{2}\right) + \lambda y\int_t^{x/2} \cos\sqrt{\lambda}(t-s)\bar{I}_1\left[\sqrt{\lambda y(x-2s)}\right]ds, \tag{26}$$

$$\psi_1^*(x) = \psi_1(x) - \tilde{w}(x),\quad \psi_2^*(x) = \psi_2(x) - \frac{1}{\sqrt{2}}\tilde{w}'(x),$$

$$\tau^*(x) = \tau(x) - \tilde{w}(x),$$

$$\tilde{w}(x) = \frac{\mu}{\lambda}\int_0^{x} \left(1-\cosh\sqrt{\lambda}(x-t)\right)\sum_{i=1}^{n} a_i(t)D_{0t}^{\alpha_i}[\nu(t)-\tau(t)]dt,$$

$\bar{I}_1(x) = I_1(x)/x$, $I_1(x)$ is the modified Bessel function (Bessel function of the first kind with imaginary argument [19]).

Differentiating (24) with respect to y and passing through the limit $y \to +0$ with the preceding notations and (23), we obtain first functional relation between the function $\tau(x)$ and $\nu(x)$, transferred from the Ω_1 to AB:

$$\nu(x) + \mu \int_0^x L_1(x,t) \sum_{i=1}^n a_i D_{0t}^{\alpha_i} [\nu(t) - \tau(t)] dt - \tag{27}$$

$$-\mu \int_0^{x/2} L_2(x,t) \sum_{i=1}^n a_i D_{0t}^{\alpha_i} [\nu(t) - \tau(t)] dt = \tau'(x) - \lambda \int_0^x \tau(t) \bar{I}_1 \left[\sqrt{\lambda}(x-t) \right] dt + f(x),$$

where

$$L_1(x,t) = \frac{1}{\sqrt{\lambda}} \sinh \sqrt{\lambda}(x-t) + \int_t^x \left(1 - \cosh \sqrt{\lambda}(s-t)\right) \bar{I}_1 \left[\sqrt{\lambda}(x-s) \right] ds,$$

$L_2(x,t), f(x)$ are continuously differentiable functions.

Further, from (6) considering the property of Problem 2.1, (22) and (23), passing through the limit we obtain:

$$\tau''(x) - \lambda \tau(x) = k + \nu(x) + w''(x) - \lambda w(x), \tag{28}$$

where k is an unknown constant to be defined.

The equality (28) is a second functional relation between $\tau(x)$ and $\nu(x)$, transferred from the domain Ω_1 to AB.

Solving equation (28) with respect to $\tau(x)$ with the conditions:

$$\tau(0) = \varphi_1(0), \quad \tau'(0) = \varphi_3(0), \tag{29}$$

we have

$$\tau(x) = \int_0^x \frac{\sinh \sqrt{\lambda}(x-t)}{\sqrt{\lambda}} \nu(t)\, dt - \frac{\mu}{\lambda} \int_0^x \left(1 - \cosh \sqrt{\lambda}(x-t)\right) \sum_{i=1}^n a_i D_{ot}^{\alpha_i} [\nu(t) - \tau(t)]\, dt -$$

$$\frac{k}{\lambda} \left(1 - \cosh \sqrt{\lambda} x\right) + \varphi_1(0) \cosh \sqrt{\lambda} x + \frac{1}{\sqrt{\lambda}} \varphi_3(0) \sinh \sqrt{\lambda} x. \tag{30}$$

Thus, we get (27) and (30) system of the equations for the functions $\tau(x)$ and $\nu(x)$. If we write relation (30), in the form

$$\tau(x) - \frac{\mu}{\lambda} \int_0^x \left(1 - \cosh \sqrt{\lambda}(x-t)\right) \sum_{i=1}^n a_i D_{ot}^{\alpha_i} \tau(t)\, dt = \int_0^x \frac{\sinh \sqrt{\lambda}(x-t)}{\sqrt{\lambda}} \nu(t)\, dt -$$

$$\frac{\mu}{\lambda} \int_0^x \left(1 - \cosh \sqrt{\lambda}(x-t)\right) \sum_{i=1}^n a_i D_{ot}^{\alpha_i} \nu(t)\, dt - \tag{31}$$

$$\frac{k}{\lambda} \left(1 - \cosh \sqrt{\lambda} x\right) + \varphi_1(0) \cosh \sqrt{\lambda} x + \frac{1}{\sqrt{\lambda}} \varphi_3(0) \sinh \sqrt{\lambda} x,$$

and assuming that:

$$\Phi(x) = \int_0^x \frac{\sinh \sqrt{\lambda}(x-t)}{\sqrt{\lambda}} \nu(t)\, dt - \frac{\mu}{\lambda} \int_0^x \left(1 - \cosh \sqrt{\lambda}(x-t)\right) \sum_{i=1}^n a_i D_{ot}^{\alpha_i} \nu(t)\, dt - \tag{32}$$

$$\frac{k}{\lambda} \left(1 - \cosh \sqrt{\lambda} x\right) + \varphi_1(0) \cosh \sqrt{\lambda} x + \frac{1}{\sqrt{\lambda}} \varphi_3(0) \sinh \sqrt{\lambda} x,$$

for $\alpha_i < 0$ and $0 < \alpha_i < 1$ applying the Dirichlet permutation integration formula and corresponding to change of variables $s = t + (x-t)v$, we obtain the second kind Volterra type integral equation:

$$\tau(x) - \mu \int_0^x \widetilde{K}(x,t) \tau(t)\, dt = \Phi(x), \tag{33}$$

where

$$\widetilde{K}(x,t)=-\frac{(x-t)^{-\alpha_i}}{\lambda\Gamma(-\alpha_i)}\int\limits_0^1\frac{A_i\left(1-\cosh\left[\sqrt{\lambda_2}\,(x-t)(1+v)\right]\right)}{v^{1+\alpha_i}}dv,\ \text{at } \alpha_i<0,$$

and at $0<\alpha_i<1$,

$$\widetilde{K}(x,t)=\frac{(x-t)^{1-\alpha_i}}{\lambda\Gamma(1-\alpha_i)}\int\limits_0^1 v^{-\alpha_i}\frac{\partial}{\partial v}\Big[A_i\Big(1-\cosh[\sqrt{\lambda_2}\,(x-t)(1+v)]\Big)\Big]dv.$$

From the representations of the functions $\widetilde{K}(x,t)$ and $\Phi(x)$, based on the general theory of integral equations [11], one can be certain that (33) has a unique solution, which is represented as:

$$\tau(x)=\Phi(x)+\int\limits_0^x\widetilde{R}(x,t)\Phi(t)dt,\quad 0\le x\le 1, \tag{34}$$

where $\widetilde{R}(x,t)$ is the resolvent of the kernel $\widetilde{K}(x,t)$. Substituting (34) in (27), consider (32) and the sewing condition, we may obtain the integral equation with a a shift, with respect to $\nu(x)$, by which a kernel exists with weak singularity. Therefore, by using successive approximations [11], with regards to the conditions of the theorem and (32), we can uniquely define the function $\nu(x)$ at $\lambda\neq 0$, $a_i=a_i(x)\in C[0,1]\cap C^3(0,1)$. Upon determining $\tau(x)$ and $\nu(x)$, we find the functions $w(x)$ from (14). Hence, by virtue of the condition $\tau(1)=\varphi_2(0)-w(1)$, k are determined uniquely.

After finding $\tau(x)$ and $\nu(x)$, the solution of the Problem NP_1 defined in Ω_2 by formula Cauchy–Goursat (24) or Cauchy in [19] and in the domain Ω_1 we arrive to the problem for a non loaded equation of the third order [12].

Thus, we now know all particulars, such that the solution of Problem 2.1, in the domains Ω_1 and Ω_2 can be constructed from (5).

Problem 2.1 is uniquely solvable. Thus, Theorem 2.2 is proved. Analogously, one can also prove the uniqueness of the solution to Problem 2.2.

References

[1] Nakhushev A.M. Loaded equations and their applications, *Differential equations*, 1983, **19**(1), P. 86–94.

[2] Wiener J., Debnath L. Partial differential equations with piecewise constant delay, Internat. *J. Math. and Math. Scz.*, 1991, **14**, P. 485-496.

[3] Dzhenaliev M.T. *A remark on the theory of linear boundary value problems for loaded differential equations*. Almaty, Institute of Theoretical and Applied Mathematics, 1995, 270 p.

[4] Nakhushev A.M. *Equations of mathematical biology*. Vishaya shkola, Moscow, 1995, 302 p.

[5] Baltaeva U.I. Solvability of the analogs of the problem Tricomi for the mixed type loaded equations with parabolic-hyperbolic operators. *Boundary Value Problems*, 2014, **21**, P. 1–12.

[6] Nakhushev A.M. Nonlocal problem and the Goursat problem for loaded hyperbolic equation and their application in prediction of ground moisture. *Soviet Math. Dokl.*, 1978, **19**(5), P. 1243–1247.

[7] Kirillova S.A., Almjashev V.I., Gusarov V.V. Spinodal decomposition in the SiO_2-TiO_2 system and hierarchically organized nanostructures formation. *Nanosystems: Phys. Chem. Math.*, 2012, **3**(2), P. 100–115.

[8] Antonov N.M., Popov I.Yu., Gusarov V.V. Model of spinodal decomposition of phases under hyperbolic diffusion. *Physics of the Solid State*, 1999, **41**(5), P. 824–826.

[9] Melikhov I.F. Asymptotic solution of ultrasonic near-field levitation problem. *Nanosystems: Phys. Chem. Math.*, 2017, **8**(2), P. 260–265.

[10] Islomov B.I., Baltaeva U.I. Boundary value problems for the loaded equations of the hyperbolic and mixed types. *Ufa mathematical journal*, 2011, **3**(3), P. 15–25.

[11] Krasnov M.L. *Integral equations. Introduction to the theory*. Moscow, Nauka, 1975.

[12] Dzhurayev T.D., Sopuev A. and Mamayhonov M. *Boundary value problems for the problems for the parabolic-hyperbolic type equations*. Tashkent, Fan, 1986.

[13] Sabytov K.B. To the theory of mixed parabolic-hyperbolic type equations with a spectral parameter, *Differential equations*, 1989, **25**(1), P. 117–126.

[14] Salakhitdinov M.S., Urinov A.K. *Boundary value problems for equations of mixed type with a spectral parameter*. Tashkent, Fan, 1997.

[15] Berdyshev A.S. Non-local boundary value problems for the mixed type equation in a domain with deviation from a characteristic. *Differential equations*, 1993, **29**(12), P. 2118–2125.

[16] Serbina L.I. *Nonlocal mathematical models of transport processes in systems with a fractal structure*. Nal'chik, 2002, 144 p.

[17] Berdyshev A.S., Karimov E.T. Some non-local problems for the parabolic-hyperbolic type equation with non-characteristic line of changing type. *Differential equations*, 2006, **4**(2), P. 183–193.

[18] Kishin B. Sadarangani, Abdullaev Obidjon Kh. About a problem for loaded parabolic-hyperbolic type equation with fractional derivatives. *International Journal of Differential equations*, Volume 2016, Article ID 9815796, 6 p.

[19] Tikhonov A.N., Samarskij A.A. *Equations of Mathematical Physics*. Nauka, Moscow, 1966.

NANOSYSTEMS: PHYSICS, CHEMISTRY, MATHEMATICS, 2017, 8 (4), P. 420–425

Time dependent quantum graph with loop

D. A. Eremin[1], E. N. Grishanov[1], O. G. Kostrov[1], D. S. Nikiforov[2], I. Y. Popov[2]

[1]Department of Mathematics and IT, Ogarev Mordovia State University
Bolshevistskaya Str. 68, Saransk, Russia

[2]Department of Higher Mathematics, ITMO University, Kroverkskiy pr. 49, St. Petersburg, 197101, Russia
popov1955@gmail.com

PACS 03.65.-w, 02.30.Tb, 02.10.Db, 73.63.Nm **DOI 10.17586/2220-8054-2017-8-4-420-425**

A quantum graph, consisting of a ring and segment is considered. We deal with the free Schrödinger ooperator at the edges and Kirchhoff conditions at the internal vertex. The lengths of the graph edges varies in time. Time evolution of wave packet is studied for different parameters of length varying law.

Keywords: quantum graph, spectrum, time evolution.

Received: 26 May 2017

Revised: 20 June 2017

1. Introduction

A quantum graph is a rather old mathematical model introduced initially to aid in the description of macromolecules [1]. Later, it was used in many problems of quantum theory. In spite of its simplicity, the model gives one a powerful instrument for investigating quantum systems. As for rigorous mathematical models of such type, they appeared in the 80's [2]. The mathematical background of the approach is the theory of self-adjoint operator extensions (see, e.g., [3, 4] and references in [5]) related to model of point-like potentials in quantum physics. There are a large number of works in the field (see, e.g., [6–9] and references therein).

The problem of time-dependent boundary conditions in the Schrödinger equation has attracted much attention in the context of quantum Fermi acceleration [10]. A detailed study of the problem can be found in [11]. In particular, it was pointed out that the problem of 1D box with a moving wall can be mapped onto that of an harmonic oscillator with time-dependent frequency confined inside the static box. Time-dependent point-like potentials and related topics of the operator extensions theory were studied in several works (see, e.g., [12] and references therein). Star-like quantum graphs having edges with time varying lengths have been discussed [13]. Problems concerning the boundary conditions for time-depended interval are discussed in [14].

In the present paper, we consider simple quantum graph with a loop (see Fig. 1). The lengths of edges vary in time. We construct a mathematical model and investigate the time evolution of initial wave packet.

2. The description of the model

2.1. Stationary problem

To describe the system evolution, we start from the stationary problem. The quantum graph is determined in a conventional way. The Hamiltonian is the free Schrödinger operator, i.e. $-\frac{d^2}{dy^2}$, at each edge and the Kircchoff conditions at the internal vertex of the graph. The length of the segment is assumed to be 1, the circle radius is r. Let us mark the electron wave function as ϕ_ℓ at the segment and as ϕ_r at the ring. Then, one has the following equation at each edge:

$$-\frac{d^2}{dy^2}\phi_\ell(y) = k^2\phi_\ell(y), 0 \le y \le 1,$$

$$-\frac{d^2}{dy^2}\phi_r(y) = k^2\phi_r(y), 0 \le y \le 2\pi r,$$

$$\begin{cases} \phi_\ell(0) = \phi_r(0) = \phi_r(2\pi r), \\ \phi_\ell(\ell) = 0, \\ \frac{d}{dy}\phi_l|_{y=0} + \frac{d}{dy}\phi_r|_{y=0} - \frac{d}{dy}\phi_r|_{y=2\pi r} = 0. \end{cases}$$

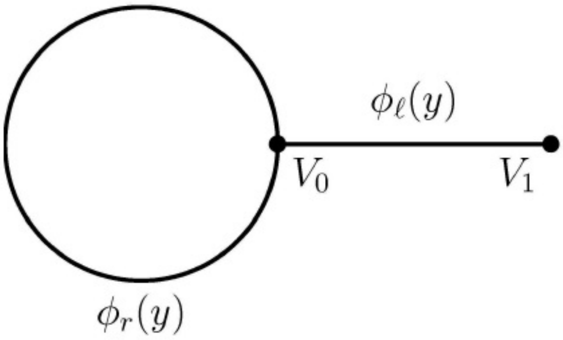

FIG. 1. Graph geometry

As for the boundary vertex of the graph, we assume here Dirichlet conditions. Eigenfunctions take the form:

$$\begin{aligned}\phi_\ell^{(n)}(y) &= \frac{1}{B_n}\frac{\sin(k_n(1-y))}{\sin(k_n)},\\ \phi_r^{(n)}(y) &= \frac{1}{B_n}\frac{\cos\left(k_n(y-\pi r)\right)}{\cos\left(k_n\pi r\right)},\end{aligned}$$

where k_n is the $n-$th positive root of the spectral equation having the form:

$$2\tan\left(\pi kr\right) = \cot k.$$

B_n is the normalizing constant:

$$B_n^2 = \frac{1}{2\sin^2(k_n)} + \frac{\pi r}{\cos^2(\pi k_n r)}.$$

2.2. Non-stationary problem

Let us consider a non-stationary graph. We assume that the edge lengths vary with time, $L_\ell = L(t)$, $L_r = 2\pi r L(t)$. Here, $L(t)$ is a smooth positive function (we will choose it later). In this case, the particle dynamics in graph are described by the following time-dependent Schrödinger equation:

$$\begin{aligned}\imath\frac{\partial}{\partial t}\Psi_\ell(x,t) &= -\frac{\partial^2}{\partial x^2}\Psi_\ell(x,t), 0\le x\le L(t),\\ \imath\frac{\partial}{\partial t}\Psi_r(x,t) &= -\frac{\partial^2}{\partial x^2}\Psi_r(x,t), 0\le x\le 2\pi r L(t),\end{aligned}$$

for the time-dependent wave function:

$$\Psi(t) = \begin{pmatrix}\Psi_\ell(x,t)\\ \Psi_r(x,t)\end{pmatrix}.$$

Here, the first argument of $\Psi_\ell(x,t)$ varies as follows $0\le x\le L(t)$ and the first argument of $\Psi_r(x,t)$ – in $0\le x\le 2\pi r L(t)$. We choose the system of units in which the Planck's constant, speed of light and the electron mass are as follows: $\hbar = c = 1$, $m = 1/2$. The following coupling conditions (Kircchoff conditions) take place at the internal vertex V_0 of the graph and the Dirichlet condition at vertex V_1:

$$\begin{cases}\Psi_\ell|_{x=0} = \Psi_r|_{\varphi=0} = \Psi_r|_{\varphi=2\pi r},\\ \Psi_\ell(L(t)) = 0,\\ \dfrac{\partial}{\partial x}\Psi_\ell|_{x=0} + \dfrac{\partial}{\partial x}\Psi_r|_{x=0} - \dfrac{\partial}{\partial x}\Psi_r|_{x=2\pi r} = 0.\end{cases} \tag{1}$$

Let us replace the variables at the edges: $y = \dfrac{x}{L(t)}$. Then, the equations change (we have the same equation both at the segment and at the ring, they differ only in variables range):

$$\imath\frac{\partial}{\partial t}\Psi_\ell(y,t) = -\frac{1}{L^2(t)}\frac{\partial^2}{\partial y^2}\Psi_\ell(y,t) + \imath\frac{\dot{L}(t)}{L(t)}y\frac{\partial}{\partial y}\Psi_\ell(y,t), \quad 0\le y\le 1,$$

$$\imath\frac{\partial}{\partial t}\Psi_r(y,t) = -\frac{1}{L^2(t)}\frac{\partial^2}{\partial y^2}\Psi_r(y,t) + \imath\frac{\dot{L}(t)}{L(t)}y\frac{\partial}{\partial y}\Psi_r(y,t), \quad 0\le y\le 2\pi r.$$

To obtain a self-adjoint problem, we make the following replacement:

$$\Psi(t)=\left(\begin{array}{c}\Psi_\ell(y,t)\\ \Psi_r(y,t)\end{array}\right)=\frac{1}{\sqrt{L(t)}}e^{\imath\frac{L\dot{L}}{4}y^2}\left(\begin{array}{c}\psi_\ell(y,t)\\ \psi_r(y,t)\end{array}\right).$$

Correspondingly, one has the following equations for functions $\psi_\ell(y,t),\psi_r(y,t)$:

$$\begin{aligned}\imath\frac{\partial}{\partial t}\psi_\ell(y,t)&=-\frac{1}{L^2(t)}\frac{\partial^2}{\partial y^2}\psi_\ell(y,t)+\frac{L\ddot{L}}{4}y^2\psi_\ell(y,t),\quad 0\le y\le 1,\\ \imath\frac{\partial}{\partial t}\psi_r(y,t)&=-\frac{1}{L^2(t)}\frac{\partial^2}{\partial y^2}\psi_r(y,t)+\frac{L\ddot{L}}{4}y^2\psi_\ell(y,t),\quad 0\le y\le 2\pi r.\end{aligned}\tag{2}$$

One can see that the Kirchoff conditions (1) remain for functions $\psi_\ell(y,t),\psi_r(y,t)$ at vertex V_0 and the Dirichlet conditions at V_1.

Taking into account that now the geometric graph is stationary after the chang of variables, we use the expansions with respect to complete system of orthogonal and normalized eigenfunctions of the self-adjoint operator (see Section 2):

$$\left(\begin{array}{c}\psi_\ell(y,t)\\ \psi_r(y,t)\end{array}\right)=\sum_n C_n(t)\left(\begin{array}{c}\phi_\ell^{(n)}(y)\\ \phi_r^{(n)}(y)\end{array}\right).\tag{3}$$

Let us insert (3) into (2) and (3). We obtain the system for coefficients C_n:

$$\imath\dot{C}_m(t)=-\frac{k_m^2}{L^2}C_m(t)+\sum_n M_{mn}C_n(t),\tag{4}$$

where:

$$M_{mn}=\frac{L\ddot{L}}{4}\left(\int\limits_0^1 y^2\phi_\ell^{(n)}(y)\overline{\phi_\ell^{(m)}(y)}dy+\int\limits_0^{2\pi r} y^2\phi_r^{(n)}(y)\overline{\phi_r^{(m)}(y)}dy\right).\tag{5}$$

This is an infinite system. We truncate it and numerically solve the obtained finite-size system. To consider the evolution of wave packet, we realize the following procedure: we take some initial value for the wave function, expand it in a series, truncate the series, solve the system for coefficients and summarize the series with coefficients corresponding to chosen time value. Correspondingly, we choose the initial condition:

$$\Psi(0)=\left(\begin{array}{c}\Psi_l(x,0)\\ \Psi_r(x,0)\end{array}\right).$$

The initial values for $\psi_\ell(y,t),\psi_r(y,t)$ are obtained in the following way:

$$\left(\begin{array}{c}\psi_\ell(y,0)\\ \psi_r(y,0)\end{array}\right)=\left(\begin{array}{c}L(0)e^{-\imath\frac{L(0)\dot{L}(0)}{4}y^2}\Psi_\ell(y,0)\\ 0\end{array}\right).$$

Correspondingly, the initial values for our system of ordinary differential equation are as follows:

$$C_n(0)=\int\limits_0^1\psi_\ell(y,0)\overline{\phi_\ell^{(n)}}dy.\tag{6}$$

The solution of the system (4) gives us values for $C_n(t)$. By inserting it into (3), we obtain the wave function for the moment t.

3. Results and discussion

We will choose the particular type of length variation, namely, the harmonic dependence:

$$L(t)=a+b\cos(\omega t).\tag{7}$$

Here, ω is the frequency of the length vibration. We take the following initial wave function (concentrated at the segment):

$$\Psi(0)=\left(\begin{array}{c}\Psi_l(x,0)\\ \Psi_r(x,0)\end{array}\right)=\left(\begin{array}{c}(1-\cos(2\pi x))\sqrt{2/3}\\ 0\end{array}\right).$$

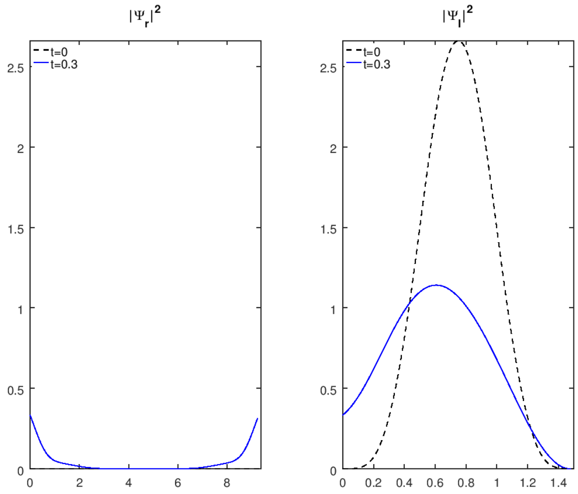

FIG. 2. The wave function at the ring (left) and segment (right) $t = 0$, $t = 0.3$ (arbitrary units)

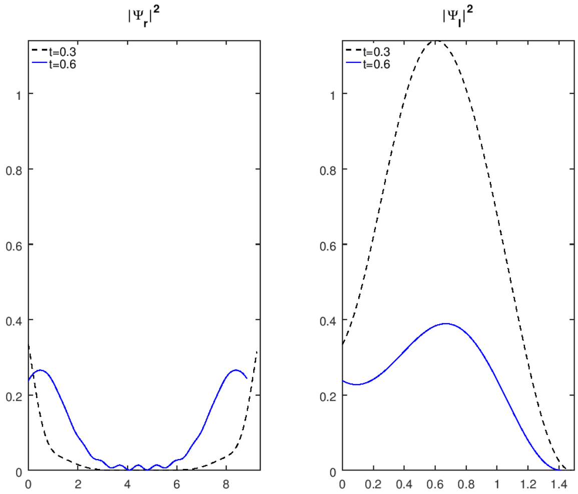

FIG. 3. The wave function at the ring (left) and segment (right) $t = 0.3$, $t = 0.6$ (arbitrary units)

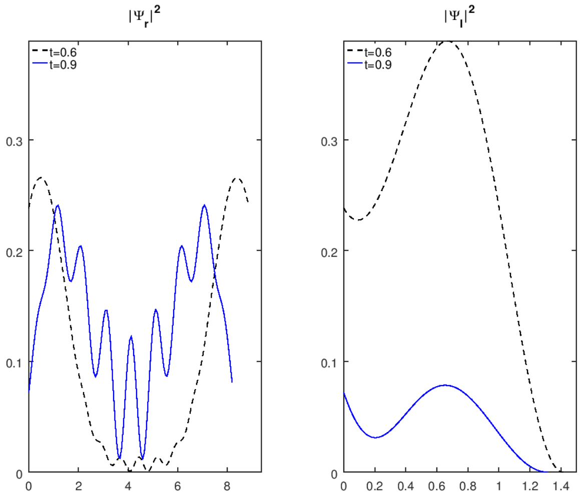

FIG. 4. The wave function at the ring (left) and segment (right) $t = 0.6$, $t = 0.9$ (arbitrary units)

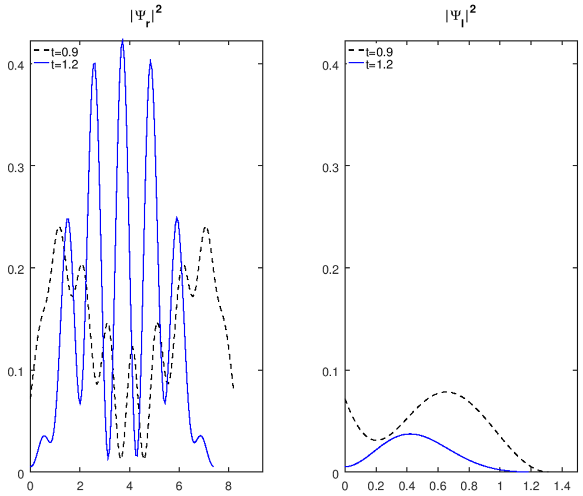

FIG. 5. The wave function at the ring (left) and segment (right) $t = 0.9$, $t = 1.2$ (arbitrary units)

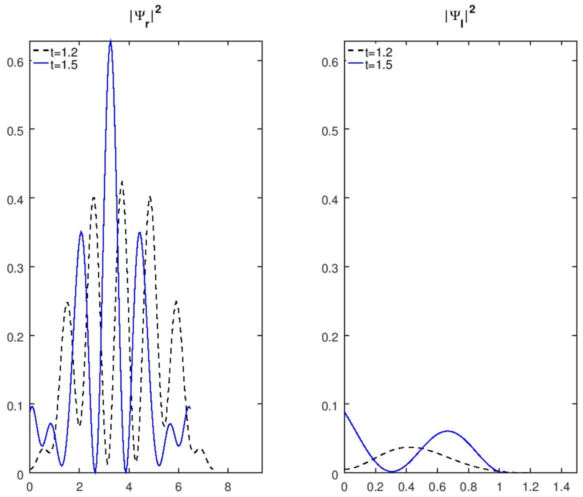

FIG. 6. The wave function at the ring (left) and segment (right) $t = 1.2$, $t = 1.5$ (arbitrary units)

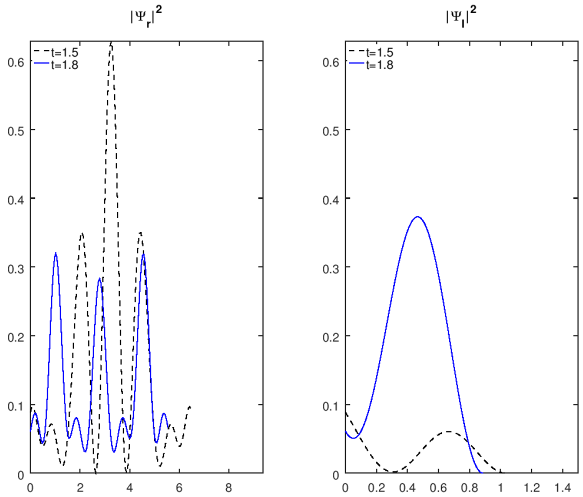

FIG. 7. The wave function at the ring (left) and segment (right) $t = 1.5$, $t = 1.8$ (arbitrary units)

The wave function for the time moment t is obtained by the procedure described in the previous section. The following parameters are chosen: $a = 1$, $b = 1/2$, $\omega = 1$, $r = 1$. Time evolution of the wave packet is shown in Figs. 2–7, corresponding to time values $t = 0$, $t = 1.1$, $t = 1.3$, $t = 1.4$ in initial coordinate system.

Acknowledgements

This work was partially financially supported by the Government of the Russian Federation (grant 074-U01), by grant MK-5161.2016.1 of the President of the Russian Federation, DFG Grant NE 1439/3-1, by grant 16-11-10330 of Russian Science Foundation.

References

[1] Pauling L. The Diamagnetic Anisotropy of Aromatic Molecules. *J. Chem. Phys.*, 1936, **4**, P. 673.

[2] Gerasimenko N.I., Pavlov B.S. Scattering problems on noncompact graphs. *Theoret. Math. Phys.*, 1988, **74**, P. 230–240.

[3] Albeverio S., Gesztesy F., Hoegh-Krohn R., Holden H. with an appendix by P. Exner. *Solvable Models in Quantum Mechanics: Second Edition*, 2005. (Providence, R.I.: AMS Chelsea Publishing).

[4] Pavlov B.S. The theory of extensions and explicity-solvable models. *Russ. Math. Surv.*, 1987, **42**(6), P. 127–168.

[5] Popov I.Y., Kurasov P.A., Naboko S.N., Kiselev A.A., Ryzhkov A.E., Yafyasov A.M., Miroshnichenko G.P., Karpeshina Yu.E., Kruglov V.I., Pankratova T.F., Popov A.I. A distinguished mathematical physicist Boris S. Pavlov. *Nanosystems: Physics, Chemistry, Mathematics*, 2016, **7**, P. 782–788.

[6] Exner P., Keating P., Kuchment P., Sumada T., Teplyaev A. Analysis on graph and its applications. Proc. Symp. Pure Math. Providence, RI, 2008, **77**.

[7] Duclos P., Exner P., Turek O. On the spectrum of a bent chain graph. *J. Phys. A: Math. Theor.*, 2008, **41**, P. 415206/1-18.

[8] Popov I.Y., Skorynina A.N., Blinova I.V. On the existence of point spectrum for branching strips quantum graph. *J. Math. Phys.*, 2014, **55**, P. 033504/1-20.

[9] Popov I.Y., Smirnov P.I. Spectral problem for branching hain quantum graph. *Phys. Lett.*, 2013, **A 377**, P. 439–442.

[10] Jose J.V., Gordery R. Study of a quantum Fermi-acceleration model. *Phys. Rev. Lett.*, 1986, **56**, P. 290.

[11] Makowski A.J., Dembinski S.T. Exactly solvable models with ime-dependent boundary conditions. *Phys. Lett.*, 1991, **A, 154**(5-6), P. 217–220.

[12] Cacciapuoti C., Mantile A., Posilicano A. Time dependent delta-prime interactions in dimension one. *Nanosystems: Phys. Chem. Math.*, 2016, **7**(2), P. 303–314.

[13] Matrasulov D.U., Yusupov J.R., Sabirov K.K., Sobirov Z.A. Time-dependent quantum graph. *Nanosystems: Phys. Chem. Math.*, 2015, **6**(2), P. 173–181.

[14] Karpova O., Sabirov K., Otajanov D., Ruzmetov A., Saidov A.A. Absorbing boundary conditions for Schrödinger equation in a time-dependent interval. *Nanosystems: Phys. Chem. Math.*, 2017, **8**(1), P. 13–19.

NANOSYSTEMS: PHYSICS, CHEMISTRY, MATHEMATICS, 2017, 8 (4), P. 426–434

Mathematical modeling of magnetic field guided colloidal particle deposition with significant electric double layer interactions

A. V. Alfimov, M. A. Shumova, E. M. Aryslanova, S. A. Chivilikhin
ITMO University, Kronverkskiy, 49, St. Petersburg, 197101, Russia
alfimov.anton@gmail.com

PACS 82.70.Dd, 75.75.Jn, 47.63.mh, 47.57.J- **DOI 10.17586/2220-8054-2017-8-4-426-434**

In this work, we propose a simple theoretical method for predicting the rate and localization of magnetic field guided particle deposition from aqueous colloids. This method accounts for the colloidal electric double layer interactions between particles and vessel walls. The obtained results suggest that the colloidal interactions can be used to increase the rate of particle deposition and improve its localization.

Keywords: particle deposition, magnetic nanoparticles, magnetic particle targeting.

Received: 1 July 2017

Revised: 25 July 2017

1. Introduction

Colloidal solutions of magnetic particles find an increasing number of applications in biomedicine and microfluidics. This is due to the fact that the transport of these particles can be remotely controlled through application of a local magnetic field.

The biocompatibility and non-toxicity of magnetic colloids has led to their extensive use in the following: targeted drug delivery [1–6]; clinical diagnostics as contrast agents for magnetic resonance imaging [6–10]; tumor therapy by controlled hyperthermia [9–12]; cytological studies [13–17]; and in catheter embolization of blood vessels [18].

The precise control and numerous manipulation techniques for magnetic delivery enable its applications in chemical analysis and processing [19–21], lab-on-a-chip construction [21–23], and in the fabrication of functional materials [24–26].

When magnetic deposition is used for guided transport and assembly of colloidal matter, the electric double layer forces can match or even exceed the driving magnetic force. However, this type of interaction is generally omitted from theoretical studies of field guided magnetic particle transport [2, 27–30].

The aim of this work is to develop a theoretical description of magnetic particle deposition that accounts for the colloidal electric double layer interactions between the particles and the vessel walls.

2. Methods

2.1. Model system

We consider an aqueous colloidal solution of spherical magnetic particles flowing through a capillary and subjected to the field of a permanent rectangular magnet (see Fig. 1A). Two coordinate systems are used throughout this work, with Cartesian coordinates (x, y, z) linked to the magnet and cylindrical coordinates (r, θ, z) linked to the capillary.

The capillary is characterized by its internal radius R and the closest separation L between the tube interior and the magnet. The permanent magnet has the dimensions d_x, d_y, d_z along the respective axes.

The particles have a compound structure with superparamagnetic cores embedded in a functionalized shell (see Fig. 1B). The cores transport the functional materials contained in the shell, guided by the applied magnetic field.

2.2. Magnetic force

The force $\mathbf{F}_\mathrm{M}$ acting on a particle containing superparamagnetic cores in a magnetic field $\mathbf{B}$ is given by [31]:

$$\mathbf{F}_\mathrm{M} = M_\Sigma \nabla |\mathbf{B}|, \tag{1}$$

where M_Σ is the total magnetic moment of the particle cores along the applied field. The magnetic moment of an ensemble of identical superparamagnetic cores above the blocking temperature can be expressed as [32]:

$$M_\Sigma = N M_0 \Lambda \left(\frac{M_0 |\mathbf{B}|}{kT} \right), \tag{2}$$

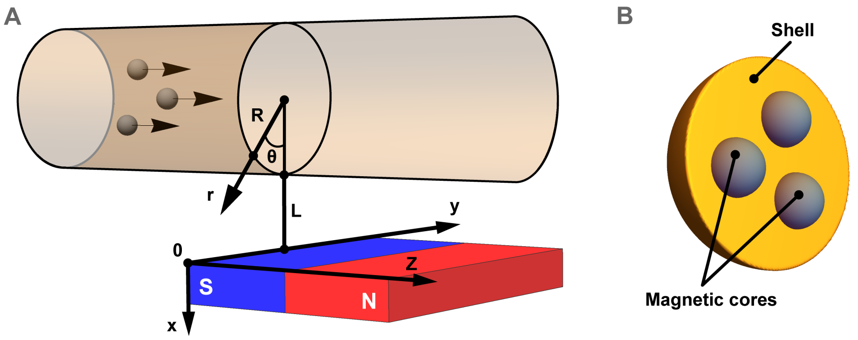

FIG. 1. A – Schematic depiction of model system. B – Model particle structure

where $\Lambda(\xi) = \coth(\xi) - 1/\xi$ – Langevin function; N – number of magnetic cores in the particle; M_0 – maximum magnetic moment of a single core; k – Boltzmann constant; T – temperature. The value of M_0 can be found by fitting an experimental magnetization curve with the expression (2).

We use the analytic expressions from [33] to find the components of the magnetic field due a rectangular permanent magnet;

$$B_x(x,y,z) = -\frac{K}{2}\Big[\Gamma(d_x - x, y, z - z_0) + \Gamma(d_x - x, d_y - y, z - z_0) - \Gamma(x, y, z - z_0) - \Gamma(x, d_y - y, z - z_0)\Big]_{z_0=0}^{z_0=d_z}, \quad (3)$$

$$B_y(x,y,z) = -\frac{K}{2}\Big[\Gamma(d_y - y, x, z - z_0) + \Gamma(d_y - y, d_x - x, z - z_0) - \Gamma(y, x, z - z_0) - \Gamma(y, d_x - x, z - z_0)\Big]_{z_0=0}^{z_0=d_z}, \quad (4)$$

$$\begin{aligned} B_z(x,y,z) = \\ -K\Big[&\Phi(y, d_x - x, z - z_0) + \Phi(d_y - y, d_x - x, z - z_0) + \Phi(x, d_y - y, z - z_0) + \Phi(d_x - x, d_y - y, z - z_0) + \\ &\Phi(d_y - y, x, z - z_0) + \Phi(y, x, z - z_0) + \Phi(d_x - x, y, z - z_0) + \Phi(x, y, z - z_0)\Big]_{z_0=0}^{z_0=d_z}, \quad (5) \end{aligned}$$

where K is a parameter characterizing the magnetization of the permanent magnet:

$$\Gamma(\xi_1, \xi_2, \xi_3) = \ln\left[\frac{\sqrt{\xi_1^2 + \xi_2^2 + \xi_3^2} - \xi_2}{\sqrt{\xi_1^2 + \xi_2^2 + \xi_3^2} + \xi_2}\right],$$

$$\Phi(\xi_1, \xi_2, \xi_3) = \begin{cases} \arctan\left[\dfrac{\xi_1}{\xi_2}\dfrac{\xi_3}{\sqrt{\xi_1^2 + \xi_2^2 + \xi_3^2}}\right], & y \neq 0; \\ 0, & y = 0. \end{cases}$$

2.3. Colloidal force

Solid-liquid interfaces tend to acquire charge due to surface group reactions, leading to the formation of electric double layers (EDLs) [34]. Overlapping diffuse parts of EDLs give rise to colloidal interaction forces between interfaces. For like-charged surfaces, these forces typically are repulsive [35].

The colloidal EDL interaction is completely defined by the interfacial charges and the spatial distribution of dissolved ions compensating those charges. It has been shown that the characteristic time scales of ion and particle motion allow one to approach the EDL structure problem as quasi-electrostatic [34]. For systems with low-to-medium surface potentials and absence of multivalent electrolytes in the solution, the mean-field Poisson-Boltzmann theory provides an adequate description of ion and potential distributions in the system [35].

In present work, we only consider the interactions between particles and capillary walls. The capillary radius R is taken to be much larger than the particle radius a and the characteristic charge-screening distance in the solution

(Debye length is less than 1 μm in aqueous solutions). Therefore, we can use the Poisson–Boltzmann equation solution for a flat wall to describe the electric potential distribution $\phi(r)$ in capillary's EDL [35]:

$$\phi(r) = 2\frac{kT}{e}\ln\left(\frac{1+\lambda\exp\left[-\kappa\left(R-r\right)\right]}{1-\lambda\exp\left[-\kappa\left(R-r\right)\right]}\right), \quad \lambda = \tanh\left(\frac{e\zeta_{\mathrm{C}}}{4kT}\right), \tag{6}$$

where ζ_{C} – surface (zeta) potential of capillary walls; κ – inverse Debye screening length:

$$\kappa^2 = \frac{2I\,e^2}{\varepsilon\varepsilon_0 kT},$$

I – ionic strength of the solution; ε – dielectric permittivity of the solution; ε_0 – dielectric constant.

The dominant component of the colloidal EDL interaction is given by the electrostatic force exerted on the particles by the charged capillary wall and the ions of its EDL. This force can be found from (6) as [35]:

$$\mathbf{F}_{\mathrm{C}} = \mathbf{n}_{\mathrm{W}} Q_{\mathrm{eff}} 4\frac{kT}{e}\frac{\kappa\lambda\exp\left[-\kappa\left(R-r\right)\right]}{1-\left(\lambda\exp\left[-\kappa\left(R-r\right)\right]\right)^2}, \tag{7}$$

where $\mathbf{n}_{\mathrm{W}} = -\mathbf{r}/|\mathbf{r}|$ – unit vector normal to the capillary wall, pointing inwards; Q_{eff} – effective particle charge that can be related to particle surface (zeta) potential ζ_{P} as [36]:

$$Q_{\mathrm{eff}} = 4\pi\varepsilon\varepsilon_0\,\zeta_{\mathrm{P}} a\exp\left(\kappa a\right).$$

2.4. Magnetic particle deposition

We now study the motion of magnetic particles in the described system. The particles are considered to be carried through the capillary by a laminar liquid flow exhibiting Poiseuille velocity profile. Only the most significant forces acting on the particles are considered: the magnetic force, the viscous drag and the colloidal EDL interaction with capillary walls. The resulting equations of motion for a magnetic colloidal particle are:

$$\begin{aligned} \dot{\mathbf{V}} &= \frac{\mathbf{F}_{\mathrm{M}}+\mathbf{F}_{\mathrm{C}}}{m} - \gamma\left(\mathbf{V}-\mathbf{V}_{\mathrm{P}}\right), \\ \mathbf{V}|_{t=0} &= \mathbf{V}_0, \end{aligned} \tag{8}$$

where $\mathbf{V}$ – particle velocity; $\mathbf{F}_{\mathrm{M}}$ – magnetic force (1); $\mathbf{F}_{\mathrm{C}}$ – colloidal force (7); m – total mass of the particle; $\gamma = 6\pi\eta a/m$ – viscous friction coefficient; η – dynamic viscosity of the liquid; $\mathbf{V}_{\mathrm{P}}$ – liquid flow velocity given by:

$$\mathbf{V}_{\mathrm{P}} = \mathbf{i}_z V_{\mathrm{P}}^{\max}\left(1-\frac{r^2}{R^2}\right), \tag{9}$$

here $\mathbf{i}_z$ – unit vector in the direction of z axis; $V_{\mathrm{P}}^{\max}$ – maximum flow velocity.

When the inertial term $\dot{\mathbf{V}}$ in (8) is negligible, the system evolves in a quasi-stationary regime (QSR). The velocity a particle would have in QSR is denoted as $\mathbf{U}$ and can be found from (8) as:

$$\mathbf{U} = \frac{\mathbf{F}_{\mathrm{M}}+\mathbf{F}_{\mathrm{C}}}{\gamma m} + \mathbf{V}_{\mathrm{P}}. \tag{10}$$

We will now derive a sufficient *a priori* condition for the quasi-stationary regime in the considered system.

The solution to the original system (8) has the following form:

$$\mathbf{V} = \mathbf{V}_0 e^{-\gamma t} + \int\limits_0^t e^{-\gamma\left(t-t'\right)}\left(\frac{\mathbf{F}_{\mathrm{M}}+\mathbf{F}_{\mathrm{C}}}{m} + \gamma\mathbf{V}_{\mathrm{P}}\right)\mathrm{d}t'. \tag{11}$$

We note that by using the definition (10), the solution (11) can be rewritten as:

$$\mathbf{V} = \mathbf{V}_0 e^{-\gamma t} + \gamma\int\limits_0^t e^{-\gamma\left(t-t'\right)}\mathbf{U}(t')\mathrm{d}t'. \tag{12}$$

Expression (12) describes a system with memory of its previous states, and the memory function is decaying exponentially. The memory span of this system can be estimated as $\Delta t = 3/\gamma$, corresponding to a tenfold decay of the exponential function.

Therefore, the particle velocity when $t > \Delta t$ can be found as:

$$\mathbf{V} = \gamma\int\limits_{t-\Delta t}^{t} e^{-\gamma\left(t-t'\right)}\mathbf{U}(t')\mathrm{d}t'. \tag{13}$$

From the first mean value theorem for definite integrals, there is such $\tilde{t}_i$, $t - \Delta t < \tilde{t}_i < t$, that:

$$V_i(t) = U_i(\tilde{t}_i)\gamma \int\limits_{t-\Delta t}^{t} e^{-\gamma(t-t')}\mathrm{d}t' = U_i(\tilde{t}_i), \tag{14}$$

where $i = x, y, z$ – coordinate index; V_i, U_i – i-th component of particle velocity vector and quasi-stationary velocity vector respectively.

According to (14), when the QSR velocity U_i varies insignificantly over the time Δt so that $U_i(\tilde{t}_i) \approx U_i(t)$, the quasi-stationary regime ensues. Hence, we can formulate the sufficient condition for the QSR:

$$\left| \frac{U_i(t) - U_i(t - \Delta t)}{U_i(t)} \right| \ll 1. \tag{15}$$

This condition, however, requires the prior knowledge of particle trajectories and cannot be checked *a priori*.

We now assume that the quasi-stationary velocity U_i varies linearly with time over the course of Δt:

$$U_i(t) - U_i(t - \Delta t) \;=\; \dot{U}_i\Big|_t \Delta t.$$

Then, the condition (15) reduces to:

$$\Delta t \left| \frac{\dot{U}_i\Big|_t}{U_i(t)} \right| \ll 1. \tag{16}$$

We note that when the forces acting on the particle and the liquid flow velocity profile do not change in time, the following is true:

$$\dot{U}_i = (\mathbf{V} \cdot \nabla U_i). \tag{17}$$

From the definition of $\tilde{t}_i$, it follows that:

$$t - \tilde{t}_i = \alpha_i \,\Delta t, \quad 0 < \alpha_i < 1, \tag{18}$$

and, using (14):

$$V_i(t) = U_i(\tilde{t}_i) = U_i(t) - \dot{U}_i\Big|_t \alpha_i \Delta t. \tag{19}$$

If the condition (16) is satisfied for all coordinates:

$$|U_i| \gg \Delta t \left|\dot{U}_i\right|, \quad \forall i, \quad i = x,\, y,\, z,$$

then, according to (18):

$$|U_i| \gg \alpha_i \Delta t \left|\dot{U}_i\right|, \quad \forall i, \quad i = x,\, y,\, z. \tag{20}$$

Thus, combining (17), (19) and (20), we can finally rewrite the sufficient condition for quasi-stationary regime (16) as:

$$\Delta t \left| \frac{(\mathbf{U} \cdot \nabla U_i)}{U_i} \right| \ll 1, \quad \forall i, \quad i = x,\, y,\, z. \tag{21}$$

The resulting expression (21) can be directly evaluated at each point of the considered system and does not require the prior knowledge of particle trajectories. Therefore, (21) is the sufficient *a priori* condition for the quasi-stationary regime.

In areas where condition (21) is met, the magnetic particle velocity field can be obtained directly from (10).

To evaluate the rate and the localization of the particle deposition in an external magnetic field, we use the obtained velocity field to calculate the particle flux onto the capillary walls. From the continuity equation for a steady flow $\nabla \cdot (C\mathbf{U}) = 0$, we get the following expression for the particle flux j_{P}:

$$j_{\mathrm{P}} = (\mathbf{n}_{\mathrm{W}} \cdot \mathbf{U})\, C_0 \exp\left[-\int\limits_{0}^{t} (\nabla \cdot \mathbf{U})\, \mathrm{d}t' \right], \tag{22}$$

where C – local particle concentration; C_0 – particle concentration far from the magnet.

3. Results and discussion

We presented a simple theoretical method for predicting the particle flux during the magnetic deposition from colloids that accounts for the EDL interactions between particles and capillary walls. The method is realized in three steps:

(1) Evaluation of the quasi-stationary regime condition (21) for the considered system to check for the method applicability.
(2) Analytical calculation of the particle velocity field from (10).
(3) Numerical computation of the particle flux onto the capillary walls using (22).

Note that for the rough estimate of particle flux, the local particle concentration can be equated to the bulk concentration C_0, resulting in analytical expression for the flux: $j_\mathrm{P} = (\mathbf{n}_\mathrm{W} \cdot \mathbf{U})\, C_0$.

Condition (21) poses limits on the spatial rate of change for forces acting on the particle and on the maximum velocity of the flow. For colloidal interactions, this generally means that the method is applicable for systems with either very high ionic strength (so that the EDL forces are rendered insignificant), or low ionic strength (less than 10^{-5} M).

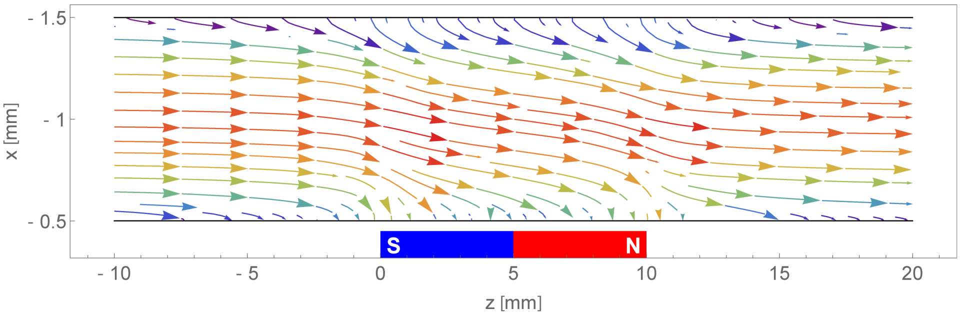

FIG. 2. Streamlines of particle velocity field in the capillary central cross section perpendicular to the surface of the magnet and the direction of liquid flow. Inner capillary radius $R = 0.5$ mm; distance from the magnet $L = 0.5$ mm (depicted not to scale); particles with radius of $a = 600$ nm are submerged in water at room temperature flowing with maximum velocity of $\mathrm{V}_P^{\max} = 0.2$ m/s; Reynolds number $Re = 10^2$

We now demonstrate how the suggested method can be used to study the effects of system parameters on magnetic particle deposition.

Properties of the magnetic cores are chosen to reflect those of the 10 nm magnetite nanoparticles reported in [37], with maximum magnetic moment of a single core $M_0 = 178 \cdot 10^{-21}$ N·m/T. The bulk particle concentration is fixed at $C_0 = 10^{15}$ 1/m^3.

With the functional material located in the particle shell, we take the shell volume to be the same for all considered particle sizes and equal to 0.065 μm^3. Because of that, the shell material mass flux is always directly proportional to the particle flux demonstrated in the following sections.

For simplicity, in this work we consider the surface potentials of the capillary and the particles to be equal: $\zeta_\mathrm{C} = \zeta_\mathrm{P} = \zeta$.

The parameters of the magnet are based on the rectangular neodymium magnet from [37], with dimensions of $d_x = 30$ mm, $d_y = 20$ mm, $d_z = 10$ mm and magnetization constant $K = 0.269$ N/A·m^2.

A typical particle velocity field for such systems is depicted in Fig. 2.

3.1. Particle flux in a system imitating a blood vessel

First, we consider a model system with parameters matching those of a human artery. The liquid is at body temperature and has the viscosity and the ionic strength of blood ($\eta = 2.8$ mPa·s and $I = 154$ mM). At high ionic strength values for this system, the EDL interactions are usually insignificant [35]. Maximum flow velocity is $V_\mathrm{P}^{\max} = 0.9$ m/s, inner vessel radius is $R = 2$ mm, Reynolds number is $Re = 6 \cdot 10^2$.

The deposition of 3 μm magnetic particles under the applied magnetic field is studied for three different separations between the vessel interior and the magnet (see Fig. 3). These correspond to different blood vessel depths. As demonstrated in Fig. 3, the suggested method allows prediction of both the rate and localization of particle deposition for the considered systems. As the magnetic force decays further away from the magnet, the particles flux decreases and becomes less localized.

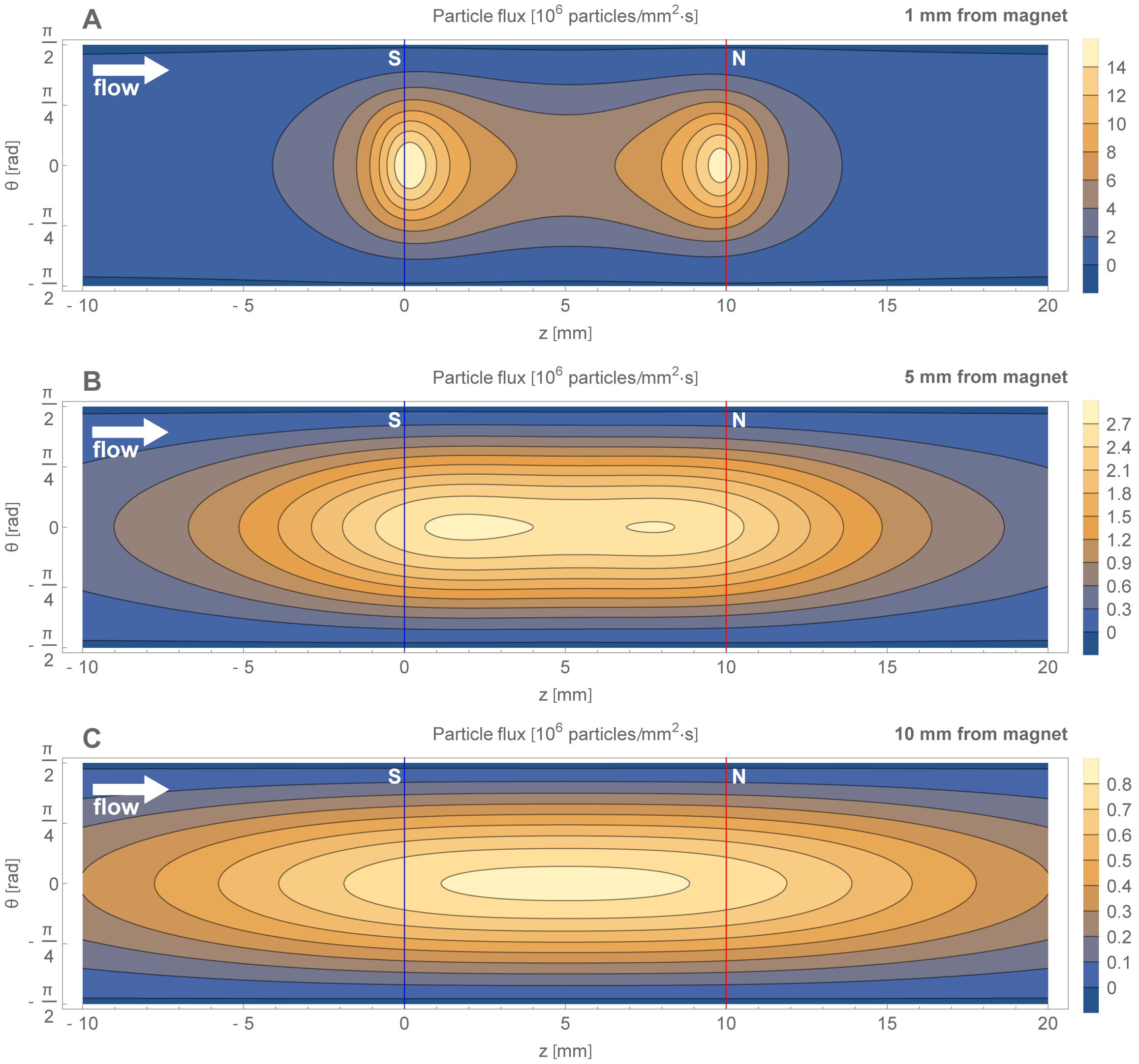

FIG. 3. Particle flux distribution over the capillary wall in a system imitating human artery with the vessel interior separated from the magnet by: A – 1 mm, B – 5 mm, C – 10 mm. Lines indicate the location of magnetic poles beneath the capillary

For a given vessel depth, the particle flux can be adjusted by changing the volume of magnetic cores embedded in the particle. This is illustrated in Fig. 4.

3.2. Particle flux in a microfluidic system at low ionic strength

Second, we consider a system with magnetic particles carried by an aqueous solution with low ionic strength. In this case, the EDL interaction between the particles and the capillary walls can be significant, depending on their surface potentials.

The liquid is at room temperature and has an ionic strength of $I = 10^{-3}$ mM. Maximum flow velocity is $V_{\mathrm{P}}^{\max} = 0.5$ m/s, capillary interior is separated from the magnet by $L = 1$ mm and has the radius of $R = 0.5$ mm; Reynolds number is $Re = 3 \cdot 10^2$.

The magnetic deposition of 700 nm particles is compared for different values of surface potentials in the system (see Fig. 5). When a non-negligible interfacial charge is present, a repulsion counteracting the magnetic force arises. As a result, with increasing surface potential the area of particle deposition localization decreases (see Fig. 5B,C) until the particle flux onto the capillary wall is terminated.

At the same time, colloidal EDL forces slow down the approaching particles and focus them around the magnet poles, thus increasing the local particle concentration. This may result in a higher particle flux when compared to a system with no colloidal repulsion, as seen in Fig. 5A,B. Further rise in surface potential, however, will lead to

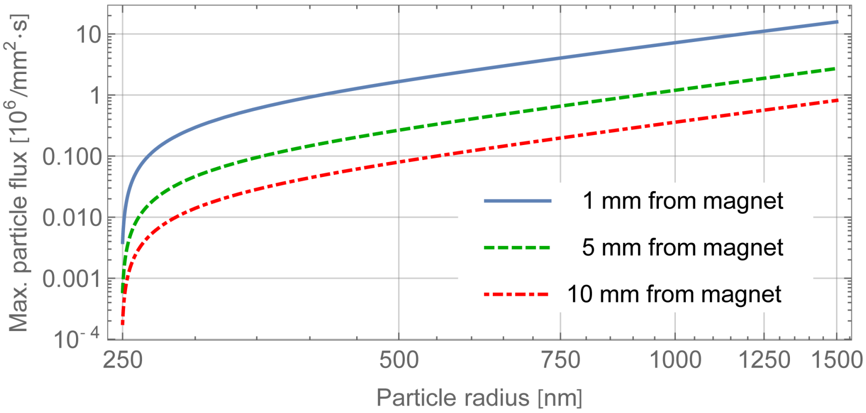

FIG. 4. Maximum particle flux as a function of particle size (with shell volume being fixed) at different separations between vessel interior and the magnet

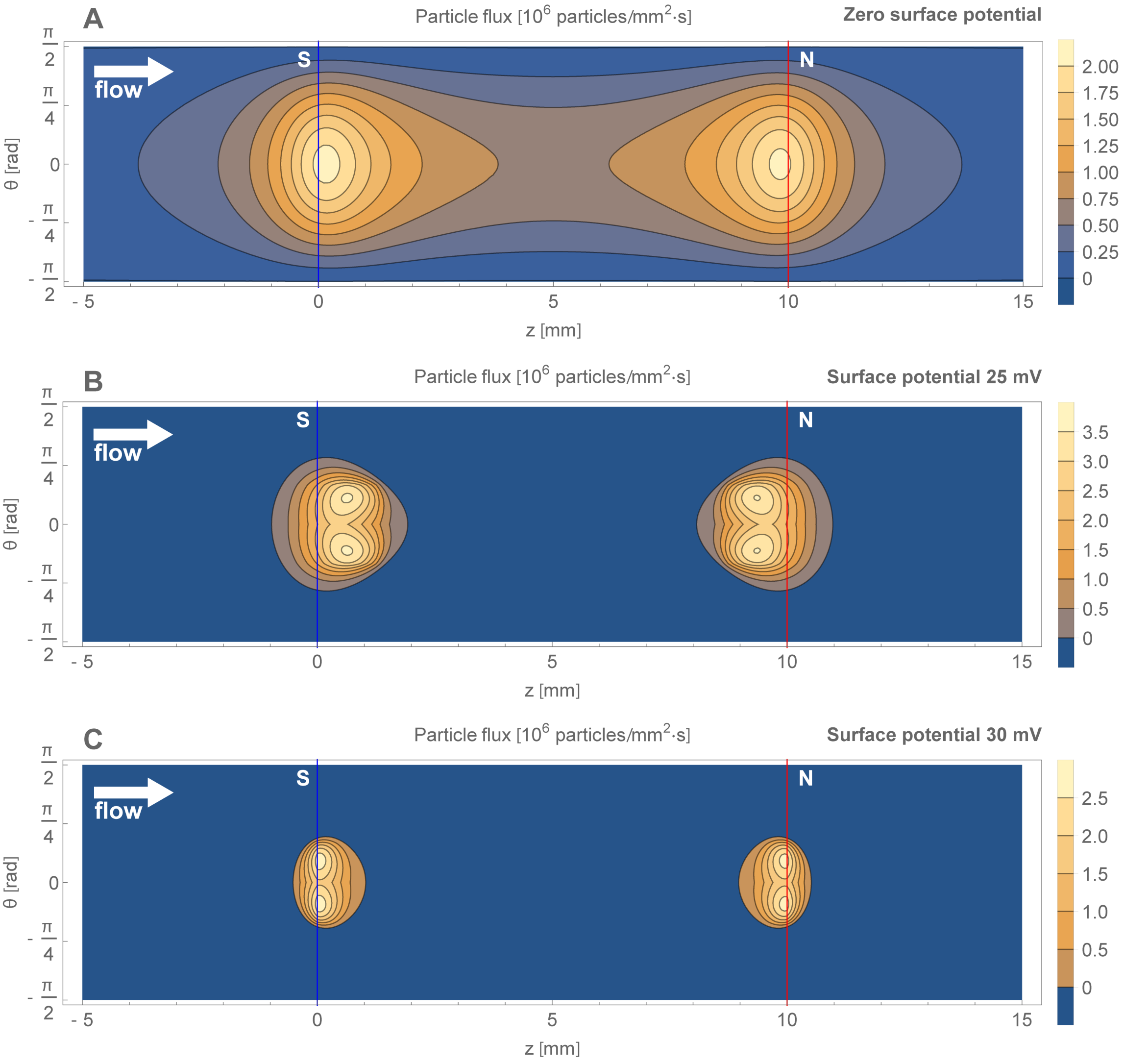

FIG. 5. Particle flux distribution over the capillary wall in systems exhibiting different surface potential: A – 0, B – 25 mV, C – 30 mV. Lines indicate the location of magnetic poles beneath the capillary

particle flux decrease (compare Fig. 5B,C). This is due to particle velocity drop overpowering the gain in local concentration. The balancing between particle concentration and velocity near capillary wall also explains the bifurcation of the flux maxima observed in Fig. 5.

4. Conclusions

The work proposes a simple theoretical method for predicting the rate and localization of magnetic particle deposition from aqueous colloids. This method accounts for electric double layer interactions between particles and capillary walls in low ionic strength solutions. When applicable, the method allows one to estimate the system parameters required for achieving a specified deposition regime.

The results obtained for the magnetic deposition with significant electric double layer forces suggest that the presence of colloidal interactions can increase the rate of particle deposition and improve its localization.

References

[1] Al-Jamal K.T., Bai J., Wang J.T.-W., Protti A., Southern P., Bogart L., Heidari H., Li X., Cakebread A., Asker D., Al-Jamal W.T., Shah A., Bals S., Sosabowski J., Pankhurst Q.A. Magnetic Drug Targeting: Preclinical in Vivo Studies, Mathematical Modeling, and Extrapolation to Humans. *Nano Lett.*, 2016, **16**, P. 5652–5660.

[2] Sharma S., Katiyar V.K., Singh U. Mathematical modelling for trajectories of magnetic nanoparticles in a blood vessel under magnetic field. *Journal of Magnetism and Magnetic Materials*, 2015, **379**, P. 102–107.

[3] Kulkarni S., Ramaswamy B., Horton E., Gangapuram S., Nacev A., Depireux D., Shimoji M., Shapiro B. Quantifying the motion of magnetic particles in excised tissue. Effect of particle properties and applied magnetic field. *Journal of Magnetism and Magnetic Materials*, 2015, **393**, P. 243–252.

[4] Shapiro B., Kulkarni S., Nacev A., Muro S., Stepanov P.Y., Weinberg I.N. Open challenges in magnetic drug targeting. *WIREs Nanomed. Nanobiotechnol.*, 2014, **7**, P. 446–457.

[5] Shapiro B., Kulkarni S., Nacev A., Sarwar A., Preciado D., Depireux D.A. Shaping Magnetic Fields to Direct Therapy to Ears and Eyes. *Annu. Rev. Biomed. Eng.*, 2014, **16**, P. 455–481.

[6] Li X., Wei J., Aifantis K.E., Fan Y., Feng Q., Cui F.-Z., Watari F. Current investigations into magnetic nanoparticles for biomedical applications. *J. Biomed. Mater. Res.*, 2016, **104**, P. 1285–1296.

[7] Bonnemain B. Superparamagnetic agents in magnetic resonance imaging: physiochemical characteristics and clinical applications-a review. *J. Drug Target*, 1998, **6**, P. 167–174.

[8] Weissleder, R., Bogdanov, A., Neuwelt, E.A., Papisov, M. Long circulating iron oxides for MR imaging. *Adv. Drug. Delivery Rev.*, 1995, **16**, P. 321–334.

[9] Berry C.C., Curtis A.S.G. Functionalisation of magnetic nanoparticles for applications in biomedicine. *J. Phys. D. Appl. Phys.*, 2003, **36**, R198–R206.

[10] Harisinghani M.G., Barentsz J., Hahn P.F., Deserno W. M., Tabatabaei S., van de Kaa C. H., de la Rosette J., Weissleder R. Noninvasive detection of clinically occult lymph-node metastases in prostate cancer. *N. Engl. J. Med.*, 2003, **348**, P. 2491–2499.

[11] Jordan A., Wust P., Fähling H., John W., Hinz A., Felix R. Inductive heating of ferromagnetic particles and magnetic fluids: physical evaluation of their potential for hyperthermia. *Int. J. Hyerthermia*, 1997, **9**, P. 51–68.

[12] Neilsen O.S., Horsman M., Overgaard J. A future hyperthermia in cancer treatment. *E. J. Cancer*, 2001, **37**, P. 1587–1589.

[13] Tibbe A.G., de Grooth B.G., Greve J., Liberti P.A., Dolan G.J., Terstappen L.W. Optical tracking and detection of immunomagnetically selected and aligned cells. *Nature Biotechnol.*, 1999, **17**, P. 1210–1213.

[14] Kularatne B.Y., Lorigan P., Browne S., Suvarna S.K., Smith M.O., Lawry J. Monitoring tumour cells in the peripheral blood of small cell lung cancer patients. *Cytometry*, 2002, **50**, P. 160–167.

[15] Zigeuner R.E., Riesenberg R., Pohla H., Hofstetter A., Oberneder R. Isolation of circulating cancer cells from whole blood by immunomagnetic cell enrichment and unenriched immunocytochemistry in vitro. *J. Urol.*, 2003, **169**, P. 701–705.

[16] Morisada S., Miyata N., Iwahori K. Immunomagnetic separation of scum-forming bacteria using polyclonal antibody that recognizes mycolic acids. *J. Microbiol. Methods*, 2002, **51**, P. 141–148.

[17] Tan W., Wang K., He X., Zhao X.J., Drake T., Wang L., Bagwe R.P. Bionanotechnology based on silica nanoparticles. *Medicinal Research Reviews*, 2004,**24**(5), P. 621–638.

[18] Korolev D.V., Naumisheva E.B., Gareev K.G., Luchinin V.V., Panov M.F., Permyakov N.V. Colloidal particles based on silica coated iron oxide for MRI-controlled catheter embolization. *Translational Medicine*, 2015, **2**(4), P. 48–53.

[19] Shukla N., Saxena A., Gupta V., Rawat A.S., Kumar V., Shrivastava S., Rajagopal C., Rai P.K. Magnetic silica nanoparticles for the removal of Pb^{+2} from water. *Nanosystems: Physics, Chemistry, Mathematics*, 2016, **7**(3), P. 488–491.

[20] Gijs M.A.M., Lacharme F., Lehmann U. Microfluidic Applications of Magnetic Particles for Biological Analysis and Catalysis. *Chem. Rev.*, 2010, **110**, P. 1518–1563.

[21] Jamshaid T., Neto E.T.T., Eissa M.M., Zine N., Kunita M.H., El-Salhi A.E. Elaissari A. Magnetic particles: From preparation to lab-on-a-chip, biosensors, microsystems and microfluidics applications. *Past, Present and Future challenges of Biosensors and Bioanalytical tools in Analytical Chemistry: a tribute to Prof Marco Mascini*, 2016, **79**, P. 344–362.

[22] Sajeesh P., Sen A.K. Particle separation and sorting in microfluidic devices: a review. *Microfluidics and Nanofluidics*, 2014, **17,** P. 1-52.

[23] Cao Q., Han X., Li L. Configurations and control of magnetic fields for manipulating magnetic particles in microfluidic applications: magnet systems and manipulation mechanisms. *Lab Chip*, 2014, **14**, P. 2762–2777.

[24] Ortega García B., Kharissova O.V., Rasika Dias H.V., Servando Aguirre T. F., Salinas Hernández J. Nanocomposites with antibacterial properties using CNTs with magnetic nanoparticles. *Nanosystems: Physics, Chemistry, Mathematics*, 2016, **7**(1), P. 161–168.

[25] Wang M., Le He, Yin Y. Magnetic field guided colloidal assembly. *Materials Today*, 2013, **16**, P. 110–116.

[26] Chen C.-H., Abate A.R., Lee D., Terentjev E.M. Weitz D.A. Microfluidic Assembly of Magnetic Hydrogel Particles with Uniformly Anisotropic Structure. *Adv. Mater.* , 2009, **21**, P. 3201–3204.

[27] Bernad S.I., Totorean A.F., Vekas L. Particles deposition induced by the magnetic field in the coronary bypass graft model. *Journal of Magnetism and Magnetic Materials*, 2016, **401**, P. 269–286.

[28] Larimi M.M., Ramiar A., Ranjbar A.A. Numerical simulation of magnetic nanoparticles targeting in a bifurcation vessel. *Journal of Magnetism and Magnetic Materials*, 2014, **362**, P. 58–71.

[29] Heidsieck A., Vosen S., Zimmermann K., Wenzel D., Gleich B. Analysis of Trajectories for Targeting of Magnetic Nanoparticles in Blood Vessels. *Mol. Pharmaceutics*, 2012, **9**, P. 2029–2038.

[30] Gitter K., Odenbach S. Investigations on a Branched Tube Model in Magnetic Drug Targeting – Systematic Measurements and Simulation. *IEEE Trans. Magn.*, 2012, **49**, P. 343–348.

[31] Kyrilenko A.V., Chekhun V.F., Podoltsev A.D., Kondratenko I.P., Kucheryavaya I.N., Bondar V.V., Shpilevaya S.I., Todor I.N. Analysis of the force action of a high-gradient magnetic field on magnetic nanoparticles in a flowing fluid. *Reports of the National Academy of Sciences of Ukraine*, 2010, **9**, P. 162–172.

[32] Kronmüller H., Parkin S. *Handbook of Magnetism and Advanced Magnetic Materials*. John Wiley & Sons, 2007, 3064 pp.

[33] Xiao-fan G., Yong Y., Xiao-jing Z. Analytic expression of magnetic field distribution of rectangular permanent magnets, *Applied Mathematics and Mechanics*, 2004, **25**(3), P. 297–306.

[34] Lyklema J. *Fundamentals of Interface and Colloid Science. Volume II: Solid-Liquid Interfaces*. Academic Press, 2005, 787 pp.

[35] Lyklema J. *Fundamentals of Interface and Colloid Science. Volume IV: Particulate colloids*. Academic Press, 2005, 692 pp.

[36] Alfimov A.V., Aryslanova E.M., Chivilikhin S.A. An analytical method for determining the interaction energy between multiple identical spherical colloidal zinc oxide nanoparticles. *J. Phys.: Conf. Ser.*, 2014, **541**, P. 012063.

[37] Korolev D.V., Galagudza M.M., Afonin M.V., Shutkevitch V.V. Magnetic field-guided delivery of magnetite nanoparticles in the model in vitro system. *Translational Medicine*, 2015, **2**(4), P. 20–27.

NANOSYSTEMS: PHYSICS, CHEMISTRY, MATHEMATICS, 2017, 8 (4), P. 435–440

Three-dimensional light bullets in heterogeneous medium of carbon nanotubes with metallic conductivity

M. B. Belonenko[1,2], I. S. Dvuzhilov[2], Yu. V. Nevzorova[2], E. N. Galkina[2,3]

[1]Laboratory of Nanotechnology, Volgograd Institute of Business,
Yuzhno-Ukrainskaya ul. 2, Volgograd, 400048, Russia

[2]Volgograd State University, Universitetskii pr. 100, Volgograd, 400062 Russia

[3]Volgograd State Medical University, Pavshikh Bortsov Sq., Volgograd, 400131, Russia

mbelonenko@yandex.ru, dvuzhilov.ilya@volsu.ru, nevzorkina@yandex.ru, galkina@gmail.com

PACS 72.20.Ht, 42.65.Re **DOI 10.17586/2220-8054-2017-8-4-435-440**

Theoretical investigation of the dynamics of three-dimensional few-cycle optical pulses (light bullets) in an inhomogeneous medium of carbon nanotubes with metallic conduction was performed. The stable propagation of pulses under research in accordance with inhomogeneous medium parameters was determined.

Keywords: carbon nanotube, few-circle optical pulses, heterogeneous medium.

Received: 27 October 2016

Revised: 20 June 2017

1. Introduction

The dynamics of three-dimensional few-cycle optical pulses propagating in an inhomogeneous medium with metallic carbon nanotubes (CNTs) have been theoretically investigated in this paper. It is well known that there are different types of CNTs (chiral, arm-chair, and zig-zag); additionally, the chiral nanotubes can be either semiconducting or metallic, corresponding to the numbers determined by the different methods of graphene rolling up into CNT. Since there is no energy gap in the electronic spectrum in metallic CNTs, effects similar to those observed in graphene layer are possible. The study of three-dimensional few-cycle optical pulse (light bullet) dynamics in different media is of great interest not only from a theoretical point of view, but is also important for practical applications [1–3]. Note that light bullets are not stable and spreading in vacuum or linear media due to dispersion impact. For stable propagation of such pulses, the nonlinear medium in which the effects associated with dispersion could be offset by the nonlinear effects is required [4–7]. From this point of view, CNTs are promising media for the three-dimensional few-cycle optical pulse propagation, since in CNTs, the nonlinearity is determined by nonparabolicity of the electron dispersion law which interact with the light pulse field [8–10]. In the above mentioned research the results were obtained for CNTs of the zig-zag type. Since we consider the interaction between the pulse's electric field and the CNT conduction band electrons, the analysis of the light bullet's stable propagation in the array of metallic CNTs due to the change in the electron dispersion law is absolutely non-trivial [11]. An increased focus on similar pulses is due to a wide range of practical applications, such as ultra-high resolution microscopy, data transfer via fiber-optic communication lines, micro- and nanoparticle manipulations, etc. [12–15]. The importance of practical applications and considerations mentioned above give considerable impetus to the present research.

2. Basic equations

The electromagnetic pulse propagation in carbon nanotube array has been considered, wherein both the pulse electric field and the current are directed along the nanotube axis. The geometry of the problem is presented in Fig. 1.

The Hamiltonian for electron system can be written in the form:

$$H = \gamma \sum_{j\Delta\sigma} a^{+}_{j\sigma} a^{+}_{j+\Delta\sigma} h.c.,$$

where $a^{+}_{j\sigma}$, $a_{j\sigma}$ are creation and annihilation operators of electrons at site j with spin σ, γ is a hopping integral, determined by the electron wave function overlapping at adjacent sites.

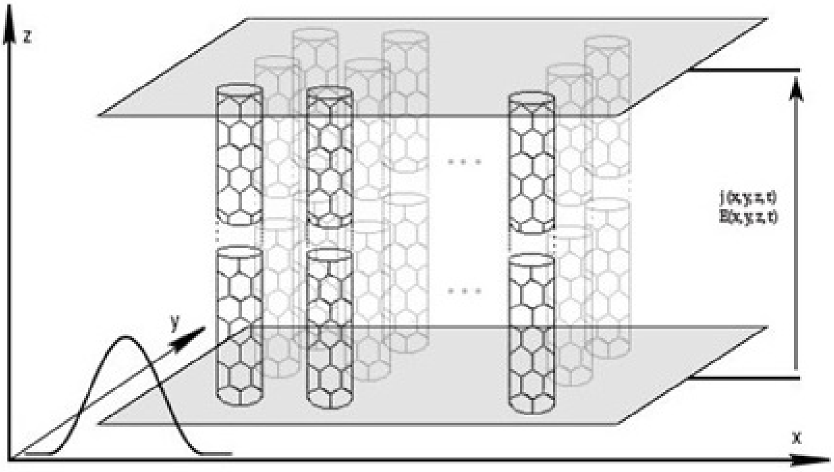

FIG. 1. Geometry of the problem, where $j(x, y, t)$ is the current along the CNT axis, $E(x, y, t)$ is the pulse electric field

Using the following Fourier series:

$$a^{+}_{n\sigma} = \frac{1}{N^{1/2}} \sum_{j} a^{+}_{j\sigma} \exp(ijn),$$
$$a_{n\sigma} = \frac{1}{N^{1/2}} \sum_{j} a_{j\sigma} \exp(-ijn), \tag{1}$$

which diagonalizes the Hamiltonian H, thus making it easy to obtain the electron's spectrum describing the properties of electron subsystem in absence of the Coulomb repulsion $\varepsilon_s(p)$.

As a rule, the study of carbon nanotubes' electronic structure is carried out in framework of aanalysis of dynamics of π-electrons in strong-coupling approximation. The CNT radius is considered to be much smaller than characteristic dimension of light bullet that allows us to neglect the field spatial inhomogeneity in nanotubes:

$$\varepsilon(k_{x,y}) = \pm\gamma_0 \left(1 + 4\cos\left(\frac{q\pi}{N_x} - \frac{N_y ka}{2N_x}\right) + 4\cos^2\left(\frac{q\pi}{N_x} - \frac{N_y ka}{2N_x}\right)\right)^{1/2}, \tag{2}$$

where $\gamma_0 \approx 2{,}7$ eV, ka belongs to the interval $[-\pi; \pi]$, k is the wave vector along the CNT axis, $a = 3b/2\hbar$, $b = 0.152$ nm are the distances between adjacent carbon atoms. $N_y a$ corresponds to the translation operation, and $\sqrt{3}N_x a$ corresponds to the rotation operation.

Suppose that $N_x = N_y$. Thus, we get the dispersion law for CNT of arm-chair type with metallic conductivity. Note that N_x is the number of hexagons along the circumference of carbon nanotubes.

A current arising in a metallic carbon nanotube is due to electrons which are described by the dispersion law for a branch crossing the Fermi level. The explored current is ballistic, i.e., flowing at times much shorter than the electron's relaxation times.

Using the standard Coulomb gauge [16] $\mathbf{E} = -\partial\mathbf{A}c\partial t$, the pulse electromagnetic field can be described by the Maxwell equations as follows:

$$\frac{\partial^2\mathbf{E}}{\partial x^2} + \frac{\partial^2\mathbf{E}}{\partial^2} + \frac{\partial^2\mathbf{E}}{\partial z^2} - \frac{n^2(x,y,z)}{c^2}\frac{\partial^2\mathbf{E}}{\partial t^2} + \frac{4\pi}{c}\mathbf{j} = 0, \tag{3}$$

where $\mathbf{E}$ is the light pulse electric field, j is the current density resulted from the pulse electric field action upon the CNT conduction band electrons, t is time, c is speed of light in the medium, $n(x, y, z)$ is the coefficient determining spatial variation of the carbon nanotube density.

The expression for the current density is given by:

$$j = e\sum_{ps} v_s(p - \frac{e}{c}A(t)) \left\langle a^{+}_{ps} a_{ps} \right\rangle, \tag{4}$$

where $v_z = \partial\varepsilon_s(p)/\partial p$, and the angle brackets denote an averaging with nonequilibrium density matrix $\rho(t)$: $\langle B \rangle = \mathrm{Sp}(B(0)\rho(t))$. Due to the motion equation, we obtain: $\left\langle a^{+}_{ps} a_{ps} \right\rangle = \left\langle a^{+}_{ps} a_{ps} \right\rangle_0$, where $\langle B \rangle_0 = \mathrm{Sp}(B(0)\rho(0))$.

Expanding $v_s(p)$ in a Fourier series and summing up over s and p, we get:

$$j = -en_0 \sum_k B_k \sin\left(\frac{ke}{c}A(t)\right),$$
$$B_k = \sum_{s=1}^{m} \int\limits_{-\pi/a}^{\pi/a} dpA_{ks}\cos(kp)\frac{\exp(-\beta\varepsilon_s(p))}{1+\exp(-\beta\varepsilon_s(p))}$$

where n_0 is the concentration of equilibrium electrons in carbon nanotubes, $\beta = 1/kT$,

$$A_{ks} = \int\limits_{-\pi/a}^{\pi/a} v_s(p)\sin(kp)dp$$

are expansion coefficients decreasing with increasing k.

Finally, the nondimensionalized equation can be written in the form:

$$\frac{\partial^2 B}{\partial z^2} + \frac{1}{r}\frac{\partial}{\partial r}\left(\frac{\partial B_z}{\partial r}\right) - n(z,r)\sin(B) + \sum_{k=2}^{\infty} B_k n(z,r)\sin(kB) = 0,\ r = \sqrt{x^2+y^2}. \tag{5}$$

Since there is a cylindrical symmetry, the summand, depending on the angle of rotation, tends to zero.

Note that equation (5) is a generalization of the well-known sine-Gordon equation.

Solving the problem, we neglect the diffraction spreading of the laser beam in direction along the CNT axis. We ignore the substrate electric field as well. Note that since both the typical size of CNTs and the distance between them are much smaller than the spatial domain typical size in which a few-cycle pulse is localized, we can use the continuous medium approximation and consider the current distributed over the volume.

3. Results of numerical calculations

Equation (5) under study has been solved numerically using the explicit finite difference cross-type schemes [17]. The time and coordinate steps were determined from standard stability conditions, and decreased until the solution changed in the eighth significant sign. Initial conditions for the vector potential of the light bullet electric field were given by the equations in Gaussian form:

$$A(z,r,0) = Q\exp\left(-\frac{(z-z_0)^2}{\gamma_z}\right)\exp\left(-\frac{r^2}{\gamma_z}\right),$$
$$\frac{dA(z,r,0)}{dt'} = \frac{2Qvz}{\gamma^2}\left(-\frac{z-z_0}{\gamma_z}\right)^2\Bigg|_{t'=0}\exp\left(-\frac{r^2}{\gamma_z}\right),$$

here Q is pulse amplitude, γ_z, γ_r are the parameters determining the pulse widths in z- and r-direction respectively, and v is the initial pulse velocity.

According to the numerical calculation results, the light bullet propagation is stable and the obtained evolution is presented in Fig. 2.

As can be seen from the figures, the solution for three-dimensional light bullet in an inhomogeneous nonlinear medium with metallic carbon nanotubes remains localized, but changes its spatial structure due to dispersion effects. The simultaneous impact of both the medium's nonlinearity and dispersion effects leads to complex structure formation on the pulse's trailing edge, which remains localized in a limited spatial domain.

The results of numerical simulation, depending on period of inhomogeneity are shown in Fig. 3. As expected, a few-cycle pulse propagates faster as the lattice constant increases. It is obvious, that under the infinite lattice constant due to lack of the interference effects the pulse will propagate with maximum velocity. Namely this fact was confirmed in consequence of the numerical analysis results. The pulse shape distortion should also be noted.

The following result deals with the dependence of both the shape and velocity of few-cycle pulses on modulation depth of nonlinear medium α and is shown in Fig. 4.

It should be noted that increase in modulation depth α leads not only to the pulse delay (for the reasons mentioned above) but to a change in its shape as well, due to the strong interference. The obtained results can also help to predict the value of pulse spreading when it slows down by means of nonlinear lattices in carbon nanotube media.

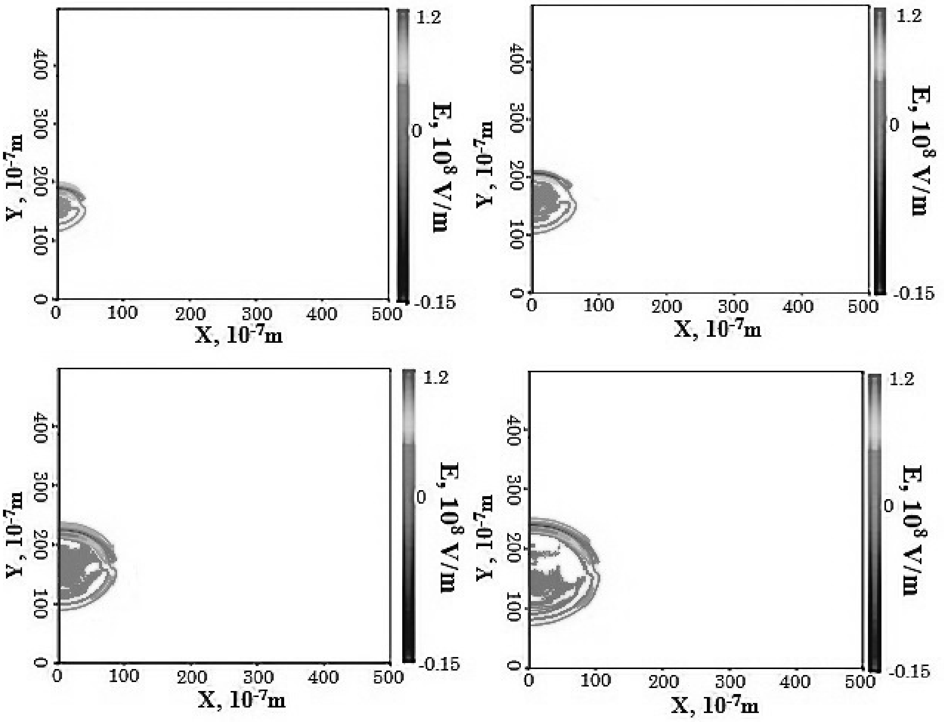

FIG. 2. Propagation of the light bullet in inhomogeneous medium of metallic CNTs (χ = 2.5 mcm is the lattice constant, $\alpha = 0.1$ is the modulation depth) at a fixed period of time T. A) 4×10^{-12} s; B) 6×10^{-12} s; C) 8×10^{-12} s; D) 10×10^{-12} s. The relative units of coordinates and electric field are along the axes

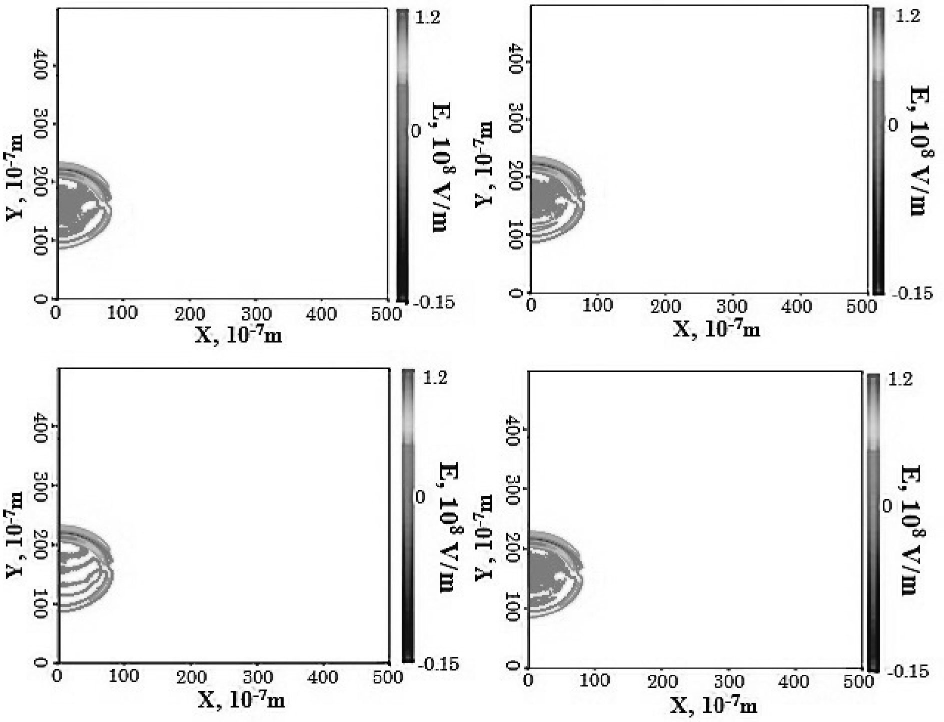

FIG. 3. Propagation of the light bullet in inhomogeneous medium of metallic CNTs at a fixed period of time $T = 8 \times 10^{-12}$ s with different value of the lattice constant χ A) 0.125 mcm; B) 0.175 mcm; C) 0.225 mcm; D) 0.25 mcm. Relative units of coordinate and electric field are along the axes

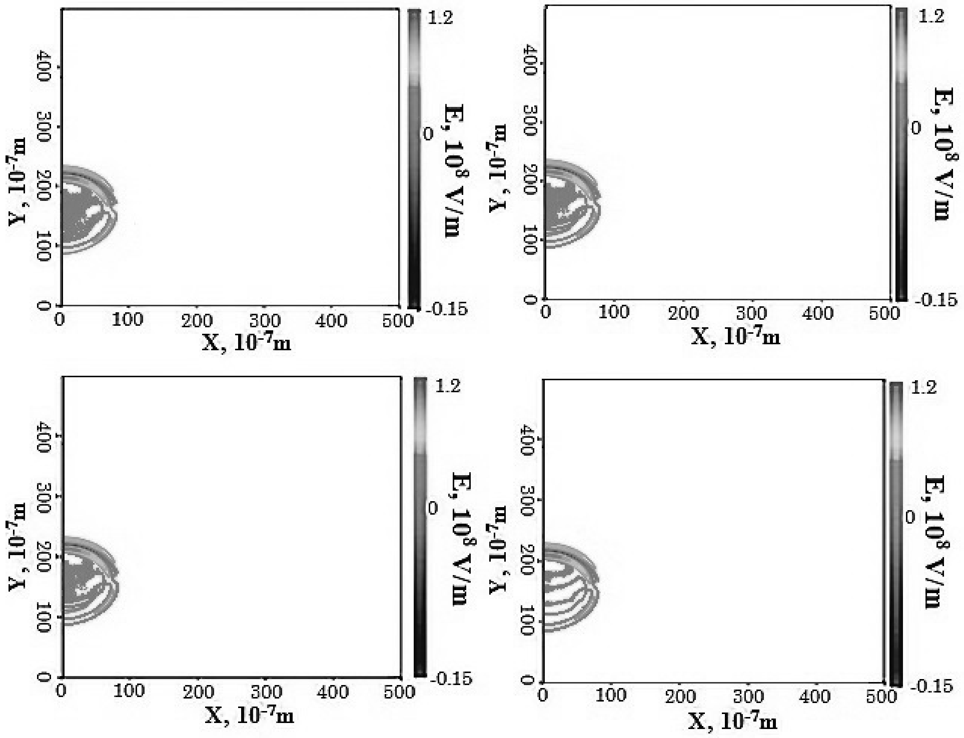

FIG. 4. Propagation of the light bullet in inhomogeneous medium of metallic CNTs ($\chi = 5$ mcm is the lattice constant) at at fixed time with different modulation depth α A) 0.1α; B) 0.3α; C) 0.7α; D) 0.9α. The relative units of coordinates and electric field are along the axes

4. Conclusion

The performed investigation allows us to make the following conclusions:

1. The three-dimensional few-cycle optical pulse (light bullet) propagation in inhomogeneous medium with metallic carbon nanotubes is stable.
2. The conversion of CNT conductivity type from semiconductor to metallic one does not significantly affect the dynamics of three-dimensional few-cycle pulse propagation, which is of great importance for practical applications.

References

[1] Kaplan A.E., Shkolnikov P.L. Electromagnetic “bubbles” and shock waves: unipolar, nonoscillatig EM solitons. *Physical Review Letters*, 1995, **75**(12), P. 2316–2319.

[2] Casperson L.W. Few-cycle pulses in two-level media. *Phys. Rev. A.*, 1998, **57**, P. 609.

[3] Brabec T., Krausz F. Intense few-cycle laser fields: Frontiers of nonlinear optics. *Reviews of Modern Physics*, 2000, **72**, P. 545–591.

[4] Schafer T. Wyane C.E. Propagation of ultra-short optical pulses in cubic-nonlinear media. *Physica D.*, 2004, **196**, P. 90–105.

[5] Kazantseva E.V., Maimistov A.I., Malomed B.A. Propagation and interaction of ultrashort electromagnetic pulses in nonlinear media with a quadratic-cubic nonlinearity. *Optics communications*, 2001, **188**, P. 195–204.

[6] Kurizki G., Kozhekin A., Opatrny T., Malomed B. Optical solitons in periodic media with resonant and off-resonant nonlinearities. *Progress in Optics E.* Wolf, ed., (Elsevier, North-Holland), 2001, **42**, P. 93–146.

[7] Maimistov A.I. Interaction of fast and slow varying electromagnetic waves propagating in paraelectric or ferroelectric material. *Nanosystems: Physics, Chemistry, Mathematics*, 2017, **8**(3), P. 334–338.

[8] Saito R., Dresselhaus M.S., Dresselhaus G. Physical properties of carbon nanotubes. *Imperial College Press*, London, 1999, 251 pp.

[9] Reich S., Thomsen C., Maultzsch J. *Carbon nanotubes. Basic concepts and physical properties*. Wiley-VCH Verlag, Berlin, 2003, 218 pp.

[10] Harris P.J.F. *Carbon nanotubes and related structures: New materials for the 21-st century*. Cambridge University Press, Cambridge, 2009, 299 pp.

[11] Belonenko M.B., Dvuzhilov I.S, Galkina E.N., Nevzorova Yu.V. Three dimensional few cycle optical pulses in nonlinear medium with carbon nanotubes. *Modern Physics Letters B*, 2016, **30**(28), P. 1650345.

[12] Pavani S.R.P., Greengard A., Piestun R. Three-dimensional localization with nanometer accuracy using a detector-limited double-helix point spread function system. *Appl. Phys. Lett.*, 2009, **95**, P. 021103.

[13] Spektor A.N.B., Shamir J. Singular beam microscopy. *Appl. Opt.*, 2008, **47**, P. A78–A87.

[14] Bozinovic N., Yue Ya., Ren Yo., Tur M., Kristensen P., Huang H., Willner A.E., Ramachandran S. Terabit-Scale Orbital Angular Momentum Mode Division Multiplexing in Fibers. *Science*, 2013, **340**, P. 1545.

[15] Abramochkin E., Kotova S., Korobtsov A., Losevsky N., Mayorova A., Rakhmatulin M., Volostnikov V. Microobject manipulations using laser beams with nonzero orbital angular momentum. *Laser Physics*, 2006, **16**, P. 842–848.

[16] Landau L.D., Lifshits E.M. *Field theory* (in Russian). Fizmatlit, Moscow, 1988, 536 pp.

[17] Bakhvalov N.S. *Numerical Methods (Analysis, Algebra, Ordinary Differential Equations)* (in Russian). Nauka, Moscow, 1975, 632 pp.

NANOSYSTEMS: PHYSICS, CHEMISTRY, MATHEMATICS, 2017, 8 (4), P. 441–446

Fiber quantum random number generator, based on vacuum fluctuations

A. E. Ivanova, S. A. Chivilikhin, G. P. Miroshnichenko, A. V. Gleim

ITMO University, Kronverkskiy, 49, St. Petersburg, 197101, Russia

newiva@mail.ru, sergey.chivilikhin@gmail.com, gpmirosh@gmail.com, aglejm@yandex.ru

PACS 03.67.-a **DOI 10.17586/2220-8054-2017-8-4-441-446**

Quantum random number generation allows one to obtain the absolutely random sequences by using nondeterministic physical processes. Fluctuations of the vacuum, recorded by homodyne detection, can be one of the entropy sources in those generators. In this paper, a system of quantum random numbers generation, based on vacuum fluctuations and using a fiber Y-splitter is presented.

Keywords: quantum random number generation, beam splitter, Y-splitter, vacuum fluctuations.

Received: 2 July 2017

Revised: 28 July 2017

1. Introduction

Random number generators based on various sources of entropy are used in many branches of science and technology. The use of nondeterministic physical processes enables one to obtain true random sequences that can be utilized in applications where a high degree of randomness is necessary, such as cryptography both classical and quantum [1]. Quantum processes, in which randomness is determined by fundamental physical principles, can be used as a source of entropy for physical generators of random numbers.

Single photon detectors are required for most parts of quantum random number generators (QRNG), which use the spatial [2,3] or the time [4,5] mode as a source of entropy. This leads to the fact that the speed characteristics of these systems are limited. The same problem arises in schemes based on measuring the number of photons in radiation [6,7]. QRNG based on vacuum fluctuations [8–11] allow one to obtain true random sequences without using single photon detection and, accordingly, with lower limitations of speed characteristics.

A QRNG scheme based on vacuum fluctuations was patented in 2007 [8]. The operation principle of this generator type is the extraction of randomness from quantum noise obtained after subtracting signals from the beam splitter outputs on the balanced detector. A coherent state is sent by a laser to first of beam splitter inputs vacuum state – to second, then these two signals are mixed at a beam splitter and output signals goes to balanced detector, where they are subtracted from each other. The obtained resulting signal is quantum noise which can be transformed into a random sequence by postprocessing. The main advantage of this scheme is the measurement of quantum states by classical detectors which is utilized in homodyne detection.

A similar QRNG with a speed of 6.5 Mbit/s [9] was demonstrated in 2010; the sequences were processed by using a cryptographic hash function. In the same year, another group of researchers achieved a generation rate of 12 Mbit/s, data was cleared from electrical noise by postprocessing [10]. A system that allows one to achieve the generation rate of 2 Gbit/s was created in 2011 [11]. In that work, two methods of postprocessing (one of them with protection against extraneous interference) were used. In all works listed above, beam splitters with two input ports and two output ports were used.

The purpose of our research was development of the fiber device for high-speed random number generation based on vacuum fluctuations that can be used in a subcarrier quantum communication system [12].

2. Theoretical modeling

In works [9–11], using beam splitters with four ports (Fig. 1a) a separate port is used to enter vacuum states. For the scheme that we use the Y-splitter acts as the splitter of radiation (Fig. 1b).

The advantages of using the Y-splitter are following: compactness of the final device, possibility of integration with solutions based on fiber optics, implementation of high-speed devices created from integrated elements and, in the future, integrated circuits.

We compared the mathematical description of the beam splitter with two input ports and two output ports with a mathematical description of the Y-splitter to analyze the possibility of applying Y-splitter in the experimental QRNG based on vacuum fluctuations.

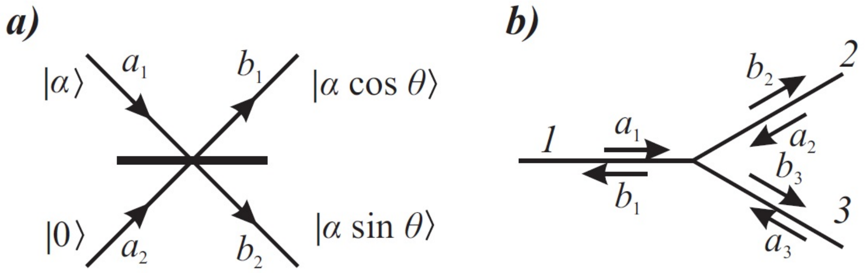

FIG. 1. a) Scheme of a beam splitter with angle θ, where to the first splitter input a coherent state is sent, and to other input - a vacuum state. b) Optical Y-splitter. a_1, a_2, a_3 – operators arriving at the 1st, 2nd and 3rd ports, respectively, b_1, b_2, b_3 – operators at the outputs of the splitter

In case if input signal a_1 that can be characterized by coherent state $|\alpha\rangle$ with parameter α is sent to one of the beamsplitter inputs and vacuum state $|0\rangle$ is sent to other input port, then output signals can be characterized by Poisson distribution: with parameter $|a\cos\theta\rangle$ at first output of beam splitter and with parameter $|a\sin\theta\rangle$ at the second output.

If beam splitter is symmetrical ($\theta = \pi/4$), then we obtain expression, describing signals B_1 and B_2 at both outputs:

$$B_1 = B_2 = \frac{1}{\sqrt{2}}A_1. \tag{1}$$

The fiber splitter (Fig. 1b) has been presented as a system with three inputs and three outputs as signal in each of the ports can be distributed in two opposite directions. Relations between input and output operators of Y-splitter were derived by using a matrix description, allowing us to show the interaction between each pair of signals:

$$\begin{pmatrix} b_1^+ \\ b_2^+ \\ b_3^+ \end{pmatrix} = \begin{pmatrix} -\sqrt{1-2\lambda^2} & \beta & \beta \\ \lambda & -\gamma & \sqrt{1-\beta^2-\gamma^2} \\ \lambda & \sqrt{1-\beta^2-\gamma^2} & -\gamma \end{pmatrix} \begin{pmatrix} a_1^+ \\ a_2^+ \\ a_3^+ \end{pmatrix}. \tag{2}$$

where λ is proportionality factor, connecting input signal at 1st port with output signals at 2nd and 3rd ports; β connects input signals at 2nd or 3rd ports with output signal at 1st port; γ connects input and output signals of 2nd or 3rd port. According to the unitarity conditions for the parameters of the matrix described above the following relations must be satisfied:

$$\begin{cases} -\sqrt{1-2\lambda^2}\beta - \lambda\gamma + \lambda\sqrt{1-\beta^2-\gamma^2} = 0, \\ \beta^2 - 2\gamma\sqrt{1-\beta^2-\gamma^2} = 0. \end{cases} \tag{3}$$

Solving the system, we get the following parameter values: $\lambda = \sqrt{2\gamma(1-\gamma)}$, $\beta = -\sqrt{2\gamma(1-\gamma)}$, so equation (2) takes the following form:

$$\begin{pmatrix} b_1^+ \\ b_2^+ \\ b_3^+ \end{pmatrix} = \begin{pmatrix} 1-2\gamma & -\sqrt{2\gamma(1-\gamma)} & -\sqrt{2\gamma(1-\gamma)} \\ \sqrt{2\gamma(1-\gamma)} & -\gamma & 1-\gamma \\ \sqrt{2\gamma(1-\gamma)} & 1-\gamma & -\gamma \end{pmatrix} \begin{pmatrix} a_1^+ \\ a_2^+ \\ a_3^+ \end{pmatrix}. \tag{4}$$

We also calculated some statistical parameters of signal at the outputs of the scheme, using a Y-splitter. Photon birth operators at outputs of ports 1, 2 and 3 can be described as follows:

$$b_1^+ = (1-2\gamma)a_1^+ - \sqrt{2\gamma(1-\gamma)}(a_2^+ + a_3^+), \tag{5}$$

$$b_2^+ = \sqrt{2\gamma(1-\gamma)}a_1^+ - \gamma\alpha_2^+ + (1-\gamma)a_3^+, \tag{6}$$

$$b_3^+ = \sqrt{2\gamma(1-\gamma)}a_1^+ + (1-\gamma)\alpha_2^+ - \gamma a_3^+. \tag{7}$$

Since a coherent state is sent to the first port of the splitter, and to ports 2 and 3 – a vacuum state $|0\rangle$, then the average number of photons at outputs of the Y-splitter can be described by these expressions:

$$\overline{n_{1out}} = \langle 0|_3 \langle 0|_2 \langle \alpha|_1 \Big((1-2\gamma)a_1^+ - \sqrt{2\gamma(1-\gamma)}(a_2^+ + a_3^+) \Big) \times \\ \Big((1-2\gamma)a_1 - \sqrt{2\gamma(1-\gamma)}(a_2 + a_3) \Big) |\alpha\rangle_1 |0\rangle_2 |0\rangle_3 = (1-2\gamma)^2\alpha^2, \tag{8}$$

$$\overline{n_{2out}} = \langle 0|_3 \langle 0|_2 \langle \alpha|_1 \left(\sqrt{2\gamma(1-\gamma)}a_1^+ - \gamma\alpha_2^+ + (1-\gamma)a_3^+\right) \times \left(\sqrt{2\gamma(1-\gamma)}a_1 - \gamma\alpha_2^(1-\gamma)a_3\right) |\alpha\rangle_1 |0\rangle_2 |0\rangle_3 = 2\gamma(1-\gamma)\alpha^2, \quad (9)$$

$$\overline{n_{3out}} = \langle 0|_3 \langle 0|_2 \langle \alpha|_1 \left(\sqrt{2\gamma(1-\gamma)}a_1^+ + (1-\gamma)\alpha_2^+ - \gamma a_3^+\right) \times \left(\sqrt{2\gamma(1-\gamma)}a_1 + (1-\gamma)\alpha_2 - \gamma a_3\right) |\alpha\rangle_1 |0\rangle_2 |0\rangle_3 = 2\gamma(1-\gamma)\alpha^2. \quad (10)$$

The differential current operator Δi can be characterized as follows:

$$\Delta i = k_2 b_2^+ b_2 - k_3 b_3^+ b_3, \quad (11)$$

where k_1, k_2 – quantum efficiencies of 1st and 2nd detectors.

In the case of detectors with different quantum efficiencies, the average value of the difference current $\langle \Delta i \rangle$ is:

$$\langle \Delta i \rangle = \langle 0|_3 \langle 0|_2 \langle \alpha|_1 (k_2 b_2^+ b_2 - k_3 b_3^+ b_3) |\alpha\rangle_1 |0\rangle_2 |0\rangle_3 = 2\gamma(1-\gamma)(k_2 - k_3)\alpha^2. \quad (12)$$

The dispersion of the differential current $D(\Delta i)$ and mean square deviation of the differential current δi from the average value can be described by the following expression:

$$D(\Delta i) = 2\gamma(1-\gamma)(k_2^2 + k_3^2)\alpha^2, \quad (13)$$

$$\delta i = \alpha\sqrt{2\gamma(1-\gamma)(k_2^2 + k_3^2)}. \quad (14)$$

In the case where the signal coming from the first port is distributed only between the outputs of ports 2 and 3 of the Y-splitter, $\gamma = 1/2$. Then, the relationship between each pair of operators at the input and at the output from the system can be displayed using the following expression:

$$\begin{pmatrix} b_1^+ \\ b_2^+ \\ b_3^+ \end{pmatrix} = \begin{pmatrix} 0 & -\frac{1}{\sqrt{2}} & -\frac{1}{\sqrt{2}} \\ \frac{1}{\sqrt{2}} & -\frac{1}{2} & \frac{1}{2} \\ \frac{1}{\sqrt{2}} & \frac{1}{2} & -\frac{1}{2} \end{pmatrix} \begin{pmatrix} a_1^+ \\ a_2^+ \\ a_3^+ \end{pmatrix}. \quad (15)$$

If we send input signal to first port only, then signals B_2 and B_3 at outputs of ports 2 and 3 can be described by the following expression:

$$B_2 = B_3 = \frac{1}{\sqrt{2}} A_1. \quad (16)$$

We can see that the signals obtained at the outputs of the beam splitter with four ports, when laser and vacuum signals were sent to inputs, coincide with signals obtained at the outputs of the Y-splitter. In this particular case, the average numbers of photons at the Y-splitter outputs are:

$$\overline{n_{1out}} = 0, \quad (17)$$

$$\overline{n_{2out}} = \overline{n_{3out}} = \frac{1}{2}\alpha^2. \quad (18)$$

In the case of detectors with different quantum efficiencies, the average value of the differential current, the dispersion, and the mean square deviation of the differential current from the mean value can be expressed as follows:

$$\langle \Delta i \rangle = \frac{1}{2}(k_2 - k_3)\alpha^2, \quad (19)$$

$$D(\Delta i) = \frac{1}{2}(k_2^2 + k_3^2)\alpha^2, \quad (20)$$

$$\delta i = \alpha\sqrt{\frac{1}{2}(k_2^2 + k_3^2)}. \quad (21)$$

The above described calculations were carried out for a symmetric Y-splitter. Since experimental devices do not have an ideal symmetry, it is necessary to consider the asymmetric case. We can describe the relationship between of the vector of the input signals A and the vector of the output signals B via the sum of the conversion matrix U

indicated in (15) and the matrix $\widetilde{U}$ describing the small perturbations on the system. We consider the case when the matrix $\widetilde{U}$ is real.

$$B = (U + \widetilde{U})A, \tag{22}$$

$$\begin{pmatrix} b_1^+ \\ b_2^+ \\ b_3^+ \end{pmatrix} = \left(\begin{pmatrix} 0 & -\dfrac{1}{\sqrt{2}} & -\dfrac{1}{\sqrt{2}} \\ \dfrac{1}{\sqrt{2}} & -\dfrac{1}{2} & \dfrac{1}{2} \\ \dfrac{1}{\sqrt{2}} & \dfrac{1}{2} & -\dfrac{1}{2} \end{pmatrix} + \begin{pmatrix} u_{11} & u_{12} & u_{13} \\ u_{21} & u_{22} & u_{23} \\ u_{31} & u_{32} & u_{33} \end{pmatrix} \right) \begin{pmatrix} a_1^+ \\ a_2^+ \\ a_3^+ \end{pmatrix}. \tag{23}$$

To observe the unitarity conditions obtained by summing the matrix, it is necessary in the linear approximation for u_{ij} to satisfy the condition:

$$\begin{cases} u_{31} = -u_{21}, \\ u_{32} = \sqrt{2}u_{12} + u_{22}, \\ u_{33} = \sqrt{2}u_{12} + u_{22} - \sqrt{2}u_{21}, \\ u_{11} = -\sqrt{2}u_{21} + \sqrt{2}u_{12} + 2u_{22}, \\ u_{23} = u_{22} - \sqrt{2}u_{21}, \\ u_{13} = -u_{12}. \end{cases} \tag{24}$$

The changes of signals, receiving on the outputs of Y-splitter ports 2 and 3, are affected by the components u_{21} and u_{31} due to asymmetry. From the expressions described above it is clear that these elements of the matrix $\widetilde{U}$ are the same in absolute value, but they are different in sign.

In the asymmetric case, the average numbers of photons at the outputs of the Y-splitter are:

$$\overline{n_{1out}} = 0, \tag{25}$$

$$\overline{n_{2out}} = \left(\frac{1}{2} + \sqrt{2}u_{21}\right)\alpha^2, \tag{26}$$

$$\overline{n_{3out}} = \left(\frac{1}{2} + \sqrt{2}u_{31}\right)\alpha^2. \tag{27}$$

In the case of detectors with different quantum efficiencies, the average value of the difference current, dispersion of the differential current, and mean square deviation of the differential current from the average value can be described by the following expressions:

$$\langle \Delta i \rangle = \left(\frac{1}{2} + 2\sqrt{2}u_{21}\right)(k_2 - k_3)\alpha^2, \tag{28}$$

$$D(\Delta i) = \left(\frac{1}{2}(k_2^2 + k_3^2) + \sqrt{2}(k_2^2 - k_3^2)u_{21}\right)\alpha^2, \tag{29}$$

$$\delta i = \alpha\sqrt{\frac{1}{2}(k_2^2 + k_3^2) + \sqrt{2}(k_2^2 - k_3^2)u_{21}}. \tag{30}$$

The practical possibility of generating true random numbers by QRNG based on vacuum fluctuations and using Y-splitter was confirmed experimentally.

3. Experimental setup and postprocessing

The scheme of our experimental setup is represented in Fig. 2. We used a 10 mW 1550 nm Teraxion-NLL laser (L). After passing fiber optical isolator (OI), based on the Faraday Effect (isolation ≥ 28 dB at 1550 nm), to reflections neutralization, and attenuator (A) the radiation goes to fiber Y-splitter with dividing coefficient 50/50. Two p-i-n photodiodes (fid13z81pz) with quantum efficiencies of 60 % at 1550 nm, sensitivity $S = 0.75$ A/W, and a 1 GHz bandwidth were used as detectors (D1, D2). The currents from two photodiodes are subtracted in electronic processing system (EP) and then resulting signal is amplified. Amplification circuit contains amplifier OPA847 (Texas Instruments) in a transimpedance configuration with a gain of 4 $k\Omega$. All components are located on a specially designed board. The frequency band of the circuit is 100 MHz. The bandwidth of the oscilloscope Tektronix dpo70604c (ADC) used to digitize the received noise is 6 GHz. After digitization, we can use various post-processing (PP) algorithms to convert true random quantum noise into a sequence of random bits.

If the initial power of laser radiation is on the order of 10 mW, power of the difference signal amplitude is about 0.1–1 μW. If we take into account the sensitivity of photodiodes, difference current is about 0.1–1 μA.

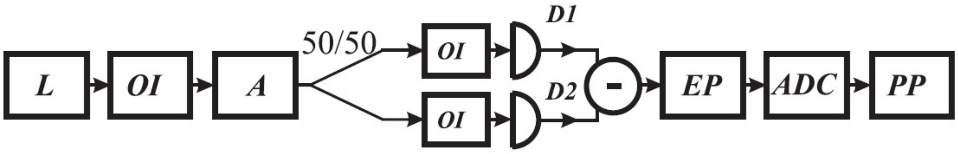

FIG. 2. Block diagram of the experimental setup. L – laser, OI – optical isolator, A – attenuator, D1, D2 – detectors, EP – electronic processing system, ADC – analog-to-digital converter, PP – postprocessing system

Since we used an amplifying scheme with one cascade gain of 4 kΩ, value of the final difference signal after amplification is on the order of mV.

During our research, a linear relationship between the intensity of laser radiation and the level of mean noise deviation was observed, that confirms that noise has a quantum nature. Quantum noise (Fig. 3a) obtained from our system had the following characteristics: mean value of fluctuations $\mu = 7 \cdot 10^{-6}$, standard deviation $\sigma = 0.2$, asymmetry coefficient $S = \mu_3/\sigma^3 = 0.01$ (where μ_3 – third central moment of the noise distribution), kurtosis (a measure of sharpness of the random variable maximum) $K = \frac{\mu_4}{\sigma^4} = -4.5 \cdot 10^{-3}$ (where μ_4 – fourth central moment of the noise distribution), probability of the most likely outcome $\max(P_i) = 3.19 \cdot 10^{-3}$ (where P_i – probability of the i-th realization of random discrete variable), min-entropy $H_{min} = -\log_2(\max(P_i)) = 8.29$.

The time dependence of obtained noise, probability distribution of noise at a mean level, autocorrelation function, and noise spectrum are shown in Fig. 3.

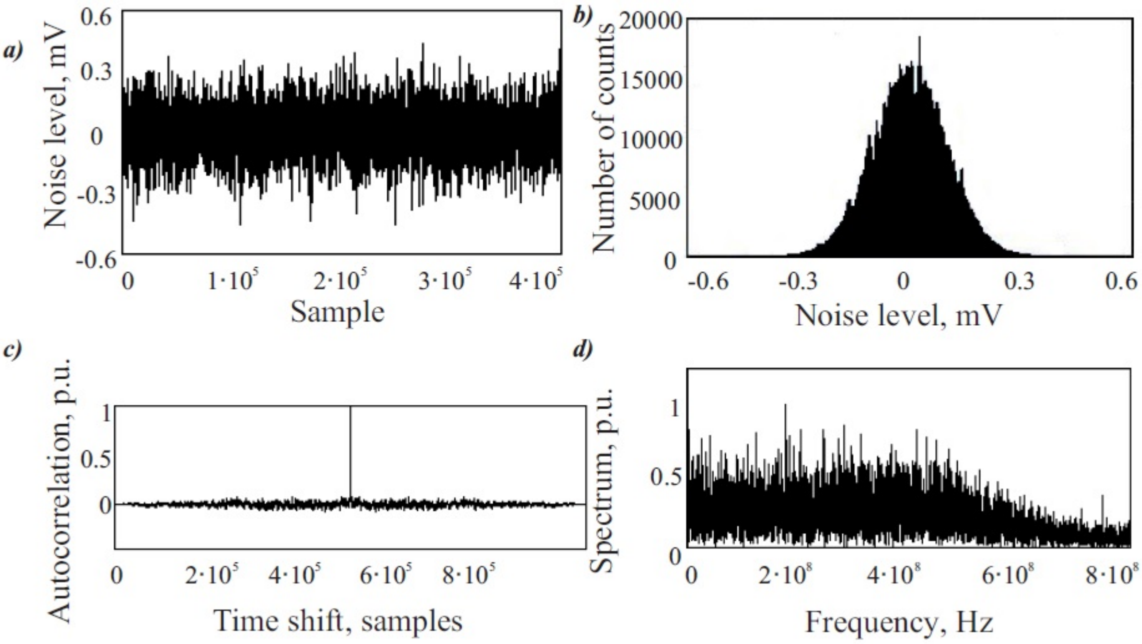

FIG. 3. a) Time dependence of obtained noise; b)Probability distribution of noise at a certain level; c) Autocorrelation function; d) Noise spectrum

During experiments, it was shown that asymmetry of fiber splitter, expressed as a change in a length of one arm of the Y-splitter, has a negative impact on the balancing of detection. For the processing of noise obtained by experimental QRNG and based on vacuum fluctuations and using a Y-splitter, we used four different conversion methods:

“A”: If noise level in count is above 0, then we write resulting bit “1”, else – “0”. Number of counts coincides with number of bits in resulting sequence;

“B”: We divide sequence of bits was obtained by method “A” into two subsequences with equal length. Then we apply XOR to all pairs of elements with same index of both subsequences and write result of this operation to resulting sequence. The generation rate is twice smaller that in method “A”, but bias between “0” and “1” bits (asymmetry of the beamsplitter may be reason for its appearance) decreases;

"C": We generate three bits from one sample [11] (convert initial Gaussian distribution to uniform distribution, applying Gaussian error function). All experimental counts are dividing to eight possible noise intervals with the same probability, each interval is coding by three bits, that allows us to increase generation rate;
"D": After analog-to-digital conversion we can discard most significant bits of digitized value of noise amplitude. Initial probability of counts being in a certain noise level is Gaussian, but when we discard most significant bits, probability is approaching to uniform distribution. This method, as the previous one, allows one to increase generation rate by extracting few bits from one count.

If we know the probabilistic properties of a true random sequence, then we can check the degree of similarity between generated sequence and random sequence. For this purpose, we performed a series of tests [13] (monobit, twobit, "poker", autocorrelation test, and runs test), and then compared their results for an ideal and experimental sequence. Results of randomness tests applied to sequences, obtained by four different post processing techniques were given in detail in [14].The results of a series of tests showed that optimal post processing technique is discarding two or three most significant bits.

4. Conclusion

In this research, we developed a quantum description of the Y-splitter in the QRNG based on fluctuations in the vacuum. The statistical parameter values of the differential current at the circuit output were obtained. We consider four postprocessing methods to convert experimental samples to bits, and after testing, we conclude that the optimal post processing technique for our system is discarding two or three most significant bits after analog-to-digital conversion.

Acknowledgements

This work was financially supported by Government of Russian Federation, Grant 074-U01 and by the Ministry of Education and Science of Russian Federation (project No. 14.578.21.0112 No 02.G25.31.0229).

References

[1] Scarany V., Bechmann-Pasquinucci H. et al. The security of practical quantum key distribution. *Rev. Mod. Phys.*, 2009, **81**, P. 1301–1350.

[2] Jennewein T., Achleitner U. et al. A fast and compact quantum random number generator. *Rev. Sci. Instrum.*, 2000, **71**(4), P. 1675–1680.

[3] Stefanov A., Gisin N. et al. Optical quantum random number generator. *Journal of Modern Optics*, 2000, **47**, P. 595–598.

[4] Dynes J. F., Yuan Z. L, et al. A high speed, post-processing free, quantum random number generator. *Appl. Phys. Lett.*, 2008, **93**, P. 031109.

[5] Wahl M. et al. An ultrafast quantum random number generator with provably bounded output bias based on photon arrival time measurements. *Applied Physics Letters*, 2011, **98**, P. 171105.

[6] Furst H. et al. High speed optical quantum random number generation. *Optics express*, 2010, **18**, P. 13029–13037.

[7] Applegate M. et al. Efficient and robust quantum random number generation by photon number detection. *Applied Physics Letters*, 2015, **107**, P. 071106.

[8] Trifonov A. and Vig H. Quantum noise random number generator, U.S. Patent N 7284024. 2007. B1.

[9] Gabriel C., Wittmann C. et al. A generator for unique quantum random numbers based on vacuum states. *Nature Phot.*, 2010, **4**, P. 711–715.

[10] Shen Y., Tian L.,Zou H. Practical quantum random number generator based on measuring the shot noise of vacuum states. *Phys. Rev. A*, 2010, **81**, P. 063814.

[11] Symul T. ,Assad S. M., Lam P. K. Real time demonstration of high bitrate quantum random number generation with coherent laser light. *Appl. Phys. Lett.*, 2011, **98**, P. 231103.

[12] Gleim A. V., Egorov V. I. et al. Secure polarization-independent subcarrier quantum key distribution in optical fiber channel using BB84 protocol with a strong reference. *Optics Express*, 2016, **24**(3), P. 2619–2633.

[13] Menezes A., van Oorschot P. , Vanstone S. *Handbook of Applied Cryptography*. CRC Press., 1996, 816 p.

[14] Ivanova A. E, Chivilikhin S. A, Gleim A. V. Quantum random number generator based on homodyne detection. *Nanosystems: Physics, Chemistry, Mathematics*, 2017, **8**(2), P. 239–242.

NANOSYSTEMS: PHYSICS, CHEMISTRY, MATHEMATICS, 2017, 8 (4), P. 447–453

Quantum measurement of photon distribution statistics for intra-cavity EM field monitored by dumping atom-pointer

A. I. Trifanov, E. S. Trifanova

ITMO University, St. Petersburg, Russia

alextrifanov@gmail.com, etrifanova@gmail.com

DOI 10.17586/2220-8054-2017-8-4-447-453

We describe and theoretically study a process of photon distribution statistics measurement for intra-cavity mode of EM field monitored by indirect photo-detection scheme. In particular, we investigate photon number distribution and Mandel's parameter (normalized dispersion) of the mode using statistics of atomic state detector clicks. In our model, a two-level atom-pointer which passes through the cavity interacts with the mode and environment, distorting the measured statistical properties of the mode. To account for this, phase distortion (decoherece) and population relaxation are introduced in the model. In this paper, we use the super-operators approach to intra-cavity mode evolution conditioned by atomic state detector clicks.

Keywords: inderect measurements, field statistics, QED interactions.

Received: 25 July 2017

Revised: 02 August 2017

1. Introduction

One of the main problems of quantum electromagnetic (EM) field photo-detection is measurement of field states statistical properties using statistics of clicks obtained from detectors and their combinations [1,2]. Coherence functions, Q- and P- distributions, phase detection are usually constructed form measured data of homodyne, heterodyne and indirect measurements [3–5]. The most simple existed schemas suggest direct measurement of photon counting rate [6] which allows one to estimate statistics for the photon number operator and reveal coherent properties of the field quantum state such as bunching and anti-bunching.

The conditional photon distribution function for the field depends significantly upon organized the interaction between the EM field and microscopic part of measurement apparatus. Furthermore, relaxation and decoherention due to the existence of environmental modes that may change measurement statistics dramatically [7, 8]. Therefore thorough description of such realistic procedure in terms of detectors POVM's is highly desirable [9].

One of the well known ways to control the interaction strength between the field and the photodetector is to use an indirect measurement scheme [10] where a two-level atom-pointer passes through the cavity and interacts with an excited single mode quantum EM field which state is monitored. After that, the state of the atom is detected in the ionizing chamber and the required statistics of intra-cavity mode is restored from atomic state detectors measured data [7, 11].

In this paper we use an indirect photodetection scheme to present the protocol for photon distribution statistics measurement [12]. In particular, we suggest monitoring of photon number distribution function and Mandel's parameter from statistics of atomic state detector clicks. Additionally, in the protocol, we account for the non-ideal measurement procedure resulting from the interaction between the atom-pointer and the external environmental modes. The cavity quality factor should be quite high in order to eliminate relaxation processes due to the interaction between intra-cavity and extra-cavity modes.

The work is organized as follows. In the second section we formulate the model of interaction between intra-cavity mode and dumping atom-pointer and obtain a system of differential equations for the elements of atom-field density matrix. After that, in section 3, we introduce a set of conditional evolution superoperators (photodetectors POVM's) and obtain a system of differential equations for them. Section 4 is devoted to solving of this operator-valued system using perturbation theory and the assumption that spontaneous relaxation and excitation rates are small compared to Rabi frequency. In section 5, we use the results of previous section to obtain analytical expressions for mean photon number and Mandel's parameter. Section 6 is for numerical modelling and discussion of obtained results. Section 7 concludes the article.

2. The model

We start with the master equation for the density operator $\rho_{AF}(t)$ of common system of interacting intra-cavity mode and dumped atom:

$$i\frac{d}{dt}\rho_{AF}(t) = [H_{int}, \rho_{AF}(t)] + iD_A\rho_{AF}(t), \tag{1}$$

where H_{int} is Hamiltonian describing the interaction between atom and mode. In the interaction picture and under the resonant approximation we can write:

$$H_{int} = \Omega\sigma_+ a \exp\left(i\Delta t\right) + \Omega^*\sigma_- a^\dagger \exp\left(-i\Delta t\right). \tag{2}$$

Here, Ω is the Rabi frequency, $\sigma_+ = |e\rangle\langle g|$ and $\sigma_- = |g\rangle\langle e|$ are atomic operators, a is an annihilation operator of cavity mode, Δ is frequency detuning. The dynamics of the dumping atom may be described in Born-Markov approximation using atomic dissipative part D_A in Lindblad form:

$$2D_A\rho = \gamma_{ge}\left(2\sigma_-\rho\sigma_+ - \sigma_+\sigma_-\rho - \rho\sigma_+\sigma_-\right) + \gamma_{eg}\left(c.c.\right), \tag{3}$$

where γ_{ge}, γ_{eg} are the coefficients of spontaneous decay and excitation rates respectively.

System (1) can be written in block-matrix form using the following decomposition for density operator $\rho_{AF}(t)$:

$$\rho_{AF}(t) = \sum_{\mu,\nu\in\{g,e\}} |\mu\rangle\langle\nu| \otimes \rho^F_{\mu\nu}(t), \tag{4}$$

where $\rho^F_{\mu\nu}(t)$ are taken for matrix elements of the density operator ρ in atomic basis. Then, following [7], we assume that the coherence relaxation time is much shorter than the typical evolution time of the system and set $\Gamma \gg \Omega$. From here, it is easy to show that the following approximation is applicable:

$$\frac{d}{dt}\left(\rho^F_{ge}e^{i\Delta t}\right) \approx \frac{d}{dt}\left(\rho^F_{eg}e^{-i\Delta t}\right) \approx 0. \tag{5}$$

Under assumption (5), system (1) may be written as differential equations for blocks $\rho^F_{\mu\nu}$, $\mu,\nu \in \{g,e\}$ where non-diagonal part ρ_{eg} and ρ_{ge} is expressed through diagonal elements ρ^F_{gg} and ρ^F_{ee}. In this way, we obtain closed system of differential equations for diagonal elements (see also [7]):

$$\begin{aligned}\dot{\rho}^F_{gg} &= \kappa\Gamma\left(2a^\dagger\rho^F_{ee}a - \rho^F_{gg}a^\dagger a - a^\dagger a\rho^F_{gg}\right) - i\kappa\Delta\left[a^\dagger a, \rho^F_{gg}\right] + \gamma_{eg}\rho^F_{ee} - \gamma_{ge}\rho^F_{gg},\\ \dot{\rho}^F_{ee} &= \kappa\Gamma\left(2a\rho^F_{ee}a^\dagger - \rho^F_{gg}aa^\dagger - aa^\dagger\rho^F_{gg}\right) - i\kappa\Delta\left[a^\dagger a, \rho^F_{ee}\right] + \gamma_{ge}\rho^F_{gg} - \gamma_{eg}\rho^F_{ee},\end{aligned} \tag{6}$$

where $\kappa = \dfrac{|\Omega|^2}{\Gamma^2 + \Delta^2}$.

3. Super-operators of conditional evolution

Just before solving the system (6), we have to give an interpretations for the introduced block-elements $\rho^F_{\mu\nu}$. Actually, they correspond to reduced density matrix of the intra-cavity mode conditioned by result of atomic state detection. Particularly, matrix $\rho^F_{\mu\nu}$ describes state evolution of the mode when atom prepared in state $|\nu\rangle$ was detected in state $|\mu\rangle$.

Using such interpretation, it is convenient to introduce super-operators of conditional evolution and express them through the set of basis elements of some beautiful algebra. In our case we can notice that maps:

$$2K_0\rho^F = a^\dagger a\rho^F + \rho^F aa^\dagger, \quad N\rho^F = \left[a^\dagger a, \rho^F\right], \tag{7}$$

$$K_+\rho^F = a^\dagger\rho^F a, \quad K_-\rho^F = a\rho^F a^\dagger, \tag{8}$$

obey commutation relations on $SU(1,1)$ algebra with Casimir operator N:

$$[K_-, K_+] = 2K_0, \quad [K_0, K_+] = K_+, \quad [K_0, K_-] = -K_-, \tag{9}$$

$$[K_0, N] = [K_+, N] = [K_-, N] = 0. \tag{10}$$

To rewrite system (6) using definitions (7) and (8), we use the following expansion for evolution super-operator of total system:

$$\rho_{AF}\left(t\right) = U\left(t\right)\rho_{AF}\left(0\right) = \sum_{\mu,\nu\in\{g,e\}} M_{\mu,\nu}\left(t\right) \otimes |\mu\rangle\rangle\langle\langle\nu|\,\rho_{AF}(0), \tag{11}$$

where we use notations $|\mu\rangle\rangle\langle\langle\mu|\,\rho_{AF} = |\mu\rangle\langle\nu|\,\rho_{AF}\,|\nu\rangle\langle\mu|$ and $M_{\mu\nu}(t)$ is taken for super-operator of conditional evolution (Kraus operator) of mode state corresponding to the case when atom prepared in state $|\mu\rangle$ was detected in state $|\nu\rangle$.

Substituting elements ρ^F_{gg} and ρ^F_{ee} of matrix $\rho_{AF}(t)$ in form (11) into (6) we obtain two independent systems for maps $M_{gg}(t)$, $M_{eg}(t)$ and $M_{ge}(t)$, $M_{ee}(t)$. The first one (which will be the subject of our interest) satisfies the following system:

$$\begin{cases} \dfrac{d}{dt}M_{gg} = -\left(\alpha K_0 + \beta + \gamma_{ge}\right) M_{gg} + \left(\alpha K_+ + \gamma_{eg}\right) M_{eg}, \\ \dfrac{d}{dt}M_{eg} = -\left(\alpha K_0 - \beta + \gamma_{eg}\right) M_{eg} + \left(\alpha K_- + \gamma_{ge}\right) M_{gg}. \end{cases} \tag{12}$$

Here, $\alpha = 2\kappa\Gamma$, $\beta = -\kappa\left(i\Delta N + \Gamma\right)$.

4. Time evolution of maps $M_{gg}(t)$ and $M_{eg}(t)$

For simplification of the following discussion, we assume resonance condition $\Delta = 0$ for interaction between atom and intra-cavity mode. These immediately give simplified expressions for parameters α and β:

$$\alpha = -2\beta = 2\frac{\Omega^2}{\Gamma} \equiv 2\Omega\varepsilon, \tag{13}$$

where $\varepsilon = \Omega/\Gamma \ll 1$. Also, we assume that spontaneous relaxation and excitation rates are small compared to parameters α and β, which means that

$$\gamma_{eg}, \gamma_{ge} \ll \varepsilon\Omega, \tag{14}$$

and apply perturbation theory to solve system (12) up to the first order.

For the zero-order approximation, the solution was found in [5]. Using definitions:

$$M_g = M_{gg}\exp\left[\left(\alpha K_0 + \beta + \gamma_{ge}\right)t\right], \tag{15}$$

$$M_e = M_{eg}\exp\left[\left(\alpha K_0 - \beta + \gamma_{eg}\right)t\right], \tag{16}$$

and setting $\gamma_{eg} = \gamma_{ge} = 0$ system (12) was reduced to exactly solvable one:

$$\begin{cases} \dfrac{d}{dt}M_g = \alpha K_+ M_e, \\ \dfrac{d}{dt}M_e = \alpha K_- M_g, \end{cases} \tag{17}$$

with solution of the form:

$$M_g = \cosh\alpha\sqrt{K_+K_-}t, \tag{18}$$

$$M_e = \left(K_-K_+\right)^{-1} K_- \sqrt{K_+K_-}\sinh\alpha\sqrt{K_+K_-}t. \tag{19}$$

Using (15) and (16), one rewrite system (12) in the form:

$$\begin{cases} \dfrac{d}{dt}M_g = e^{(\gamma_{ge}-\gamma_{eg})t}\left(\alpha K_+ + \gamma_{eg}e^{-\alpha t}\right) M_e, \\ \dfrac{d}{dt}M_e = e^{(\gamma_{ge}-\gamma_{eg})t}\left(\alpha K_- + \gamma_{ge}e^{\alpha t}\right) M_g. \end{cases} \tag{20}$$

and solution of this system will be obtained using perturbation theory by parameters γ_{eg}/Ω and γ_{ge}/Ω:

$$\begin{cases} M_g = M_g^{(0)} + M_g^{(1)}, \\ M_e = M_e^{(0)} + M_e^{(1)}, \end{cases} \tag{21}$$

starting from (18), (19) and with initial conditions $M_g(0) = E$, $\dfrac{d}{dt}M_g(0) = 0$.

Using previous results for zero-order terms $M_g^{(0)}$ and $M_e^{(0)}$ we have:

$$\begin{cases} \dfrac{d}{dt}M_g^{(1)} = \\ \Big[\gamma_{eg}e^{-\alpha t} + \left(\alpha K_+ + \gamma_{eg}e^{-\alpha t}\right)\left(\gamma_{ge} - \gamma_{eg}\right)t\Big]M_e^{(0)} + \Big[\alpha K_+ + \gamma_{eg}e^{-\alpha t} + \left(\alpha K_+ + \gamma_{eg}e^{-\alpha t}\right)\left(\gamma_{ge} - \gamma_{eg}\right)t\Big]M_e^{(1)}, \\ \dfrac{d}{dt}M_e^{(1)} = \\ \Big[\gamma_{ge}e^{\alpha t} - \left(\alpha K_- + \gamma_{ge}e^{\alpha t}\right)\left(\gamma_{ge} - \gamma_{eg}\right)t\Big]M_g^{(0)} + \Big[\alpha K_- + \gamma_{ge}e^{\alpha t} - \left(\alpha K_- + \gamma_{ge}e^{\alpha t}\right)\left(\gamma_{ge} - \gamma_{eg}\right)t\Big]M_g^{(1)}. \end{cases} \tag{22}$$

For very short time intervals $t \ll \tau = 1/\Omega$ value $(\gamma_{ge} - \gamma_{eg})\, t$ is negligibly small compared to γ_{ge} and γ_{eg}, which allows elimination of terms $(\gamma_{ge} - \gamma_{eg})\, tM^{(1)}_{e,g}$, $\gamma_{ge,eg}\, (\gamma_{ge} - \gamma_{eg})\, tM^{(0)}_{e,g}$ and replacement of terms $\gamma_{eg}e^{-\alpha t}M^{(1)}_{e,g}$ and $\gamma_{ge}e^{\alpha t}M^{(1)}_{e,g}$ by $\gamma_{eg}M^{(1)}_{e,g}$ and $\gamma_{ge}M^{(1)}_{e,g}$ correspondingly. From this, we obtain:

$$\begin{cases} \dfrac{d}{dt}M^{(1)}_g = \gamma_{eg}e^{-\alpha t}M^{(0)}_e + (\alpha K_+ + \gamma_{eg})\, M^{(1)}_e, \\ \dfrac{d}{dt}M^{(0)}_e = \gamma_{ge}e^{\alpha t}M^{(0)}_g + (\alpha K_- + \gamma_{ge})\, M^{(1)}_g. \end{cases} \tag{23}$$

This inhomogeneous system may be reduced to a second-order linear differential equation for $M^{(1)}_g$:

$$\frac{d^2}{dt^2}M^{(1)}_g - (\alpha K_+ + \gamma_{eg})\,(\alpha K_- + \gamma_{ge})\, M^{(1)}_g = \Big[\alpha\gamma_{ge}K_+e^{\alpha t} + \alpha\gamma_{eg}K_-e^{-\alpha t} + \gamma_{eg}\gamma_{ge}\Big]M^{(0)}_g - \alpha\gamma_{eg}e^{-\alpha t}M^{(0)}_e \tag{24}$$

with initial conditions $M^{(1)}_g(0) = 0$ and $\dfrac{dM^{(1)}_g}{dt}(0) = 0$.

Using the fact that $t \ll \tau$, we can expand the solution of (24) by the power series of the form:

$$M^{(1)}_g(t) = A_0 + A_1 t + A_2 t^2 + \dots. \tag{25}$$

From the initial conditions, it immediately follows that $A_0 = A_1 = 0$. To find A_2, we compare coefficients of the zero-order degree by t in the left and right sides of (24). From here, we obtain:

$$M^{(1)}_g(t) = \frac{1}{2}\Big[\alpha\gamma_{eg}K_- + \alpha\gamma_{ge}K_+ + \gamma_{ge}\gamma_{eg}\Big]t^2 + \dots. \tag{26}$$

Finally, for the map $M_{gg}(t)$, we obtain:

$$M_{gg}(t) = 1 - (\alpha K_0 + \beta + \gamma_{ge})\, t + \frac{1}{2}\Big[\alpha^2K_+K_- + (\alpha K_0 + \beta)^2 + \alpha\gamma_{eg}K_- + \alpha\gamma_{ge}K_+ + \gamma_{ge}\gamma_{eg}\Big]\, t^2 + \dots. \tag{27}$$

5. Ground state counting rate

Formula (27) gives expression for conditional evolution of the intra-cavity field state for the case when atom-pointer prepared in its ground state $|g\rangle$ after interaction with the mode was detected in the same state. To calculate probability $P_{gg}(t) = \langle M_{gg}(t)\rangle$ of this event let us calculate corresponded quantities for operators $K_\pm$ and K_0:

$$\begin{aligned} \langle K_-\rangle &= \mathrm{Tr}\,(K_-\rho) = \mathrm{Tr}\,\big(a\rho a^\dagger\big) = \mathrm{Tr}\,\big(a^\dagger a\rho\big) = \big\langle a^\dagger a\big\rangle\,, \\ \langle K_+\rangle &= \mathrm{Tr}\,(K_+\rho) = \mathrm{Tr}\,\big(a^\dagger\rho a\big) = \mathrm{Tr}\,\big(aa^\dagger\rho\big) = \big\langle aa^\dagger\big\rangle = \big\langle a^\dagger a\big\rangle + 1, \\ \langle K_0\rangle &= \mathrm{Tr}\,(K_0\rho) = \frac{1}{2}\,\mathrm{Tr}\,\big(a^\dagger a\rho + aa^\dagger\rho\big) = \big\langle a^\dagger a\big\rangle + \frac{1}{2}. \end{aligned} \tag{28}$$

Then, for probability $P_{gg}(t)$, we will have:

$$P_{gg}(t) = \langle M_{gg}(t)\rangle = \mathrm{Tr}(M_{gg}(t)\rho) = 1 - \big(\alpha\big\langle a^\dagger a\big\rangle + \gamma_{ge}\big)\, t + \left[\alpha^2\left\langle\big(a^\dagger a\big)^2\right\rangle + \frac{1}{2}\big(\alpha\,(\gamma_{ge} + \gamma_{eg})\big\langle a^\dagger a\big\rangle + \alpha\gamma_{ge} + \gamma_{ge}\gamma_{eg}\big)\right] t^2 + \dots, \tag{29}$$

or in symmetrical form:

$$P_{gg}(t) = 1 - \big(\alpha\big\langle a^\dagger a\big\rangle + \gamma_{ge}\big)\, t + \left[\alpha^2\left\langle\big(a^\dagger a\big)^2\right\rangle + \frac{\alpha}{2}\gamma_{eg}\big\langle a^\dagger a\big\rangle + \frac{\alpha}{2}\gamma_{ge}\big\langle aa^\dagger\big\rangle + \frac{\gamma_{ge}\gamma_{eg}}{2}\right] t^2 + \dots. \tag{30}$$

From this expression, the mean value of photon number operator $\langle a^\dagger a\rangle$ and its square $\left\langle\big(a^\dagger a\big)^2\right\rangle$ may be obtained by differentiating probability function $P_{gg}\,(t)$ over t for $t = 0$:

$$\big\langle a^\dagger a\big\rangle = -\frac{1}{\alpha}\left(\frac{dP_{gg}(0)}{dt} + \gamma_{ge}\right), \tag{31}$$

$$\left\langle\big(a^\dagger a\big)^2\right\rangle = \frac{1}{2\alpha^2}\left[\frac{d^2}{dt^2}P_{gg}(0) + \frac{d}{dt}P_{gg}(0)\,(\gamma_{eg} + \gamma_{ge}) + \gamma_{ge}\,(\gamma_{ge} - \alpha)\right]. \tag{32}$$

6. Numerical results and discussion

In this section, we compare obtained analytical results with numerical simulation of photo-detection procedure. Fig. 1 contains this comparison for probability to detect atom in its ground state $|g\rangle$ for Fock state with $n = 4$ photons, $\Gamma = 10$ and $\gamma_{eg} = \gamma_{ge} = 0.5$ in frequency units of Ω. Three cases are under consideration: numerical simulation (blue solid line), zero-order (green doted line) and first-order (red dashed line) approximation of the solution. All three lines are quite close nearby the origin and first order approximation shows familiar behaviour with exact solution on considered time interval.

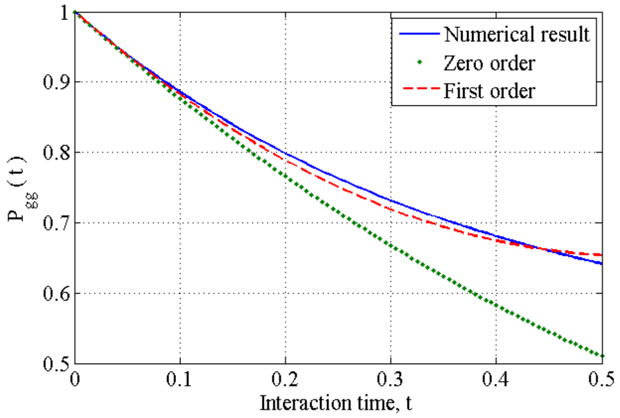

FIG. 1. Probability P_{gg} to detect atom in its ground state: numerical simulation (blue solid line), zero-order (green dotted line) and first-order (red dashed line) approximation

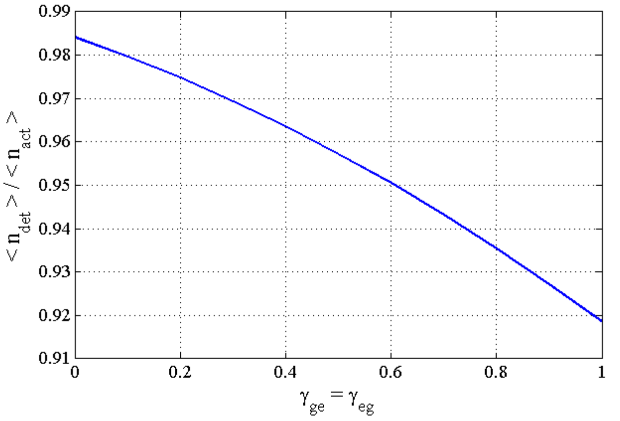

FIG. 2. Relation between actual n_{act} and detected n_{det} mean photon number as a function of spontaneous decay and excitation rates

In Fig. 2, we show the relation between actual n_{act} and detected n_{det} mean photon number as a function of spontaneous decay and excitation rates for the case $\gamma_{eg} = \gamma_{ge}$ when other parameters are taken the same as in previous figure. All values were calculated for probability function $P_{gg}(t)$ obtained from exact solution. From here, we can see that number of detected intra-cavity photons decrease with increasing spontaneous decay and excitation rates.

Figure 3 shows the relation between actual n_{act} and detected n_{det} mean photon number as a function of interaction time between atom and mode prepared in Fock state with $n = 4$. Calculations are made for different values of the coefficient of spontaneous excitation (γ_{eg}, first number in the legend) and decay (γ_{ge}, second number in the legend). We can see that curves are grouped in threes according to the same value of γ_{ge} which determines accuracy.

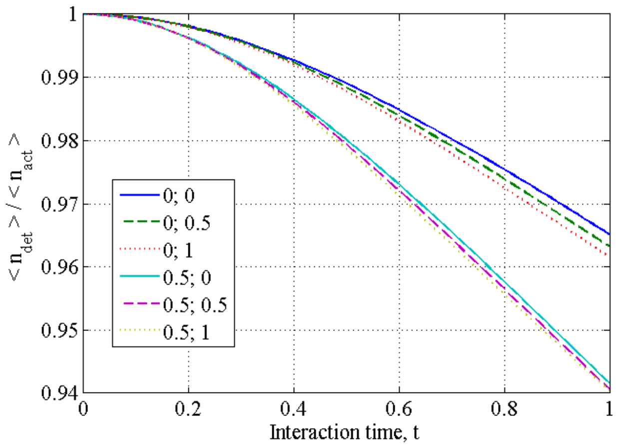

FIG. 3. Relation between actual n_{act} and detected n_{det} mean photon number as a function of spontaneous decay and excitation rates

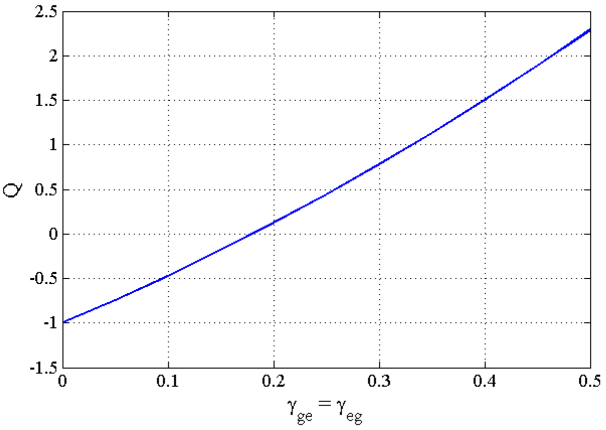

FIG. 4. Estimated value of Mandel's parameter as a function of spontaneous decay and excitation rates

Finally, we investigate estimated value of Mandel's parameter:

$$Q = \frac{\langle n^2 \rangle - \langle n \rangle^2}{\langle n \rangle} - 1, \quad n = a^\dagger a, \tag{33}$$

as a function of spontaneous decay and excitation rates for the case of initial Fock state with $n = 4$ and $\gamma_{eg} = \gamma_{ge}$. When losses are absent, we have typical value $Q = -1$ for the state with definite photon number. For non-zero values of γ_{eg} and γ_{ge} parameter Q increases reaching the value corresponding to thermal fields. This means that thermal radiation originated from decaying process become predominant.

7. Conclusion

In present paper we suggest and analyze an indirect photo-detection protocol of intra-cavity mode statistical properties which may be obtained from statistics of atomic state detector clicks. The obtained probability distribution for detecting atom in its ground state contains, in general, all degrees of photon number operator and allows in principle to restore full statistics of the mode calculating all elements of power series for P_{gg}. However, this process is bounded by the finite duration of interaction time between the atom and the mode because calculation accuracy of time derivative is degrades with higher order derivatives.

The estimated number of experiments required for obtaining appropriate statistics for atomic detector clicks at point $t_0 = 0.1$ mcs is $N = 100$ (where $P_{gg}(0.1) = 0.99$ is theoretical estimation). We repeat this cycle of measurements at each point for about 100-200 points and in that way, the overall number of measurement cycles is on the order of 10^4.

Indirect photo-detection with atom-pointer in use gives beautiful model of quantum measurement due to the possibility of controlling interaction strength and inclusion relaxation process into the model. From this point of view, formulation protocols analogous to well known homodyne and heterodyne detection in terms of indirect model would be very interesting.

Acknowledgements

This work was partially financially supported by the Government of the Russian Federation (grant 074-U01), by grant MK-5161.2016.1 of the President of the Russian Federation, grant 16-11-10330 of Russian Science Foundation.

References

[1] Kelley P.L., W.H. Kleiner Theory of electromagnetic field measurement and photo-electron counting. *Physical Review*, 1964, **136** (2A), P. 316–334.

[2] Braginsky B., Khalili F.Ya. *Quantum Measurement*, Cambridge University Press, Cambridge, 1992.

[3] Miroshnichenko G.P., Trifanova E.S., Trifanov A.I. An indirect measurement protocol of intracavity mode quadratures dispersion in dynamical Casimir effect. *Eur. Phys. J. D*, 2015, **69**, P. 137.

[4] Smithey D.T., et al, Measurement of the Wigner Distribution and the Density Matrix of a Light Mode Using Optical Homodyne Tomography: Application to Squeezed States and the Vacuum. *Phys. Rev Lett.*, 1993, **70** (8), P. 1244–1247.

[5] Pregnel K.L., Pegg D.T., Binomial states and the phase distribution measurement of weak optical elds. *Phys. Rev. A*, 2003, **67**, 063814.

[6] Srinivas M.D., Davies E.B., Photon counting probabilities in quantum optics. *Optica Acta*, 1981, **28** (7), P. 981–996.

[7] Trifanov A.I., Miroshnichenko G.P. Reduced conditional dynamic of quantum system under indirect quantum measurement. *Nanosystems: Physics, Chemistry, Mathematics*, 2013, **4** (5), P. 635–647.

[8] Dodonov A.V., Mizrahi S.S. Inclusion of nonidealities in the continuous photodetection model. *Phys. Rev. A*, 2007, **75**, 013806.

[9] Mario Ziman, Process positive-operator-valued measure: A mathematical framework for the description of process tomography experiments. *Phys. Rev. A*, 2008, **77**, 062112.

[10] Briegel H.-J., Englert B.-G., Sterpi N., Walther H. One-atom maser: Statistics of detector clicks. *Phys. Rev. A*, 1994, **49**, P. 2962.

[11] Trifanova E.S., Trifanov A.I. Monitoring of quantum mode correlation functions in the presence of pointer state phase relaxation. *J. of Phys.: Conf. Ser.*, 2016, **735**, 012044.

[12] Johnson D.B., Schieve W.C., Detection statistics in the micromaser. *Phys. Rev. A*, 2001, **63**, 033808.

NANOSYSTEMS: PHYSICS, CHEMISTRY, MATHEMATICS, 2017, 8 (4), P. 454–461

Calculations of the onset temperature for tunneling in multispin systems

S. M. Vlasov[1,2], P. F. Bessarab[1,2], V. M. Uzdin[1,3], H. Jónsson[2,4]
[1]ITMO University, Kronverkskiy, 49, St. Petersburg, 197101, Russia
[2]Science Institute and Faculty of Physical Sciences, Univ. of Iceland, 107 Reykjavík, Iceland
[3]St. Petersburg State University, St. Petersburg, 198504, Russia
[4]Department of Applied Physics, Aalto University, Espoo, FIN-00076, Finland
v_uzdin@mail.ru

PACS 75.45.+j , 82.20.Xr **DOI 10.17586/2220-8054-2017-8-4-454-461**

Transitions between magnetic states of a system coupled to a heat bath can occur by exceeding the energy barrier, but as temperature is lowered quantum mechanical tunneling through the barrier becomes the dominant transition mechanism. A method is presented for estimating the onset temperature for tunneling in a system with an arbitrary number of spins using the second derivatives of the energy with respect to the orientation of the magnetic vectors at the first order saddle point on the energy surface characterizing the over-the-barrier mechanism. An application to a monomer and a dimer of molecular magnets containing a Mn_4 group is presented and the result found to be in excellent agreement with reported experimental measurements.

Keywords: magnetic transitions, tunneling, rate theory, molecular magnet.

Received: 5 August 2017

Revised: 15 August 2017

1. Introduction

An assessment of the stability of magnetic states is an important problem in the theory of magnetism [1, 2]. Magnetic nanosystems are candidates for spintronics and high density storage devices where a critical issue is the lifetime of prepared magnetic states. A given magnetic state of a nanosystem coupled to a heat bath can have a finite lifetime because of thermally activated transitions involving leaps over an energy barrier separating it from other magnetic states of the system. But, at low enough temperature, quantum mechanical tunneling through the barrier will become the dominant transition mechanism. It is important to have a tool to estimate the temperature at which the tunneling mechanism becomes predominant, thereby reducing the lifetime from what would be expected based on the over-the-barrier mechanism.

Quantum tunneling in spin systems has been the topic of many theoretical [3] and experimental studies [4–7] over the past few decades. At high enough temperature, quantum effects are not significant and transitions are due to thermal activation described by the Arrhenius law. However, in the limit of zero temperature, only tunneling out of the lowest energy level of the initial state can occur. In an intermediate temperature range, tunneling can be thermally assisted, i.e. occurring from thermally activated levels of the initial state. The crossover from over-the-barrier to quantum tunneling can, in such cases, be relatively smooth. The shape of the energy surface affects how sharp this crossover is [8].

Several theoretical studies of the crossover in simple spin models containing one [9–12] or two [13] spins have been carried out using the effective potential method [14]. The effective potential method uses an exact mapping of a spin system onto a particle system with an effective potential and mass that can be coordinate dependent. However, this method is not general and can only be applied to simple model systems. High-order anisotropy terms, such as $(\hat{S}_+^2 + \hat{S}_-^2)$ and $(\hat{S}_+^4 + \hat{S}_-^4)$, have not been incorporated in the mapping approach [15], but can significantly affect the tunneling rate [5, 16]. So far, systems with high-order anisotropy have only been studied numerically by direct diagonalization of the Hamiltonian [17, 18].

Here, a method for calculating the onset temperature of thermally assisted tunneling in a multispin system is presented and applied to two systems: a monomer and a dimer of molecular magnets containing Mn_4 groups. The method involves an analysis of the shape of the energy surface in the vicinity of the first order saddle point on the energy surface representing the transition state of the over-the-barrier mechanism. The present article extends a previous report on systems consisting of a single magnetic vector (a single spin, or multiple spins within the macro-spin approximation) [19]. With the present formulation, the onset temperature for tunneling in systems consisting of an arbitrary number of spins can be estimated.

The article is organized as follows: In the next section, the methodology for estimating the lifetime of a magnetic state due to over-the-barrier transitions is briefly reviewed. Then, the expression for the onset temperature for quantum mechanical tunneling is derived in section 3. Applications are presented in section 4, first to a monomer and then to a dimer of molecular magnets. The article concludes with a summary in section 5.

2. Over-the-barrier transitions

A system of N spins is described by the orientation of each of the spins, $\omega = \{\theta_1, \phi_1, \theta_2, \ldots \phi_N, \}$, where θ and ϕ are spherical polar coordinates. The energy as a function of these variables, $U(\omega)$, represents an energy surface and the magnetic states of the system correspond to local minima on this surface. The mechanism of a transition from one state to another involving a jump over an energy barrier is characterized by a minimum energy path (MEP) connecting the corresponding minima. At every point on an MEP, the gradient of the energy point is along the path. The MEP is a transition path with maximal statistical weight, assuming a Boltzmann distribution is established and maintained in the initial state. The MEP can be found using the geodesic nudged elastic band method where the path is discretized by generating a set of replicas of the system and an optimization algorithm is used to bring the replicas from some initial location to an MEP [20].

The point of highest energy along the MEP, $\omega^\dagger$, represents a first order saddle point on the energy surface, a point where the Hessian has one and only one negative eigenvalue. Within harmonic transition state theory (HTST), the transition state is taken to be a hyperplane going through the saddle point with normal pointing along the direction of the unstable mode (the eigenvector corresponding to the negative eigenvalue of the Hessian) [21,22]. An estimate of the activation energy for the transition is then obtained as $\Delta E = U(\omega^\dagger) - U(\omega_m)$, where $U(\omega^\dagger)$ is the energy at the first order saddle point and $U(\omega_m)$ is the energy of the initial state minimum.

The rate of thermally activated transitions involving jumps over the energy barrier can be estimated using HTST for magnetic systems [21]

$$\Gamma^{HTST} = \nu_0 e^{-\Delta E/k_B T}, \tag{1}$$

where ν_0 is a pre-exponential factor that depends on the Hessian evaluated at the saddle point and at the minimum of the energy surface. Calculations of transition rates in magnetic systems using this approach have been carried out in studies of, for example, remagnetization in small islands adsorbed on a solid surface [23], analysis of temperature dependence of hysteresis loops [24], annihilation of magnetic skyrmions [25,26] and interaction of a magnetic tip with a solid surface [27].

Quantum mechanical effects can influence the transition rate even at temperature above the onset temperature for tunneling. This occurs because of the zero point energy (ZPE) which can raise the energy of the initial state and the transition state to a different extent. Within the harmonic approximation, the correction is obtained by adding the ZPE for each vibrational (magnon) mode to the initial state energy and the saddle point energy. As there is one fewer vibrational mode at the transition state than at the initial state, this effect tends to reduce the energy barrier and lower the activation energy for the transition, analogous to the so-called kinetic isotope effect in atomic rearrangements (chemical reactions and atom diffusion). The ZPE corrected activation energy is

$$\Delta E^{ZPEC} = \left(U(\omega^\dagger) + \frac{1}{2}\sum_{i=1}^{N-1} \nu_{\dagger,i} \right) - \left(U(\omega_m) + \frac{1}{2}\sum_{i=1}^{N} \nu_{m,i} \right), \tag{2}$$

where $\nu_{\dagger,i}$ and $\nu_{m,i}$ are the vibrational frequencies [28,29] calculated at the saddle point and at the minimum, respectively. As can be seen from the molecular magnet example below, the ZPE correction can significantly change the acitvation energy and thereby the slope in the Arrhenius graf.

3. Onset temperature for tunneling

Tunneling through an energy barrier can take place because of quantum mechanical delocalization which enables the system to avoid the top of the energy barrier. In a thermalized system, the effect of delocalization can be described in a convenient way using statistical Feynman Path Integrals. The instanton technique can be used to identify when quantum delocalization becomes large enough to make tunneling the dominant transition mechanism. In instanton theory the transition rate is written in terms of the imaginary-time ($\tau = it$) action, S, and a stationary phase approximation [30–32]. The transition rate constant can be expressed as

$$\Gamma = D \exp\left(-S[\omega(\tau)]_{inst}/\hbar\right), \tag{3}$$

where $\omega(\tau)$ is a path corresponding to a periodic trajectory with period $\tau = \beta\hbar$ satisfying $\omega(0) = \omega(\beta\hbar)$, and the pre-factor D takes into account the probability of paths deviating from $\omega(\tau)$. This special path, often referred to as the instanton, corresponds to a stationary point of the action, a saddle point on the action surface where the path is extended, corresponding to quantum delocalization [32–34].

In our previous work [19], we considered systems with a single spin. Here, a generalization to many-spin systems is described. The Hilbert space of a many-spin system is a tensor product of the Hilbert space of the individual spins. The Euclidean (imaginary-time) action for a system with N spins of length s is defined by [35–37]

$$S(\mathbf{\Omega}) = -is \int_{-\beta/2}^{\beta/2} \sum_{j=1}^{N} (1-\cos\theta_j)\dot{\phi}_j d\tau + \int_{-\beta/2}^{\beta/2} U(\omega(\tau)) d\tau, \tag{4}$$

where the first term is the sum of the Berry phase of the individual spins and $\mathbf{\Omega} = \omega(\tau)$ represents a closed trajectory with period β.

From here on we use atomic units with $\hbar = 1$, $\mu_B = 1/2$ and the mass and charge of an electron have unit value, $e = 1$ and $m_e = 1$. A scaled gyromagnetic ratio is defined as $\tilde{g} = g/2$.

In order to find the onset temperature for tunneling, T_c, the action is expanded to second order in the vicinity of the first order saddle point on the energy surface, $\mathbf{\Omega} = \omega^\dagger + \epsilon\delta\mathbf{\Omega}$,

$$S(\mathbf{\Omega}) = \beta U(\omega^\dagger) + \delta S + \frac{1}{2}\delta^2 S, \tag{5}$$

$$\delta^2 S = -2is \int_{-\beta/2}^{\beta/2} \sum_{j=1}^{N} \left(\delta\theta_j \delta\dot{\phi}_j \sin\theta_j\right) d\tau + \int_{-\beta/2}^{\beta/2} \delta\mathbf{\Omega}\ \mathcal{H}\ \delta\mathbf{\Omega}^T d\tau, \tag{6}$$

where $\mathcal{H}$ is the Hessian matrix of the energy surface $U(\omega)$ at the saddle point $\omega^\dagger$. As $\epsilon \to 0$, $\delta^2 S$ becomes a quadratic form of the Hessian, $\mathcal{H}$, which has one and only one real negative eigenvalue.

The task is to find the temperature at which $\mathbf{\Omega}$ becomes an instanton, *i.e.* a saddle point at the action surface with quantum delocalization. At that point, a zero mode appears corresponding to displacement along the path and thus constant S. This signals the transition from thermally activated jumps to quantum tunneling [32,33].

Since the instanton is a closed path, $\delta\theta_k$ and $\delta\phi_k$ can be expanded in a Fourier series and $\delta^2 S$ in eqn. (6) rewritten as

$$\frac{1}{2}\delta^2 S(\theta^\dagger, \phi^\dagger) = \beta \sum_{n=0}^{\infty} \left(\sum_{k=0}^{N} \left[\frac{2\pi s \sin\theta_k^\dagger}{\beta} n(\phi_n^k \theta_n^{k^*} - \phi_n^{k^*} \theta_n^k) \right] + \right.$$
$$\left. \sum_{j,k} \left[a\theta_n^k \theta_n^{j^*} + b\left(\phi_n^k \theta_n^{j^*} + \phi_n^{k^*} \theta_n^j\right) + c\phi_n^k \phi_n^{j^*} \right] \right). \tag{7}$$

The matrix representing the quadratic form of the action is infinite and has a block diagonal form

$$G = \begin{pmatrix} \gamma_0 & & & & \\ & \gamma_1 & & & \\ & & \ddots & & \\ & & & \gamma_n & \\ & & & & \ddots \end{pmatrix}, \tag{8}$$

where

$$\gamma_n = \mathcal{H} + \left(\begin{array}{ccc|ccc} 0 & \cdots & 0 & -k_1^n & \cdots & 0 \\ 0 & \ddots & 0 & 0 & \ddots & 0 \\ 0 & \cdots & 0 & 0 & \cdots & -k_N^n \\ \hline k_1^n & \cdots & 0 & 0 & \cdots & 0 \\ 0 & \ddots & 0 & 0 & \ddots & 0 \\ 0 & \cdots & k_N^n & 0 & \cdots & 0 \end{array} \right), \tag{9}$$

where $k_j^n = 2\pi n T s \sin\theta_j^\dagger$.

An expression for the onset temperature for tunneling can be obtained by analyzing the determinant of G:

$$\det(G) = \prod_{n=0}^{\infty} \det(\gamma_n). \tag{10}$$

Consider first γ_0 which is the Hessian of the energy surface at the first order saddle point. There, γ_0 contains one negative eigenvalue so $\det(\gamma_0) < 0$. However, the other blocks, γ_n (for $n > 0$), depend on temperature and at $T \gg T_c$ are positive definite

$$\det(\gamma_n) \sim (2\pi s n)^{2N} \prod_{j=1}^{N} \sin^2 \theta_j^\dagger > 0, \tag{11}$$

and $\det(G) < 0$. As the temperature is lowered to T_c, a zero of G appears signaling a stationary point involving quantum delocalization. This must arise from γ_1 since the temperature in each γ_n is scaled by n and blocks with $n > 1$ thus have zeros at even lower temperature. The onset temperature for tunneling is, therefore, found by solving

$$\det(\gamma_1(T_c)) = 0. \tag{12}$$

This can be easily done numerically for multi-spin systems. All that is required for the calculation are the second derivatives of the energy at the first order saddle point corresponding to the over-the-barrier mechanism.

For a single-spin system, an analytical expression for the onset temperature can be obtained

$$T_c = \frac{\sqrt{b^2 - ac}}{2\pi s k_B \sin\theta^\dagger}, \tag{13}$$

where

$$a \equiv \left.\frac{\partial^2 U(\theta^\dagger, \phi^\dagger)}{\partial \theta^2}\right|_{\theta^\dagger,\, \phi^\dagger}, \; c \equiv \left.\frac{\partial^2 U(\theta^\dagger, \phi^\dagger)}{\partial \phi^2}\right|_{\theta^\dagger,\, \phi^\dagger}, \; b \equiv \left.\frac{\partial^2 U(\theta^\dagger, \phi^\dagger)}{\partial \theta \partial \phi}\right|_{\theta^\dagger,\, \phi^\dagger}. \tag{14}$$

The pair of eigenvalues of the γ_1 block are

$$\lambda = \frac{a+c}{2} \pm \frac{\sqrt{(a-c)^2 + 4b^2 - 4k^2}}{2}. \tag{15}$$

In addition to the crossover temperature, we can define the temperature T_0 at which the two eigenvalues become complex conjugates

$$T_0 = \frac{\sqrt{(a-c)^2 + 4b^2}}{4\pi s k_B \sin\theta^\dagger}. \tag{16}$$

At this temperature, both eigenvalues are equal to $(a + c)/2$ and could be negative. At higher temperature, the eigenvalues are complex. In the temperature range between T_c and T_0 the two eigenvalues are real, either both are positive or both are negative.

4. Applications. Molecular magnets

Previously, we have presented calculations and compared with experimental results for the single molecular magnet containing a Mn_4 group [19]. We briefly review those calculations here before discussing the dimer. The molecular magnet has a total spin of $s = 9/2$ and can be described with the following Hamiltonian

$$\hat{H} = -D\hat{S}_z^2 - B\hat{S}_z^4 - g\mu_0 \hat{\mathbf{S}} \cdot \mathbf{H} + \hat{H}_{trans}, \tag{17}$$

where D and B are axial anisotropy constants, B is an applied magnetic field and H_{trans} gives the in-plane anisotropy which is small compared with D. The values of the parameters have been determined from experimental measurements (not involving tunneling) [38]: $D = 0.74$ K, $B = -3.8$ mK and $g = 2$. The transverse term is chosen to be fourth-order $E(\hat{S}_+^4 + \hat{S}_-^4$ with $E = 9.8 \times 10^{-4}$ K [38].

For the single molecular magnet it is possible to give an analytical formula for the onset temperature. Expanding (12) with the Mn_4 system Hamiltonian (17) at the saddle point gives

$$T_c = \frac{4s^2\sqrt{DE - 4E^2 s^2}}{\pi}, \tag{18}$$

and $T_c = 0.61$ K. This result is in close agreement with the reported experimental results giving 0.67 K [38]. The dependence of eigenvalues on temperature is shown in Fig. 1.

The calculated transition rate using HTST (applicable for $T > T_c$) and the predicted onset temperature for tunneling in the monomer are shown in Fig. 2, along with experimental data. At temperature below T_c, the tunneling rate is expected to be similar to the HTST rate at T_c. The agreement between the calculations and measurements is good.

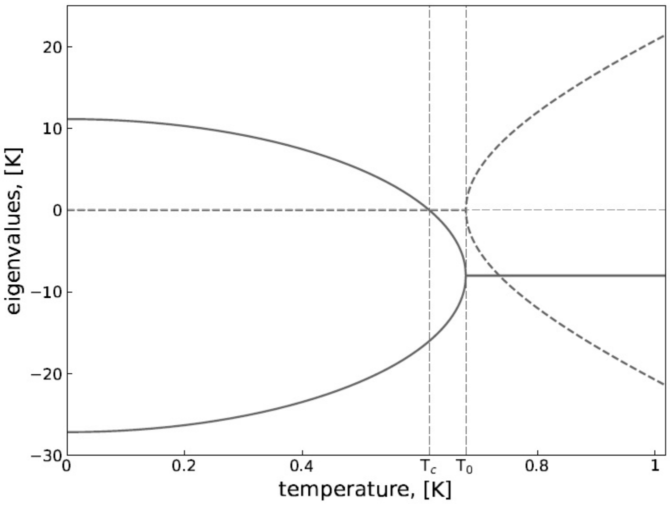

FIG. 1. Eigenvalues of the γ_1 matrix block for the monomer (eq. (17)) Mn_4 molecular magnet. Solid line: real part. Dashed line: imaginary part. At temperature above T_0 the eigenvalues are complex conjugates and give a positive contribution into the determinant. At temperature below the T_c, γ_1 has only one negative eigenvalue, therefore the determinant changes sign at T_c. In the temperature interval $T_c < T < T_0$ γ_1 has two negative eigenvalues

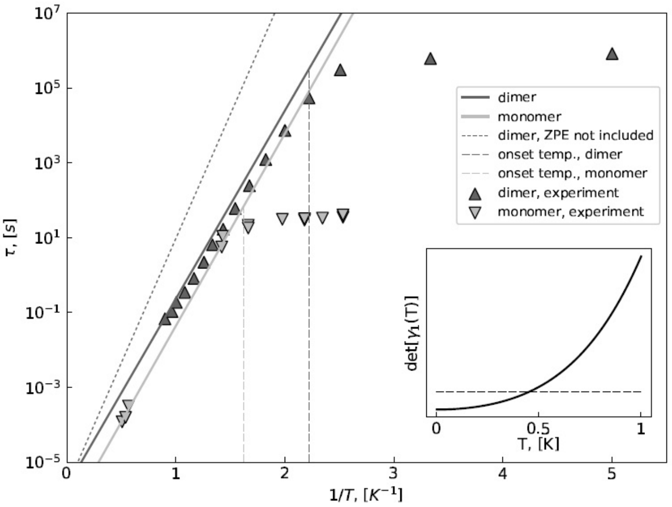

FIG. 2. The calculated lifetime for a monomer and a dimer of molecular magnets containing Mn_4 groups. Results of calculations using harmonic transition state theory with zero point energy correction for the monomer (solid gray line) and the dimer (solid black line) are shown. Calculated lifetime for the dimer without ZPE correction (dashed line) is also shown for comparison. Calculated values for the onset temperature for tunneling calculated from (18) using the Hamiltonian in (17) for the monomer and (19) for the dimer (dashed vertical lines) with parameters taken from experimental measurements are also shown. Experimentally measured transition rate for the monomer [38] is shown with gray triangles and for the dimer [40] with black triangles. Below T_c, the tunneling rate is expected to be similar to the HTST rate at T_c. Excellent agreement is obtained between the calculated and measured results. Inset: The determinant of the γ_1 matrix block for the dimer, showing how it becomes negative at T_c

We turn now to calculations for a dimer of Mn_4 molecular magnets and compare with experimental measurements on $[Mn_4O_3Cl_4(O_2CEt)_3(py)_3]_2$. Each unit of the dimer is described with a magnetic moment of $s = 9/2$, and the Hamiltonian of the system is taken to be

$$\hat{H} = \hat{H}_1 + \hat{H}_2 + J\hat{\mathbf{S}}_1 \cdot \hat{\mathbf{S}}_2, \tag{19}$$

where both $\hat{H}_1$ and $\hat{H}_2$ have the same form as (17) with the parameters taken from [39] and $J = 0.12$ K is isotropic superexchange [40]. The transverse term is chosen to include both 4th- and 2nd-order anisotropies: $C(\hat{S}_+^2 + \hat{S}_-^2)$ and $E(\hat{S}_+^4 + \hat{S}_-^4)$, with $C = 0.032$ K and $E = -7.5 \times 10^{-5}$ K, in order to match the experimental results of the rate above T_c. The energy surface and a minimum energy path for a transition are shown in Fig. 3.

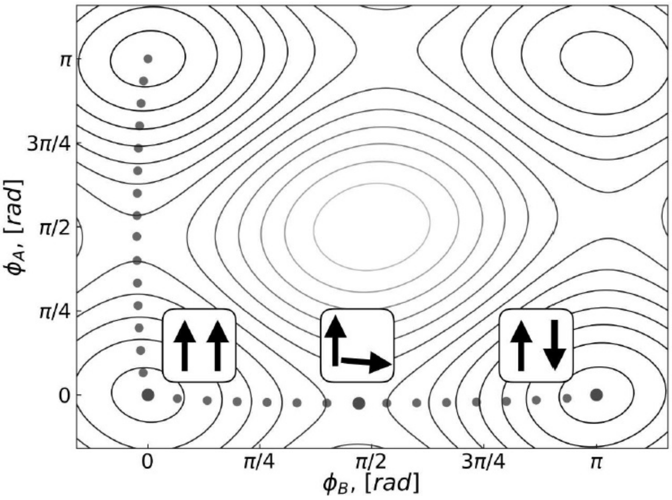

FIG. 3. Energy surface for a dimer molecular magnets containing Mn_4 group when $\theta_A = \theta_B = \pi/2$. The minimum energy path for a remagnetization transition is shown with black dots. The insets show the orientation of the 9/2 spins of each Mn_4 unit at the initial state (left), first order saddle point (middle), and product state (right).

The calculated crossover temperature for the dimer is $T_c = 0.40$ K in close agreement with experimental measurements [40]. Due to the weak exchange interaction every spin flips almost independently.

In order to see the effect of coupling between the two units more clearly, we also calculated and analyzed a system with larger exchange interaction, taken to be of the same order as the anisotropy, $J = 0.6$ K. The calculated onset temperature for the tunneling is found to be $T_c = 0.35$ K. Due to the strong exchange interaction between spins eigenvalues of γ_1 behave differently, but we still can see the temperature at which one of them crosses zero (see Fig. 4).

The result of calculation of the HTST transition rate and onset temperature for tunneling of the dimer (19) using experimentally determined parameter values is shown in Fig. 2. The ZPE correction changes the slope in the Arrhenius graph, bringing the calculated HTST results closer to the experimental values.

5. Summary

A method is presented for finding the onset temperature of thermally activated tunneling in magnetic systems that are characterized by spin vectors with orientation prescribed by continuous angular variables. A study is made for the Mn_4 molecular magnets where both the high temperature jump rate and the onset temperature for tunneling are calculated and compared with experimental data. Excellent agreement is obtained. The rate calculated above the onset temperature for tunneling includes zero point energy correction. The onset temperature for tunneling is found by analyzing eigenvalues of the γ_1 matrix block at the first order saddle point on the energy surface.

Previously, the onset temperature for tunneling in single-spin or simple (without higher-order anisotropy) two-spin systems can be assessed by other methods, such as the effective potential method or numerical methods involving direct diagonalization of the Hamiltonian, but the method presented here is applicable to systems with an arbitrary number of spins. The method presented here, makes it possible to estimate the onset temperature for tunneling in a magnetic system described by spin vectors as long as the second derivatives of the energy with respect to the angles describing the orientation of vectors can be evaluated at the saddle point on the energy surface.

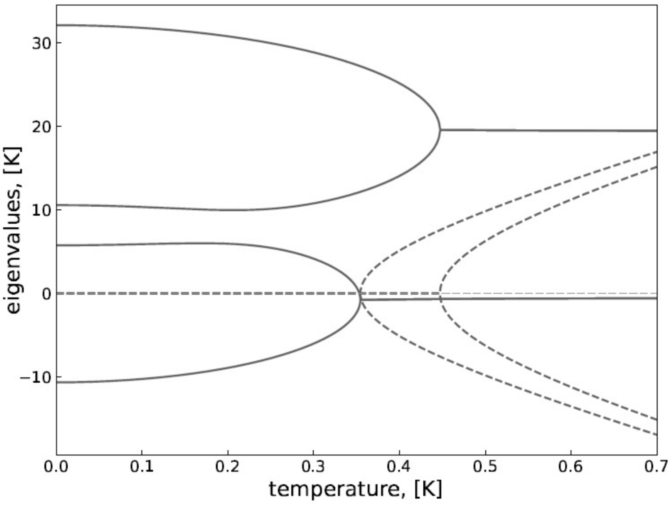

FIG. 4. Eigenvalues of the γ_1 matrix block of the dimer (eq. (19)) when the exchange parameter is chosen to be $J = 0.6$ K. Solid line: real part. Dashed line: imaginary part. The eigenvalues depend on temperature in a similar way as is shown for the monomer in Fig. 1. A pair of eigenvalues becomes real and remains positive, while a second pair of eigenvalues changes sign at T_c from negative to positive as temperature is lowered

The most peculiar characteristic of magnetic systems is that the onset temperature for tunneling depends not only on second derivatives along the unstable mode at the first order saddle point, as in particle systems, but on the curvature of the energy surface at the first order saddle point. This is due to the inseparability of the spin Hamiltonian.

Acknowledgements

This work was supported by the Icelandic Research Fund and the Academy of Finland (grant 278260) and partially financially supported by the Government of the Russian Federation (grant 074-U01).

References

[1] Brown, Jr. W.F. Thermal Fluctuations of Fine Ferromagnetic Particles. *IEEE Transactions on Magnetics*, 1979, **MAG-15**, P. 1196–1208.
[2] Braun H.-B. Kramers's rate theory, broken symmetries and magnetization reversal. *J. Appl. Physics*, 1994, **76**, P. 6310–6315.
[3] Chudnovsky E.M., Tejada J. *Macroscopic Quantum Tunneling of the Magnetic Moment.* Cambridge University Press, New York.: 1998.
[4] Bokacheva L., Kent A.D. and Walters M.A. Crossover between Thermally Assisted and Pure Quantum Tunneling in Molecular Magnet Mn_{12}-Acetate. *Phys. Rev. Lett.*, 2000, **85**, P. 4803–4806.
[5] Mertes K.M., Zhong Y., *et al.* Abrupt crossover between thermally activated relaxation and quantum tunneling in a molecular magnet. *Europhys. Lett.*, 2001, **55**, P. 874–879.
[6] Wernsdorfer W., Murugesu M. and Christou G. Resonant Tunneling in Truly Axial Symmetry Mn_{12} Single-Molecule Magnets: Sharp Crossover between Thermally Assisted and Pure Quantum Tunneling. *Phys. Rev. Lett.*, 2006, **96**, 057208 (4 pp.)
[7] Loth S., Baumann S., *et al.* Bistability in atomic-scale antiferromagnets. *Science*, 2012, **335**, P. 196–199.
[8] Chudnovsky E.M. Phase transitions in the problem of the decay of a metastable state. *Phys. Rev. A*, 1992, **46**, P. 8011–8014.
[9] Chudnovsky E. M., Garanin D. A. First- and Second-Order Transitions between Quantum and Classical Regimes for the Escape Rate of a Spin System. *Phys. Rev. Lett.*, 1997, **79**, P. 4469–4472.
[10] Park C.-S., Yoo S.-K. and Yoon D.-H. Quantum-classical crossover of the escape rate in a biaxial spin system with an arbitrarily directed magnetic field. *Phys. Rev. B*, 2000, **61**, P. 11618–11624.
[11] Kim G.-H. and Chudnovsky E.M. Escape-rate crossover between quantum and classical regimes in molecular magnets: A diagonalization approach. *Europhys. Lett.*, 2000, **52**, P. 681–687.
[12] Garanin D.A. and Chudnovsky E.M. Quantum statistical metastability for a finite spin. *Phys. Rev. B*, 2000, **63**, 024418 (7 pp.)
[13] Owerre S. A. and Paranjape M. B. Phase transition between quantum and classical regimes for the escape rate of dimeric molecular nanomagnets in a staggered magnetic field. *Phys. Lett. A*, 2014, **378**, P. 1407–1412.
[14] Ulyanov V.V. and Zaslavskii O.B. New methods in the theory of quantum spin systems. *Phys. Rep.*, 1992, **216**, P. 179–251.
[15] Owerre S. A., Paranjape M. B. Macroscopic quantum tunneling and quantum-classical phase transitions of the escape rate in large spin systems. *Phys. Rep.*, 2015, **546**, P. 1–60.
[16] Wernsdorfer W. and Sessoli R. Quantum Phase Interference and Parity Effects in Magnetic Molecular Clusters. *Science*, 1999, **284**, P. 133–135.
[17] Kang D.H. and Kim G.-H. Theoretical study of abrupt or gradual crossover of the escape rate in single-molecule magnets. *Phys. Rev. B*, 2006, **74**, 184418 (5 pp.)

[18] Kim G.-H., Kang D.H. and Shin M.C. Quantum-classical crossover of the escape rate in the biaxial nanomagnets with a higher order symmetry. *Eur. Phys. J. B*, 2011, **83**, P. 63–67.

[19] Vlasov S., Bessarab P.F., Uzdin V.M. and Jónsson H. Classical to quantum mechanical tunneling mechanism crossover in thermal transitions between magnetic states. *Faraday Discuss.*, 2016, **195**, P. 93–109.

[20] Bessarab P.F., Uzdin V.M. and Jónsson H. Method for finding mechanism and activation energy of magnetic transitions, applied to skyrmion and antivortex annihilation. *Comp. Phys. Commun.*, 2015, **196**, P. 335–347.

[21] Bessarab P.F., Uzdin V.M. and Jónsson H. Harmonic Transition State Theory of Thermal Spin Transitions. *Phys. Rev. B*, 2012, **85**, 184409 (4 pp.)

[22] Bessarab P.F., Uzdin V.M. and Jónsson H. Potential Energy Surfaces and Rates of Spin Transitions. *Z. Phys. Chem.*, 2013, **227**, P. 1543–1557

[23] Bessarab P.F., Uzdin V.M. and Jónsson H. Size and Shape Dependence of Thermal Spin Transitions in Nanoislands. *Phys. Rev. Lett.*, 2013, **110**, 020604 (5 pp.)

[24] Moskalenko M. , Bessarab P.F., Uzdin V.M. and Jónsson H. Qualitative Insight and Quantitative Analysis of the Effect of Temperature on the Coercivity of a Magnetic System. *AIP Advances*, 2016, **6**, 025213 (8 pp.)

[25] Lobanov I., Jónsson H. and Uzdin V. M. Mechanism and activation energy of magnetic skyrmion annihilation obtained from minimum energy path calculations. *Phys. Rev. B*, 2016, **94**, 174418 (7 pp.)

[26] Bessarab P.F. Comment on “Path to collapse for an isolated Néel skyrmion”. *Phys. Rev. B*, **95**, 2017, 136401 (2 pp.)

[27] Ivanov A. , Bessarab P.F., Uzdin V.M. and Jónsson H. Magnetic exchange force microscopy: Theoretical analysis of induced magnetization reversals. *Nanoscale*, 2017, Accepted Manuscript, DOI: 10.1039/C7NR04036A

[28] Smit J., Beljers H. Ferromagnetic resonance absorption in $BaFe_{12}O_{19}$, a highly anisotropic crystal. *Philips Res. Rep.*, 1955, **10**, P. 113–130.

[29] Suhl H. Ferromagnetic resonance in nickel ferrite between one and two kilomegacycles. *Phys. Rev.*, 1955, **97**, P. 555–557.

[30] Miller W.H. Semiclassical limit of quantum mechanical transition state theory for nonseparable systems. *J. Chem. Phys.*, 1975, **62**, P. 1899–1906.

[31] Callen C., Coleman S. Fate of the false vacuum. II. First quantum corrections. *Phys. Rev. D*, 1977, **16**, P. 1762–1768

[32] Benderskii V. A., Goldanskii V. I. and Makarov D. E. Quantum dynamics in low-temperature chemistry. *Phys. Rep.*, 1993, **233**, P. 195–339.

[33] Mills G., Schenter G. K., Makarov D. E. and Jónsson H. Generalized path integral based quantum transition state theory. *Chem. Phys. Letters*, 1997, **278**, P. 91–96.

[34] Mills G., Schenter G. K., Makarov D. E. and Jónsson H. RAW Quantum transition state theory. proceeding of “Classical and Quantum Dynamics in Condensed Phase Simulations”, Villa Marigola, Lerici, Italy, 1997, 405 pp.

[35] KIauder J. Path integrals and stationary-phase approximations. *Phys. Rev. D*, 1979, **19**, P. 2349–2356.

[36] Kochetov E. SU(2) coherentstate path integral. *J. Math. Phys.*, 1995, **36**, P. 4667–4679.

[37] Fradkin E. *Field Theories of Condensed Matter Physics.* Cambridge University Press, New York.: 2013, 190 pp.

[38] Aubin S. M. J. *et. al.* Resonant Magnetization Tunneling in the Trigonal Pyramidal $Mn^{IV}Mn_3^{III}$ Complex $[Mn_4O_3Cl(O_2CCH_3)_3(dbm)_3]$. *J. Am. Chem. Soc.*, 1998, **120**, P. 4991–5004.

[39] Edwards R. S., Hill S., *et. al.* A comparative high frequency EPR study of monomeric and dimeric Mn_4 single-molecule magnets, *Polyhedron*, 2003, **22**, P. 1911–1916.

[40] Wernsdorfer W., Aliaga-Alcalde N., Hendrickson D. N., Christou G. Exchange-biased quantum tunnelling in a supramolecular dimer of single-molecule magnets. *Nature*, 2002, **416**, P. 406–409.

NANOSYSTEMS: PHYSICS, CHEMISTRY, MATHEMATICS, 2017, 8 (4), P. 462–470

Synthesis of CaF_2–YF_3 nanopowders by co-precipitation from aqueos solutions

P. P. Fedorov[1], M. N. Mayakova[1], S. V. Kuznetsov[1], V. V. Voronov[1], Yu. A. Ermakova[1], A. E. Baranchikov[2]

[1]A. M. Prokhorov General Physics Institute, Russian Academy of Sciences
38 Vavilov Street, Moscow, 119991, Russia

[2]N. S. Kurnakov Institute of General and Inorganic Chemistry,
Russian Academy of Sciences, Leninskii pr. 31, Moscow, 119991, Russia

ppfedorov@yandex.ru

DOI 10.17586/2220-8054-2017-8-4-462-470

Study of the CaF_2–YF_3 system by co-precipitation from aqueous nitrate solutions revealed the formation of $Ca_{1-x}Y_xF_{2+x}$ solid solution precipitate containing up to 20 mol. % yttrium fluoride ($x \leq 0.2$). A higher yttrium to calcium ratio in the starting solutions caused additional precipitation of orthorhombic β-YF_3 nanophase elongated along the $\langle b \rangle$ axis. Cubic $(H_3O)Y_3F_{10}$ phase was also formed (SSG *Fm3m*, a = 11.60 Å, KY_3F_{10} structural type).

Keywords: calcium fluoride, yttrium fluoride, nanopowders.

Received: 19 July 2017

Revised: 2 August 2017

1. Introduction

The CaF_2–YF_3 system, along with the NaF–YF_3 system [1–4], plays a particularly important role among binary fluoride systems. Solid solution of yttrium fluoride in calcium fluoride is a classic example of heterovalent isomorphism [5]. Its study was initially discussed by Vogt in treatises on yttrofluorite [6], and has continued for more than a hundred years [7–24] (for a more detailed history of this study, please see [18]): the said CaF_2–YF_3 system has become a model for describing the interaction of calcium fluoride with the rare earth fluorides from yttrium group of elements (see Fig. 1). The CaF_2–YF_3 system is also the basis for several natural fluoride minerals [6, 15, 25–27].

Yttrium cation substitutes calcium ions in the fluorite structure, and supplementary fluoride anions, penetrating the formed crystal lattice, compensate for the corresponding changes in electrostatic charges for the sake of electrical neutrality of the system. The formed cationic and anionic defects associate among themselves, thus forming defect clusters [28, 29]. $Ca_{1-x}Y_xF_{2+x}$ solid solution maintains its original fluorite-type structure within the $0 \leq x \leq 0.38$ interval limits. A smooth maximum in the melting curves of $Ca_{1-x}Y_xF_{2+x}$ at $x = 0.11$ (Fig. 1) allows the growth of high-quality $Ca_{1-x}Y_xF_{2+x}$ single crystals from its melts with $x \leq 0.15$.

Such synthetic $Ca_{1-x}Y_xF_{2+x}$ yttrofluorite crystals have become widely used photonics materials, including solid state laser matrices [13]. Also, introducing yttrium fluoride into the calcium fluoride crystal lattice causes dramatic changes in its physical properties, including fluoride-ion ionic conductivity, hardness, cleavage and heat conductivity (the latter two parameters decrease significantly) [23, 30]. Relatively high yttrium concentrations complicate $Ca_{1-x}Y_xF_{2+x}$ single crystal growth from the melts due its incongruent melting, and the formation of a cellular substructure [31, 32], and local ordering of the formed solid solution [7, 12]. Additional increase in the YF_3 content in the CaF_2–YF_3 system leads to the formation of another berthollide-type variable-composition solid solution at 65–75 mol. % YF_3 with hexagonal LaF_3 tysonite-type structure [10, 11]. This phase undergoes metastable ordering under cooling. Another solid solution, based on high-temperature α-YF_3 polymorph, is also formed in the CaF_2-YF_3 system [33].

Fedorov [21] reported the lower temperature part of the phase diagram of the CaF_2–YF_3 system, taking into account the results for Kuntz's [15] hydrothermal studies and Bergstol et al. [25] investigation of tveitite mineral formation under natural conditions (tveitite is an ordered fluorite-type phase), and considering that fluorite-type solid solutions undergo ordering with the formation of a series of fluorite-type phases when cooled [4, 12]. The latter fluorite-type phases contain Y_6F_{37} clusters in their crystal lattices with Thompson antiprism coordination yttrium polyhedra. Such clusters fit in naturally in the fluorite crystal lattice (Fig. 2) and appear to be the dominant type of structural defects in $Ca_{1-x}Y_xF_{2+x}$ solid solutions at higher yttrium concentrations [14, 16, 28, 29]. The heterovalent substitution mechanism for the formation of the aforementioned solid solutions (Fig. 2) can be described by the following equation:

$$(M_6F_{32})^{20-} \rightarrow (Y_6F_{37})^{19-} + F^-_{int}. \qquad (1)$$

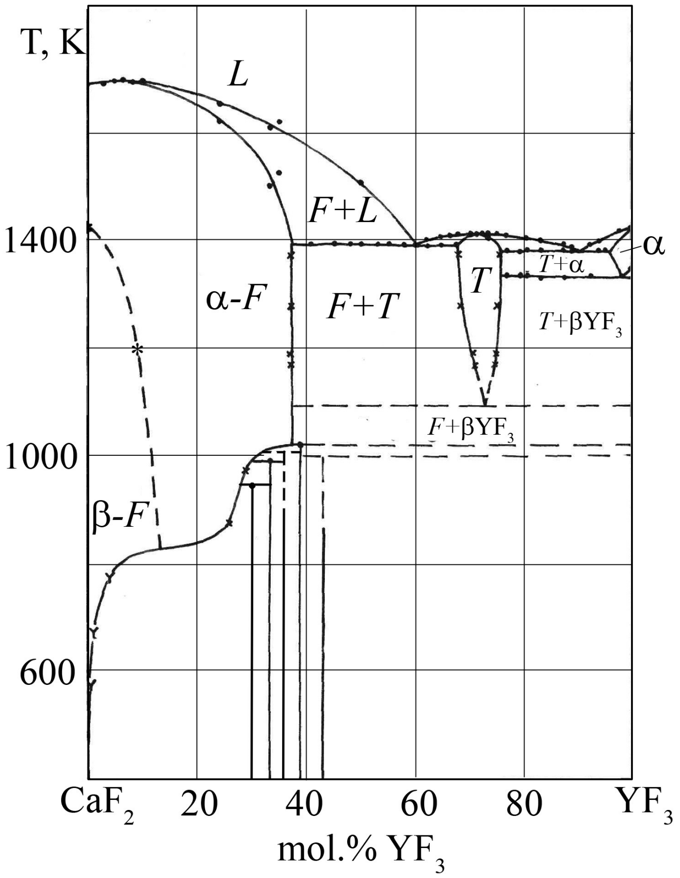

FIG. 1. Phase diagram of the CaF_2–YF_3 system [17]. L – melt, F –$Ca_{1-x}Y_xF_{2+x}$ fluorite-type solid solution, T – tysonite (LaF_3) type berthollide phase

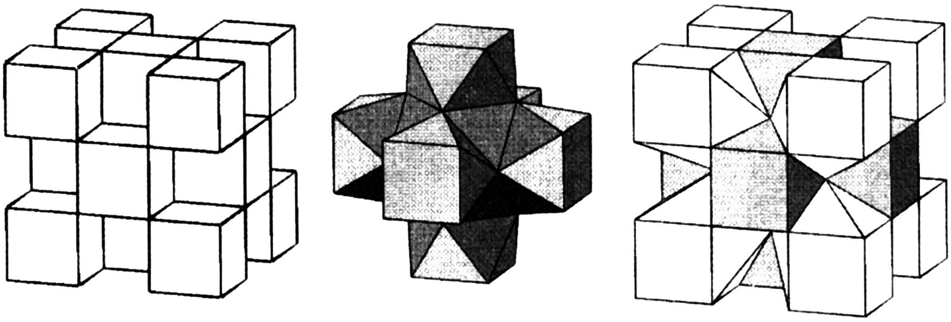

FIG. 2. Insertion of R_6F_{37} clusters into the fluorite matrix

Nanofluorides are another rapidly developing area of the modern science [34–39], for nanofluorides are widely implemented as luminophores, catalysts, biomedical and electrochemical materials; the CaF_2–YF_3 system has also become crucially important in this area, as well. Low-temperature and soft chemistry syntheses of nanofluorides (e.g, mechanochemical [40, 41], sol-gel [24], solvothermal [42] methods and some other techniques [35]) are especially prominent because of their technological advantages. Recently, we have successfully used our co-precipitation from aqueous solutions methods for nanofluoride preparations [34,35,43–48], including our systematic studies of phase formations in the BaF_2–YF_3 [49], BaF_2–BiF_3 [50], BaF_2–ScF_3 [51], BaF_2–CeF_3 [52], SrF_2–YF_3 [53] and CaF_2–HoF_3 [54] systems. We have observed varieties of phase fields in the studied MF_2–YF_3 and NaF–RF_3 systems, including non-equilibrium phases with wide areas of homogeneity; we have also observed the absence of the ordered phases that exist under higher temperature equilibrium conditions [4].

Thus, according to the background given above, the purpose of the present study was the investigation of nanophase formation in the CaF_2–YF_3 system under co-precipitation from aqueous solutions at lower temperatures.

2. Experimental

We used 99.99 wt.% pure $Y(NO_3)_3 \cdot 6H_2O$ and $Ca(NO_3)_2 \cdot 4H_2O$ (manufactured by OOO Lanchit), as well as 99.9 % pure 40 wt.% aqueous HF (manufactured by TECH System) and double distilled water as starting materials without any further purification.

Specimens in the CaF_2–YF_3 system were prepared by co-precipitation from aqueous solutions in polypropylene reactors according to previously-described procedures [4,49,53,54]. 0.2 Mol/L aqueous nitrate solutions in double distilled water were vigorously mixed with magnetic stirring bar and then added dropwise under continued stirring to a 2-fold excess of 5 vol.% aqueous HF. The formed precipitates were decanted, rinsed with double distilled water until a pH of 5–6 was obtained. In some experiments, precipitates were additionally neutralized with aqueous ammonia (99.9 % pure) and then rinsed again with double distilled water until a pH of 5–6 was maintained. All precipitates were air-dried at 40 °C.

Phase composition of the synthesized samples was characterized by X-ray powder diffraction (Bruker D8 diffractometer; CuK_α radiation; TOPAS software package for experimental data treatment and coherent scattering domain and microdeformation size calculations). Particle dispersity and morphology were controlled by scanning electron microscopy (SEM) (NVision 40 microscope). The same NVision 40 microscope was also used for the sample chemical analyses (X-ray spectroscopy). Specimen chemical composition was also studied by atomic emission spectroscopy (AES) with the use of LEA-S500 analyzer (OOO SOL Instruments, Minsk, Belarus) (see Supporting Information for the further details). MOM Q-1500D PaulikPaulikErdey derivatograph has been utilized for the thermal analysis investigations (Pt crucibles, air).

3. Results and Discussion

Colloid solutions in the CaF_2–YF_3 system were obtained during the synthesis in which the precipitate formed very slowly (couple of weeks) (Figs. 3–7; Tables 1, 2). SEM data (Fig. 3) confirmed that the precipitated nanoparticles were actually of the small sizes. Chemical analyses of both types, X-ray spectroscopy and AES (Table 1, also see Supplemental Information), have shown that the metal ratios in the formed solid precipitates were close to the corresponding ratios in the starting aqueous solutions/mixtures even if the observed ratio differences were a little bit larger than in the case of the previously studied SrF_2–YF_3 [53] and BaF_2–YF_3 [49] systems.

X-Ray diffraction data indicated that precipitates formed from solutions with 20 mol. % YF_3 or less were CaF_2-based fluorite-type solid solutions (cubic system, $Fm3m$ SSG). SEM image of the 10 mol. % YF_3 specimen (i.e., precipitated from the 10 % Y^{3+} and 90 % Ca^{2+} solution) contained readily-visible/resolved agglomerates of the same phase particles 30–50 nm in diameter. Experimental data for the unit lattice parameters of precipitated $Ca_{1-x}Y_xF_{2+x}$ solid solutions coincided within the 0.004 Å range with the a(x) concentration dependency function for $Ca_{1-x}Y_xF_{2+x}$ solid solutions, synthesized at higher temperatures [55] (Fig. 7). However, in addition to the increasing crystal lattice parameter, X-ray diffraction patterns of precipitates $Ca_{1-x}Y_xF_{2+x}$ contained weak (200) lines at about 32.5 ° 2θ (this line is absent in the X-ray diffraction pattern of the pure face-centered CaF_2). The latter observation was an additional evidence of the solid solution formation.

X-Ray diffraction patterns of $Ca_{1-x}Y_xF_{2+x}$ samples with 30 mol. % or more YF_3 contained broadened lines of β-YF_3 nanoparticles (orthorhombic system, *Pnma* SSG [18]) (Figs. 4–5). However, relative clarity of (020) β-YF_3 line at about 26 ° 2θ indicated that crystal lattices of the said β-YF_3 nanoparticles were stretched along $\langle b \rangle$ axis.

All precipitated fluorides were hydrated and contained about 5.5 ± 0.3 wt. % water (DTA data, see Supplemental Information). Heating of these specimens was accompanied with mass losses that continued to 450–500 °C. X-Ray diffraction patterns of such samples annealed at 450–500 °C contained only narrowed lines, and the latter phenomenon was an unequivocal evidence of the nanoparticle enlargement.

Synthesis of the 90 % YF_3 – 10 % CaF_2 solid solution resulted in the formation of the novel phase (Fig. 4) with the X-ray diffraction pattern indexed in the P-cubic system with a = 5.800(2) Å parameter (Table 2) or in the F-cubic system with a = 11.60 Å (calculated size of the coherent scattering domain D = 25 nm). The SEM image of this specimen contained joined together plate-type nanocrystals (Figs. 3c and 3d).

The X-Ray diffraction pattern of this phase was similar to the one of KY_3F_{10} (*Fm3m* SSG, Z = 8), so one could assume that it was $(H_3O)Y_3F_{10}$ compound with hydroxonium ions occupying potassium sites in the crystal lattice. Heating the specimen resulted in about 11.3 wt. % mass loss (Supplemental Information), which might

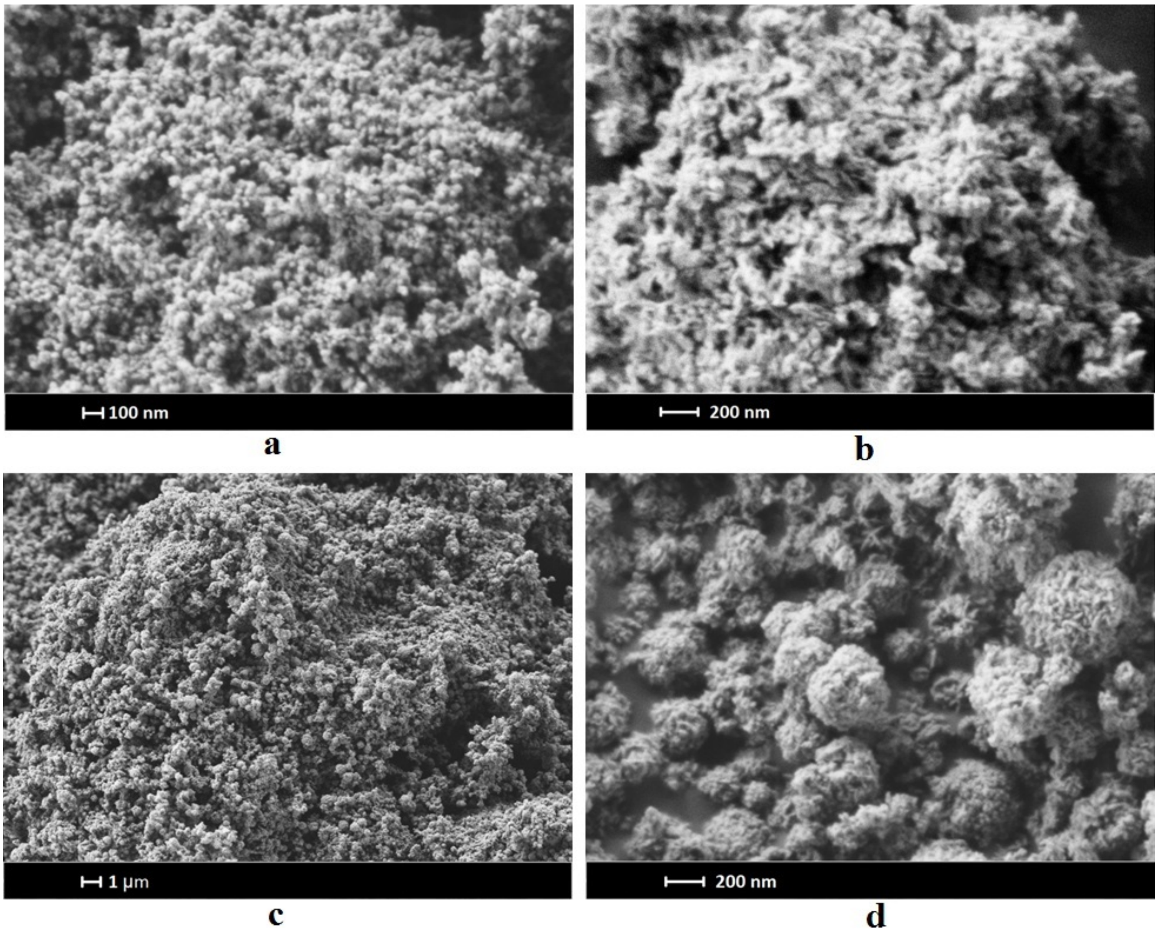

FIG. 3. SEM images of the CaF_2-YF_3 specimens: 10 mol. % YF_3 (a), 50 % mol. YF_3 (b), 90 % mol.% YF_3 (c, d)

TABLE 1. Chemical analysis of CaF_2–YF_3 specimens

Sample composition	Refined YF_3 content, mol. %		
	X-Ray spectroscopy (electron microscopy)	Atomic emission spectroscopy (AES)	
		290 nm excitation wavelength	320 nm excitation wavelength
$Ca_{0.70}Y_{0.30}F_{2.30}$ (30.0 mol. % YF_3)	–	26.06±0.75	25.85±0.92
$Ca_{0.50}Y_{0.50}F_{2.50}$ (50.0 mol. % YF_3)	52.4	52.01±1.69	54.14±1.85
$Ca_{0.30}Y_{0.70}F_{2.70}$ (70.0 mol. % YF_3)	–	68.83±2.16	73.31±1.41
$Ca_{0.10}Y_{0.90}F_{2.90}$ (90.0 mol. % YF_3)	90.8	–	–

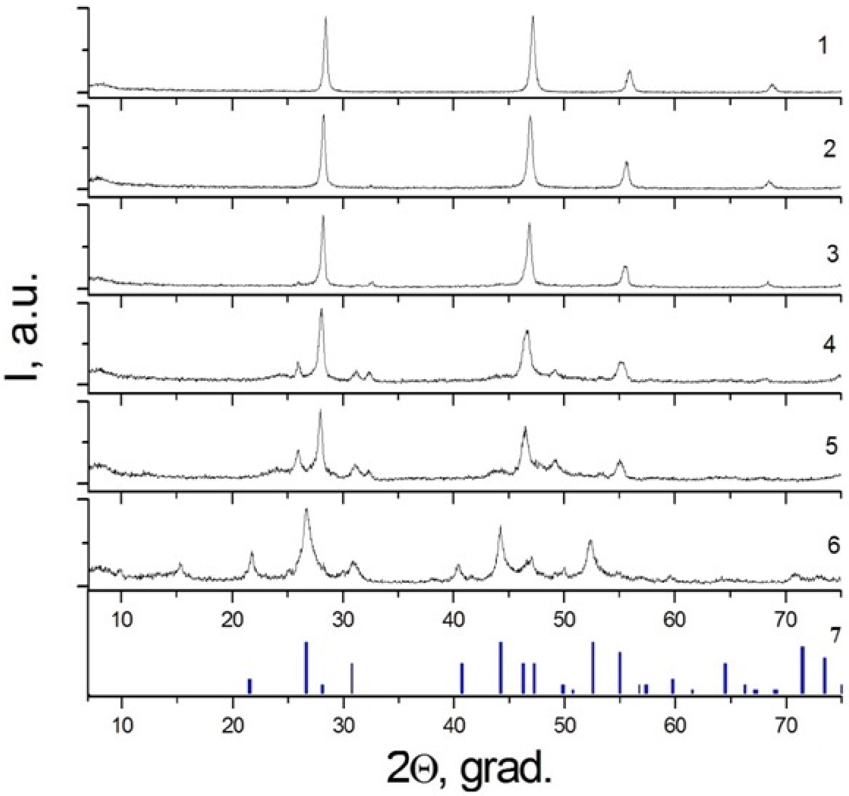

FIG. 4. X-Ray powder diffraction patterns for the specimens obtained by co-precipitation of calcium and yttrium fluorides from aqueous nitrate solutions: 10 mol.% (1); 20 mol.% (2); 30 mol.% (3); 50 mol.% (4); 70 mol.% (5); 90 mol.% (6) YF_3 (nominal compositions), and JCPDS Card No. 27-0465 for KY_3F_{10} phase (7)

TABLE 2. X-Ray diffraction pattern of the $Ca_{0.10}Y_{0.90}F_{2.90}$ specimen ($Q = 10^4/d^2$. P-cubic lattice, $a = 5.800(2)$ Å, $F(14) = 11.9$, $M(14) = 25.8$)

N	$2O$(obs)	d(obs), Å	Q(obs)	I/I_0,%	h k l	Q(calc)	ΔQ
1	15.320	5.7789	299.44	15	1 0 0	297.25	2.19
2	21.730	4.0866	598.79	39	1 1 0	594.50	4.29
3	26.740	3.3312	901.15	100	1 1 1	891.75	9.40
4	30.900	2.8915	1196.06	15	2 0 0	1189.00	7.06
5	38.020	2.3648	1788.18	5	2 1 1	1783.50	4.68
6	44.240	2.0457	2389.55	75	2 2 0	2378.00	11.55
7	47.000	1.9318	2679.64	30	2 2 1	2675.25	4.38
8	52.350	1.7463	3279.16	50	3 1 1	3269.75	9.40
9	54.740	1.6755	3562.14	10	2 2 2	3567.00	−4.86
10	59.530	1.5516	4153.75	7	3 2 1	4161.50	−7.75
11	64.170	1.4502	4754.93	3	4 0 0	4756.01	−1.07
12	70.820	1.3294	5658.34	8	3 3 1	5647.76	10.58
13	72.810	1.2979	5936.32	5	4 2 0	5945.01	−8.68

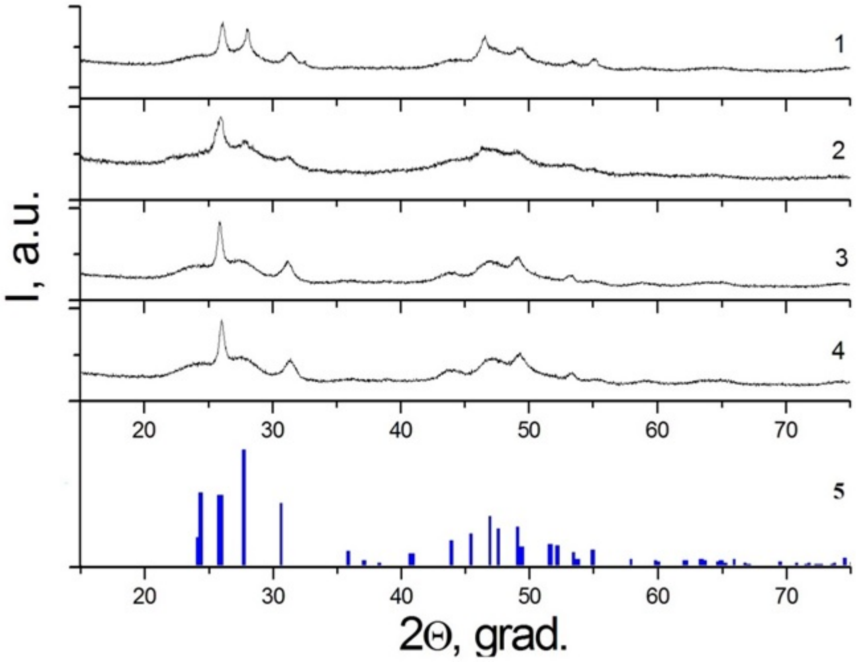

FIG. 5. X-Ray powder diffraction patterns for the specimens obtained by co-precipitation of calcium and yttrium fluorides from aqueous nitrate solutions (second set of experiments): 80 mol.% (1), 85 mol. % (2), 90 mol. % (3), 95 mol.% (4), and JCPDS Card No. 74-0911 for β-YF_3 phase (5)

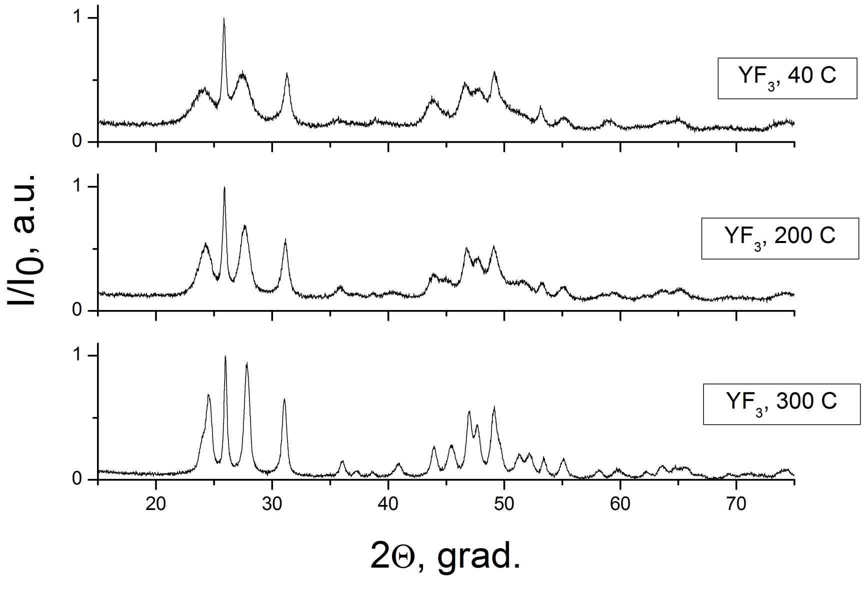

FIG. 6. X-Ray powder diffraction patterns for the YF_3 specimens: freshly prepared, $a = 6.294(3)$, $b = 6.867(4)$, $c = 4.528(3)$ Å (1), annealed at 200 °C, $a = 6.317(2)$, $b = 6.875(2)$, $c = 4.469(2)$ Å (2), YF_3 annealed at 300 °C, $a = 6.346(1)$, $b = 6.861(1)$, $c = 4.419(1)$ Å (3)

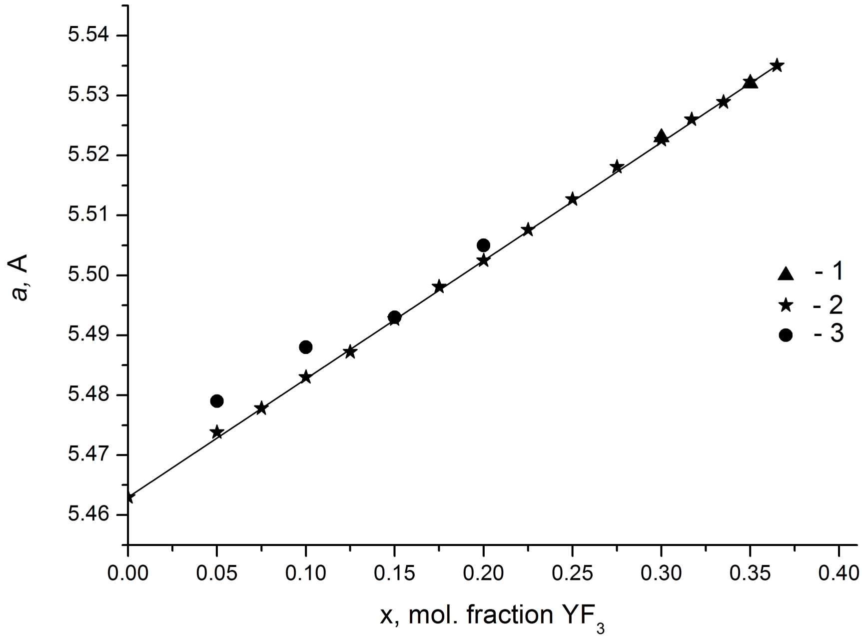

FIG. 7. Unit cell parameters for $Ca_{1-x}Y_xF_{2+x}$ fluorite-type solid solutions as per Fedorov et al. [7] (1) and Gettmann and Greis [12] (2), (all specimens were synthesized by solid phase synthesis) along with the present work data for $Ca_{1-x}Y_xF_{2+x}$ nanopowders (3). Straight-line dependence according to Fedorov and Sobolev [55]

have come from 8 wt. % loss from decomposition:

$$(H_3O)Y_3F_{10} \rightarrow 3YF_3 + H_2O + HF \tag{2}$$

along with additional evaporation of hydration water from the solid sample.

Structure of KY_3F_{10} type is derived from fluorite. It consists of a 3D framework formed by $(Y_6F_{35})^{18-}$ clusters (Fig. 2) interconnected by their vertices. Monovalent cations occupy cavities of the aforementioned framework [14, 55, 56]. KR_3F_{10} (R = Dy–Lu, Y) and RbR_3F_{10} (R = Sm–Tb) [3] crystallize in this structure type. However, the structure for KY_3F_{10} can also can be described as a 3D framework of $(Y_6F_{32})^{14-}$ clusters (constructed from Thompson antiprism coordination yttrium polyhedra in another way) [57] that are also present in the structure of $(H_3O)Y_3F_{10}nH_2O$ phase (*Fd3m* SSG, $Z = 16$) [36]. However, the latter clusters are packed in a different manner, and the previously described $(H_3O)Y_3F_{10}nH_2O$ phase (*Fd3m* SSG, $Z = 16$) is not a fluorite-type phase, in contrast with the phase obtained in our experiments for 90 % YF_3-10% CaF_2 solid solution specimen (Table 2).

The above results for the CaF_2–YF_3 system, obtained by co-precipitation method, are similar to our data for the CaF_2–HoF_3 system [54]. They are also in a good agreement with data [43] regarding $Ca_{1-x}R_xF_{2+x}$ solid solutions. Weak additional lines in the X-ray diffraction patterns, corresponding to β-YF_3 nanoparticles, were also observed for $Ca_{0.6}Y_{0.4}F_{2.4}$, also synthesized by the aforementioned co-precipitation in [45].

It is also worth mentioning that we did not observe the formation of tysonite-type phase(s) in the co-precipitated specimens at the lower temperatures. This should not be surprising if one takes into account that such a tysonite-type phase is stable at higher temperatures only (Fig. 1). Nevertheless, it is quite strange that there was no fluorite-type solid solutions formed in the CaF_2-RF_3 systems (R = rare earth element) that contain a relatively high concentration of the rare earth metals (35–40 mol. % RF_3) and possess ordered fluorite-type structures (such ordered phases are usually thermodynamically stable at the lower temperatures). The other previously studied MF_2–RF_3 systems (e.g., SrF_2–YF_3 [53], BaF_2–YF_3 [49], BaF_2–CeF_3 [52]) with M = Sr and Ba have exhibited different features: each of these systems had the concentration ranges, where ordered fluorite-type phases were observed under equilibrium conditions at the higher temperatures, the unordered solid solutions were formed. Currently, it is hard to find a reasonable explanation for the different results for calcium fluoride systems.

In conclusion, results of our study demonstrate that in the course of the synthesis of $Ca_{1-x}Y_xF_{2+x}$ solid solutions by co-precipitation from aqueous media, the single phase specimens have been formed for the relatively low yttrium content only (up to 20 mol. % YF_3). These samples, apparently, are not under equilibrium, but they are fairly stable and do not undergo any detectable changes over the course of a few years. The latter is crucially important for the preparation of materials of practical value [58].

Acknowledgments

The authors express their appreciation to R. Ermakov for his kind assistance in the X-ray diffraction experiments as well as to V. K. Ivanov for his valuable discussion of the obtained results. The authors also wish to thank E. V. Chernova and A. I. Popov for their help in the preparation of the present manuscript.

This work was partially supported by RFBR 15-08-02481-a grant.

References

[1] Thoma R.E., Hebert G.M., Insley H., Weavwe C.F. Phase equilibria in the system sodium fluoride-yttrium fluoride. *Inorg. Chem.*, 1963, **2**(5), P. 1005–1012.

[2] Fedorov P.P., Sobolev B.P., Belov S.F. Fusibility diagram of the system NaF-YF_3, and the cross-section $Na_{0.4}Y_{0.6}F_{2.2}$-YOF *Inorg. Mater.*, 1979, **15**(5), P. 640–643.

[3] Fedorov P.P. Systems of alcali and rare-earth metal fluorides. *Russian J. Inorg. Chem.*, 1999, **44**(11), P. 1703–1727.

[4] Fedorov P.P., Kuznetsov S.V., Osiko V.V. Elaboration of nanofluorides and ceramics for optical and laser applications. Chapter in the book *Photonic & Electronic Properties of Fluoride Materials*, Ed. Tressaud A., Poeppelmeier K., Amsterdam et al.: Elsevier, 2016, P. 7–31.

[5] Fedorov P.P. Heterovalent isomorphism and solid solutions with a variable number of ions in the unit cell. *Russ. J. Inorg. Chem.*, 2000, **45**, Suppl. 3, P. S268–S291.

[6] Vogt T. Uber die Flusspat-Yttrofluoritgruppe. *Neues Jahrb. Mineral*, 1914, **2**(1), P. 9–13.

[7] Fedorov P.P., Izotova O.E., Alexandrov V.B., Sobolev B.P. New phases with fluorite-derived structure in CaF_2 - (Y, Ln)F_3 systems. *J. Solid State Chem.*, 1974, **9**(4), P. 368–374.

[8] Seiranian K.B., Fedorov P.P., Garashina L.S., Molev G.V., Karelin V.V., Sobolev B.P. Phase diagram of the system CaF_2 -YF_3. *J. Crystal Growth*, 1974, **26**(1), P. 61–64.

[9] *Crystals with the fluorite structure*. Ed. Hayes W. Oxford: Clarendon Press, 1974, 448 pp.

[10] Fedorov P.P., Sobolev B.P. Variable-composition phases with the LaF_3 structure in the systems MF_2-(Y,Ln)F_3. II. The systems CaF_2-(Y,Ln)F_3 (thermal characteristics and formation of berthollides). *Kristallografiya*, 1975, **20**(5), P. 584–586.

[11] Sobolev B.P., Aleksandrov V.B., Fedorov P.P., et al. Variable-composition phases with the LaF_3 structure in the systems MF_2-(Y,Ln)F_3. IV. X-ray characteristics, heterovalent isomorphic substitutions. *Kristallografiya*, 1976, **21**(1), P. 49–54.

[12] Gettmann W., Greis O. Uber fluorit- und tysonitverwandte Ordnungsphasen im System CaF_2-YF_3. *J. Solid State Chem.*, 1978, **26**(2), P. 255–263.

[13] Kaminskii A.A. *Laser crystals: their physics and properties*. Berlin, Heidelberg: Springer Verlag, 1990, 459 pp.

[14] Greis O., Hashke J.M. Rare earth fluorides. In *Handbook on the Physics and Chemistry of Rare Earth*. Amsterdam: Elsevier, 1982, v.**5**, P. 387–460.

[15] Kuntz A.F. Fluorite crystallization under hydrothermal conditions. *Proc. of Geology Institute, Komi department of USSR Academy of Sciences*, 1982, **39**, P. 31–41. (in Russian)

[16] Otroshchenko L.P., Aleksandrov V.B., Bydanov N.N., Simonov V.I., Sobolev B.P. Neutron-diffraction structure refinement of the $Ca_{0.90}Y_{0.10}F_{2.10}$ solid solution. *Kristallografiya*, 1988, **33**(3), P. 764–765. (in Russian)

[17] Ivanov-Shits A.K., Sorokin N.I., Fedorov P.P., Sobolev B.P. Specific features of ionic transport in nonstoichiometric fluorite-type $Ca_{1-x}R_xF_{2+x}$ (R = La-Lu, Y, Sc) phases. *Solid State Ionics*, 1990, **37**, P. 125–137.

[18] Sobolev B.P. *The rare earth trifluorides. Part 1. The high temperature chemistry of the rare earth trifluorides*. Barcelona: Institut d‘Estudis Catalans, 2000, 520 pp.

[19] Sobolev B.P. *The rare earth trifluorides. Part 2. Introduction to materials sience of multicomponent metal fluoride crystals.* Barcelona: Institut d‘Estudis Catalans, 2001, 459 pp.

[20] Karimov D.N., Krivandina E.A., Zhmurova Z.I., Sobolev B.P., Bezhanov V.A., Chernov S.P., Shapochkin G.M. Investigation of multicomponent fluoride optical materials in the UV spectral region: I. Single crystals of $Ca_{1-x}R_xF_{2+x}$ (R = Sc, Y, La, Yb, Lu) solid solutions. *Crystallogr. Rep.*, 2006, **51**(6), P. 1009–1015.

[21] Fedorov P.P. Third law of thermodynamics as applied to phase diagrams. *Russ. J. Inorg. Chem.*, 2010, **55**(11), P. 1722–1739.

[22] Bolotina N.B., Kalyukanov A.I., Chernaya T.S., Verin I.A., Buchinskaya I.I., Sorokin N.I., Sobolev B.P. X-ray and neutron diffraction study of the defect crystal structure of the as-grown nonstoichiometric phase $Y_{0.715}Ca_{0.285}F_{2.715}$. *Crystallogr. Rep.*, 2013, **58**(4), P. 575–585.

[23] Popov P.A., Fedorov P.P., Osiko V.V. Thermal conductivity of single crystals of the $Ca_{1-x}Y_xF_{2+x}$ solid solution. *Doklady Physics*, 2014, **59**(5), P. 199–202.

[24] Krahl T., Scholz G., Kemnitz E. Solid Solutions CaF_2-YF_3 with fluorite structure prepared on the solgel route: investigation by multinuclear MAS NMR spectroscopy. *J. Phys. Chem. C*, 2014, **118**, P. 21066–21074.

[25] Bergstol S., Jensen B.B., Neuman H. Tveitite, a new calcium yttrium fluoride. *Lithos*, 1977, **10**, P. 81–87.

[26] Bevan D.J.M., Strahle J., Greis O. The crystal structure of tveitite, an ordered yttrofluorite mineral. *J. Solid State Chem.*, 1982, **44**, P. 75–81.

[27] Atencio D., Bastos Neto A.C., Pereira V.P., et al. Waimirite-(Y), orthorhombic YF_3, a new mineral from the Pitinga mine, Presidente Figueiredo, Amazonas, Brazil and from Jabal Tawlah, Saudi Arabia: description and crystal structure. *Mineral. Magazine*, 2015, **79**(3), P. 767–780.

[28] Fedorov P.P. Association of point defects in non stoichiometric $M_{1-x}R_xF_{2+x}$ fluorite-type solid solutions. *Butll. Soc. Cat. Cien.*, 1991, **12**(2), P. 349–381.

[29] Kazanskii S.A., Ryskin A.I., Nikiforov A.E., Zaharov A.Yu., Ougrumov M.Yu., Shakurov G.S. EPR spectra and crystal fleld of hexamer rare-earth clasters in fluorites. *Phys. Rev. B*, 2005, **72**, 014127 P. 1–11.

[30] Popov P.A., Dykel'skii K.V., Mironov I.A., Demidenko V.A., Smirnov A.N., Smolyanskii P.L., Fedorov P.P., Osiko V.V., Basiev T.T.. Thermal conductivity of CaF_2 optical ceramics. *Doklady Physics*, 2007, **52**(1), P. 7–9.

[31] Turkina T.M., Fedorov P.P., Sobolev B.P. Stability of plane crystallization front in growth of single crystals of solid solutions $M_{1-x}R_xF_{2+x}$ (where M = Ca,Sr,Ba, R = rare earth) from a melt *Kristallografiya*, 1986, **31**(1), P. 83–87.

[32] Kuznetsov S.V., Fedorov P.P. Morphological Stability of Solid-Liquid Interface during Melt Crystallization of Solid Solutions $M_{1-x}R_xF_{2+x}$. *Inorg. Mater.*, 2008, **44**(13), P. 1434–1458. (Supplement)

[33] Sobolev B.P., Fedorov P.P. Hexagonal YF_3' structure type and high-temperature modifications of rare-earth trifluorides isostructural with YF_3. *Kristallografiya*, 1973, **18**(3), P. 392.

[34] Kuznetzov S.V., Osiko V.V., Tkatchenko E.A., Fedorov P.P. Inorganic nanofluorides and related nanocomposites. *Russian Chem. Rev.*, 2006, **75**(12), P. 1065–1082.

[35] Fedorov P.P., Luginina A.A., Kuznetsov S.V., Osiko V.V. Nanofluorides. *J. Fluorine Chem.*, 2011, **132**(12), P. 1012–1039.

[36] Lucier B.E.G., Johnston K.E., Arnold D.C., et. al. Comprehensive Solid-State Cheracterization of Rare Earth Fluoride Nanoparticles. *J. Phys. Chem. C*, 2014, **118**(2), P. 1213–1228.

[37] Van Veggel F.C.J.M. Upconversion of Ln^{3+}-based Nanoparticles for Optical Bio-imaging. In: *Luminescence of Lanthanide Ions in Coordination Compounds and Nanomaterials*. John Wiley Sons, 2014, P. 269–302.

[38] Fedorov P.P., Luginina A.A., Popov A.I. Transparent Oxyfluoride Glass Ceramics. *J. Fluorine Chem.*, 2015, **172**, P. 22–50.

[39] Naccache R., Yu Q., Capobianco J.A. The fluoride host: nucleation, growth, and upconversion of lanthanide-doped nanoparticles. *Adv. Optical Mater.*, 2015, **3**(4), P. 482–509.

[40] Düvel A., Bednarcik J., Šepelák V., Heitjans P. Mechanosynthesis of the fast fluoride ion conductor $Ba_{1-x}La_xF_{2+x}$: from the fluorite to the tysonite structure. *J. Phys. Chem. C*, 2014, **118**, P. 7117–7129.

[41] G. Scholz, S. Breitfeld, T. Krahl, A. Düvel, P. Heitjans, E. Kemnitz. *Solid State Sciences*, 2015, **50**, P. 32–41.

[42] Lei Lei, Daqin Chen, Feng Huang , Yunlong Yu, Yuansheng Wang. *J. Alloys Comp.*, 2012, **540**, P. 27–31.

[43] Kouznetzov S.V., Yarotskya I.V., Fedorov P.P., Voronov V.V., Lavristchev S.V., Basiev T.T., Osiko V.V. Preparation of Nanopowdered $M_{1-x}R_xF_{2+x}$ (M = Ca, Sr, Ba; R = Ce, Nd, Er, Yb) Solid Solutions. *Russian J. Inorg. Chem.*, 2007, **52**, P. 315–320.

[44] Fedorov P.P., Kuznetsov S.V., Voronov V.V., Yarotskya I.V., Arbenina V.V. Soft chemical synthesis of $NaYF_4$ nanopowders. *Russian J. Inorg. Chem.*, 2008, **53**(11), P. 1681–1685.

[45] Fedorov P.P., Kuznetsov S.V., Mayakova M.N., et al. Coprecipitation from aqueous solutions to prepare binary fluorides. *Russian J. Inorg. Chem.*, 2011, **56**(10), P. 1525–1531.

[46] Luginina, A.A., Fedorov, P.P., Kuznetsov, S.V., et al., Synthesis of ultrafine fluorite $Sr_{1-x}Nd_xF_{2+x}$ powders. *Inorg. Mater.*, 2012, **48**(5), P. 531–538.

[47] Kuznetsov, S.V., Ovsyannikova, A.A., Tupitsyna, E.A., Yasyrkina, D.S., Voronov, V.V., Fedorov, P.P., Batyrev, N.I., Iskhakova, L.D., Osiko, V.V. Phase formation in LaF_3-$NaGdF_4$, $NaGdF_4$-$NaLuF_4$, $NaYF_4$-$NaLuF_4$ systems: synthesis of powders by co-precipitation from aqueous solutions. *J. Fluor. Chem.*, 2014, **161**, P. 95–101.

[48] S.V. Kuznetsov, D.S. Yasyrkina, A.V. Ryabova, D.V. Pominova, V.V. Voronov, A.E. Baranchikov, V.K. Ivanov, P.P. Fedorov. α-$NaYF_4$:Yb:Er@AlPc(C_2O_3)$_4$ -Based efficient up-conversion luminophores capable to generate singlet oxygen under IR excitation. *J. Fluor. Chem.*, 2016, **182**, P. 104–108.

[49] Fedorov P.P., Mayakova M.N., Kuznetsov S.V., Voronov V.V., Ermakov R.P., Samarina K.S., Popov A.I., Osiko V.V. Co-Precipitation of yttrium and barium fluorides from aqueous solutions. *Mat. Res. Bull.*, 2012, **47**, P. 1794–1799.

[50] Fedorov P.P., Mayakova M.N., Kuznetsov S.V., Voronov V.V., Osiko V.V., Ermakov R.P., Gontar' I.V., Timofeev A.A., Iskhakova L.D. Coprecipitation of barium–bismuth fluorides from aqueous solutions: nanochemical effects. *Nanotechnologies in Russia*, 2011, **6**, P. 203–210.

[51] Mayakova M.N., Kuznetsov S.V., Voronov V.V., Baranchikov A.E., Ivanov V.K., Fedorov P.P. Soft chemistry synthesis of powders in the BaF_2-ScF_3 system. *Russian J. Inorg. Chem.*, 2014, **59**(7), P. 773–777.

[52] Mayakova M.N., Voronov V.V., Iskhakova L.D., Kuznetsov S.V., Fedorov P.P. Low-temperature phase formation in the BaF_2-CeF_3 system. *J. Fluorine Chem.*, 2016, **187**, P. 33–39.

[53] Mayakova M.N., Luginina A.A., Kuznetsov S.V., Voronov V.V., Ermakov R.P., Baranchikov A.E., Ivanov V.K., Karban' O.V., Fedorov P.P. Synthesis of SrF_2-YF_3 nanopowders by co-precipitation from aqueous solutions. *Mendeleev Communications*, 2014, **24**(6), P. 360–362.

[54] Fedorov P.P., Mayakova M.N., Kuznetsov S.V., Voronov V.V. Low temperature phase formation in the CaF_2 - HoF_3 system. *Russian J. Inorg. Chem.*, 2017, **62**(9), P. 1173–1176.

[55] Fedorov P.P., Sobolev B.P. Concentration dependence of unit-cell parameters of phases $M_{1-x}R_xF_{2+x}$ with the fluorite structure. *Sov. Phys. Crystallogr*, 1992, **37**(5), P. 651–656.

[56] Ayala F.P., Oliveira M.A.S., Gesland J.-Y., Moreira R.L. Electrical and dielectrical investigation of the conduction processes in KY_3F_{10} crystals. *J. Phys. C.: Condensed Matter*, 1998, **10**, P. 5161–5170.

[57] Podberezskay N.V., Potapova O.G., Borisov S.V., Gatilov Yu. V. KTb_3F_{10}crystal structure – cubic pacing of $[Tb_6F_{32}]^{14-}$ polyanions. *J. Struct. Chem.*, 1976, **17**(5), P. 948–950. (in Russian)

[58] Vahrenev R.G., Mayakova M.N., Kuznetsov S.V., Ryabova A.V., Pominova D.V., Voronov V.V., Fedorov P.P. The research of synthesis and luminescent characteristics of calcium fluoride doped with ytterbium and erbium for biomedical application. *Condensed Media and Interface Borders*, 2016, **18**(4), P. 478–484.

NANOSYSTEMS: PHYSICS, CHEMISTRY, MATHEMATICS, 2017, 8 (4), P. 471–475

The effect of microtube formation with walls, containing Fe_3O_4 nanoparticles, via gas-solution interface technique by hydrolysis of the $FeCl_2$ and $FeCl_3$ mixed solution with gaseous ammonia

V. E. Gurenko, V. P. Tolstoy, L. B. Gulina

Institute of Chemistry, Saint Petersburg State University,
26 University Pr., St. Peterhof, Saint Petersburg, 198504, Russia

v.tolstoy@spbu.ru, l.gulina@spbu.ru, limeman14@gmail.com

PACS 75.70.Ak **DOI 10.17586/2220-8054-2017-8-4-471-475**

In this work, microtubes with walls, containing Fe_3O_4 nanoparticles, obtained by "rolling up" of the interfacial films, were synthesized by the gas-solution interface technique (GSIT), using a mixture of aqueous solutions of $FeCl_2$ and $FeCl_3$ and gaseous ammonia. The synthesized microtubes were characterized by Scanning Electronic Microscopy (SEM), Energy-Dispersive X-ray spectroscopy (EDX), X-Ray Diffraction analysis (XRD) and magnetization measurements. It was established that under optimal synthetic conditions the microtube diameter ranged from 5 to 10 μm, the length was up to 120 μm and the thickness of walls was about 0.6 μm, the walls themselves being formed by nanoparticles with a size of about 10 nm. The reversible hysteresis behavior, the low coercive force, the low remanence magnetization and the approaching of M_r/M_s to zero, confirmed the superparamagnetic nature of the synthesized microtubes. A hypothesis on the formation of microtubes by the gas-solution interface technique was proposed.

Keywords: Fe_3O_4, microtubes, magnetic behavior, superparamagnetic, Gas-Solution Interface, GSIT.

Received: 26 July 2017

Revised: 5 August 2017

1. Introduction

Iron oxides are known to be a significant class of inorganic compounds, which have great potential for practical application [1–8]. Among them, special attention is drawn to Fe_3O_4 oxide with cubic crystal structure of magnetite and its unique magnetic, electrical and chemical properties [9–11]. These properties determine their possible application in the capacity of electrodes in lithium-ion batteries and sensors, wastewater treatment, and drug delivery. Therefore, a number of synthetic methods are used now, including precipitation of $FeCl_2$ and $FeCl_3$ mixture in an ammonium hydroxide solution [12].

Recently, much attention has been paid to the creation of hollow microparticles or, in a different terminology, microcapsules with walls formed by Fe_3O_4 nanoparticles. These microcapsules have relatively high specific surface and can be applied in the creation of core–shell multifunctional nanostructures [13, 14]. Hollow Fe_3O_4 microcapsules, for example, were obtained by hydrothermal method [15], one-pot solvothermal method using $Fe(NO_3)_3{\cdot}6H_2O$ as the iron source, and glycerol, isopropyl alcohol (IPA) together with a small amount of water as a solvent [16], solvothermal method with template from surfactant micelles [17], and Ostwald ripening in magnetic field [18]. In such a case, the problem of synthesizing of the hollow microparticles with tubular morphology has a particular importance given that such microparticles will exhibit the unique combination of magnetic, optical and magneto-optical properties.

The aim of the present work was to investigate the possibility of obtaining microtubes with walls, containing Fe_3O_4 nanoparticles, via GSIT as a result of the interfacial reaction between gaseous ammonia and a mixed solution of $FeCl_2$ and $FeCl_3$.

The GSIT method was implemented for the synthesis of arsenic sulfide microtubes [19], manganese oxide [20, 21] and lanthanum fluoride [22–24]. A distinctive feature of this method is that, firstly, due to the solution surface reaction with gaseous reagent, the solid film with composition and density gradient and thickness from 100 nm to 1 μm is formed. Subsequently, after the removal of unreacted reagent excess and reaction products, the film rolls up during drying into microtubes or, in a different terminology, microscrolls with the diameter from 5 to 100 μm and length from 100 μm to 2 mm.

2. Experimental methods

$FeCl_2 \cdot 4H_2O$ (provided by Aldrich) and $FeCl_3 \cdot 6H_2O$ (chemically pure, from Vecton) were used as reagents. Aqueous solutions were prepared using Milli-Q high purity water with a resistivity of more than 18 MΩ/cm. A $FeCl_2/FeCl_3$ mixed solution with ratio of salts of 1/2 and total concentration of 0.05 was used as the aqueous precursor. An aqueous solution of ammonium hydroxide (25 %, extra pure, from Vekton) served as the source of gaseous NH_3 The synthesis procedure was as follows: 4 mL of the mixed salt solution was poured into a flat vessel and added to a glass-lined 50 cm^3 chemical reactor. Next, 2 mL of NH_4OH solution was poured into a second vessel and put in reactor near the solution vessel. The treatment lasted from 0.5 to 10 min. The thin brownish-black transparent film was formed on the solution surface during the treatment. After that, the film was twice transferred to the surface of distilled water in order to remove excess of reagent solution for 5 minutes. After washing, the film was transferred to the surface of a Teflon wafer and then dried at room temperature for 5 hours. During drying, the thin solid film was transformed into microtubes (microscrolls). Characterization of microtubes was carried out by X-ray diffraction (XRD), Scanning electron microscopy (SEM), electron probe microanalysis (EPMA). X-ray powder diffraction was performed on a Rigaku Miniflex II diffractometer. The measurement conditions were Cu Kα radiation, 30 kV, and 10 mA. The morphology of microtube sample was determined using scanning electron microscopy (Zeiss EVO-40EP or Merlin). The chemical composition of the samples was controlled by EDX analysis using a scanning electron microscope equipped with an INCA 350 Energy EDX analyzer (Oxford Instruments). The magnetic properties of the microtubes samples were investigated by a Lake Shore 7410 vibrating sample magnetometer at room temperature.

3. Results

When the surface of an aqueous $FeCl_2$ and $FeCl_3$ solution is exposed to gaseous ammonia, a brownish-black transparent thin solid film with thickness from 0.5 to 1.5 μm, depending on the time of treatment, is formed. As a result of air drying at room temperature, thin solid film, acquired by the treatment during 30 seconds, transforms into the microtubes with diameter from 5 to 10 μm and length of 80–120 μm (Fig. 1(a,b)). The thin films synthesized with a shorter processing time are mechanically unstable. The thick films synthesized with a longer treatment time do not form a microtubule structure, apparently because they have thickness of more than 1 μm. Therefore, mechanical strains arising during drying are not enough to bend them into the microtubes. The microtube wall consists of nanoparticles with diameter about 10 nm (Fig. 1(c)). According to the EPMA results (not reported here), the tubes consist of Fe and O atoms. Furthermore, no Cl and N atoms, which could possibly build the composition of microtubes from the solution or gaseous reagent, are detected in the sample.

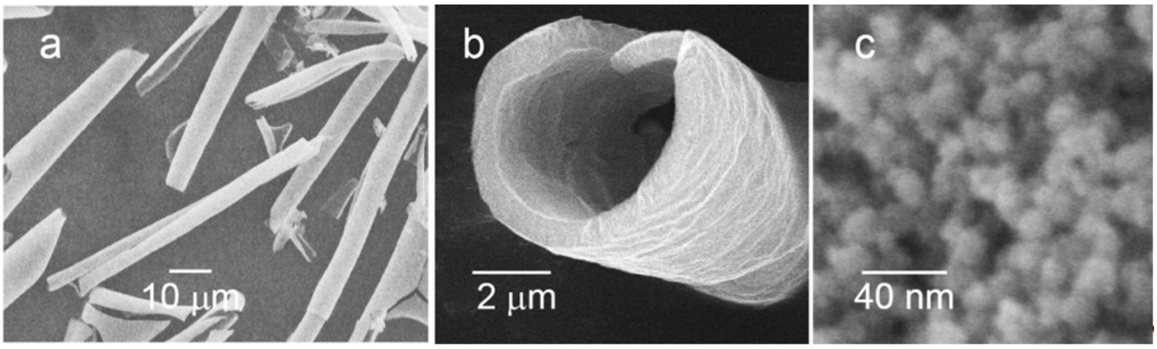

FIG. 1. SEM images of the Fe_3O_4 microtubes: a) general view; b) cross view of a single microtube; c) view on the surface of microtube wall

Figure 2 shows the XRD patterns of synthesized microtubes. One can see a series of diffraction peaks at $2\Theta = 30.1, 35.4, 43.0, 53.4, 56.9, 62.5$ and so on related to the Fe_3O_4 with *Fd-3m* space group (JCPDS card 01-080-6403).

Vibrating sample magnetometer analysis was used to investigate the magnetic behavior of the formed Fe_3O_4 microtubes. The magnetic data obtained from the as-prepared microtubes of Fe_3O_4 is presented in Fig. 3. Fig. 3(a) shows the hysteresis loop M (H) of the Fe_3O_4 microtubes at room temperature from −20 kOe to 20 kOe. The Fig. 3(b) shows the magnified hysteresis loop around the zero field. The saturation magnetization value is 9.5 emu/g, remanence magnetization value is 0.2 emu/g, coercive force is 8.1 Oe, and $M_r/M_s = 0.02$. These parameters indicate the synthesized microtubes have a superparamagnetic nature.

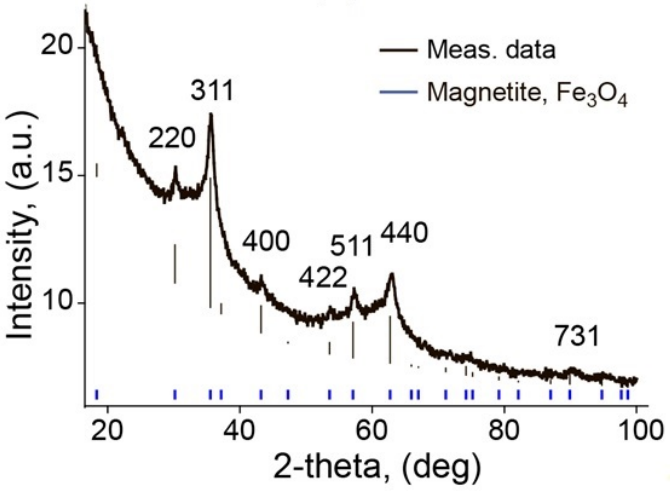

FIG. 2. XRD patterns of as-synthesized Fe_3O_4 microtubes

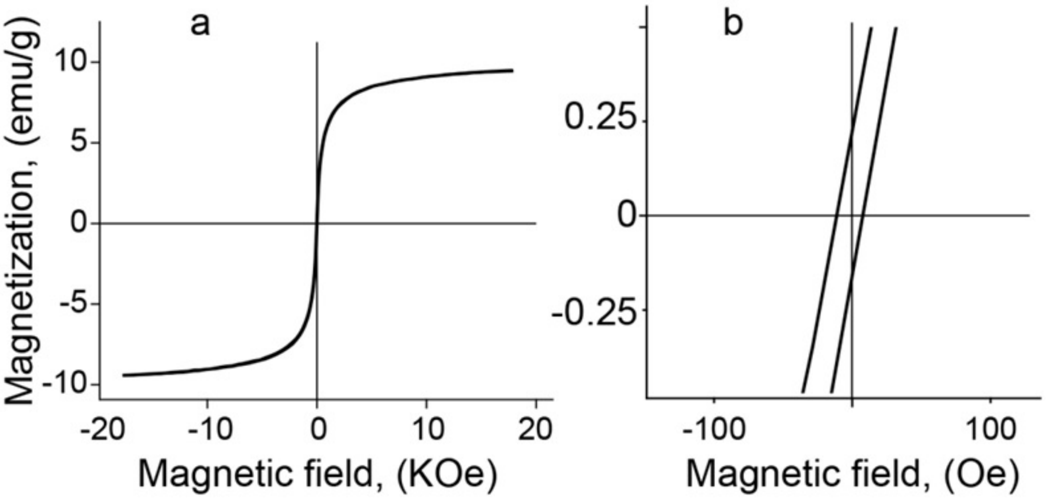

FIG. 3. Magnetization curves of as-synthesized Fe_3O_4 microtubes: a) magnetic hysteresis loop at room temperature; b) details around zero field

4. Discussion

When analyzing the experimental results, attention is primarily drawn to the fact that the obtained saturation magnetization value of 9.5 emu/g is several times smaller than the value characteristic for Fe_3O_4 nanoparticles. Apparently, this value can be explained by the fact that the microtubule wall contains both water-solvent molecules, that did not completely evaporate upon room temperature air-drying, as well as amorphous $Fe(OH)_3$ hydroxide, which could form at the interface between the solution of $FeCl_2$–$FeCl_3$ salts mixture and gaseous ammonia at the first moment of treatment. Objectively, as it follows from the dependences of solubility logarithms of Fe(II) and Fe(III) hydroxides from the solution pH, calculated by Hydra-Medusa program [25], when the pH is increased in such a solution, precipitation of $Fe(OH)_3$ is observed on the first stage and then, precipitate of $Fe(OH)_2$ is formed at a pH of 7.5–12 (Fig. 4). According to the results of [26], the formation of Fe_3O_4 nanoparticles in the process of precipitation of $FeCl_2$–$FeCl_3$ salts mixture is observed in the pH range of about 11–12. Consequently, one can assume that during synthesis, under gaseous ammonia treatment, $Fe(OH)_3$ nanoparticles are formed on the solution surface and only after that Fe_3O_4 nanoparticles emerge. In our view, this effect provides composition anisotropy along the thickness of the growing film, which ultimately leads to the appearance of a density gradient and mechanical forces distorting the flat geometry of the thin film as result of drying. It is known that effect of the film composition on geometrical parameters of tubular structures was found for nanoscrolls, obtained using hydrothermal synthesis conditions [27,28].

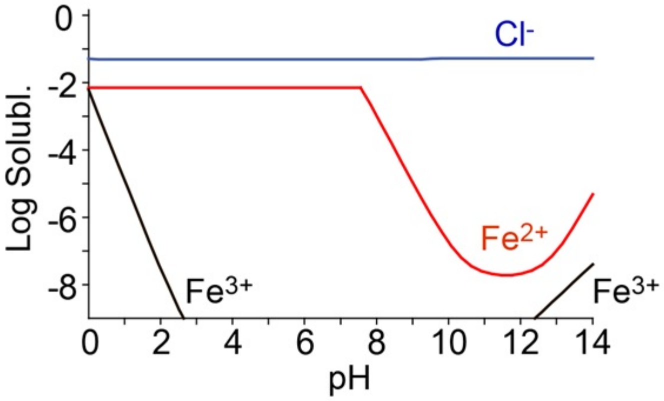

FIG. 4. Logarithms of solubility vs pH of $FeCl_2/FeCl_3$ mixed solution. $C_{(FeCl2)}$= 0.017 M, $C_{(FeCl3)}$= 0.033 M

5. Conclusion

For the first time ever, a facile interface-mediated synthesis method for the fabrication of microtubes, containing Fe_3O_4 nanoparticles, in the absence of catalysts or templates under soft chemistry conditions has been developed. As a result of the interaction between the mixed aqueous solution of Fe(II) and Fe(III) salts with gaseous phase ammonia a solid film is formed on the surface of the solution. During air-drying at room temperature the thin film was transformed into microtubes with diameters approximately 5–10 μm and up to 120 μm long with walls 0.6 μm thick. SEM, EPMA and XRD analyzes established that the microtubes contain Fe_3O_4 nanoparticles. The low coercive force and remanence magnetization, approaching of M_r/M_s to zero and the reversible hysteresis behavior confirm the superparamagnetic nature of the microtubes. The effect of film "rolling up" occurs due to the film composition gradient along its thickness, which when the film is dried, leads to the appearance of forces that distort its planar geometry and results in the formation of a more stable microtubular structure.

Acknowledgments

This work was supported by the Russian Science Foundation (project No. 16-13-10223). We thank the Centre for X-ray Diffraction Studies and Centre for Innovative Technologies of Composite Nanomaterials of Saint Petersburg State University for their technical assistance with the investigation of the synthesized product.

References

[1] Hong-Ying Su, Chang-Qiang Wu, Dan-Yang Li, Hua Ai. Self-assembled superparamagnetic nanoparticles as MRI contrast agents. A review. *Chinese Physics B*, 2015, **24**, P. 127506.

[2] Lomanova N.A., Gusarov V.V. Influence of synthesis temperature on $BiFeO_3$ nanoparticle formation. *Nanosystems: Physics, Chemistry, Mathematics*, 2013, **4**(5), P. 696–705.

[3] Almjasheva O.V., Gusarov V.V. Prenucleation formations in control over synthesis of $CoFe_2O_4$ nanocrystalline powders. *Russ. J. Appl. Chem.*, 2016, **89**, P. 851–855.

[4] Popkov V.I., Almjasheva O.V. Formation mechanism of $YFeO_3$ nanoparticle under the hydrothermal conditions. *Nanosystems: Physics, Chemistry, Mathematics*, 2014, **5**(5), P. 703–708.

[5] Tugova E.A., Zvereva I.A. Formation mechanism of $GdFeO_3$ nanoparticles under the hydrothermal conditions. *Nanosystems: Physics, Chemistry, Mathematics*, 2013, **4**(6), P. 851–856.

[6] Zherebtsov D.A., Mirasov V.Sh., Kleschev D.G., Polyakov E.V. Nanodisperse oxide compounds of iron formed in the $FeSO_4$-KOH-H_2O-H_2O_2 system (4.0 pH 13.0). *Nanosystems: Physics, Chemistry, Mathematics*, 2015, **6**(4), P. 593–604.

[7] Lomanova N.A., Tomkovich M.V., Sokolov V.V., Gusarov V.V. Special Features of Formation of Nanocrystalline $BiFeO_3$ via the Glycine-Nitrate Combustion Method. *Russian Journal of General Chemistry*, 2016, **86**(10), P. 2256–2262.

[8] Lomanova N.A., Pleshakov I.V., Volkov M.P., Gusarov V.V. Magnetic properties of Aurivillius phases $Bi_{m+1}Fe_{m-3}Ti_3O_{3m+3}$ with m = 5.5, 7, 8. *Materials Science and Engineering: B*, 2016, **214**, P. 51–56.

[9] Yang C., Wu J., and Hou Y. Fe_3O_4 nanostructures: synthesis, growth mechanism, properties and applications. *Chemical Communications*, 2011, **47**(18), P. 5130–5141.

[10] Kuklo L.I., Tolstoy V.P. Successive ionic layer deposition of $Fe_3O_4@H_xMoO_4\cdot nH_2O$ composite nanolayers and their superparamagnetic properties. *Nanosystems: Physics, Chemistry, Mathematics*, 2016, **7**(6), P. 1050–1054.

[11] Hudson R. Coupling the magnetic and heat dissipative properties of Fe_3O_4 particles to enable applications in catalysis, drug delivery, tissue destruction and remote biological interfacing. *RSC Advances*, 2016, **6**, P. 4262–4270.

[12] Massart R. Preparation of aqueous magnetic liquids in alkaline and acidic media. *IEEE Transactions on Magnetics*, 1981, **17**(2), P. 1247–1248.

[13] Qian G., Aiwu Zh., Hongyan G. et al. Controlled synthesis of Au–Fe_3O_4 hybrid hollow spheres with excellent SERS activity and catalytic properties. *Dalton Transactions*, 2014, **43**, P. 7998–8006.

[14] Shan J., Wang L., Yu H., Ji J., Amer W. A., Chen Y., Jing G., Khalid H., Akram M., Abbasi N. M. Recent progress in Fe_3O_4based magnetic nanoparticles: from synthesis to application. *Materials Science and Technology*, 2016, **32**(6), P. 602–614.

[15] Chao X., Xiaolong L., Honglian D. The Synthesis of Size-Adjustable Superparamagnetism Fe_3O_4 Hollow Microspheres. *Nanoscale Research Letters*, 2017, **12**, P. 234.

[16] Fei-Xiang M., Han H., Hao Bin W., Cheng-Yan X., Zhichuan X., Liang Zh., Xiong W. Lou. Formation of Uniform Fe_3O_4 Hollow Spheres Organized by Ultrathin Nanosheets and Their Excellent Lithium Storage Properties. *Advanced Materials*, 2015, **27**, P. 4097–4101.

[17] Goswami M.M., Dey Ch., Bandyopadhyay A., Sarkar D., Ahir M. Micelles-driven magnetite (Fe_3O_4) hollow spheres and a study on AC magnetic properties for hyperthermia application. *Journal of Magnetism and Magnetic Materials*, 2016, **417**, P. 376–381.

[18] Wei D., Lin Hu, Zhigao Sh. et al. Magneto-acceleration of Ostwald ripening in hollow Fe_3O_4 nanospheres. *CrystEngComm*, 2016, **18**, P. 6134.

[19] Tolstoy V.P., Gulina L.B. New way of As_2S_3 microtubules preparation by roll up thin films synthesized at the air-solution interface. *Journal of Nano- and Electronic Physics*, 2013, **5**(1), P. 01003-1-01003-3.

[20] Tolstoy V.P., Gulina L.B. Synthesis of birnessite structure layers at the solution-air interface and the formation of microtubules from them. *Langmuir*, 2014, **30**(28), P. 8366–8372.

[21] Tolstoy V.P., Gulina L.B. Ozone interaction with manganese acetate solution. Formation of $H_xMnO_2{\cdot}nH_2O$ layers and microtubes based on them. *Russian Journal of General Chemistry*, 2013, **83**(9), P. 1635-1639.

[22] Gulina L.B., Schäfer M., Privalov A.F., Tolstoy V.P., Murin I.V., Vogel M. Synthesis and NMR investigation of 2D nanocrystals of the LaF_3 doped by SrF_2. *Journal of Fluorine Chemistry*, 2016, **188**, P. 185–190.

[23] Gulina L.B., Tolstoy V.P., Kasatkin I.A., Petrov Y.V. Facile synthesis of LaF_3 strained 2D nanoparticles and microtubes at solution-gas interface. *Journal of Fluorine Chemistry*, 2015, **180**, P. 117–121.

[24] Gulina L.B., Tolstoy V.P. Reaction of gaseous hydrogen fluoride with the surface of lanthanum chloride solution to form $LaF_3{\cdot}nH_2O$ film and microtubes thereof. *Russian Journal of General Chemistry*, 2014, **84**(8), P. 1472–1475.

[25] Semishchenko K., Tolstoy V., Lobinsky A. A Novel Oxidation-Reduction Route for Layer-by-Layer Synthesis of TiO_2 Nanolayers and Investigation of Its Photocatalytical Properties. *Journal of Nanomaterials*, 2014, Article ID 632068, 7 pp.

[26] Kang Y.S., Risbud S., Rabolt J.F. and Stroeve P. Synthesis and Characterization of Nanometer-Size Fe_3O_4 and γ-Fe_2O_3 Particles. *Chemistry of Materials*, 1996, **8**(9), P. 2209–2211.

[27] Krasilin A.A., Suprun A.M., Ubyivovk E.V., Gusarov V.V. Morphology vs. chemical composition of single Ni-doped hydrosilicate nanoscroll, *Materials Letters*, 2016, **171**, P. 68–71.

[28] Krasilin A.A., Gusarov V.V. Control over morphology of magnesium-aluminum hydrosilicate nanoscrolls, *Russian Journal of Applied Chemistry*, 2015, **88**(12), P. 1928–1935.

NANOSYSTEMS: PHYSICS, CHEMISTRY, MATHEMATICS, 2017, 8 (4), P. 476–502

Oxide material synthesis by combustion of organic-inorganic compositions

A. A. Ostroushko, O. V. Russkikh

Ural Federal University named after the first President of Russia B. N. Yeltsin, Ekaterinburg, Russia

alexander.ostroushko@urfu.ru

DOI 10.17586/2220-8054-2017-8-4-476-502

This review analyzes and summarizes the research results for oxide material synthesis by combustion of organic-inorganic mixtures. We have outlined the range of physical and chemical factors influencing the precursor processes and the oxide material synthesis itself, as well as have shown the ways and options to control these processes and nanoscale materials' properties. We have highlighted several issues concerning the analysis methods for the resulting materials and processes. We have exemplified the practical implementation of the methods under discussion.

Keywords: synthesis, oxides, combustion method, organic-inorganic compositions.

Received: 15 March 2017

Revised: 4 August 2017

1. Introduction

Among the methods for oxide compounds and oxide-based materials, those using salts of different composition as starting materials and the reaction environments occupy an important place both in terms of scientific research [1–13] and for practical purposes [14–18]. These methods for oxide material synthesis have been proposed as alternative for solid-phase synthesis of oxide reagents, the implementation of which requires, as a rule, high-temperature and long-term cyclic thermal powder treatment [19–25]. It should be noted that there are methods for solid-phase synthesis with high-rate solid-phase chemical oxide interaction, however, the number of such methods is limited [26–33].

Solid-phase oxide reagent synthesis does not often make it possible to produce single-phase products if their thermal stability is limited. Such instances may be the synthesis of $LaNiO_3$ [34–36], $BiFeO_3$ [20, 37–39]. In the source-oxide synthesis of $LaNiO_3$ and $BiFeO_3$, as noted in [20, 34], the acceptable process rate is achieved at temperatures exceeding the thermal stability interval of these compounds. The application of such techniques as solid-phase nanoscale oxide powder synthesis does not always yield positive results. Such cases are addressed, e.g. in [40–42]. The method utilizing thin-film layered complex composition oxides for synthesis, sometimes permits high-rate solid-phase interaction of components at relatively low temperatures [29, 32], although this method is not always feasible since it is technologically complex to produce such compositions. It is not always possible to sufficiently increase the solid-phase interaction of oxide powders by using mechanochemical synthesis [43–50]. The scope of high-rate chemical solid-phase reactions at relatively mild temperature conditions, as mentioned in [28], is somewhat limited.

In this regard, various alternatives of the "soft chemistry" methods [14, 51–85] have been rapidly developed recently. Various "soft chemistry" methods have helped produce a large number of oxide compounds of varying compositions, structure, dispersity, including as nano-powders. In a great number of "soft chemistry" methods, the disadvantages are, as a rule, complex preparation of precursors and the source reaction compositions, complex instrumentation for the synthetic process, low reaction yields. In some cases, it makes it impractical to use such methods. Thus, despite the prospects of developing "soft chemistry" methods to produce oxide materials, especially nanomaterials, in many cases, these methods cannot, for the above reason, satisfy the demands in the synthesis of oxide materials, including nanostructured materials.

The methods that will be discussed below are based on the pyrolysis of mixtures consisting of salts or related forms of the source reagents and the organic part. Unlike the Pechini method [14], this review will consider the oxide synthesis processes as occurring in terms of redox reactions that are considerably exothermic. The initial state of the precursors used is, as a rule, a solution. Therefore, these methods are termed Solution Combustion Synthesis (SCS) [86, 87]. If nitrates or other oxidizing agents are used as salt forms, the pyrolysis processes can occur after their initiation, in particular the thermal one, in modes similar to that of self-propagating high-temperature synthesis (SHS) [88–91].

Pyrolytic synthesis may be related to the group of methods in which the phase formation processes take place in conditions far removed from equilibrium [92]. Such methods include co-sedimentation, solvent replacement, thermal salt decomposition, spray pyrolysis, Sol-gel methods, cryochemical synthesis, mechanochemical synthesis, etc.

In general, methods that use salts as reagents allow reduction of the synthetic temperature and duration, producing oxide compounds in the form of fine powders, including nano-powders. Herewith, some of these methods have inherent disadvantages such as possible lack of the resulting product homogeneity due to spatial separation of reagents during the synthetic process [29]. The implementation of some of these methods may lead to waste products, requiring disposal or recycling, for example, hazardous wastewater, toxic gases. The methods related to SCS are relatively simple, allowing mitigation of the negative aspects inherent in many methods where salts are applied as reagents. Different variants of SCS methods have enabled synthesis of a large number of oxide compounds in the form of nano-powders which are promising for functional and structural material manufacture [93–136]. For this reason, the SCS methods have recently attracted considerable attention.

For this review, one of the objectives is to address the specificities of SCS methods and those physicochemical aspects that are important for the most effective SCS implementation. The review is based on the results obtained by the authors, which have not been hitherto analyzed and summarized in a review on the oxide synthesis of by SCS method. In this respect, this review can be considered as complementary to the currently available reviews on material production by SCS methodology [137–148].

Different materials have been produced using compositions containing water-soluble nonionic surface-active polymers, mainly Polyvinyl alcohol (PVA), Polyvinylpyrrolidone (PVP) and metal nitrates as the salt components. For example, high-temperature superconductors [149–154], oxide magnetic materials with magnetoplumbite structure [155], perovskite-structured compounds [156–161] with catalytic and other properties allowing their application as catalysts for atmospheric protection from toxic emissions, as components of solid oxide fuel cells, electrochemical oxygen source and in other fields, solid solutions based on fluorite-type cerium dioxide [162] which also has a variety of applications, monazite-type alkali metal doped lanthanum vanadate [127] which was used as a catalyst for soot oxidation by nitrogen oxides and atmosheric oxygen, and other materials. The oxides, as previously mentioned, can be obtained not only as powders, but as deposited coatings [151–154, 156, 157, 160, 163]. In particular, nanostructured catalysts for atmosphere protection from toxic emissions have been obtained by the SCS method [126, 127, 130, 156–158, 160, 164].

In addition to the above-mentioned water-soluble polymers, in some cases, other compounds may be used as the organic component as well: polymethyl methacrylate, polyacrylamide, polyethylene glycol (PEG), methylcellulose (MC). The application of such polymers arises from their specific properties, in particular, melts flowing into cavities may be produced when heating PEG-based systems. MC is able to form gels at relatively low concentrations. One SCS method utilizes a process whereby initial solutions are evaporated until reaching the initial temperature of spontaneous pyrolysis. The other is performed by drying the composition at a relatively low temperature, ambient evaporation, vacuum, low infrared heating drying, etc. The second variant of the SCS methodology is more frequently used for the production of functional coatings.

In materials technology, the potential to produce oxide materials by pyrolytic methods not only as powders but as coatings on various carriers is important. Given this fact, a special SCS variant was suggested [165], in which the nonionic surfactant water-soluble polymers having, inter alia, a good film-forming ability were used as the organic precursor. SCS coating production will also be discussed in this review.

The results of oxide material synthesis by SCS method are influenced by a range of physical and chemical factors which should be logically considered in the same sequence of basic procedures of final production. The most important material features ensuring their functional properties include phase composition, homogeneous chemical composition of phases or the specified ratio of components within them, dimensions and morphology of particles, their boundary or surface state, including the mobility of components which is manifested, in particular, in sintering processes [166, 167], etc.. At the first stage of precursor production, one of the main tasks is to ensure homogeneity. Herewith, this requirement remains relevant for removal of the solvent during its evaporation and precursor drying. The second of the most important aspects is the actual pyrolysis (combustion) of the mixtures. The choice of systems containing inorganic and organic components has a significant effect on the combustion characteristics and the products' properties. Let us add that the target additives such as low-ash content surfactants improve the source composition spreading on the carrier surface etc., may sometimes be introduced into the polymer-salt compositions (PSC). Water is a universal solvent for precursors, although non-aqueous solutions can be also used to produce oxides.

2. Organic-inorganic precursors

The existence of homogeneous precursors is determined by both thermodynamic and kinetic factors. In order to thermodynamically analyze the possible of existence of homogeneously consistent systems, it is customary to use phase state diagrams which are the physicochemical basis for developing new materials and technologies [168]. In cases of precursors being produced at atmospheric pressure and room temperature, one can use isobaric-isothermal sections of state diagrams. It should be noted that the presence of nitrate salts in the precursors is in no way a strict requirement. For instance, formates [151], acetates [169], and other thermally degradable forms of the respective metals may be used. This choice affects the specificities of both the precursor production and the combustion process. A number of metals such as vanadium, molybdenum, tungsten may be included in source compositions as part of oxygen-containing anions (in particular, polyoxometallates): VO_4^- $Mo_7O_{24}^{6-}$, $W_{12}O_{41}^{10-}$. However, in case of cationic metal forms, the nitrate systems which ensure active exothermic reactions during pyrolysis are used most frequently. In fact, metals can also constitute part of the precursor compositions as oxygen-containing cations, such as zirconyl ZrO^{2+}. In [170–177], the corresponding phase diagrams were made for some rather typical representatives of polymer-salt-water systems used as precursors. Similar diagrams can also be made for systems containing low-molecular organic components. The common system type is one in which diagrams have areas of homogeneity separated by areas where two or three phases coexist (Fig. 1-4). Limited homogenous areas are adjacent to each of the triangle vertices where the system is enriched with one of components: aqueous solutions of the corresponding salt and polymer, the polymer matrix comprising water and a salt component, and a salt phase which may include both water and a polymer component. The two-phase areas include, for example, aqueous saline solution containing a polymer gel, drip formation of an aqueous saline solution in the polymer film (Fig. 5), the salt crystals in the polymer matrix or in an aqueous solution, etc. Upon removal of solvent (water), the system composition passes through a line (Fig. 1, the dotted line with long dashes) which corresponds to the constant ratio between the salt and polymer weight, transitioning to heterogeneous areas, including the three-phase diagram segment. This type of diagram is typical for polymers which partially mix with water, such as PVA, as well as for organic components (e.g., glycine) which are sparingly water-soluble.

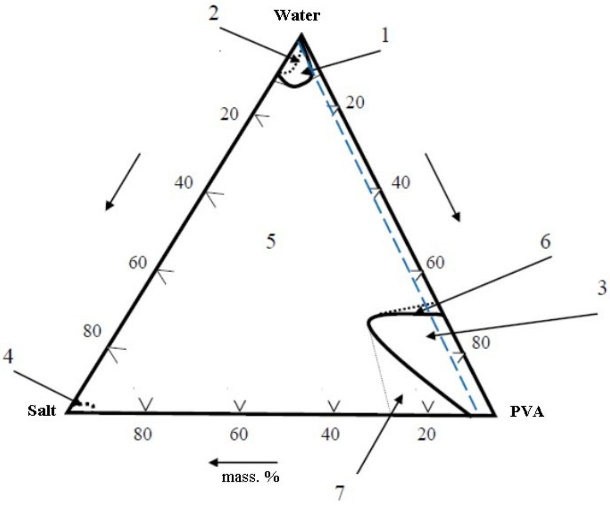

FIG. 1. Isothermal phase diagram section, tetrahydrate heptamolybdate ammonium - water - polyvinyl alcohol (PVA) system. 1 – area of existence of homogeneous polymer-saline solutions in water in the light; 2 – the same in the dark; 3 – homogeneous area of solid-phase samples; 4 – hypothetical solid, polymer-containing, salt component-based solutions; 5 – area of three-phase coexistence: liquid polymer-saline solutions, solid polymer-saline solutions, and saline phase; 6 – biphasic area with a solid matrix, comprising solid and liquid polymer-saline solutions; 7 – biphasic area corresponding to the equilibrium between the solid polymer-saline solutions and the salt phase.

Despite the fact that the precursor homogeneity should, as a rule, be broken when removing the solvent in the above system, there are a number of factors, due to which the occurrence of multiphase systems can be substantially inhibited. Thus, the possibility to adsorb the organic components on the surface of the emerging salt microcrystals has a positive effect on the decreasing trend in system phase separation. In particular, the polymeric shell prevents their growth by blocking, at least partially, the ion supply from the solution [178, 179]. The increase in the rate of solvent removal, e.g. in precursor vacuuming, allows quicker passage through heterogeneous areas of the phase diagram, and in some cases, phases which were supposed to have formed do not have time to take shape spatially. This leads, for example, to the formation of metastable glassy films. Under similar conditions, the polymers of

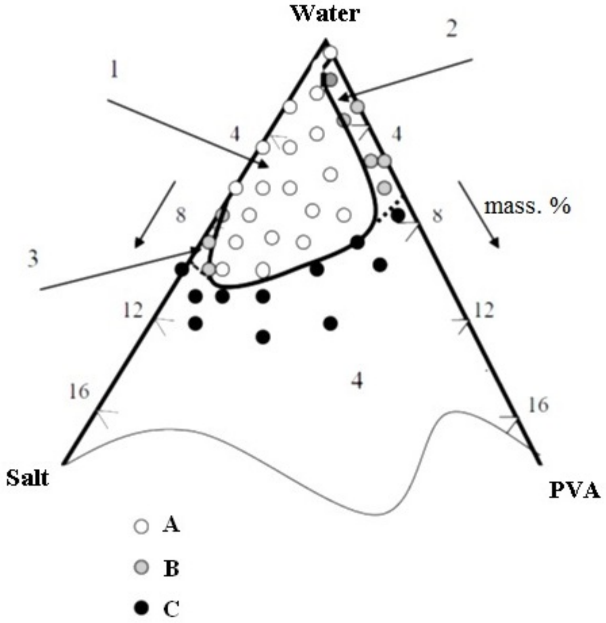

FIG. 2. A fragment of the phase salt – water – polymer diagram in the light. A – single-phase area of aqueous polymer-saline solutions (1); B – biphasic areas of existence of liquid and solid solutions with liquid disperse medium (2) and of the liquid solution and the salt phase (3); C – triphasic area of coexistence of liquid and solid solutions with the salt phase (4)

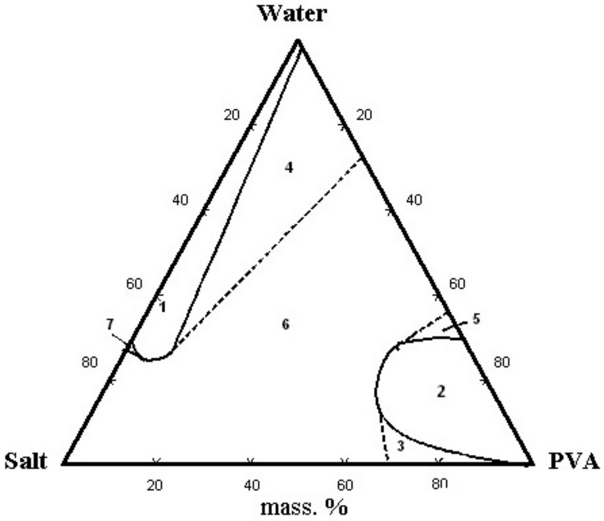

FIG. 3. Isothermal section of the phase diagram of the $La(NO_3)_3 \cdot 6H_2O$ system – polyvinyl alcohol – water at room temperature. 1, 2 – areas of homogeneous solutions (aqueous and polymer-based), 3, 4, 5, 7 – biphasic areas (with salt crystallization – 5, 7, gelation – 4, drip inclusions in the polymer matrix), 6 – triphasic area with gelation and crystalline salt precipitation occurred simultaneously

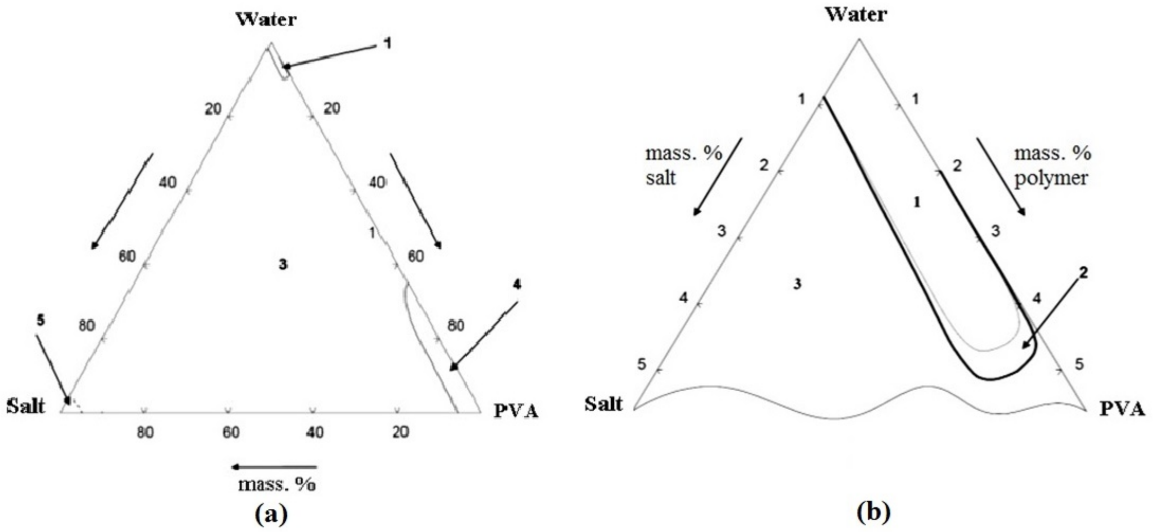

FIG. 4. Isothermal section of phase diagram of the ammonium vanadate system – polyvinyl alcohol – water at room temperature: 1 – area of homogeneous aqueous solutions under natural light; 2 – the same after exposure to UV radiation; 3 – heterogeneous area; 4 – area of homogeneous polyvinyl alcohol-based solutions; 5 – polymer-saline, ammonium vanadate based complexes

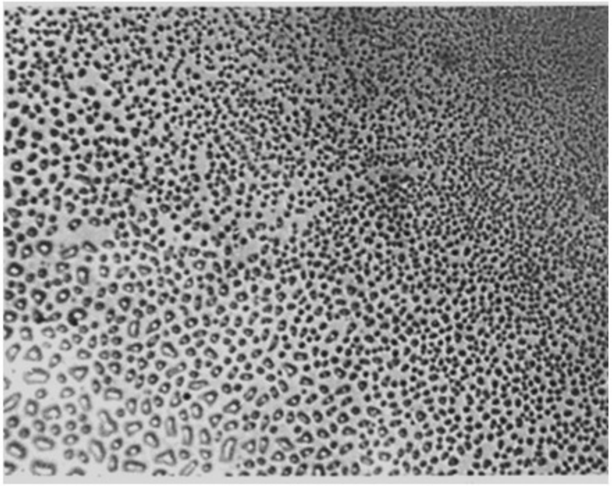

FIG. 5. Micrograph of drip formations in the PVA film containing copper nitrate (200x)

lower molecular weight are better able to suppress the growth of crystallites [153], which is a result of fewer steric difficulties in their adsorption on the solid-phase nuclei.

The polymers and organic compounds which are absolutely water-miscible are characterized by another type of phase diagram (Figs. 6–8). This type allows solvent removal while remaining within the homogeneous region. If the salt component dissolves rather poorly in water, the homogeneity range is narrow and is difficult to be practically employed (Fig. 6). The most advantageous type to preserve the precursor homogeneity is a diagram with good salt solubility (Figs. 7,8). It involves, in particular, those practically important systems which include PVP and soluble metal nitrates such as lanthanum and its analogs, as well as of transition metals, e.g. copper, nickel, cobalt, manganese, etc. Glycerin-inclusive systems are also practically relevant. We should note that such systems are characterized by the existence of a liquid-phase immiscibility area, i.e. the existence of the area in which two liquid phases coexist. The availability of liquid-phase immiscibility (Figs. 9,10) can be observed depending on existence of a lower or upper critical point in the phase diagram when the liquid precursor temperature is changed, for example, when it is heated for water evaporation, which must also be considered in practical terms.

In the ammonium heptamolybdate – polyvinylpyrrolidone – water system, in particular, at room temperature (Fig. 9), there is a field of homogeneous solutions (1), the areas of the salt component crystallization (2) and (3),

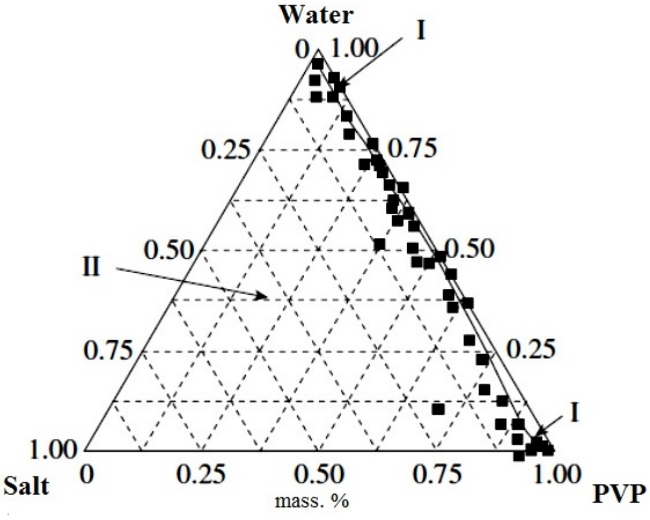

FIG. 6. Phase state diagram for the ammonium tungstate – polyvinylpyrrolidone – water system. The content of components in mass proportions. I – the area of homogeneous solutions; II – heterogeneous area of coexistence of the salt phase and the solution

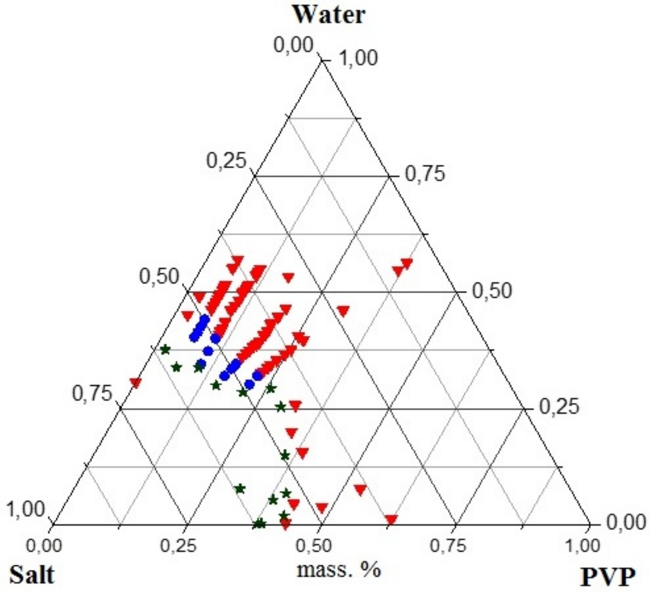

FIG. 7. Isothermal section of the phase state diagram for the lanthanum nitrate – polyvinylpyrrolidone – water system. 1 – the area of existence of homogeneous aqueous polymer-saline solutions (the respective compositions of experimental samples are marked with triangles); 2 – the area of liquid immiscibility (circles); 3 – the triphasic area of coexistence of two liquid phases and salt crystals (asterisks)

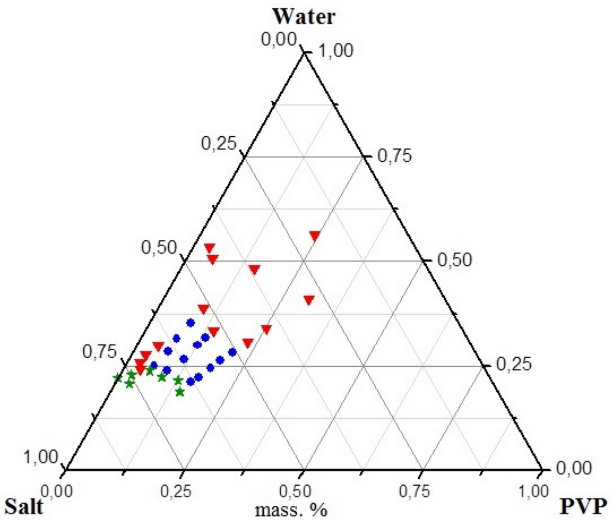

FIG. 8. Isothermal section of the phase state diagrams for the copper nitrate – polyvinylpyrrolidone – water system. The symbols are the same as in Fig. 7

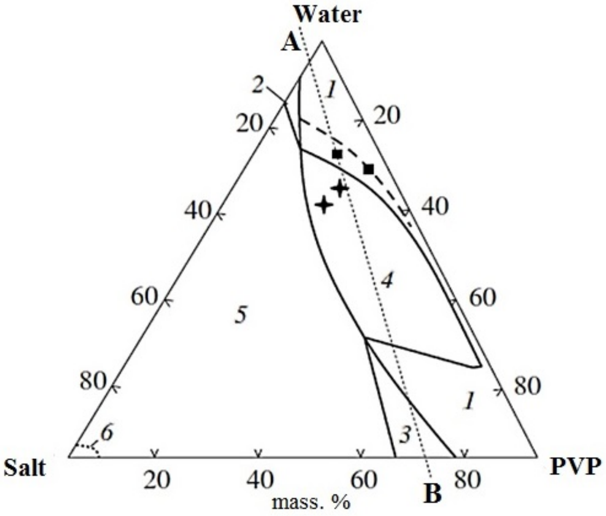

FIG. 9. The phase state diagram for the tetrahydrate ammonium heptamolybdate – polyvinylpyrrolidone – water system. The explanations are given in the text

where the liquid and solid phases coexist. Unlike the previous diagram types where there is amorphous crystal immiscibility, we can see the area of amorphous liquid immiscibility in the system (4). The salt phase (6) coexists with two liquid phases in the area (5). The study of the temperature effect on the phase separation processes of this system showed that the amorphous immiscibility area expands by the temperature increase (in particular, at 70°C). This is reflected as a dotted-line projection in the diagram (Fig. 9). At a lower temperature (15°C), the samples whose compositions are marked with asterisks, by contrast, did not show liquid immiscibility. Fig. 10 shows the poly-thermal phase diagram section along the A–B line, it is clear that the complexity of this diagram is caused by the upper and lower critical immiscibility points. The ammonium heptamolybdate – PVA – water system is also characterized by liquid-phase immiscibility which manifests itself with temperature increase (Fig. 11).

It should also be noted that the formation of complexes or associates between the metal ions and the organic component can have a favorable effect on the solubility of salt components, thus expanding the area of homogeneity for the solutions [180–182]. Some well-known examples of these samples are glycerin and glycine complexes of transition metals, in particular copper. Table 1 gives data for comparing the strength of glycine and other transition metal complexes. The possibility to form associates between similar metal ions and polymer components expands the homogeneity area on the phase diagrams, as well as inhibits secretion and growth of phase non-homogeneities

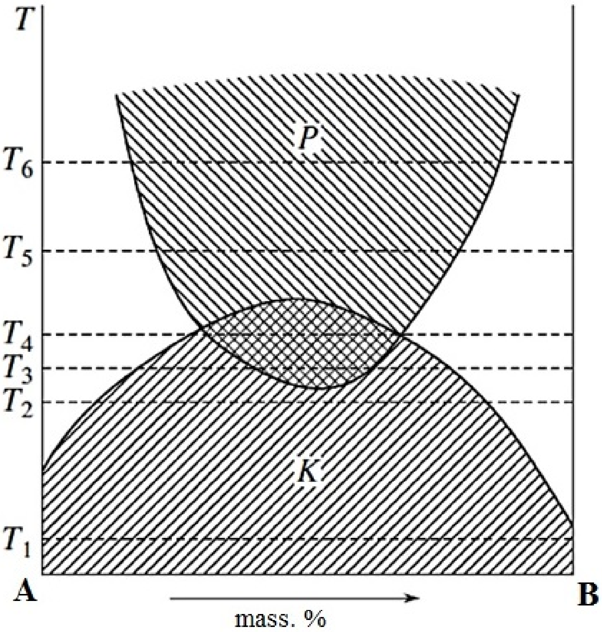

FIG. 10. Poly-thermal diagram section (Fig. 9). K – the area of salt crystallization; P – the area of liquid-phase (amorphous) immiscibility. Further explanations are given in the text

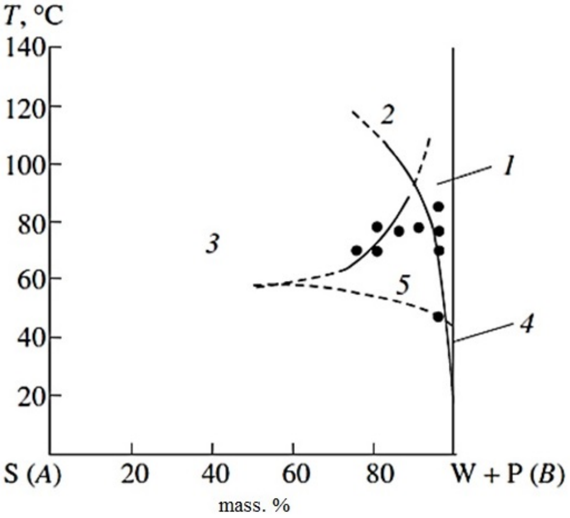

FIG. 11. Poly-thermal sectional phase-diagram fragment (Fig. 1) along the A–B line. The dots denote experimental points. 1 – Homogeneous solutions; 2, 4 – area of coexistence of two liquid phases; 3 – the coexistence of liquids and crystals; 5 – the area of amorphous crystalline immiscibility

in the process of solvent removal. The literature has data for the transition metal complexation with water-soluble nonionic polymers; the information regarding the PVA is given in Table 2. The papers [180, 181] studied the thermodynamics of polymer complexation, and their low molecular weight analogs, with metal cations and anionic forms including a multicharged metal (Mo) in some systems. In particular, it was found, as exemplified by the interaction of PVA, PVP, polyethylene glycol (PEG) with ions of cadmium(II) and copper(II), that PVP interacts the most actively with the divalent ions. This is shown for Cd^{2+} at higher negative values of the interaction enthalpy, the Gibbs energy and the complex formation constant. For Cu^{2+} ions, as compared to cadmium complexation, the constant is even higher; however, the energy factor does not contribute to spontaneous emergence of its complexes. Table 3 shows the significant role of the entropy factor in the complexation. The complexation is accompanied, in particular, by dehydration of ions and functional groups of organic compounds which act as ligands. Herewith, the water molecules released during dehydration gain translational mobility. Due to this, in particular, the system's entropy may increase. In [183], it was shown that water-soluble polymers of various origins can differently influence the water structure and the ability of ions to form the ion complexes (associates) with the polymer. The damaged structure of water in solutions of rather more hydrophobic PVA causes increased hydration interactions between the ions and water molecules. Stabilization of water structure in hydrophilic PVP solutions should determine greater development of polymer – ion solvation effects and the increase in the tendency for ion association or complexation with polymer molecules. The determining role of the above entropy factor was also confirmed by the example of the studied complex polyoxometalates, including a polymer component (PVA) [184]. The study of ammonium heptamolybdate-containing systems revealed that the low-molecular substance (ethylene glycol which can also be considered as a glycerin analogue), as compared to the high-molecular compounds of similar structure (PVA), is able to interact more actively with heptamolybdate (Table 3).

TABLE 1. The stability constants for complexes of heavy metals with organic ligands [185]

Ligand	IgKc				
	Ni^{2+}	Zn^{2+}	Cd^{2+}	Cu^{2+}	Pb^{2+}
NH_3	2.8	2.37	2.65	4.25	
Glutathione (RS^{1-})	4.0	5.0	6.16		
Imidazole (=N)	3.0	2.52	2.8		
Acetate (O^{1-})	0.8	0.7	1.2		
Glycine		5.52	4.8	8.62	5.47
Oxalate		4.68	4.0	6.19	4.0
OH		4.4	4.6	6.3	6.2
Carbonate		4.8	4.0	6.77	6.2
Humic acids (pH8)		5.3	5.0	5.0	5.3-8
Surface particles (pH8)		-3.6	-3.7	-1.8	-1.7

TABLE 2. Complexation constants and thermodynamic parameters of M(II) – PVA reactions [186]

M(II)	lg(K_1)	lg(K_2)	lg(K)	ΔG, kcal/mol		
				$-\Delta G_1$	$-\Delta G_2$	$-\Delta G_{aver.}$
Co	5.67	5.32	11.06	8.18	6.42	16.0
Ni	6.21	5.60	11.82	8.36	7.90	16.0
Cu	8.07	7.86	15.93	11.53	11.10	22.52
Zn	6.94	6.63	13.57	10.14	9.52	19.23

One study [187] suggested a structure model for complexes of oxygen-containing ions with polymers (Fig. 12). As shown in [182, 186], the interaction of different ions with the polymer macromolecules, in view of significant influence of the entropy factor as well, is of the specific features as manifested in heterogeneous ion distribution in the solution, both between the macromolecules therein and within a single macromolecule joined in the interaction. The interconnection of ions and the polymer is facilitated on the chain section which is adjacent to the previously attached ion. In the case of polyoxometalate ions, this leads to induced-rigidity portions of the polymer chains, while the solutions, which become similar to liquid crystals, gain mesomorphic properties [187, 188]. The films derived from these solutions indicate a coaxial orientation for the rigid fragments of the polymer-saline associates (Fig. 13); in this case, apparently, they are perpendicular to the film surfaces. This is shown by a specific kind of x-ray diffraction patterns of the films [187,189]. When deriving oxide materials from textured films, you can expect

TABLE 3. Thermodynamic parameters of Cd^{2+} and Cu^{2+} ion complexation with PVA, PEG, PVP at room temperature [181]

System	K_p	ΔG^0_{compl}	ΔH^0_{compl}	$T\Delta S^0_{compl}$
		kJ/mol		
Cd^{2+} – PVA	$2.3 \cdot 10^4$	−24.9	−0.25	24.6
Cd^{2+} – PEG	$2.2 \cdot 10^8$	−47.6	−0.46	46.9
Cd^{2+} – PVP	$9.1 \cdot 10^4$	−28.3	−0.75	27.5
Cu^{2+} – PVA, PEG	$3.1 \cdot 10^6$	−37.1	24.0	61.1

at least partial texture inheritance by the complex oxide coatings on the media [163]. The issues regarding the pyrolytic production of textured coatings are of practical interest. The phenomenon of directional salt component crystallization is evident in the polymer-saline compositions (PSC) on single crystal substrates in those cases where crystallization is not suppressed (Fig. 14). It is practically possible to produce textured oxide films from such precursors, (Fig. 15), for example, the superconducting ones [163], in which the crystallites have a preferential orientation.

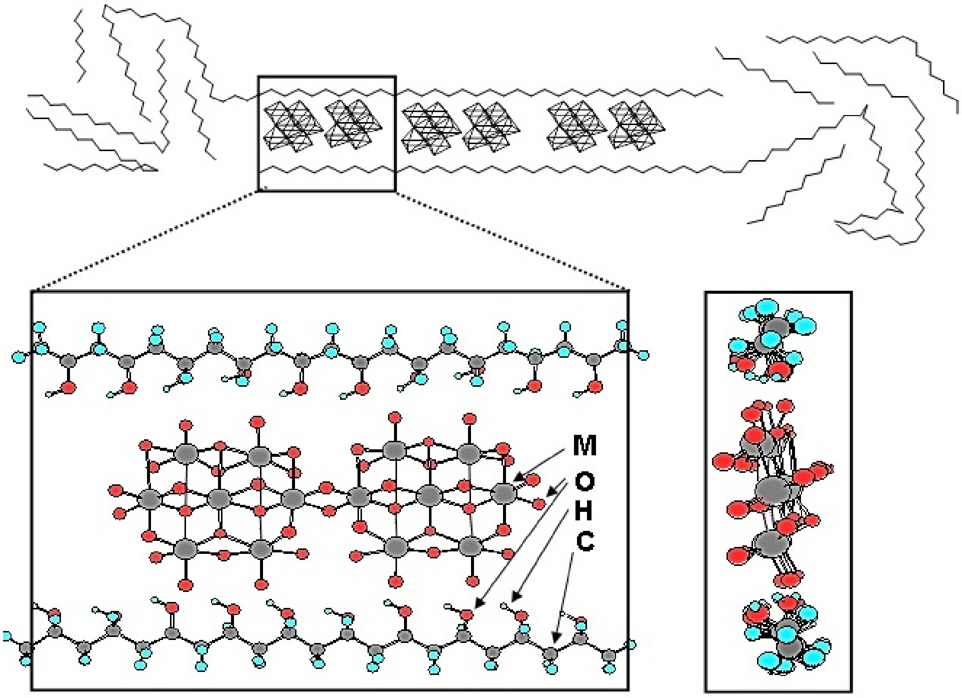

FIG. 12. Polymer-saline ammonium heptamolybdate and polyvinyl alcohol complex structure M=Mo

When exposed to light, the precursors comprising ions of such metals as vanadium, tungsten, molybdenum allow for partial reduction of metals due to photochemical reactions of the electron transfer from the polymer component to the oxygen-containing ion. Any earlier associates remain unchanged; however, the formation of charge-transfer complexes may affect the type of the phase diagram, thus expanding in particular the homogeneity area (Figs. 1,4) due to the better solubility of such complexes. Incidentally, such PSC may be used as catalytic materials for photochemical processes under mild conditions [190, 191]: e.g. the sulfide oxidation to polysulfide, selective oxidation of α-pinene to verbenol or verbenone etc. The flow of autocatalytic oscillatory reactions discovered in PSC themselves [192, 193] contributes to this as well. Polymer film compositions which include partially recovered vanadium, molybdenum and tungsten ions have been proposed for use as membranes of ion-selective electrodes which are sensitive to the aforementioned ion concentrations in the solutions studied [179, 194].

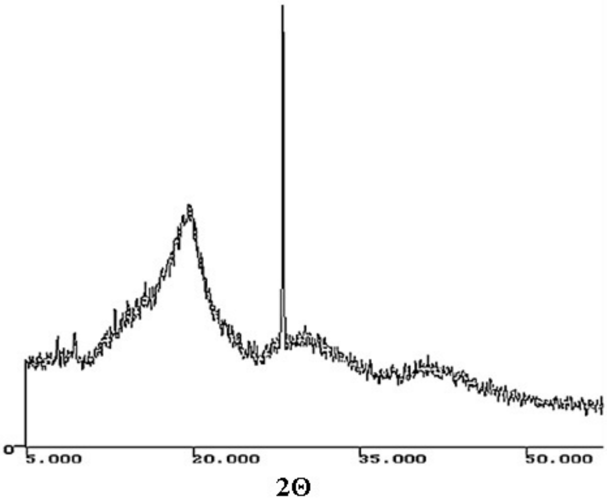

FIG. 13. X-ray diffraction pattern (CuK-radiation) of the polymer-saline ammonium tungstate – PVA (2 and 10 % w, in initial solution respectively) film composition

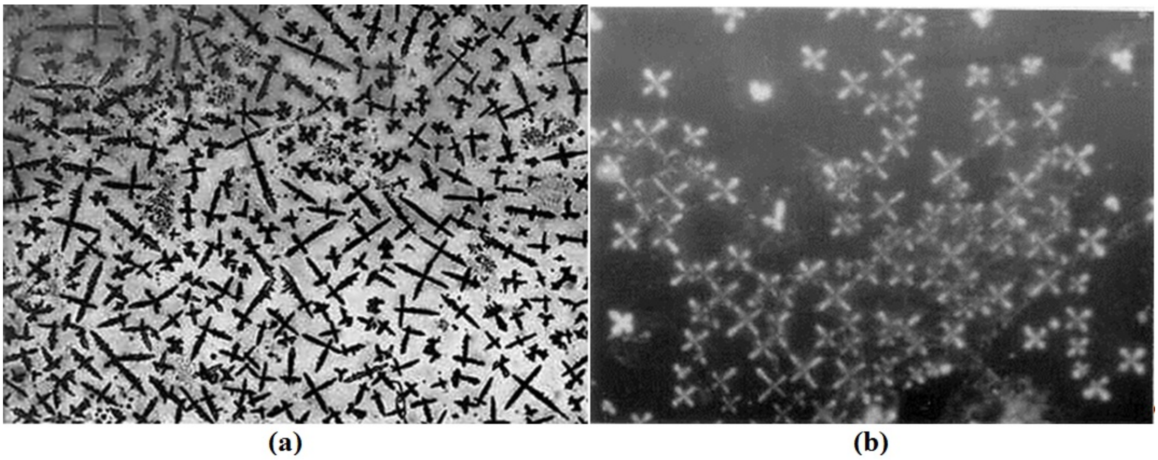

FIG. 14. Salt component (Y, Ba, Cu nitrates) crystallization in the PVA films to derive $YBa_2Cu_3O_{7-\delta}$ (YBC) **a** – on the glass (200×); **b** – on the single crystal MgO substrate (100x). The least soluble barium nitrate crystallizes prevalently, then, crystallites grow from the primary crystal faces

To conclude this Section, we should mention another option to produce homogeneous precursors in those cases where the oxides are composed of ions of vanadium, molybdenum, tungsten [195–198] and metals with similar chemical properties. There is precipitation when introducing the ions of most alkaline earth, rare earth, and transition metals into such metallic saline solutions to produce the respective complex oxides. The precipitate contents of the low-solubility compounds are variable and depend on several factors: temperature, concentration, acidity, the mixing sequence of initial solutions, and in some cases, even on the mixing intensity. This makes it difficult to produce a complex oxide a strictly defined stoichiometry. The mixing of solutions, with a polymeric component available, allows production of a stable gel with a given composition [199, 200] due to the fact that the reagents are pre-connected with a polymer into the complexes. Then, a three-dimensional spatial grid which includes the corresponding ions as uniformly distributed by volume is formed in the gel. It is possible to remove water from such gels without breaking their homogeneity, and to carry out pyrolytic synthesis of complex oxide, including on the media, as implemented in the course of producing the lanthanum-cesium vanadate, the soot oxidation catalyst [201]. The alkali metal compounds (in this case, the cesium nitrate) participate scarcely in complexation, and are included in the precursor as the dispersed-phase components of the polymer-salt matrix. The systems described can be represented by diagrams of the gel stability to spatial phase separation, as similar visually to the phase diagrams (Fig. 16) having a lower critical immiscibility point.

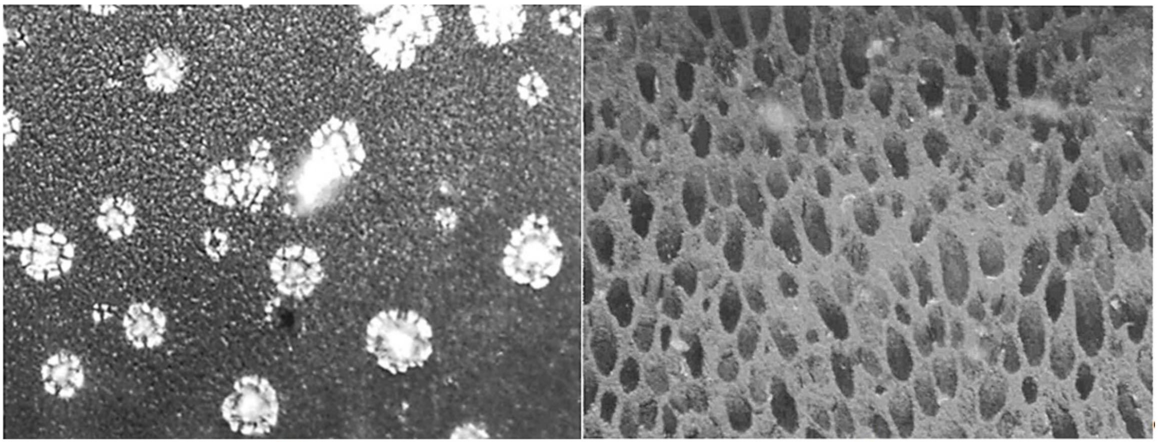

(a) (b)

FIG. 15. Stages of the oriented YBC film formation of the polymer-saline composition: **a** – 500×; **b** – 1000×

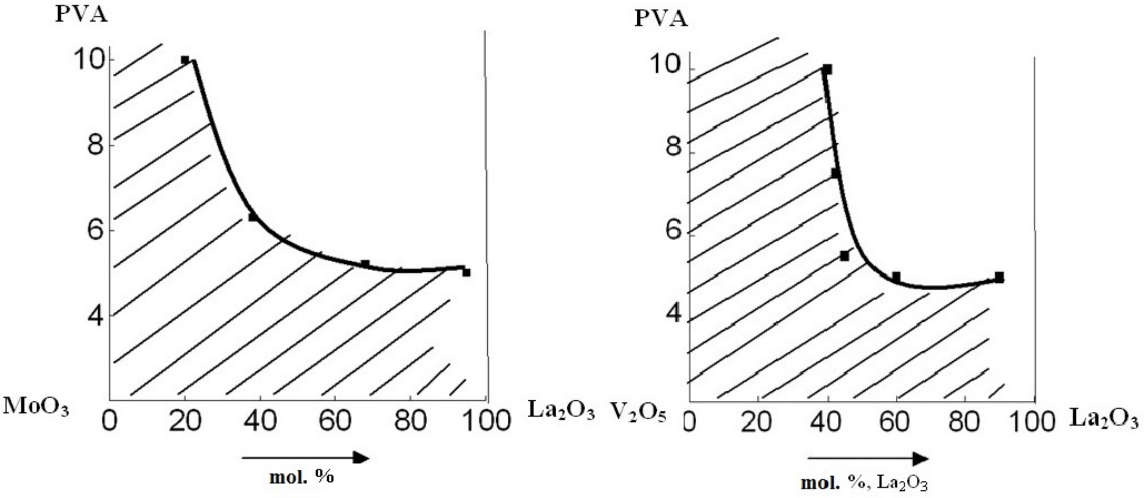

(a) (b)

FIG. 16. Stability diagrams for polymer-saline gels with a total salt content of 0.35 mass % in the ammonium heptamolybdate – lanthanum (III) nitrate (a) and ammonium metavanadate – lanthanum (III) nitrate (b) systems. PVA – polyvinyl alcohol concentration in mass %; $MoO_3(V_2O_5)$ – La_2O_3 content in mol. %. The gel separation area is shaded

It should be noted that when there are acidic reactions in the solutions, the anionic forms of oxygen-containing ions of molybdenum, tungsten, and vanadium are able to transform into cationic molybdenyl- and vanadyl-type forms. In the case of tungsten, especially without any organic component, there may be precipitation of the so-called tungstic acidic mixture. The precursor's acidity has an effect on the results of pyrolytic synthesis of these metallic oxides, which was shown, in particular, in [198].

3. Features of precursor combustion and oxide material synthesis

When producing oxide materials, the precursor combustion is characterized by a number of parameters such as the burning rate, pyrolysis localization in the volume of the reaction medium, its temperature, the composition and temperature of the gases released, etc. These parameters are determined by the nature of components used in the original compositions, the ratio of the oxidant (mainly, the nitrate part of the system) and reductant (the organic component). The nitrate ions are the oxidizing agent as part of homogeneous organic-inorganic compositions. The thermal nitrate decomposition itself is accompanied by release of gaseous products which have oxidizing properties (oxygen, nitrogen oxides), herewith, an active oxidizing agent may be the atomic oxygen at the time of its emission (nascent state). On the contrary, during thermal degradation, the salts of organic acids (formates, acetates, etc.) create a reducing environment due to the availability of such gases as carbon mono- and dioxide and, sometimes, hydrogen. The organic salt decomposition may generate carbon; the degradation of these salts may result in reduced forms of metals such as copper – Cu^+, Cu^0. Considering that it is possible to create mixed precursors comprising salts of different origin, this aspect can be used to regulate the intensity of pyrolysis, production of materials which include low-oxidized metals. Nitrates of various metal groups undergo thermal decomposition at significantly different temperatures. In addition, degradation can occur stepwise. Below, we address such a case exemplified by the salt destruction when producing $YBa_2Cu_3O_{7-\delta}$ (YBC).

$$Ba(NO_3)_2 = Ba(NO_2)_2 + O_2$$

$$Ba(NO_2)_2 = BaO + NO + NO_2$$

$$Y(NO_3)_3 = YONO_3 + 2NO_2 + 1/2O_2$$

$$2YONO_3 = Y_2O_3 + 2NO_2 + 1/2O_2$$

$$Cu(NO_3)_2 = CuO + 2NO_2 + 1/2O_2$$

It should be noted that the step degradation may lead to broken homogeneity in the synthesis products due to the growing granules of the newly formed intermediate oxide phases. Stepwise salt destruction is usually manifested in the complex oxide production by thermal salt mixture decomposition which is not accompanied by the use of organic components. The thermal destruction temperatures vary greatly for nitrates of different metals, for example, these temperatures are ranged 100 to 800°C when producing YBC. Part of the nitrates, the salts of alkaline earth and some transition metals, are decomposed through a melting stage. The resulting melts are corrosive and can interact actively with the materials of reaction vessels.

Application of nitrate-organic precursors enables one to solve most of these problems. First of all, the exothermic pyrolysis temperature of the system decreases upon introduction of organic components into the mixture of metal nitrates (Fig. 17). In most cases, the combustion itself is reflected in the thermal analysis results as a single intensive exothermic effect. Experiments show that, other things being the same, the maximum combustion rates and the developing temperatures are usually achieved in the nitrate precursors comprising organic components with nitrogen atoms in the oxidation degree of 3−, as entering into an energetic reaction (up to explosion) of comproportionation with nitrate nitrogen (5+) atoms. These (nitrogen (3−)) include, for example, polyvinylpyrrolidone, glycine. Therefore, these substances can be considered as analogs in a sense, in terms of implementation of the pyrolytic oxide synthesis. Polyvinyl alcohol, ethylene glycol, glycerol consisting of a carbon skeleton with hydroxyl groups attached act as another precursor group of similar interaction. The thermograms (Figs. 17,18) [165, 169] show that in the process of heating, the salt mixture decomposition is accompanied by a number of endothermic effects of the stepwise decomposition of the respective nitrates, whereas with a polymer available, the sign of thermal effects changes, the decomposition temperature decreases due to the combustion effect, the sample mass stabilizes at a substantially lower temperature.

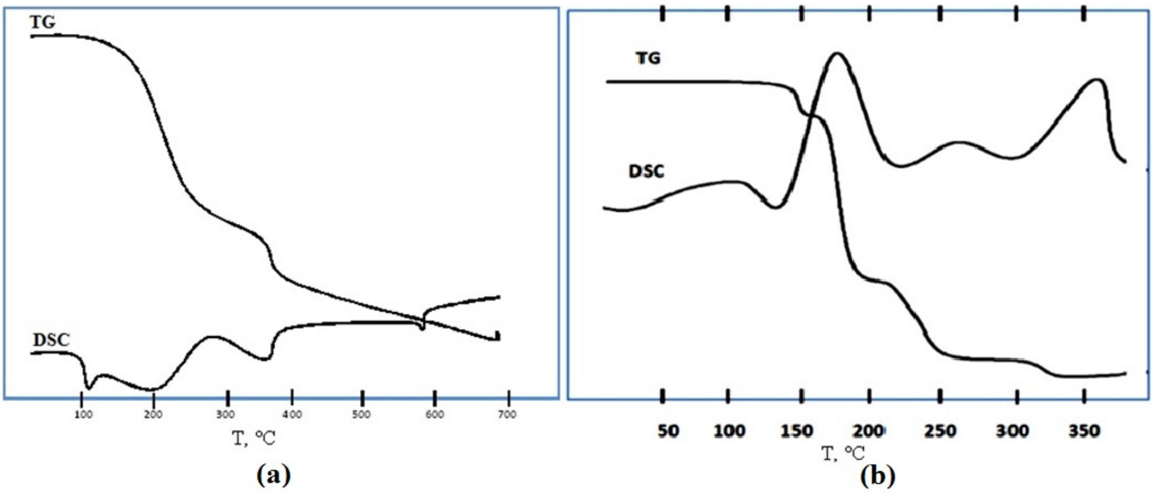

FIG. 17. Thermograms (D-1500Q derivatograph) of reaction mixtures; **a** – cobalt, lanthanum, strontium nitrates; **b** – the same with PVA introduced

Calculation of precursor combustion reactions is usually carried out based on the condition of carbon dioxide, water and molecular nitrogen release as evolved gaseous products (see for instance [94, 112, 118, 202]). The defined ratio between the nitrate part of the system and the organic component is considered stoichiometric, which corresponds to the imputation rate $\varphi = 1$. When $\varphi < 1$, the reaction system lacks the organic component, and when $\varphi > 1$, there is an excess which may ultimately require additional oxidation, for example, by atmospheric oxygen. Oxidants, in particular, additional oxygen may be required and should be taken into account when the metal components are available low valent compounds in the salt compositions, e.g., Co^{2+}, Mn^{2+} rather than characteristic (3+ and 4+) for many oxides. In some cases, where there are stably oxidized metallic components, a simplified stoichiometry calculation scheme can be used. This should take into account a free nitric acid as well, when they use acid solutions with its excess:

$$\text{—}CH_2\text{-}\underset{\text{OH}}{\underset{|}{C}H}\text{—} + 2HNO_3 \longrightarrow 2CO_2 + 3H_2O + N_2$$

It can be assumed that pyrolysis processes occur the most intensively in various systems if the ratio is $\varphi = 1$. In this respect, the experiments on the measurement of the real temperature-time combustion parameters are deemed quite interesting. Such experiments have been implemented, in particular, by synthesis of calcium zirconate $CaZrO_3$ [112, 118] as a practically important material for producing dielectric and refractory ceramics, a component of the photocatalytic and luminescent systems, solid electrolytes with different conductivity. Calcium metazirconate was synthesized by the SCS method [203], using various organic reagents such as β-alanine [204], citric acid [205,206] or citric acid with urea [207], glycine [138, 208] for the combustion reaction. To determine the combustion parameters in [112, 118], the synthesis was carried out in glycine-nitrate systems. To achieve reproducible results, they provided the same geometry of the reaction vessel and the same type of solvent evaporation. The synthesis temperature of $CaZrO_3$ was recorded using two thermocouples with a measurement period of 0.12–0.2 s. The temperature of the gases released was measured by an infrared pyrometer. The gas composition was determined by a gas analyzer. Depending on the φ-value, there were three types of pyrolytic processes observed. When $\varphi < 0.8$ (Fig. 19), the pyrolysis occurred in amorphization (smoldering combustion), the reaction was gradually spreading in the reactant environment as a narrow combustion front occurring at relatively low temperature and gentle temperature profile. When the φ-values were ranged $0.8-1.1$ (overall combustion), the process time was minimal (Fig. 19), the combustion spread quickly over the whole reaction volume. When $\varphi \geq 1.2$, the combustion occurred in a manner similar to that of SHS. The reaction medium was highly heated some time after the combustion front had occurred. The maximum process temperature did not meet the stoichiometric ratio, and was achieved at $\varphi = 1.3$ (Fig. 20). At low φ-values, significant amounts of nitrogen oxides were released, as calcium and zirconyl nitrates could decompose thermally like salts. At high φ-values, there was increased content of carbon monoxide in the gaseous environment. The absence of the area where combustion occurred with no release of nitrogen oxides and carbon monoxide suggests that the actual processes differ from the design scheme. It must be assumed that divergence of the processes from theoretical ideas will increase with local inhomogeneities appearing in the overall component distribution. The use of PVP precursors as an organic component can lead to the formation of another redox interaction product when an excess of nitrogen, being initially oxidized as 3-, is incompletely oxidized by the nitrogen nitrate and forms a lower nitrogen oxide. The data from GC-MS analysis of the gas composition during air pyrolysis of the film PVP composition with Ag, La, Mn nitrates showed that after removal of water, there were two stages of N_2O release, followed by significant CO_2 emission with impurities of organic substances. Against this background, there were emissions of certain amounts of NO and NO_2 (Fig. 21; the thermogram is shown in Fig. 18). In some cases, the oxide SCS products can contain the residual carbon coloring white materials with a gray or brownish tint.

In the thermal analysis of the oxide SCS production processes, the thermograms display, in addition to the main exothermic effect, the availability of at least another one being less intensive (Fig. 17,18). The origin of this maximum can be explained by the burnout of residual carbon. At a relatively low temperature in the additional thermal treatment of the SCS products, the carbon is almost completely removed. Thus, the carbon content did not exceed thousandths of a percent in the $YBa_2Cu_3O_{7-\delta}$ samples produced by the SCS method in the metallic nitrates – PVA system where its presence is critical [153]. The carbon oxidation by oxygen is accelerated during additional heat treatment of the materials produced, and facilitated with catalytic properties of the oxide systems. Such properties, to different extents, are characteristic for many oxides, including $YBa_2Cu_3O_{7-\delta}$, which are composed of transition metals [202]. It is especially typical for oxides based on metals which change rather easily the oxidation degree and are capable to form compounds with low metal - oxygen binding energy, such as Cu, Mn, Co, etc. The carbon is also oxidized effectively in the oxides, including lanthanum vanadates [201]

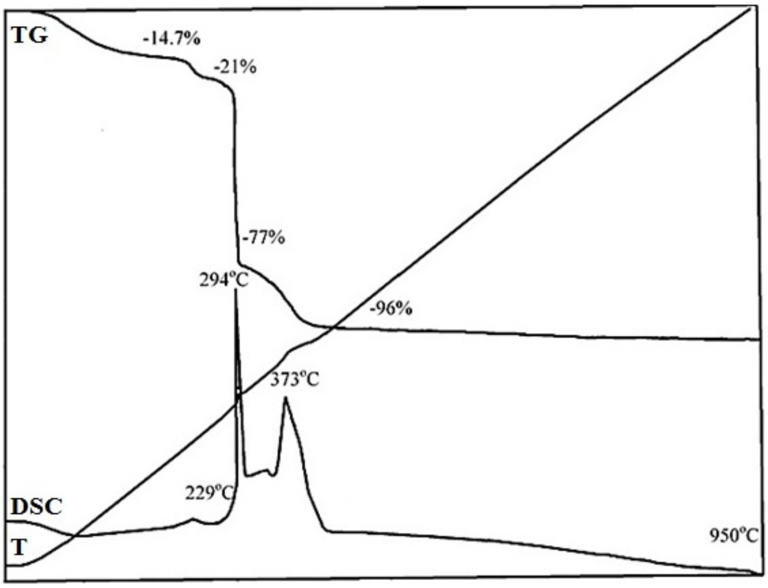

FIG. 18. Thermogram of the reaction mixture (polymer saline composition) containing the nitrates of lanthanum (III), silver (I) manganese (II) and PVP, the heating rate is 10°C/min. T is the temperature

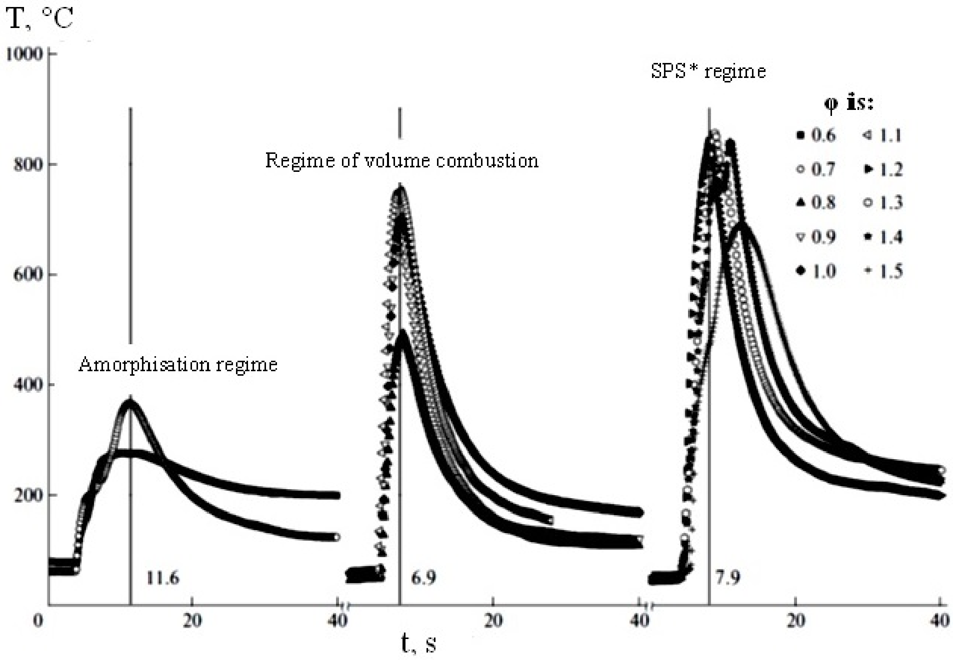

FIG. 19. Temperature combustion profiles in the $CaZrO_3$ synthesis

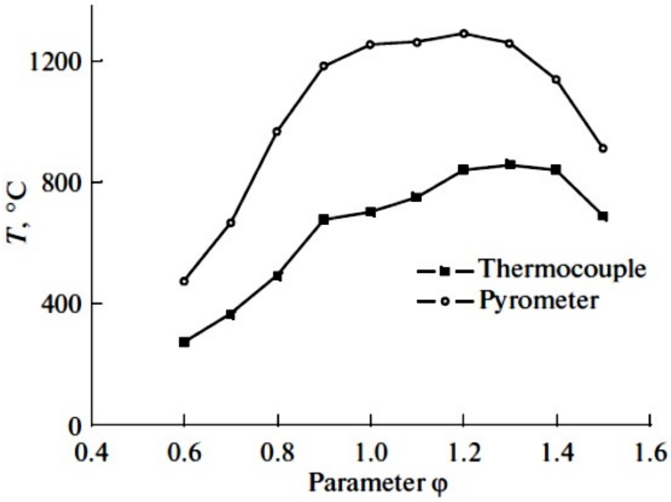

FIG. 20. Maximum combustion temperatures attained as depending on the φ-parameter

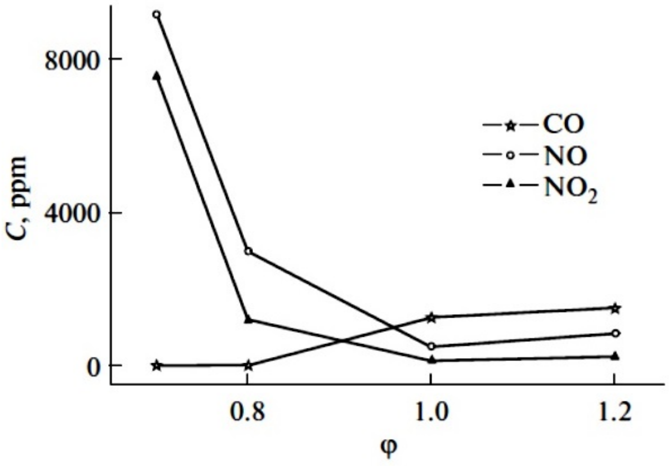

FIG. 21. CO, NO, NO_2 concentration in combustion products

doped with alkali metal ions where, as expected, the intermediate unstable carbonate complexes are formed. In general, the catalytic processes have a sufficiently strong effect on the precursor production and pyrolysis [202]. Some compounds with labile-oxidized metals affect organic compounds at the stage of preparing solutions. Thus, in concentrated solutions of the moderately heated iron (III) nitrate and PVA, the intensive redox reaction starts with gassing and self-heating. In some cases, a catalytic effect is evident after the production of film precursors. It is typical, for example, for compounds of molybdenum and tungsten, especially in an acidic environment. When poorly heated and exposed to light, there are reactions with partial metal reduction to the oxidation degree of (5+), the appearance of blue color, and, sometimes, of the spongy film structure due to gases released. During combustion of the compositions, the catalytic properties of their constituent compounds are achieved.

Special studies have shown that the combustion rate of the PVA-based film precursors depends essentially on the possibility to change the oxidation degree of the metal components, and the availability of catalytic properties in the intermediate phases and the synthesis products. The precursors containing nitrates of stably oxidized alkaline and rare earth elements combust slowly and unstably, there is no intense pyrolysis [202] (Tables 4, 5). More stable and high-rate combustion is characteristic for the films containing the transition metallic nitrates and silver (Table 5). The factors decreasing the combustion rate may be the existence of crystalline hydrates formed by nitrates. The combustion rate may enhance the catalytic properties, which is clearly exemplified by the systems in which the respective complex oxides are formed. The catalytic action of metallic silver which appears as nanoparticles during combustion may result from the ability to change its oxidation, $Ag^0 \leftrightarrow Ag^{1+}$. It can be assumed that the paramount importance to enable the catalytic effect on precursors at different synthesis stages is a result of the Red/Ox potentials for the respective ions which are given in Table 4 to illustrate the above.

TABLE 4. Oxidation potential of reactions and the catalytic effect of inorganic ions

No	Reaction	E, V	No	Reaction	E, V
1	$Fe^{3+} + \bar{e} \rightarrow Fe^{2+}$	+0.771*	10	$MoO_2^{2+} + \bar{e} \rightarrow MoO_2^{+}$	+0.48**
2	$Mn^{3+} + \bar{e} \rightarrow Mn^{2+}$	+1.51***	11	$WO_4^{2-} + 4H_2O + 6\bar{e} \rightarrow W^0 + 8OH^-$	−1.05
3	$Co^{3+} + \bar{e} \rightarrow Co^{2+}$	+1.95***	12	$WO_4^{2-} + 8H^+ + 6\bar{e} \rightarrow W^0 + 4H_2O$	+0.05
4	$Co^{2+} + 2\bar{e} \rightarrow Co^0$	−0.29	13	$Sr^{2+} + 2\bar{e} \rightarrow Sr^0$	−2.89
5	$Cu^{2+} + \bar{e} \rightarrow Cu^+$	+0.159	14	$La^{3+} + 3\bar{e} \rightarrow La^0$	−2.52
6	$Cu^{2+} + 2\bar{e} \rightarrow Cu^0$	+0.345	15	$NO_3^- + 2H^+ + \bar{e} \rightarrow NO_2 + H_2O$	+0.80
7	$Cu^+ + \bar{e} \rightarrow Cu^0$	+0.531	16	$NO_3^- + 4H^+ + 3\bar{e} \rightarrow NO + 2H_2O$	+0.96
8	$Cr^{3+} + \bar{e} \rightarrow Cr^{2+}$	−0.41	17	$NO_3^- + 2H_2O + 3\bar{e} \rightarrow NO + 4OH^-$	−0.14
9	$Ag^+ + \bar{e} \rightarrow Ag^0$	+0.7994**	18	$2NO_3^- + 12H^+ + 10\bar{e} \rightarrow N_2 + 6H_2O$	+0.73

*The catalytic effect is manifested directly in solutions;

**the effect begins to reveal in films;

***the catalytic effect during pyrolysis.

TABLE 5. Combustion rate of PVA-based compositions

No	Saline constituents of the composition	Combustion rate, $cm.min^{-1}$
1	Cobalt nitrate	3–4
2	Strontium nitrate	3–5
3	Lanthanum nitrate	2–4**
4	Manganese nitrate	5–7
5	Silver nitrate	10–15
6	Strontium nitrate and cobalt nitrate ($SrCoO_x$)*	11–13
7	Lanthanum nitrate and cobalt nitrate ($LaCoO_{3\pm y}$)*	14–18
8	Lanthanum nitrate and manganese nitrate ($LaMnO_{3\pm y}$)*	13–16
9	Lanthanum nitrate, silver nitrate, and manganese nitrate ($La_{1-x}Ag_xMnO_{3\pm y}$)*	15–20
10	Silver nitrate and manganese nitrate ($AgMn_2O_4$)*	30–40

*The synthesized oxide composition

**Unstable combustion

The basic mechanisms of pyrolytic oxide synthesis reveal in the thermochemical processes in the reactors where the solutions of organic-inorganic compositions are sprayed in a heated zone (spray pyrolysis). The positive effect of the available organic component also manifests in this case, since the fractional component crystallization, as well as stepwise thermal destruction, may occur in the pure salt mixtures, starting with the least soluble component. Ceramic oxide coatings are produced similarly, when the solutions are sprayed in doses on a heated media [169]. In addition, the polymer component provides for the formation of the initial film, which is then pyrolized, on the surface of the media.

Studies of polymer-salt compositions (PSC) revealed a phenomenon that can significantly affect the results of the oxide material synthesis, the effect of thermochemical precursor charge generation [209]. Initially, this phenomenon was explored in polymer-saline, primarily PVA-based films by heating them below the initial combustion temperature [209, 210]. A clear demonstration of charges in the films which were homoelectrets in that case, i.e. the two of their sides had the charge of the same polarity, represented an experiment where two samples were suspended parallel to each other and repulsed mutually and intensely, along with their deformation (bend), when heated. Placing the film between two electrodes which created a DC electric field, they managed to identify the film polarities which could vary depending on the composition. The measurement of potentials generated in the films gave a rather substantial charge density, around $1.7 \cdot 10^{-6}$ C/cm^2. The charges existed steadily in the samples. During polarization by constant field based on salt-doped PVA films, they produced chemoheteroelectrets. The origin of charges can be attributed to a number of reasons. One of the main reasons is, in particular, the possibility of emission of volatile substances from the film by heating, which are composed of charged particles able to carry off the electrons or, on the contrary, have a positive charge by transferring an electron to the film. Such particles may be considered to be the ammonium molecules if the films include any salts of ammonium, water, $H_2O(-)$, nitrogen oxide ($NO+$), carbon dioxide, etc. Inter alia, the possibility of formation of particles with the "sticking" $CO_3(-)$ electron cannot be ruled out [210, 211]. Therefore, the film charge depends on the nature of the outbound charged particles in each case, as the charge polarity may change during heating.

The emergence of charges is facilitated by the fact that when the films are heated, some ions included in the film structure, as noted above, tend to change its oxidation state. In particular, a number of ions tend to be recovered by interaction with organic components (copper ions), while another to be oxidized by reactions with nitrates. Consequently, the charge polarity can be determined by the predominantly occurring redox processes and Red/Ox potentials. Moreover, there is a possibility of such a phenomenon as mechanic electron emission out of polymeric materials [210, 211] with decreased electron liberation, the tunneling phenomena are known to occur in these materials. When heated, the polymer saline films, as shown in [150, 196], undergo significant changes, sometimes alternating, in their geometry, which can lead in particular to mechanical stresses.

We give the charge polarities in some films as an example. In particular, positive charges are formed in the PVA ammonium heptamolybdate-containing compositions, the negative are formed in the copper nitrate compositions [210]. The negative charge was observed in nitrate-polymer precursors intended for synthesis of superconducting $YBa_2Cu_3O_{7-\delta}$. When the formates of the respective metals were used as the salt constituents of this system, the initial positive charge was then changed to negative. In most cases, the most intensive process of film charge formation was temperature-correlated with maximum emission of gaseous compounds revealed during gravimetric analysis of the samples. The assessment showed that the measured film charges can emerge if a single elementary charge is generated upon removal of about 230,000 molecules out of the film to the gaseous environment. The charge-filling density of conditional traps per a space charge at specific film weight of 1.4 g/cm^3, according to the estimation, reaches the values of about $2 \cdot 10^{15}$ charges per cubic centimeter, i.e., approaches the limit values for certain polymeric film materials [211].

It is important that the newly formed charges are preserved on the oxide nanoparticles emerged after PSC pyrolysis at higher temperatures. Thus, during the synthesis of the samarium-doped cerium oxide, $Ce_{1-x}Sm_xO_{2-d}$, there is a negative potential of about 400 V at the stage of solvent removal from the polymer-nitrate aqueous solutions by heating in a porcelain cup. After the composition combustion, the powder product produced had a negative charge and potential of about 200 V with respect to ground. The eponymous charges of the particles lead to their mutual repulsion. Depending on the magnitude of the particle charge, the combustion process forms the materials in which the aggregation is implemented to different extents, which greatly affects their ability to be sintered, in particular, the temperature interval of intensive powder sintering when producing ceramics. In the case of maximum charges, there are powders produced with minimal contact between the particles, large excess surface energy values, and accordingly, enhanced sintering behavior. In the case of lower charges, the excess surface energy is partly consumed during combustion, which leads to more close contacts, ensuring further existence of ensembles of particles which are more resistant to sintering. It helps control the properties of the resulting powders [212].

4. Oxide material production by SCS

The application of the above-described SCS method allows producing oxide nanomaterials both as nanopowders and nanocrystalline coatings on a variety of media, as well as controlling the properties of materials. Since the previous section addressed the occurrence of charges in precursors, we should comment on the ability to control the properties of materials using this phenomenon. There are ratios of organic components and nitrates which correspond to the most intensive SCS flow and the maximum thermal generation during the reaction (see, for example [94, 96, 112, 118, 213]). However, more significant charge accumulation was observed in compositions containing a substantial excess of the organic component. The combination of these factors leads to the fact that, in the first case, the synthesis leads to closely contacted ensembles of particles which are more resistant to sintering. In the second case, there are spot-contacted ensembles which are more prone to sintering at lower temperatures. This approach to control the powder properties is useful, for example, in producing solid-oxide fuel cells or electrochemical oxygen sources [214] when single-cycle sintering of the oxygen-conducting membrane with electrodes is economically and technically feasible. This requires, in particular, synchronizing the run of sintering temperature curves for different materials, for instance, for the strontium-doped lanthanum manganite and yttrium oxide-stabilized zirconium dioxide (YSZ). When using a similar material as a component of the applied catalytic systems, this, by contrast, requires providing greater resistance to sintering and preserving a specific surface area. It should be noted that the specific surface of the SCS-produced initial powders, however, differs slightly with different degree of particle contacts.

It should be noted that it is possible to generate oxides with variously sized crystallites by incrementally increasing the thermal treatment temperature of the SCS-produced powders [94–99, 130, 161]. As SCS oxide nanoparticles are prone to aggregation, their structure and dimensions should be studied by a complex of methods [215]. The studies in [157, 158, 161, 162, 169, 197, 198, 212, 216] showed the necessity to use such methods as the x-ray diffraction, line broadening analysis, small-angle x-ray and neutron scattering, transmission electron microscopy, low-temperature gas adsorption curve analysis, etc.

One of the features of oxide material synthesis from organic-inorganic compositions is that the main or a substantial material portion formed in the combustion can be amorphous [95, 96, 98, 99, 126, 169, 197, 198]. This, in particular, results in the possibility to significantly reduce the temperature of additional thermal treatment for final production. The transition from the amorphous to the crystalline superfine state can lead to formation of globular particles with a well-developed, including fractal, surface [130, 159, 169, 197, 198]. Generally, the increased firing temperature leads to a smoothed surface of the particles [157–159, 161, 169, 197, 198]. At the time of crystallization, some of the material, as shown in [157–159, 169, 197, 198] represents a combination of one- or two-dimensional formations, to which the concept of specific surface area is just conditionally applicable. Experimental measurements of the specific surface by sorption methods can give rather high values in these cases [157–161, 169, 197, 198]. Thus, the specific surface and fractal structure maxima can be incompatible, and the different structures of particles can be realized at the same value of the specific surface. For example, small globular particles with a smoother surface or greater ones, but with non-smooth boundary, can be formed. The latter may be preferable for use as catalysts, in particular with respect to the active center distribution and energetics. This should be considered when choosing conditions for the synthesis of catalysts and oxide materials of a different functional purpose.

The results of examining the possibilities and causes of impurity phases in oxide systems in the SCS processes bear interest in practical terms. We should note here that these impurity phases do not interfere with the successful use of materials in many cases [126, 130, 158, 160, 165, 169, 201, 212], although it is sometimes necessary to make the material be single-phase [94, 96, 99, 106, 107, 112, 118, 159, 169]. Heterogeneous solid-phase systems are used in catalysis where the impurity phases often play the role of promoters and co-catalysts, as in the silver-inclusive lanthanum manganites [126, 130, 158, 160]. In the superconducting materials, a newly formed impurity can serve as a pinning center [169]. The possibilities of impurity emergence may be divided at least into two stages [169, 217] in accordance with the steps of precursor production and combustion. In the first step, the formation of impurities (solutions) may be contributed by the relatively low solubility of specific salts, their formation of low-soluble compounds with other components, and hydrolysis of some compounds resulting in hydroxides. The latter applies, for example, to salts of transition metals, particularly iron, in cases where the acidity of solutions is insufficient. Against the background of organic-inorganic compositions, the newly formed hydroxides are sometimes difficult to see visually, however, their formation may be irreversible after aging of precipitations, which leads to broken homogeneity of the precursors.

At the stage of combustion, the formation of impurity phases is also possible due to the fact that different gas environment appears in SCS, depending on the precursor composition, as noted above. In terms of the reducing environment, some metal components are capable, as ions, of reducing up to the formation of impurity phases which include low-valent metals [130, 150, 151, 165, 169, 202, 217]. Such facts were recorded during the synthesis, although they were not always paid adequate attention. As an example, when producing ferrites, cobaltites, manganites with ABO_3 (A stands for rare - earth and alkaline-earth elements, B stands for transition metal ions) perovskite structure, the impurity phases are often found [130, 158, 169, 217], in particular, show that during the synthesis, the amount of the impurity phase depends on the component φ-ratio (PVA – nitrate). The distribution of impurities in the material produced can have a significant effect on its functional properties. In most cases, the optimal is the existence of nanoscale impurities as uniformly distributed in the main phase environment. By choosing the appropriate synthesis conditions in [130], it was managed to achieve, in particular, this distribution of silver nanoparticles in the doped lanthanum manganite.

There are interesting attempts to purposefully influence the texture of the resulting SCS oxide materials. Thus, in [155,169], the synthesis was carried out in a magnetic field of the magnetic oxide phases with magnetoplumbite-type structure based on lanthanum and cobalt-doped strontium hexaferrite, $Sr_{1-x}La_xFe_{12-x}\ Co_xO_{19}$. As a result, they managed to increase the coercive material force, although they failed to significantly affect the magnitude of the residual specific magnetization. [155, 169] showed the influence of the synthesis environment on coercive force of the magnets, which was increased during SCS in a reducing environment due to the generation of defects resulting from iron reduction to Fe^{2+}.

In SCS production of oxide materials as catalytic coatings, they observed another variant of impurity phase formation which occurred due to interaction between the active nanosized catalyst particles and the intermediate carrier [212]. In particular, the formation of aluminum-manganese spinel of several nanometers thick, as found in [212], showed a marked promoter-wise effect in relation to the system which included aluminum oxide and perovskite. The effect was observed in oxidizing catalytic reactions of carbon monoxide and organic compounds, reduction of nitrogen oxides in a gaseous environment.

5. Environmental aspects of the SCS implementation

As shown in [112,118] and demonstrated in Fig. 21, an appreciable amount of carbon monoxide and nitrogen oxides may be released during SCS. To solve the problem of environmental protection, as it turned out, the nanostructured catalysts deposited on nickel foam with an aluminum oxide sublayer serve the purpose, as well as doped lanthanum manganites produced by SCS [130, 158, 160, 202, 212]. Even with a volley emission of nitrogen oxides and carbon monoxide during the pyrolysis of original compositions, the devices based on these catalysts can successfully cope with the purification of gases [130, 157, 158, 160, 202, 212]. This is facilitated by both CO and NOx available in the waste gases, which are catalytically converted into CO_2 and N_2 in the hot pyrolytic gases.

Rapidly flowing SCS processes can be accompanied by significant emission of dust particles from the reaction zone. Taking into account the charges on the particles, the use of electrostatic precipitators is possible to trap the particles and their aggregates. Moreover, in some cases, additional ionization of the trapped particles is not required, and the process is implemented due to their own charge.

Acknowledgments

The authors thank sincerely their colleagues with whom they carried out this joint research, the results of which have been reflected in the review. A significant piece of work was performed with financial support within the State Assignment of the Ministry of Education and Science of the Russian Federation (Project No. 4.6653.2017/BP) and the Ural Federal University Competitiveness Program (Project Code 14.594.21.0011).

References

[1] Knurova M.V., Mittova I.Ya., Perov N.S., Al'myasheva O.V., Tien N.A., Mittova V.O., Bessalova V.V., Viryutina E.L. Effect of the degree of doping on the size and magnetic properties of nanocrystals $La_{1-x}Zn_xFeO_3$ synthesized by the sol–gel method. *Russ. J. Inorg. Chem.*, 2017, **62**(3), P. 281–287.

[2] Tien N.A., Mittova I.Ya., Solodukhin D.O., Al'myasheva O.V., Mittova V.O., Demidova S.Yu. Sol–gel formation and properties of nanocrystals of solid solutions $Y_{1-x}Ca_xFeO_3$. *Russ. J. Inorg. Chem.*, 2014, **59**(2), P. 40–45.

[3] Tac D.V., Mittova V.O., Almjasheva O.V., Mittova I.Ya. Synthesis, structure, and magnetic properties of nanocrystalline $Y_{3-x}\ La_x\ Fe_5O_{12}(0 \leq x \leq 0.6)$. *Inorgan. Mater.*, 2012, **48**(1), P. 74–78.

[4] Tac D.V., Mittova V.O., Almjasheva O.V., Mittova I.Ya. Synthesis and magnetic properties of nanocrystalline $Y_{1-x}Cd_xFeO_{3-\delta}$ $(0 \leq x \leq 0.2)$. *Inorgan. Mater.*, 2011, **47**(10), P. 1141–1146.

[5] Tien N.A., Mittova I.Ya., Al'myasheva O.V. Influence of the synthesis conditions on the particle size and morphology of yttrium orthoferrite obtained from aqueous solutions. *Russ. J. Appl. Chem.*, 2009, **82**(11), P. 1915–1918.

[6] Chen L., He B.-Y., He S., Wang T.-J., Su C.-L., Jin Y. Fe-Ti oxide nano-adsorbent synthesized by co-precipitation for fluoride removal from drinking water and its adsorption mechanism. *Powder Technology*, 2012, **227**, P. 3–8.

[7] Kolen'ko Y.V., Maksimov V.D., Garshev A.V., Mukhanov V.A., Oleynikov N.N., Churagulov B.R. Physicochemical properties of nanocrystalline zirconia hydrothermally synthesized from zirconyl chloride and zirconyl nitrate aqueous solutions. *Russ. J. Inorg. Chem.*, 2004, **49**(8), P. 1133–1137.

[8] Almamoun O., Ma S.Y. Effect of Mn doping on the structural, morphological and optical properties of SnO_2 nanoparticles prepared by sol-gel method. *Mater. Lett.*, 2017, **199**, P. 172–175.

[9] Mahdavi R., Talesh S.S.A. The effect of ultrasonic irradiation on the structure, morphology and photocatalytic performance of ZnO nanoparticles by sol-gel method. *Ultrasonics Sonochemistry*, 2017, **39**, P. 504–510.

[10] Vasilevskaya A.K., Almjasheva O.V., Gusarov V.V. Formation of nanocrystals in the ZrO_2–H_2O system. *Russ. J. Gen. Chem.*, 2015, **85**(12), P. 2673–2676.

[11] Sharipov Kh.B., Yapryntsev A.D., Baranchikov A.E., Boytsova O.V., Kurzeev S.A., Ivanova O.S., Borilo L.P., Gil'mutdinov F.Z., Kozik V.V., Ivanov V.K. Synthesis of manganese dioxide by homogeneous hydrolysis in the presence of melamine. *Russ. J. Inorg. Chem.*, 2017, **62**(2), P. 139–149.

[12] Zhang M., An T., Liu X., Hu X., Fu J. Preparation of a high-activity ZnO/TiO_2 photocatalyst via homogeneous hydrolysis method with low temperature crystallization. *Materials Letters*, 2010, **64**(17), P. 1883–1886.

[13] Sadrieyeh S., Malekfar R. The effects of hydrolysis level on structural properties of titania aerogels. *J. Non-Crystall. Solids*, 2017, **457**, P. 175–179.

[14] Pechini M.P. Method of preparing lead and alkaline earth titanates and niobates and coating method using the same to form a capacitor. US 3330697 A. Filed Aug. 26, 1963, Ser. N 304, 437 Ckaims July 11, 1967.

[15] Abiev R.S., Almyasheva O.V., Gusarov V.V., Izotova S.G. Method of producing nanopowder of cobalt ferrite and microreactor to this end. Patent for invention N RU 2625981 C1. Date of publication: 20.07.2017 Bull. N 20. Effective date for property rights: 16.09.2016.

[16] Zhabrev V.A., Efimenko L.P., Baryshnikov V.G., Polyakova I.G., Gumennikov A.V. Synthesis of $BaTiO_3$ Powders of Different Dispersities by the Exchange Reactions in Molten Salts. *Glass Physics and Chemistry*, 2008, **34**(1), P. 91–96.

[17] Khokhlov V.A., Dokutovich V.N., Modenov D.V., Kochedykov V.A., Zakir'janova I.D., Korzun I.V., Nikolaeva E.V. Method of producing nanosize particles of complex metal oxides. RU 2461668 C1. Date of filing: 16.03.2011. Date of publication 20.09.2012. Bull. 26.

[18] Zhou H., Mao Y., Wong S.S. Probing Structure-Parameter Correlations in the Molten Salt Synthesis of $BaZrO_3$ Perovskite Submicrometer-Sized Particles. *Chem. Mater*, 2007, **19**, P. 5238–5249.

[19] Han P., Jiang X. Regulation on the synthesis temperature and optical properties of $SmBO_3$ prepared by chloride fluxes assisted the solid state reaction method. *Advanced Powder Technology*, 2015, **26**(3), P. 977–982.

[20] Morozov M.I., Lomanova N.A., Gusarov V.V. Specific features of $BiFeO_3$ formation in a mixture of bismuth(III) and iron(III) oxides. *Russ. J. Gen. Chem.*, 2003, **73**(11), P. 1676–1680.

[21] Bingbing Liu, Yuanbo Zhang, Zijian Su, Manman Lu, Zhiwei Peng, Guanghui Li, Tao Jiang Formation mechanism of $Mn_xFe_{3-x}O_4$ by solid-state reaction of MnO_2 and Fe_2O_3 in air atmosphere: Morphologies and properties evolution. *Powder Technology*, 2017, **313**, P. 201–209.

[22] Morozov M.I., Mezentseva L.P., Gusarov V.V. Mechanism of formation of $Bi_4Ti_3O_{12}$. *Russ. J. Gen. Chem.*, 2002, **72**(7), P. 1038–1040.

[23] Morozov M.I., Gusarov V.V. Synthesis of $A_{m-1}Bi_2M_mO_{3m+3}$ compounds in the $Bi_4Ti_3O_{12}$-$BiFeO_3$ system. *Inorganic Materials*, 2002, **38**(7), P. 723–729.

[24] Mikhailov M.M., Vlasov V.A., Utebekov T.A., Sokolovskiy A.N., Lovizkii A.A., Smolin A.E. Solid-state synthesis of $LaSrMnO_3$ powders for smart coatings. *Mater. Research Bull.*, 2017, **89**, P. 154–160.10.1016/j.materresbull.2017.01.038)

[25] Belkova T.B., Kostikov Yu.P., Neiman A.Ya. Solid-State Reactions of Bismuth Oxide with Transition-Metal Oxides (Cr_2O_3, Mn_2O_3, Co_3O_4). *Russ. J. Inorg. Chem.*, 1999, **44**(2), P. 161–166.

[26] Gusarov V.V., Suvorov S.A. Autocatalytic solid-phase reaction. *J. Appl. Chem. USSR*. 1987, 60(12), P. 1805–1808.

[27] Gusarov V.V., Suvorov S.A. Autocatalytic solid-phase reaction of chrysoberyl formation. *Zhurnal Obshchei Khimii*, 1988, **58**(4), P. 932–934. (in Russian)

[28] Gusarov V.V. Fast Solid-Phase Chemical Reactions. *Russ. J. Gen. Chem.*, 1997, **67**(12), P. 1846–1851.

[29] Gusarov V.V., Ishutina Z.N., Malkov A.A., Malygin A.A. Peculiarities of the solid-phase chemical reaction in formation of mullite in the nanosize film composition. *Doklady Akademii Nauk*, 1997, **357**(2), P. 203–205. (in Russian)

[30] Smirnova Z.N., Gusarov V.V., Malkov A.A., Firsanova T.V., Malygin A.A., Suvorov S.A. High-speed synthesis of mullite. *Zhurnal Obshchei Khimii*, 1995, **65**(2), P. 199–204. (in Russian)

[31] Gusarov V.V., Malkov A.A., Malygin A.A., Suvorov S.A. Generation of aluminum titanate in compositions with high-level of space and structural conjugation of components. *Zhurnal Obshchei Khimii*, 1994, **64**(4), P. 554–557. (in Russian)

[32] Gusarov V.V., Malkov A.A., Ishutina Z.N., Malygin A.A. Phase formation in a nanosize silicon oxide film on the surface of aluminum oxide. *Technical Physics Letters*, 1998, **24**(1), P. 3–8.

[33] Fedorov N.F., Samonin V.V., Kruglikova I.V. Thermal decomposition of some hydroxides in metal melts. *Russ. J. Appl. Chem.*, 1997, **70**(2), P. 323–325.

[34] Kiselev E.A., Cherepanov V.A., Proskurnina N.V., Voronin V.I. Phase equilibria and crystal structures of phases in the La-Fe-Ni-O system at 1370 K in air. *Inorgan. Mater*, 2007, **43**(2), P. 167–175.

[35] Bannikov D.O., Cherepanov V.A. Thermodynamical Stability of the Nickel-Lanthanum Complex Oxides. *Z. Anorg. Allg. Chem.*, 2002, **628**, P. 2180–2182.

[36] Kiselev E.A., Cherepanov V.A. P(O_2)-stability of $LaFe_{1-x}Ni_xO_{3-\delta}$ solid solutions at 1100°C. *J. Solid State Chem.*, 2010, **183**(9), P. 1992–1997.

[37] Lu J., Qiao L.J., Fu P.Z., Wu Y.C. Phase equilibrium of Bi_2O_3-Fe_2O_3 pseudo-binary system and growth of $BiFeO_3$ single crystal. *J. Cryst. Growth.*, 2011, **318**, P. 936–941.

[38] Valant M., Axelsson A.-M., Alford N. Peculiarities of a solid-state synthesis of multiferroic polycrystalline $BiFeO_3$. *Chem. Mater.*, 2007, **19**, P. 5431–5436.

[39] Selbach S.M., Einarsrud M.-A., Grande T. On the thermodynamic stability of $BiFeO_3$. *Chem. Mater.*, 2009, **21**, P. 169–173.

[40] Almjashev O.V., Gusarov V.V. Effect of ZrO_2 nanocrystals on the stabilization of the amorphous state of alumina and silica in the ZrO_2-Al_2O_3 and ZrO_2-SiO_2 systems. *Glass Phys. Chem.*, 2006, **32**(2), P. 162–166.

[41] Al'myashev O.V., Gusarov V.V. Features of the phase formation in the nanocomposites. *Russ. J. Gen. Chem.*, 2010, **80**(3), P. 385–390.

[42] Al'myasheva O.V., Gusarov V.V. Nucleation in media in which nanoparticles of another phase are distributed. *Doklady Physical Chemistry*, 2009, **424**(2), P. 43–45.

[43] Boldyrev V.V. Mechanochemistry and mechanical activation of solids. *Russ. Chem. Rev.*, 2006, **75**(3), P. 177–189. 10.1070/RC2006v075n03ABEH001205)

[44] Kalinkin A.M., Balyakin K.V., Nevedomskii V.N., Kalinkina E.V. Solid-state synthesis of nanocrystalline strontium zirconate assisted by mechanical activation. *Russ. J. Gen. Chem.*, 2016, **86**(4), P. 785–791.

[45] Maurya D., Thota H., Nalwa K.S., Garg A. $BiFeO_3$ ceramics synthesized by mechanical activation assisted versus conventional solid-state-reaction process: A comparative study. *J. Alloys Compd.*, 2009, **477**, P. 780–784.

[46] Urakaev F.Kh. Mechanochemical synthesis of nanoparticles by a dilution method: optimization of the composition of a powder mixture. *Mendeleev Communications*. 2011, **21**(5), P. 266–269.

[47] Liu W., Wang Q., Zhang J., Xie X., Xia B. Isothermal kinetic analysis of the effects of high-energy ball milling on solid-state reaction of $Li_4Ti_5O_{12}$. *Powder Technology*, 2016, **287**, P. 373–379.

[48] Clarke T.J., Davies T.E., Kondrat S.A., Taylor S.H. Mechanochemical synthesis of copper manganese oxide for the ambient temperature oxidation of carbon monoxide. *Applied Catalysis B: Environmental*, 2015, **165**, P. 222–231.

[49] Maghsoudlou M.S.A., Ebadzadeh T., Sharafi Z., Arabi M., Zahabi K.R. Synthesis and sintering of nano-sized forsterite prepared by short mechanochemical activation process. *J. Alloys Compd.*, 2016, **678**, P. 290–296.

[50] Pavel O.D., Zăvoianu R., Bîrjega R., Angelescu E., Pârvulescu V.I. Mechanochemical versus co-precipitated synthesized lanthanum-doped layered materials for olefinoxidation. *Applied Catalysis A: General*, 2017, **542**, P. 10–20.

[51] Livage J. Vanadium pentoxide gels. *Chem. Mater.*, 1991, **3**(4), P. 578.

[52] Kumar M., Srikantha S., Ravikumar B., Alex T.C, Das S.K. Synthesis of pure and Sr-doped $LaGaO_3$, $LaFeO_3$ and $LaCoO_3$ and Sr, Mg-doped $LaGaO_3$ for ITSOFC application using different wet chemical routes. *Mater. Chem. Phys.*, 2009, **113**, P. 803–815.

[53] Agafonov A.V., Afanas'ev D.A., Borilo L.P., Kraev A.S., Gerasimova T.V. Synthesis of nanostructured iron titanates by soft chemistry methods. *Russ. J. Inorg. Chem.*, 2016, **61**(5), P. 560–566.

[54] Li Y., Xu S. Hydrothermal synthesis of lanthanide (hydr)oxide micro/nanorods in presence of tetrabutylammonium hydroxide. *J. Rare Earths*, 2016, **34**(6), P. 618–625.

[55] Bugrov A.N., Rodionov I.A., Zvereva I.A., Smyslov R.Yu., Almjasheva O.V. Photocatalytic activity and luminescent properties of Y, Eu, Tb, Sm and Er-doped ZrO_2 nanoparticles obtained by hydrothermal method. *Int. J. Nanotechnology*, 2016, **13**(1/2/3), P. 147–157.

[56] Yu J., Tian N., Deng Y.F., Zhang H.H. Ultraviolet photodetector based on sol–gel synthesized MgZnO nanoparticle with photoconductive gain. *J. Alloys Compd.*, 2016, **667**, P. 359–362.

[57] Salavati-Niasari M., Soofivand F., Sobhani-Nasab A., Shakouri-Arani M., Bagheri S. Synthesis, characterization, and morphological control of $ZnTiO_3$ nanoparticles through sol–gel processesand its photocatalyst application. *Adv. Pow. Tech.*, 2016, **27**(5), P. 2066–2075.

[58] Nguyen A.T., Phan Ph.H.Nh., Mittova I.Ya., Knurova M.V., Mittova V.O. The characterization of nanosized $ZnFe_2O_4$ material prepared by coprecipitation. *Nanosystems: Physics, Chemistry, Mathematics*, 2016, **7**(3), P. 459–463.

[59] Tretyakov Yu.D., Shlyakhtin O.A. Recent progress in cryochemical synthesis of oxide materials. *J. Mater. Chem.*, 1999, **9**(1), P. 19–24.

[60] Tretyakov Yu.D., Oleynikov N.N., Shlyakhtin O.A. *Cryochemical Technology of Advanced Materials*. London: Chapman & Hall, 1997. 319 p.

[61] Brylev O.A., Shlyakhtin O.A., Egorov A.V., Tretyakov Yu.D. Phase formation and electrochemical properties of cryochemically processed $Li_{1+x}V_3O_8$ materials. *J. Power Sources*, 2007, **164**(2), P. 868–873.

[62] Byrappa K., Yoshimura M. *Handbook of Hydrothermal Technology*. Published in the United States of America by Noyes Publications. 2001. NY.

[63] Suchanek W.L., Riman R.E. Hydrothermal Synthesis of Advanced Ceramic Powders. *Advances in Science and Technology*, 2006, **45**, P. 184–193.

[64] Pyda W., Haberko K., Bucko M.M. Hydrothermal crystallization of zirconia and zironia solid solutions. *J. Am. Ceram. Soc.*, 1991, **74**(10), P. 2622–2629.

[65] Somiya S., Akiba T. Hydrothermal zirconia powders: a bibliography. *J. Europ. Ceram. Soc.*, 1999, **19**, P. 81–87.

[66] Pozhidaeva O.V., Korytkova E.N., Drozdova I.A., Gusarov V.V. Phase state and particle size of ultradispersed zirconium dioxide as influenced by condition of hydrothermal synthesis. *Russ. J. Gen. Chem.*, 1999, **69**(8), P. 1219–1222.

[67] Meskin P.E., Baranchikov A.E., Ivanov V.K., Afanas'ev D.R., Gavrilov A.I., Churagulov B.R., Oleinikov N.N. Ultrasonically activated hydrothermal synthesis of fine TiO_2 and ZrO_2 powders. *Inorg. Mater.*, 2004, **40**(10), P. 1208–1215.

[68] Al'myasheva O.V., Korytkova E.N., Maslov A.V., Gusarov V.V. Preparation of nanocrystalline alumina under hydrothermal conditions. *Inorg. Mater.*, 2005, **41**(5), P. 540–547.

[69] Kimel R.A., Adair J.H. Aqueous synthesis at 200°C of sub-10 nanometer yttria tetragonally stabilized zirconia using a metal-ligand approach. *J. Am. Ceram. Soc.*, 2005, **88**(5), P. 1133–1138.

[70] Li J., Luo S., Ding X., Wang Q., He P. Hydrothermal synthesis of $LiAlO_2$ nanostructures with high specific surface area by using anodized aluminum oxide template. *Materials Letters*, 2017, **196**, P. 183–186.

[71] Meskin P.E., Ivanov V.K., Baranchicov A.E., Churagulov B.R., Tretyakov Yu.D. Ultrasonically assisted hydrothermal synthesis of nanocrystalline ZrO_2, TiO_2, $NiFe_2O_4$ and $Ni_{0.5}Zn_{0.5}Fe_2O_4$ powders. *Ultrasonis Sonochemistry*, 2006, **13**, P. 47–53.

[72] Zhu H., Yang D., Xi Z., Zhu L. Hydrothermal synthesis and characterization of zirconia nanocristallites. *J. Am. Ceram. Soc*, 2007, **90**(4), P. 1334–1338.

[73] Almjasheva O.V., Gusarov V.V. Hydrothermal synthesis of nanosized and amorphous alumina in the ZrO_2-Al_2O_3-H_2O system. *Russ. J. Inorg. Chem.*, 2007, **52**(8), P. 1194–1200.

[74] Korytkova E.N., Pivovarova L.N., Semenova O.E., Drozdova I.A., Povinich V.F., Gusarov V.V. Hydrothermal synthesis of nanotubular Mg-Fe hydrosilicate. *Russ. J. Inorg. Chem.*, 2007, **52**(3), P. 338–344.

[75] Kuklo L.I., Tolstoy V.P. Successive ionic layer deposition of $Fe_3O_4@H_xMoO_4 \cdot nH_2O$ composite nanolayers and their superparamagnetic properties. *Nanosystems: Physics, Chemistry, Mathematics*, 2016, **7**(6), P. 1050–1054.

[76] Kuznetsova V.A., Almjasheva O.V., Gusarov V.V. Influence of microwave and ultrasonic treatment on the formation of $CoFe_2O_4$ under hydrothermal conditions. *Glass Phys. Chem.*, 2009, **35**(2), P. 205–209.

[77] Anikeev V.I. Hydrothermal synthesis of metal oxide nano- and microparticles in supercritical water. *Russ. J. Phys. Chem.*, 2011, **85**(3), P. 377–382.

[78] Gavrilov A.I., Kapitanova O.O., Baranov A.N., Churagulov B.R. Specifics of hydrothermal synthesis of oriented zinc oxide nanorods on metallic zinc substrates. *Russ. J. Inorg. Chem.*, 2012, **57**(9), P. 1182–1186.

[79] Phuruangrat A., Thongtem S., Thongtem T. Microwave-assisted hydrothermal synthesis and characterization of CeO_2 nanowires for using as a photocatalytic material. *Materials Letters*, 2017, **196**, P. 61–63.

[80] Cheng W., Xu X., Wu F., Li J. Synthesis of cavity-containing iron oxide nanoparticles by hydrothermal treatment of colloidal dispersion. *Materials Letters*, 2016, **164**, P. 210–212.

[81] Popkov V.I., Almjasheva O.V. Formation mechanism of $YFeO_3$ nanoparticles under the hydrothermal condition. *Nanosystems: Physics, Chemistry, Mathematics*, 2014, **5**(5), P. 703–708.

[82] Bugrov A.N., Almjasheva O.V. Effect of hydrothermal synthesis conditions on the morphology of ZrO_2 nanoparticles. *Nanosystems: Physics, Chemistry, Mathematics*, 2013, **4**(6), P. 810–815.

[83] Almjasheva O.V. Formation and structural transformations of nanoparticles in the TiO_2–H_2O system. *Nanosystems: Physics, Chemistry, Mathematics*, 2016, **7**(6), P. 1031–1049.

[84] Almjasheva O.V., Garabadzhiu A.V., Kozina Yu.V., Litvinchuk L.F., Dobritsa V.P. Biological effect of zirconium dioxide-based nanoparticles. *Nanosystems: Physics, Chemistry, Mathematics*, 2017, **8**(3), P. 391–396.

[85] Simonenko N.P., Nikolaev V.A., Simonenko E.P., Generalova N.B., Sevastyanov V.G., Kuznetsov N.T. Preparation of nanostructured titania thin films by sol–gel technology. *Russ. J. Inorg. Chem.*, 2016, **61**(12), P. 1505–1511.

[86] Chick L.A., Pederson L.R., Maupin G.D., Bates J.L., Thomas L.E., Exarhos G.J. Glycine-nitrate combustion synthesis of oxide ceramic powders. *Mater. Lett.*, 1990, **10**(1-2), P. 6–12.

[87] Aruna S.T. Solution combustion synthesis. *Concise Encyclopedia of Self-Propagating High-Temperature Synthesis*, 2017, P. 344–346.

[88] Merzhanov A.G., Borovinskaya I.P. Self-Propagating High-Temperature Synthesis of Refractory Inorganic Compounds. *Dokl. Akad. Nauk SSSR*, 1972, **204**, P. 429–432.

[89] Rogachev A.S., Varma A., Merzhanov A.G. The mechanism of self-propagating high-temperature synthesis of nickel aluminides. Pt. 1. Formation of the product microstructure in a combustion wave. *Int. J. SHS*, 1993, **2**(1), P. 25–38.

[90] Merzhanov A.G. SHS Process: Combustion Theory and Practice. *Archivum Combustionis*, 1981, **1**, P. 23–48.

[91] Merzhanov A.G. Theory and Practice of SHS: Worldwide State of the Art and the Newest Results. *Int. J. SHS*, 1993, **2**(2), P. 113–158.

[92] Tret'yakov Yu.D. Self-organisation processes in the chemistry of materials. *Russ. Chem. Reviews*, 2003, **72**(8), P. 651–679.

[93] Tugova E., Yastrebov S., Karpov O., Smith R. $NdFeO_3$ nanocrystals under glycine nitrate combustion formation. *J. Crystal Growth*, 2017, **467**, P. 88–92.

[94] Popkov V.I., Almjasheva O.V. Yttrium orthoferrite $YFeO_3$ nanopowders formation under glycine-nitrate combustion conditions. *Russ. J. Appl. Chem.*, 2014, **87**(2), P. 167–171.

[95] Popkov V.I., Almjasheva O.V., Gusarov V.V. The investigation of the structure control possibility of nanocrystalline yttrium orthoferrite in its synthesis from amorphous powders. *Russ. J. Appl. Chem.*, 2014, **87**(10), P. 1417–1421.

[96] Popkov V.I., Almjasheva O.V., Nevedomskiy V.N., V.V. Sokolov V.V., Gusarov V.V. Crystallization behaviour and morphological features of $YFeO_3$ nanocrystallites obtained by glycine-nitrate combustion. *Nanosystems: Physics, Chemistry, Mathematics*, 2015, **6**(6), P. 866–874.

[97] Popkov V.I., Almjasheva O.V., Schmidt M.P., Izotova S.G., Gusarov V.V. Features of nanosized $YFeO_3$ formation under heat treatment of glycine–nitrate combustion products. *Russ. J. Inorg. Chem.*, 2015, **60**(10), P. 1193–1198.

[98] Popkov V.I., Almjasheva O.V., Panchuk V.V., Semenov V.G., Gusarov V.V. The Role of pre-nucleus states in formation of nanocrystalline yttrium orthoferrite. *Doklady Chemistry*, 2016, **471**(2), P. 356–359.

[99] Lomanova N.A., Tomkovich M.V., Sokolov V.V., Gusarov V.V. Special Features of Formation of Nanocrystalline $BiFeO_3$ via the Glycine-Nitrate Combustion Method. *Russ. J. Gen. Chem.*, 2016, **86**(10), P. 2256–2262.

[100] Shravana Kumara K.N., Nagaswarupa H.P., Vishnu Mahesh K.R., Prashantha S.C., Mylarappa M., Siddeshwara D.M.K. Synthesis and characterization of nano ZnO and MgO powder by low temperature solution combustion method: studies concerning electrochemical and photocatalytic behavior. *Nanosystems: Physics, Chemistry, Mathematics*, 2016, **7**(4), P. 662–666.

[101] Rubalajyothi P., Nehru L.C. Photoluminescence characteristics of nanocrystalline $Ba_{0.97}Ca_{0.03}SO_4$:Eu by combustion method. *Nanosystems: Physics, Chemistry, Mathematics*, 2016, **7**(3), P. 561–564.

[102] Chen Y., Yang J., Wang X., Feng F., Zhang Y., Tang Y. Synthesis $YFeO_3$ by salt-assisted solution combustion method and its photocatalytic activity. *J. Ceram. Soc. Japan.*, 2014, **122**(2), P. 146–150.

[103] Wu L., Yu J.C., Zhang L., Wang X., Li S. Selective self-propagating combustion synthesis of hexagonal and orthorhombic nanocrystalline yttrium iron oxide. *J. Solid State Chem.*, 2004, **177**(10), P. 3666–3674.

[104] Komlev A.A., Vilezhaninov E.F. Glycine-nitrate combustion synthesis of nanopowders based on nonstoichiometric magnesium-aluminum spinel. *Russ. J. Appl. Chem.*, 2013, **86**(9), P. 1373–1380.

[105] Komlev A.A., Gusarov V.V. Glycine-nitrate combustion synthesis of nonstoichiometric Mg-Fe spinel nanopowders. *Inorg. Mater.*, 2014, **50**(12), P. 1247–1251.

[106] Zaboeva E.A., Izotova S.G., Popkov V.I. Glycine-nitrate combustion synthesis of $CeFeO_3$-based nanocrystalline powders. *Russ. J. Appl. Chem.*, 2016, **89**(8), P. 1228–1236.

[107] Layek S., Verma H.C. Magnetic and dielectric properties of multiferroic $BiFeO_3$ nanoparticles synthesized by a novel citrate combustion method. *Adv. Mat. Lett.* 2012, **3**(6), P. 533–538.

[108] Zhuravlev V.D., Bamburov V.G., Beketov A.R., Perelyaeva L.A., Baklanova I.V., Sivtsova O.V., Vasil'ev V.G., Vladimirova E.V., Shevchenko V.G., Grigorov I.G. Solution combustion synthesis of α-Al_2O_3 using urea. *Ceram. Int.*, 2013, **39**(2), P. 1379–1384.

[109] Popkov V.I., Almjasheva O.V., Semenova A.S., Kellerman D.G., Nevedomskiy V.N., Gusarov V.V. Magnetic properties of $YFeO_3$ nanocrystals obtained by different soft-chemical methods. *J. Mater. Sci.: Materials in Electronics*, 2017, **28**(10), P. 7163–7170.

[110] Yang J., Li X., Zhou J., Tang Y., Zhang Y., Li Y. Factors controlling pure-phase magnetic $BiFeO_3$ powders synthesized by solution combustion synthesis. *J. Alloys Compd.*, 2011, **509**, P. 9271–9277.

[111] Farhadi S., Zaidi M. Bismuth ferrite ($BiFeO_3$) nanopowder prepared by sucrose-assisted combustion method: A novel and reusable heterogeneous catalyst fore acetylation of amines, alcohols and phenols under solvent-free conditions. *J. Molecular Catalysis A: Chemical*, 2009, **299**, P. 18–25.

[112] Khaliullin Sh.M., Zhuravlev V.D., Russkikh O.V., Ostroushko A.A., Bamburov V.G. Thermal characteristics, gassing in solution combustion synthesis and conductivity of $CaZrO_3$. *Internat. J. Self-Propag. High-Temp. Synt.*, 2015, **24**(2), P. 83–88.

[113] Ye T., Guiwen Z., Weiping Z., Shangda X. Combustion synthesis and photoluminescence of nanocrystalline Y_2O_3:Eu phosphors. *Mater. Res. Bull.*, 1997, **32**(5), P. 501–506.

[114] Nagaveni K., Hegde M.S., Madras G. Structure and Photocatalytic Activity of $Ti_{1-x}M_xO_{2\pm\delta}$ (M = W, V, Ce, Zr, Fe, and Cu) Synthesized by Solution Combustion Method. *J. Phys. Chem. B.*, 2004, **108**(52), P. 20204–20212.

[115] Mokkelbost T., Kaus I., Grande T., Einarsrud M.-A. Combustion Synthesis and Characterization of Nanocrystalline CeO_2-Based Powders. *Chem. Mater.*, 2004, **16**(25), P. 5489–5494.

[116] Jose R., James J., John A.M., Sundararaman D., Divakar R., Koshy J. A new combustion process for nanosized $YBa_2ZrO_{5.5}$ powders. *Nanostructured Mater.*, 1999, **11**(5), P. 623–629.

[117] Chiu T.-W., Yu B.-S., Wang Y.-R., Chen K.-T., Lin Y.-T. Synthesis of nanosized $CuCrO_2$ porous powders via a self-combustion glycine nitrate process. *J. Alloys Compd.*, 2011, **509**(6), P. 2933–2935.

[118] Khaliullin Sh.M., Bamburov V.G., Russkikh O.V., Ostroushko A.A., Zhuravlev V.D. $CaZrO_3$ synthesis in combustion reactions with glycine. *Dokl Chem.*, 2015, **461**(2), P. 93–95.

[119] Bansal N.P., Zhong Z. Combustion synthesis of $Sm_{0.5}Sr_{0.5}CoO_{3-x}$ and $La_{0.6}Sr_{0.4}CoO_{3-x}$ nanopowders for solid oxide fuel cell cathodes. *J. Power Sources*, 2006, **158**(1), P. 148–153.

[120] Yang X., Cheng X., Yan X., Yang J., Fu T., Qiu J. Synthesis of ZrO_2/ZrW_2O_8 composites with low thermal expansion. *Compos. Sci. Technol.*, 2007, **67**(6), P. 1167–1171.

[121] Smirnova M.N., Nikiforova G.E., Kop'eva M.A., Beresnev E.N., Kondrat'eva O.N., Ketsko V.A., Geras'kin A.A. Features of $Mg(Fe_{0.8}Ga_{0.2})_2O_4$ synthesis by glycine-nitrate method. *Russ. J. Inorg. Chem.*, 2015, **60**(8), P. 930–933.

[122] Ketsko V.A., Beresnev E.N., Komova M.G., Kop'eva M.A., Geras'kin A.A., Kuznetsov N.T. $MgAl_{0.4}Fe_{1.6}O_4$ powders prepared via gel combustion. *Russ. J. Inorg. Chem.*, 2012, **57**(6), P. 794–796.

[123] Smirnova M.N., Goeva L.V., Simonenko N.P., Beresnev E.N., Kop'eva M.A., Ketsko V.A. Gel formation specifics in the synthesis of $Mg(Fe_{0.8}Ga_{0.2})_2O_4$ by the glycine–nitrate method. *Russ. J. Inorg. Chem.*, 2016, **61**(10), P. 1301–1306.

[124] Beresnev E.N., Smirnova M.N., Simonenko N.P., Makaev S.V., Kop'eva M.A., Ketsko V.A., Kuznetsova O.B. Gel decomposition and formation of $MgFe_{1.6}Ga_{0.4}O_4$ powders. *Russ. J. Inorg. Chem.*, 2016, **61**(8), P. 1026–1030.

[125] Chen X., Liang S.-J., Bi J.-H., Gao J., Wu L. Self-propagating Combustion Synthesis of Nanocrystalline Yttrium Iron Oxide Solid Solution Photocatalysts. *Chinese J. Inorg.Chem.*, 2009, **25**(11), P. 1922–1927.

[126] Ostroushko A.A., Russkikh O.V., Chezganov D.S. Formation and morphology of nickel foam–complex oxide coatings with the perovskite structure. *J. of Surf. Invest. X-ray, Synch. and Neut. Tech*, 2015, **9**(6), P. 1237–1242.

[127] Ostroushko A.A., Mogil'nikov Yu.V., Ostroushko I.P. Synthesis of Molybdenum- and vanadium-Containing Mixed Oxides in Polymer-Salt Systems. *Inorg. Mat.*, 2000, **36**(12), P. 1256–1263.

[128] Ingle J.T., Sonekar R.P., Omanwar S.K., Wang Y., Zhao L. Solution combustion synthesis and optimization of phosphors for plasma display panels. *Optical Materials*, 2014, **36**(8), P. 1299–1304.

[129] Abasht B., Mirkazemi S. M., Beitollahi A. Solution combustion synthesis of Ca hexaferrite using glycine fuel. *J. Alloys Compd.*, 2017, **708**, P. 337–343.

[130] Russkikh O.V., Ivanov D.V., Isupova L.A., Chezganov D.S., Ostroushko A.A. Synthesis, Morphology, and Activity of $La_{1-x}Ag_xMnO_{3\pm y}$ Catalysts. *Kin. and Cat.*, 2016, **57**(5), P. 712–721.

[131] Wang X., Qin M., Fang F., Jia B., Wu H., Qu X., Volinsky A.A. Effect of glycine on one-step solution combustion synthesis of magnetite nanoparticles. *J. Alloys Compd.*, 2017, **719**, P. 288–295.

[132] Novikov V., Xanthopoulou G., Knysh Yu., Amosov A.P. Solution combustion synthesis of nanoscale Cu-Cr-O spinels: Mechanism, properties and catalytic activity in CO oxidation. *Ceramics International*, 2017.

[133] Vojisavljevizh K., Wicker S., Can I., Benan A., Barsan N., Malia B. Nanocrystalline cobalt-oxide powders by solution-combustion synthesis and their application in chemical sensors. *Advanced Powder Technology*, 2017, **28**(4), P. 1118–1128.

[134] Petschnig L.L., Fuhrmann G., Schildhammer D., Tribus M., Schottenberger H., Huppertz H. Solution combustion synthesis of $CeFeO_3$ under ambient atmosphere. *Ceramics International*, 2016, **42**(3), P. 4262–4267.

[135] Nabiyouni M., Zhou H., Luchini T.J.F., Bhaduri S.B. Formation of nanostructured fluorapatite via microwave assisted solution combustion synthesis. *Materials Science and Engineering: C*, 2014, **37**, P. 363–368.

[136] Tarragó D.P., de Fraga Malfatti C., de Sousa V.C. Influence of fuel on morphology of LSM powders obtained by solution combustion synthesis. *Powder Technology*, 2015, **269**, P. 481–487.

[137] Varma A., Mukasyan A.S., Deshpande K.T., Pranda P., Erri P.R. Combustion Synthesis of Nanoscale Oxide Powders: Mechanism, Characterization and Properties. *MRS Proc.*, 2003, **800**, P. AA4.1–AA4.12.

[138] Mukasyan A.S., Epstein P., Dinka P. Solution combustion synthesis of nanomaterials. *Proc. Combust. Inst.*, 2007, **31**(2), P. 1789–1795.

[139] Aruna S.T., Mukasyan A.S. Combustion synthesis and nanomaterials. *Curr. Opin. Solid State Mater. Sci.*, 2008, **12**(3-4), P. 44–50.

[140] Patil K.C., Hegde M.S., Rattan T., Aruna S.T. *Chemistry of Nanocrystalline Oxide Materials – Combustion Synthesis, Properties and Applications*. Singapore: World Scientific Publishing Co. Pte. Ltd., 2008, 364 pp.

[141] Chen X., Liang S.-J., Bi J.-H., Gao J., Wu L. Self-propagating Combustion Synthesis of Nanocrystalline Yttrium Iron Oxide Solid Solution Photocatalysts. *Chinese J. Inorg.Chem.*, 2009, **25**(11), P. 1922–1927.

[142] Rogachev A.S., Mukasyan A.S. Combustion of heterogeneous nanostructural systems. *Combust. Explos. Shock Waves*, 2010, **46**(3), P. 243–266.

[143] Sutka A., Mezinskis G. Sol–gel auto-combustion synthesis of spinel-type ferrite nanomaterials. *Front. Mater. Sci.*, 2012, **6**(2), P. 128–141.

[144] Gonzalez-Cortes S.L., Imbert F.E. Fundamentals, properties and applications of solid catalysts prepared by solution combustion synthesis (SCS). *Appl. Catal. A Gen.*, 2013, **452**, P. 117–131.

[145] Rogachev A.S., Mukasyan A.S. *Combustion for Material Synthesis*. Boca Raton: CRC Press. 2014. 424 pp.

[146] Li F.-T., Ran J., Jaroniec M., Qiao S.Z. Solution combustion synthesis of metal oxide nanomaterials for energy storage and conversion. *Nanoscale*, 2015, **7**(42), P. 17590–17610.

[147] Varma A., Mukasyan A.S., Rogachev A.S., Manukyan K.V. Solution Combustion Synthesis of Nanoscale Materials. *Chem. Rev.*, 2016, **116**(23), P. 14493–14586.

[148] Khaliullin S.M., Zhuravlev V.D., Bamburov V.G. Solution-combustion synthesis of oxide nanoparticles from nitrate solutions containing glycine and urea: Thermodynamic aspects. *Int. J. SHS.*, 2016, **25**(3), P. 139–148.

[149] Ostroushko A.A., Shuravljova L.I., Portnova S.M., Krasilov Yu.I. Formation of grains in $YBa_2Cu_3O_{7-\delta}$ powders. *Zhurn. Neorg. Khim.*, 1991, **36**(1), P. 3–5. (in Russian)

[150] Ostroushko A.A., Portnova S.M., Krasilov Yu.I., Ostroushko I.P. The processes involved in the synthesis of oxide compounds from polymer-containing salt solutions. *Zhurn. Neorg. Khim.*, 1991, **36**(4), P. 465–468.

[151] Ostroushko A.A., Shuravljova L.I., Portnova S.M., Krasilov Yu.I. The use of formats to obtain HTSC films. *Zhurn. Neorg. Khim.*, 1991, **36**(5), P. 623–625.

[152] Ostroushko A.A., Shuravljova L.I. Osipov V.V. Some special properties of $La_{1-x}Sr_xCoO_{3\pm y}$ films fabricated with the spray-pyrolysis method. *Mat. Sci. and Eng.*, 1992, **149**(2), P. L.17–L.19.

[153] Ostroushko A.A., Mironova N.V., Ostroushko I.P., Petrov A.N. Crystallization of saline components in polymer films during $YBa_2Cu_3O_{7-\delta}$ synthesis. *Zhurn. Neorg. Khim.*, 1992, **37**(12), P. 2627–2631. (in Russian)

[154] Ostroushko A.A., Kwasnitza K., Widmer Ch, Aksionova V.I., Petrov A.N. Interaction of $YBa_2Cu_3O_{7-\delta}$ Coating with Metallic Substrates. *Zhurn. Neorg. Khim.*, 1993, **38**(3), P. 436–438. (in Russian)

[155] Udilov A.E., Ostroushko A.A., Kudrevatyh N.V., Andreev S.V., Veselkina V.N. Preparing of the fine powdered $Sr_{1-x}La_xFe_{12-x}Co_xO_{19}$ (x=0; 0.2) by pyrolysis of polymeric-salt compositions. Abstracts of XIV International Conference on Permanent Magnets, Suzdal, 22-26 September 2003, P. 97.

[156] Ostroushko A.A., Shuravjova L.I., Kononchuk O.F., Petrov A.N. Fabrication of films $La_{1-x}SrCoO_3$ from salt solutions through pyrolysis method. *Zhurn. Neorg. Khim.*, 1991, **36**(1), P. 6–8. (in Russian)

[157] Ostroushko A.A., Zhuravleva L.I., Mogil'nikov Yu.V., Pirogov A.N. Catalytic Activity of Mixed-oxide Coating Based on Perovskite Lanthanum Strontium Cobaltate. *Russ. J. of Inorg. Chem.*, 1997, **42**(6), P. 836–840.

[158] Ostroushko A.A., Shubert E., Zhuravleva L.I., Isupova L.A., Alikina G.M., Bogdanov S.G., Valiev E.Z., Pirogov A.N., Teplykh A.E., Mogil'nikov Yu.V., Udilov A.E., Ostroushko I.P. Synthesis and Physicochemical and catalytic Properties of Perovskites $ABO_{3\pm y}$ (A = La, Sr, Ag; B = Mn, Co, Fe, Cu, Ti, Mo, V). *Russ. J. Appl. Chem.*, 2000, **73**(8), P. 1383–1392.

[159] Bogdanov S.G., Valiev E.Z., Pirogov A.N., Teplykh A.E., Ostroushko A.A, Udilov A.E. Magnetic and Fractal Properties of Nanocrystalline $LaMnO_3$. *The Phys. of Met. and Metallog.*, 2001, **91**(1), P. S229–S233.

[160] Ostroushko A.A, Schubert E., Makarov A.M., Minaev V.I., Udilov A.E., Elokhina L.V., Aksionova V.I. Catalytic Activity of Complex-Oxide Perovskit Containing Compositions in Reactions of CO and Organic Compounds Oxidation. Russ. *J. Appl. Chem.*, 2003, **76**(8), P. 1292–1297.

[161] Teplykh A.E., Bogdanov S.G., Valiev E.Z., Pirogov A.N., Dorofeev Yu.A., Kazantsev V.A., Kar'kin A.E., Ostroushko A.A., Udilov A.E. Size Effect in Nanocrystalline Manganites $La_{1-x}A_xMnO_3$ (A = Ag, Sr). *Phys. Solid State*, 2003, **45**(12), P. 2328–2333.

[162] Ostroushko A.A., Russkikh O.V., Prosvetova M.V., Petrova S.A., Zakharov R.G. Phase Composition and Thermal Properties of $Ce_{1-x}Ln_xO_{2-d}$ (Ln = Sm, Pr) Solid Solutions. *Inorg. Mat.*, 2010, **46**(9), P. 959–964.

[163] Ostroushko A., Kwasnitza K., Widmer Ch. *Crysallization of* $YBa_2Cu_3O_{7-\delta}$ *on films with single crystal and powder-metallic substrats made from salt-polymer solutions*. Final book of abstracts. Intern. Conf. on Advanced Materials (ICAM-91). Strasbourg. France. 1991. A1-XII/P.58.

[164] Ostroushko A.A., Russkih O.V., Pivchenko S.V. Study of properties of catalysts for the oxidation of carbon black prepared by "ceramic" synthesis and by pyrolysis of polymeric salt compositions. *Russ. J. Appl. Chem.*, 2010, **83**(6), P. 1102–1105.

[165] Ostroushko A.A. Polymer-salt composites based on nonionic water-soluble polymers and preparation of oxide materials from them. *Mendeleev Chem. J.*, 1998, **42**(1–2), P. 153–168.

[166] Gusarov V.V., Suvorov S.A. Transformations of nonautonomous phases and densification of polycrystalline systems. *J. Appl. Chem. USSR*, 1992, *65*(7), P. 1227–1235.

[167] Gusarov V.V., Malkov A.A., Malygin A.A., Suvorov S.A. Thermally activated transformations of 2D nonautonomous phases and contraction of polycrystalline oxyde materials. *Inorg. Mater.*, 1995, **31**(3), P. 320–323.

[168] Mazurin O.V., Gusarov V.V. The future of information technologies in materials science. *Glass Phys. Chem.*, 2002, **28**(2), P. 50–58.

[169] Anziferov V.N., Ostroushko A.A., Makarov A.M. *Synthesis, properties and applications of catalysts based on modified complex oxide compositions of highly porous cellular materials*. (Sintez, svoistva i primenenie katalizatorov na osnove modifizirovannikh slognooksinimi komposiziyami visokoporistykh yacheistikh materialov). Perm: Izd-vo Perm. gos. teh. un-ta, 2008, 204 pp. (in Russian).

[170] Ostroushko A.A., Vilkova N.V. Phase relations in ammonium heptamolybdate-poly(vinyl alcohol)-water mixtures. *Russ. J. Inorg. Chem.*, 2001, **46**(8), P. 1240–1243.

[171] Ostroushko A.A., Reshetnikova N.V. Phase relations and physicochemical properties of the ammonium vanadate – poly(vinyl alcohol) – water system. *Russ. J. Inorg. Chem.*, 2002, **47**(11), P. 1745–1749.

[172] Ostroushko A.A., Minyaev V.I. Phase relations in the lanthanum nitrate – poly(vinyl alcohol) – water system. *Russ. J. Inorg. Chem.*, 2003, **48**(11), P. 1728–1730.

[173] Ostroushko A.A., Sennikov M.Y. Ammonium heptamolybdate – poly(vinylpyrrolidone) – water system. *Russ. J. Inorg. Chem.*, 2003, **48**(4), P. 572–577.

[174] Ostroushko A.A., Mikhalev D.S. Phase relations and physicochemical properties of the ammonium paratungstate – polyvinyl alcohol – water system. *Russ. J. Inorg. Chem.*, 2003, **48**(3), P. 431–434.

[175] Ostroushko A.A., Sennikov M.Y., Glazyrina Y.A. Phase transitions in the ammonium heptamolybdate – poly(vinyl alcohol) – water system. *Russ. J. Inorg. Chem.*, 2005, **50**(2), P. 280–285.

[176] Ostroushko A.A., Sennikov M.Yu., Glazyrina Yu.A. Phase state and physicochemical properties of systems containing ammonium tungstate or ammonium vanadate, polyvinylpyrrolidone, and water. *Russ. J. Inorg. Chem.*, 2007, **52**(2), P. 254–257.

[177] Ostroushko A.A., Sennikov M.Yu. Phase relations in the lanthanum nitrate (copper nitrate) – poly(vinylpyrrolidone) – water systems. *Russ. J. Inorg. Chem.*, 2007, **52**(10), P. 1634–1637.

[178] Ostroushko A.A., Slinkina M.V., Volosentseva L.I., Ostroushko I.P, Mironova N.V., Pimenov D.A. Study of cation migration in polymer saline compositions based on polyvinyl-alcohol. *Zhurn. Fizich. Khim.*, 1993, **67**(11), P. 2267–2270. (in Russian)

[179] Ostroushko A.A., Zubarev A.Yu., Grzhegorzhevskii K.V. Evolution of Ammonium Metavanadate Crystals in Polyvinyl Alcohol Films. *Cryst. Reports*, 2016, **61**(2), P. 320–326.

[180] Safronov A.P., Zyryanova A.N., Gabdrafikova Y.M., Ostroushko A.A. Enthalpy of interaction in poly(vinyl alcohol) – ammonium heptamolybdate composition: Effect of complex formation and structural changes. *Polym. Scien. Ser. A.*, 2003, **45**(10), P. 1052–1058.

[181] Safronov A.P., Gabdrafikova Y.M., Ukhalina O.L., Ostroushko A.A. Enthalpy of formation of poly(vinyl alcohol), poly(ethylene glycol), and polyvinylpyrrolidone complexes with copper and cadmium ions in aqueous solutions. *Polym. Scien. Ser. A.*, 2004, **46**(5), P. 541–547.

[182] Ostroushko A.A., Zubarev A.Y., Bublik I.V., Sennikov M.Y., Iskakova L.Y., Safronov A.P. Modeling and calculation of the association processes between oxygen-containing polyanions and nonionic polymers. *Russ. J. Inorg. Chem.*, 2004, **49**(7), P. 1028–1033.

[183] Lileev A.S., Lyashchenko A.K., Ostroushko A.A., and Sennikov M.Yu. Dielectric Properties of Aqueous Solutions of the Ammonium Heptamolybdate – Poly(vinyl Alcohol) – Water System. *Russ. J. Inorg. Chem.*, 2006, **51**(4), P. 656–661.

[184] Ostroushko A.A., Adamova L.V., Eremina E.V. Thermodynamic Characteristics of the Interaction between Methanol and Keplerate-Type Poly(vinyl alcohol) – Polyoxomolybdate Composites. *Russ. J. Phys. Chem. A*, 2017, **91**(8), P. 1535–1538. (DOI: 10.1134/S0036024417080258)

[185] Kuznetsova A.E., Gradova N.B. *Scientific basis of environmental biotechnology*. Moscow, Mir, 2006, 504 pp. (in Russian)

[186] Pomogailo A.D. *Polymeric immobilized metal-complex catalysts*. Moscow, Nauka, 1988, 303 pp. (in Russian)

[187] Ostroushko A.A., Vilkova N.V., Mogil'nikov U.V. Structure and properties of molybdate and tungstate complexes of polyvinyl alcohol. *Russ. J. Gen. Chem.*, 2002, **72**(1), P. 1–8.

[188] Zubarev A.Yu., Ostroushko A.A., Bublik I.V., Sennikov M.Yu. Simulation of the rheological properties of liquid media containing solid anisometric particles. *Coll. J.*, 2007, **69**(6), P. 726–734.10.1134/S1061933X07060087)

[189] Ostroushko A.A., Mogil'nikov Y.V., Popov K.A. Polymer-salt compositions containing anionic d-metal species. *Zhurn. Neorg. Khim.*, 1998, **43**(6), P. 840–845.

[190] Men'shikov S.Yu., Sennikov M.Yu., Romanova Yu.V., Sycheva N.S., Ostroushko A.A. Homogeneous and polymer-supported catalysts in the oxidation of α-pinene with oxygen. *Russ. J. Org. Chem.*, 2004, **40**(6), P. 790–794.

[191] Men'shikov S.Yu., Mishina Yu.V., Mikushina Yu.V., Ostroushko A.A. A comparative study of aerobic oxidation of turpentine. *Russ. J. Appl. Chem.*, 2008, **81**(1), P. 52–54.

[192] Ostroushko A.A., Sennikov M.Yu., Sycheva N.S. Features of photochemical reactions in polymer-salt compositions containing ammonium heptamolybdate and poly(vinyl alcohol). *Russ. J. Inorg. Chem.*, 2005, **50**(7), P. 1050–1054.

[193] Ostroushko A.A., Sennikov M.Yu. The Kinetics of Photochemical Processes in Polymer–Salt Systems. *Russ. J. Phys. Chem. A*, 2009, **83**(1), P. 111–115.

[194] Ostroushko A.A., Sennikov M.Yu., Gerasimova E.L. Electrochemical and electrophysical parameters of polymer-salt compositions based on poly(vinyl alcohol) and ammonium heptamolybdate. *Russ. J. Inorg. Chem.*, 2005, **50**(3), P. 428–432.

[195] Ostroushko A.A., Mogil'Nikov Yu.V., Popov K.A. Thermal destruction of polymer-salt compositions containing d-metals in the form of oxygen-bearing anions. *Inorg. Mat.*, 2000, **36**(6), P. 603–611.

[196] Ostroushko A.A., Mogil'nikov Yu.V., Vilkova N.V., Popov K.A. Combined analysis of parameters and thermal behavior of polymer-salt formulations containing anionic d-metal species. *Russ. J. Appl. Chem.*, 2000, **73**(10), P. 1684–1690.

[197] Valiev E., Bogdanov S., Pirogov A., Teplykh A., Ostroushko A., Mogilnikov Yu. The formation processes of oxide phases from polymer-salt complexes of ammonium molybdate and tungstate. *Phys. B: Cond. Mat.*, 2000, **276**, P. 854–855.

[198] Bogdanov S.G., Ostroushko A.A., Valiev E.Z., Pirogov A.N., Teplykh A.E. Effect of acidity of polymer-salt compositions on the formation mechanism of the tungsten and molybdenum oxide particles. *Poverkh. Rentgen. Sinkhr. i Nejtron. Issledov.*, 2004, **2**, P. 21–33.

[199] Ostroushko A.A., Mikhalev D.S., Reshetnikova N.V. Stability of polymeric-salt gels used to synthesize complex-oxide materials. *Rus. J. of Appl. Chem.*, 2002, **75**(8), P. 1219–1222.

[200] Ostroushko A.A., Mogil'Nikov Y.V., Popov K.A., Vilkova N.V., Zhuravleva L.I., Ostroushko I.P. Interactions between M^{2+} and M^{3+} cations and d-metal complex anions in polymer-containing solutions. *Russ. J. Inorg. Chem.*, 1999, **44**(8), P. 1328–1334.

[201] Ostroushko A.A., Makarov A.M., Minyaev V.I. Oxidation of carbon in the presence of catalysts based on cesium lanthanum vanadate. *Russ. J. Appl. Chem.*, 2004, **77**(7), P. 1121–1129.

[202] Ostroushko A.A. Catalytic activity of metal ions in redox processes in polymer-salt systems during synthesis of mixed oxides. *Inorg. Mat.*, 2004, **40**(3), P. 259–263.

[203] Kingsley J.J., Patil K.C. A novel combustion process for the synthesis of fine particle α-alumina and related oxide materials. *Mater. Lett.*, 1988, **6**(11/12), P. 427–432.

[204] Ianos R., Barvinschi P. Solution combustion synthesis of calcium zirconate, $CaZrO_3$, powders. *J. Solid. State. Chem.*, 2010, **183**, P. 491–496.

[205] Prasanth C.S., Kumar H.P, Pazhani R., Solomon S., Thomas J.K. Synthesis, characterization and microwave dielectric properties of nanocrystalline $CaZrO_3$ ceramics. *J. Alloys Compd.*, 2008, **464**, P. 306–309.

[206] Deganello F., Liotta L.F., Marci G., Fabbri E., Traversa E. Strontium and iron-doped barium cobaltite prepared by solution combustion synthesis: exploring a mixed-fuel approach for tailored intermediate temperature solid oxide fuel cell cathode materials. *Mat. for Renew. and Sust. En.*, 2013, **2**(1), P. 2–8.

[207] Deganello F., Marci G., Deganello G. Citrate–nitrate auto-combustion synthesis of perovskite-type nanopowders: a systematic approach. *J. Europ. Ceram. Soc*, 2009, **29**(3), P. 439–450.

[208] Boobalan K., Varun A., Vijayaraghavan R., Chidambaram K., Kamachi Mudalic U. Facile, scalable synthesis of nanocrystalline calcium zirconate by the solution combustion method. *Ceram. Int.*, 2014, **40**(4), P. 5781–5786.

[209] Ostroushko A.A., Sennikov M.Yu. Thermochemical charge generation in polymer-salt films. *Rus. J. of Inorg. Chem.*, 2005, **50**(6), P. 933–936.

[210] Ostroushko A.A., Sennikov M.Yu. Thermochemical charge generation in polymer-salt films as a function of temperature. *Rus. J. of Inorg. Chem.*, 2008, **53**(8), P. 1172–1175.

[211] Lusheikin G.A. *Polymer electrets*. Moscow, Khimiya, 1976, 224 pp. (in Russian)

[212] Ostroushko A.A., Russkikh O.V., Kormil'tzev I.I., Kolosov V.Y., Tsvetkov D.S., Vylkov A.I. Study of nanostructured catalysts on the basis of complex oxides deposited on a carrier. *J. Surf. Invest.*, 2011, **5**(4), P. 677–682.

[213] Ostroushko A.A., Russkikh O.V., Filonova E.A., Melnikova A.A. A comprehensive analysis of processes of complex oxide materials synthesis, the influence of charge generating process on synthesis results. XX Mendeleev Congress on general and applied chemistry. Five-volumes book. Vol. 2a : abstracts. Ekaterinburg: Ural Branch of the Russian Academy of Sciences, 2016, P. 92.

[214] Ivanov B.V., Lipilin A.S., Spirin A.V., Rempel Al.A., Paranin S.N., Khrustov B.R., Shkerin S.N., Valentsev A.V., Zhuravlev V.D. The formation of multilayer structures of solid oxide fuel cells. *Int. Scien. J. for Altern. Energy. and Ecol.*, 2007, **2**(46), P. 75–88. (in Russian) .

[215] Almjasheva O.V., Fedorov B.A., Smirnov A.V., Gusarov V.V. Size, morphology and structure of the particles of zirconia nanopowder obtained under hydrothermal conditions. *Nanosystems: Physics, Chemistry, Mathematics*, 2010, **1**(1), P. 26–37. (in Russian)

[216] Vasilevskaya A., Almjasheva O.V., Gusarov V.V. Peculiarities of structural transformations in zirconia nanocrystals. *J. Nanopart. Res.*, 2016, **18**(188), P. 1–11.

[217] Ostroushko A.A., Udilov A.E. Some features of processes of formation of complex oxide products by pyrolysis of polymer-salt compositions. *Izvestiya VUZov. Ser. Khimiya i Khim. Tehn.*, 2007, **50**(10), P. 118–122. (in Russian)

NANOSYSTEMS: PHYSICS, CHEMISTRY, MATHEMATICS, 2017, 8 (4), P. 503–506

Grating influence study of GaAs solar cell structures

S. Saravanan, R. S. Dubey

Department of Nanotechnology, Swarnandhra College of Engineering and Technology, Seetharampuram,
Narsapur–534280, (A.P.), India
rag_pcw@yahoo.co.in

DOI 10.17586/2220-8054-2017-8-4-503-506

Thin film solar cells are having the problem of low absorption of light, particularly at longer wavelengths and hence, efficient light trapping engineering is demanded. Here, we propose a design of ultra thin GaAs solar cell with enhanced light absorption with the use of dual (dielectric and metal) gratings. In this way, light trapping can be enhanced at longer wavelengths for both TE and TM polarization modes.

Keywords: solar cells, ultra thin, GaAs, dielectric, metal, polarization mode.

Received: 28 September 2016

Revised: 20 May 2017

1. Introduction

Presently, GaAs solar cells have shown high power conversion efficiency relative to other solar cell technologies. Among semiconductor materials, GaAs has the better optical performance, e.g. high energy photons can be easily absorbed in short region, less power consumption, high crystal quality, and operating frequency. Additionally, various theoretical and experimental light trapping mechanisms have been reported for the better harvesting of light with the use of nanograting, nanoparticles and back reflectors etc. [1–3]. Hong et al. have reported designing GaAs thin film solar cells by incorporating a silver nanoparticles in a periodical manner. They have observed enhanced absorption due to the surface plasmon induced by metal nanoparticles. GaAs based solar cells could result in 31 % improvement in short-circuit current as compared to a planar solar cell [4]. Nakayama et al. have experimentally demonstrated an improvement in GaAs solar cells by using silver nanoparticles fabricated by masked deposition. They have observed strong scattering by the interacting surface plasmons and increased optical path for the incident photons which could give an 8 % increase in the short-circuit current density [5]. Chang et al. have presented a modeling of GaAs solar cells using the finite-difference time domain (FDTD) method. The fabricated device consisted of self-assembled two-dimensional microspheres and was found to be efficient for light harvesting. Comparison of the designed solar cell with the fabricated one could show a 25 % enhanced conversion efficiency [6]. Grandidier et al. have demonstrated the design of perfectly flat GaAs solar cell structures of varying thicknesses that were comprised of a double layer antireflection coating, silica nanosphere array on top and a back reflector. The solar cell with 100 nm thickness showed better improvement however, in the case of the cell having 1000 nm thickness, a 2.5 % improvement was observed with the optimization of the sphere size and the spacing between them [7]. Zhang et al. have presented a study of light trapping properties of GaAs nanoneedle arrays based solar cells by employing rigorous coupled wave analysis and finite element method. They compared nanowire array-based solar cells with thin film layer based and observed enhanced light absorption. This enhancement has been attributed to the graded refractive index of nanoneedle arrays that could couple the incident light in an efficient manner and also was observed to be less dependent on the incident angle. With an optimized solar cell structure, they observed enhanced absorption, as much as more than 90 % compared to the band gap [8].

In this paper, we present a modeling and simulation of GaAs solar cells based on the dual gratings. In section 2, the design approach with simulation details is presented and results are discussed in section 3. Finally, section 4 concludes the paper.

2. Design approach

The schematic diagram of the solar cell structure with proposed light trapping mechanism is depicted in Fig. 1. This design architecture consists of 70 nm anti-reflection coating (ARC) of silicon nitride (Si_3N_4), top dielectric grating (height 30 nm) of indium-tin-oxide, bottom metal grating (height 30 nm) of aluminum, 40 nm GaAs active layer and 150 nm aluminum (Al) substrate. Here, the use of dielectric and metal gratings produce multiple bouncings of the incident photons in the active region which prolongs optical path length or lifetime of the photons.

Modeling of the proposed structure was investigated by using finite-difference-time-domain method, which deals with Maxwell's equations of electromagnetic waves. For the simulation, the periodic boundary conditions

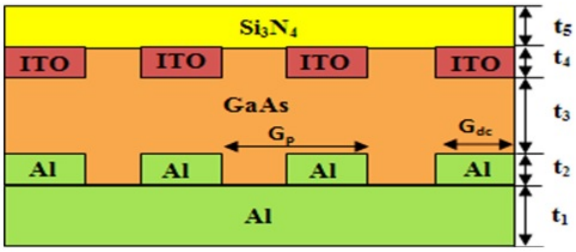

FIG. 1. Schematic diagram of proposed GaAs solar cell

were applied in x- and y-directions while a perfectly matched layer condition was applied in the z-direction to prevent the reflections. In this work, the FDTD method was employed to analyze the electric and magnetic field distributions in the proposed solar cell and results will be explored in the next section.

However, the performance of solar cells was analytically evaluated by employing the basic characteristics equations. The expressions of short-circuit current (J_{sc}) and open-circuit voltage V_{oc} can be expressed as:

$$J_{sc} = eN_{e-h}\left[\frac{A}{m^2}\right], \tag{1}$$

$$V_{oc} = \frac{kT}{e}\ln\left(\frac{J_{sc}}{J_{so}}+1\right)[V], \tag{2}$$

where k is the Boltzmann's constant, T is the absolute temperature and J_{so} is the reverse-bias saturation current.

Using the short-circuit current and open-circuit voltage equations (1) and (2), one can write an expression of fill factor (FF) as:

$$FF = \frac{J_{mp}\times V_{mp}}{J_{sc}\times V_{oc}}. \tag{3}$$

Therefore, fill factor is defined as the ratio of maximum power and product of short-circuit current and open-circuit voltage.

By using equations (1), (2) and (3), one can evaluate the solar cell efficiency (η) with the following expression:

$$\eta = \frac{J_{sc}\times V_{oc}\times FF}{P_{in}}, \tag{4}$$

where P_{in} is the total incident power.

The above resultant equation is used to evaluate the performance of the solar cell as a function of short-circuit current, open-circuit voltage, fill factor and the incident power.

3. Results and Discussion

For a comparative study of the light absorption in the proposed dual grating based solar cell (named as D), we have designed three solar cells; A: reference solar cell without grating, B: with only bottom grating and C: with only top grating. Fig. 2(a,b) shows absorption curves of various solar cells for both the transverse electric (TE) and magnetic (TM) polarizations respectively. Refer to Fig. 2(a) for the TE case, optimal enhancement in light absorption can be observed for the dual grating based solar cell however, reference solar cell shows poor absorption from the wavelength 600 nm. The enhanced absorption from the solar cell D has been attributed to the scattering effect of metal and guiding effect of dielectric gratings respectively. Fig. 2(b) shows absorption of various designed solar cells for the TM case. In the case of reference solar cell, low absorption can be observed while dual grating based solar cell shows optimal absorption over a broad range of the wavelength region due to the induced plasmonic effect.

For the case of bottom grating based design, localized surface plasmon and guided modes are observed. Generally, the metallic grating structure excites localized surface plasmon resonance which prolongs the optical path length of photons in the absorbing layer [1,9]. In the case of solar cell D, the combined effect of dual grating supported by plasmonic and photonic modes is observed. We have calculated the relative enhancement of short-circuit current density of the solar cell D with reference to the solar cell A by using an expression $(Cell\ D_{Jsc} - Cell\ A_{Jsc}/Cell\ A_{Jsc})$. A relative enhancement in short-circuit current density about 101.6 and 216.7 % are obtained for TE and TM respectively. The use of either top or bottom grating shows enhanced absorption as compared to the reference solar cell A. However, the performance of solar cell D is dominant, which is due to the light trapping phenomena.

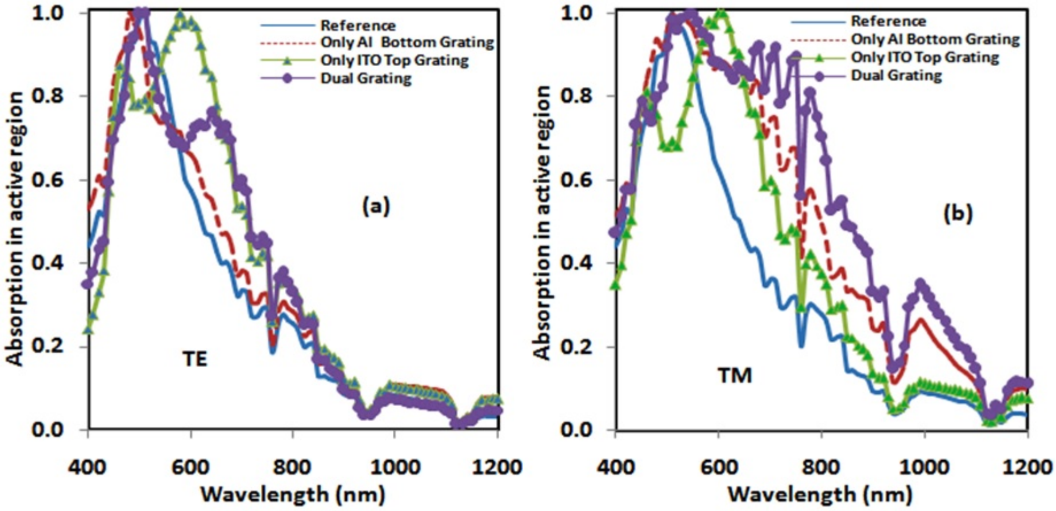

FIG. 2. Light absorption for TE Fig.(a) and TM Fig.(b) cases

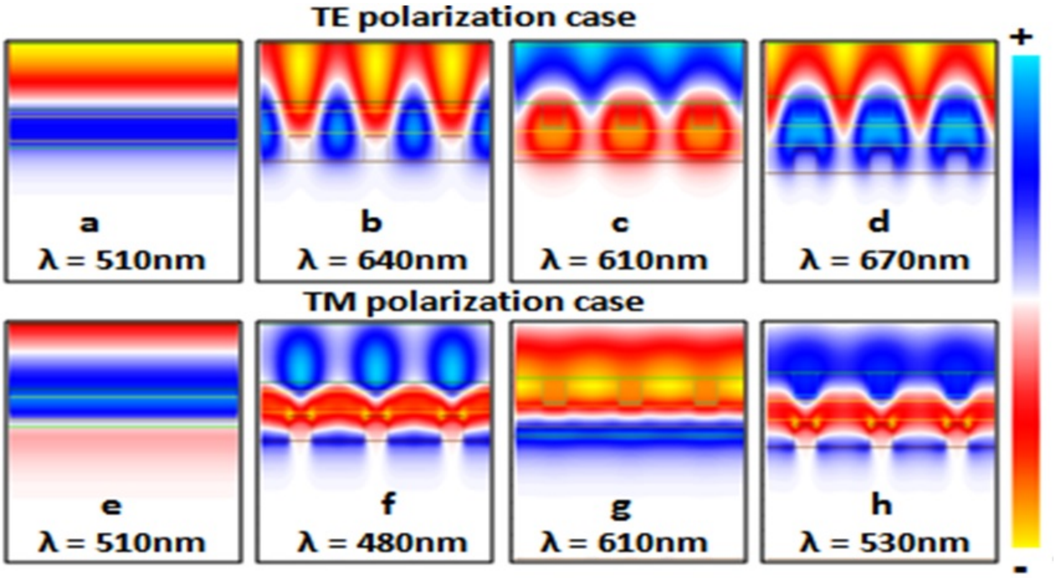

FIG. 3. Transverse electric and magnetic field distributions in different solar cell structures

After collecting the peak values of different solar cell designs from absorption curves plotted in Fig. 2, we have studied the field profile for both the cases of TE and TM polarizations which is shown in Fig. 3. The usual behavior of field distribution can be seen in Fig. 3(a,e) for the case of reference solar cell A. Also, in Fig. 3(b-d) and Fig. 3(f-h) an improvement in field profile is also observed from different solar cells based on bottom, top and dual gratings in reference to solar cells B, C and D respectively. However, a distinct field profile is observed for the transverse magnetic field mode. With the solar cell D, as shown in Fig. 3(h) the localized surface plasmon (LSP) supported by the guided modes can be observed. This magnetic field distribution behavior is responsible for the enhanced cell efficiency.

4. Conclusion

We have investigated the optical performance of ultrathin dual grating GaAs solar cell and compared that with a reference solar cell. Among other designed solar cells, dual grating based solar cell could yield maximum short-circuit current density 17.41 for TE and 29.66 mA/cm^2 for the TM case. This enhancement has been attributed to the combined effect of photonic and plasmonic modes. Finally, a relative enhancement in short-circuit current density about 101.6 and 216.7 % has been obtained for TE and TM respectively.

Acknowledgments

The financial support from DRDO is acknowledged.

References

[1] Ronen Chriki, Avner Yanai, Joseph Shappir and Uriel Levy. Enhanced efficiency of thin film solar cells using a shifted dual grating plasmonic structure. *Opt. Express*, 2013, **21**(S3), P. A381–A391.

[2] Yanpeng Shi, Xiaodong Wang, Wen Liu, Tianshu Yang, Rui Xu, and Fuhua Yang. Multilayer silver nanoparticles for light trapping in thin film solar cells. *J. Appl. Phys.*, 2013, **113**, P. 176101-1-3.

[3] Sangjun Lee and Sangin Kim. Optical absorption characteristic in thin a-Si film embedded between an ultrathin metal grating and a metal reflector. *IEEE Photon. J.*, 2013, **5**(5), P. 4800610-1-9.

[4] Lei Hong, Rusli, Xincai Wang, Hongyu Zheng, Lining He, Xiaoyan Xu et. al. Design principles for plasmonic thin film GaAs solar cells with high absorption enhancement. *J.Appl. Phys.*, 2012, **112**, P. 054326-1-5.

[5] Keisuke Nakayama, Katsuaki Tanabe and Harry A. Atwater. Plasmonic nanoparticle enhanced light absorption in GaAs solar cells. *Appl.Phys.Lett.*, 2008, **93**, P. 121904-1-3.

[6] Te-Hung Chang, Pei-Hsuan Wu, Sheng-Hui Chen, Chia Hua Chan, Cheng-Chung Lee et. al. Efficiency enhancement in GaAs solar cells using self-assembled microspheres. *Opt. Express*, 2009, **7**(9), P. 6519–6524.

[7] Jonathan Grandier, Callahan Dennis M., Munday Jeremy N. and Atwater Harry A. Gallium arsenide solar Cell absorption enhancement using whispering gallery modes of dielectric nanospheres. *IEEE J. Photovolt.*, 2012, **2**(2), P. 123–128.

[8] Xu Zhang, Xiao-Hong Sun and Liu-Di Jiang. Absorption Enhancement Using Nanoneedle Array for Solar Cell. *Appl. Phys. Lett.*, 2013, **103**, P. 211110-1-5.

[9] Saravanan S., Dubey R.S., Kalainathan S., More M.A. and Gautam D.K. Design and optimization of ultrathin crystalline silicon solar cells using an efficient back reflector. *AIP Adv.*, 2015, **5**, P. 057160-1-9.

NANOSYSTEMS: PHYSICS, CHEMISTRY, MATHEMATICS, 2017, 8 (4), P. 507–511

The surface morphology of ZnS–CdS solid solution films

V. N. Semenov, O. V. Zvyagina, T. V. Samofalova, A. N. Nituta
Voronezh State University, Universitetskaya sq., 1, Voronezh–394018, Russia
asiyat.nituta@yandex.ru

DOI 10.17586/2220-8054-2017-8-4-507-511

This paper presents the results of a study of surface morphology of pyrolytic films of solid solutions of ZnS–CdS. We discovered that the change of roughness parameters and microstructure of the surface of the coating film depended on the quantitative composition of the solid solution.

Keywords: scanning atomic force microscopy, roughness parameters, cadmium sulfides, zinc, solid solutions.

Received: 18 July 2017

Revised: 9 August 2017

1. Introduction

Modern materials science is constantly stimulating the creation of new technologies from the point of view of the synthesis of compound semiconductors with controlled properties. Much attention is given by scientists to chalcogenide metals for their ability to easily form double and ternary compounds and solid solutions based on them. The desired physical and chemical properties primarily depend on their composition. The considered compounds have many applications, including photodetectors, optical coatings, photovoltaic devices, electro-optic modulators, field effect transistors [1–3]. The methods of obtaining semiconductor compounds allow us to synthesize them in different "types": quantum dots, nanocrystals, thin films, poly- and single crystals.

One of the more common and economical methods for the synthesis of chalcogenide films with a given crystal structure and properties is the method of spraying aqueous solutions of thiourea coordination compounds (TCC) onto a heated substrate [4]. Previous studies [5] have shown that the surface morphology of lead sulfide films obtained from TCC solutions $[Pb(N_2H_4CS)_2Cl_2]$ depends on the deposition temperature and composition of the initial solution. In this work, it was shown that increasing the concentration of thiourea in the spray solution, and the deposition temperature during the synthesis of lead sulfide films leads to a more perfect structure and close grain packing [5]. The aim of this work was to study the surface morphology of the ZnS–CdS film system, deposited by the pyrolysis of aqueous solutions of coordination compounds aerosol $[M(N_2H_4CS]$ (M = Cd, Zn).

2. Materials and methods

The synthesis of films of the ZnS–CdS system was carried out by the pyrolysis of an aerosol of thiourea coordination compound solutions $[M(N_2H_4CS)_2Br_2]$. To obtain the TCC we used the salt $CdBr_2{\cdot}4H_2O$, $ZnBr_2$ brand "chemically pure", and thiourea N_2H_4CS brand "ultra pure". Coordination compounds synthesized at room temperature in an aqueous solution containing 0.05 M bromide of the appropriate metal and thiourea (0.2 M). The samples were sprayed at a temperature of 400 °C for 1 minute. As substrates, sital plates were used.

The morphological study of the surface characteristics of the obtained samples was performed using a scanning atomic-force microscope SOLVER P47 (AFM) and determined the average (Ra) and root-mean-square (RMS) (Rq) roughness [6]. For estimation of the surface microrelief of the samples, an analysis of the morphology of the synthesized structures in the following sequence of actions was performed: filtering the phase image of the sample; cross-sectional according to the obtained image; a histogram calculation; determination of roughness parameters.

The film thicknesses were determined by the use of a Jeol JSM-6510LV scanning electron microscope (SEM).

3. Results and discussion

A feature of the aerosol pyrolysis method is that depending on the deposition conditions (temperature, rate of spraying of the aerosol, the type of precursor and the substrate, the concentration of the initial solution), the formation of sulfides of metals with varying structural, optical and electrical properties is possible [7–10]. The chemical nature of the precursor, together with the deposition conditions, can influence the crystalline structure of the formed sulfides. When using solutions of $[M(N_2H_4CS)_2Br_2]$ complexes and a deposition temperature of 400 °C, the formation of solid solutions of wurtzite structure $Cd_xZn_{1-x}S$ with unlimited solubility occurs [8].

The mechanism of new phase formation can have a significant impact on the subsequent growth of the film and its structure. In previous studies, the discontinuous nature of the film growth of metal chalcogenides by using the method of aerosol pyrolysis was revealed [9, 11]. The particle formation of $\mathrm{Cd}_x\mathrm{Zn}_{1-x}\mathrm{S}$ is as follows. The pyrolysis of aerosol on a heated substrate formed nanoparticle phase sulfides and they were fixed on the surface of the glass-ceramic. Further growth of the film occurs due to the stretching possibilities of the fragments M–S released in the process of thermal decomposition of the complexes and interacts with the sulfide, which is formed on the active center of the substrate. The impact of continuous flow aerosol leads to the enlargement of nanoparticles in the islets, which create a mesh-like structure permeated with pores and channels. The surface roughness on the substrate reduces the nucleation barrier and allow the film structure to crystallize in different directions before the final stage at which the growth rate decreases and usually eventually stops ("the effect of growth saturation") and that can be associated with aerosolized sulfide [9, 11].

Fig. 1 shows the surface scans, obtained by mapping the phase and density histograms of the distribution of surface heights within the scanned area obtained during the topographical measurement by AFM, showing the surface morphology of the films CdS, $\mathrm{Cd}_{0.5}\mathrm{Zn}_{0.5}\mathrm{S}$ and ZnS. The scanning area was 1×1 $\mu\mathrm{m}^2$.

An analysis of AFM images showed that the growth of the investigated films is accompanied by the development of surface topography in the form of densely packed grains with distinct boundaries. In the studied areas, recorded elements (units) are rounded, formed by sulfide nanoparticles, which spread in different directions to completely cover the surface of the substrate. As can be seen from Fig. 1(a,c,e), the surface of the films formed by the components have average sizes of 40–80 nm.

With the transition from cadmium sulfide to zinc sulfide there is a change of the surface topography and the average size of nanoparticle aggregates. Thus, the average size of the elements on the surface of the CdS films is 35–60 nm, $\mathrm{Cd}_{0.5}\mathrm{Zn}_{0.5}\mathrm{S}$ 60–80 nm, and for samples of ZnS they are observed in larger aggregates with an average size of 70–90 nm. Thus, there is a gradual enlargement of cells on the surface of the films with increasing content of zinc sulfide. This may be due to the following reasons. In the formation of solid solutions of $\mathrm{Cd}_x\mathrm{Zn}_{1-x}\mathrm{S}$ the substitution of cadmium atoms in smaller atoms of zinc (rZn = 0.125 nm; rCd = 0.141 nm [12]) leads to a deformation distortion and compression of the crystal lattice of the resulting sulfide. Perhaps this, in turn, contributes to the merging of closely spaced crystallites and generally leads to the enlargement of the cells on the surface of the films, similar in composition to ZnS. It is also possible the influence of the amorphous crystal structure of zinc sulfide [13].

Density histograms for the distribution of surface elevation values (Fig. 1(b,d,f)) show that the height of the largest number of particles within the scanned area is increased from 18–25 to 35–50 nm for films of CdS and ZnS, respectively. For these samples, the average roughness values change from 2.43 (ZnS) to 8.61 (CdS) nm and RMS roughness from 4.12 (ZnS) to 8.26 (CdS) nm. The graphic dependence is shown in Fig. 2. An analysis of the roughness parameters for all the membranes of the ZnS–CdS system showed that equimolar composition can be observed for the minimum values of Ra and Rq, which are 2.30 and 3.02 nm respectively. The obtained results allow us to conclude that film compositions close to zinc sulfide have less deviation of the roughness profile relative to the mean plane (Ra). A similar dependence is characteristic for the standard deviation of the surface profile relative to the baseline. For the composition $\mathrm{Cd}_{0.5}\mathrm{Zn}_{0.5}\mathrm{S}$, the minimum values of the main parameters were noted. This can be explained by the formation of a uniform crystal lattice during the formation of solid solutions of substitution by cadmium and zinc ions as the film coating is formed. Because of this, the effect of a smooth surface is created.

Electron microscopic study of the surface morphology of the synthesized $\mathrm{Cd}_x\mathrm{Zn}_{1-x}\mathrm{S}$ films showed that they are uniform and continuous, and their thickness is 500–1000 nm. As an example, Fig. 3 shows electron microscopic image obtained by the SEM in the study of the cleavage of cadmium sulfide films.

4. Conclusion

The study of the surface morphology of films of $\mathrm{Cd}_x\mathrm{Zn}_{1-x}\mathrm{S}$ using atomic force microscopy revealed a highly developed surface of deposited layers of the terrain which has a height difference of 50 nm. The average size of aggregates formed by nanoparticles of the corresponding sulfide is 35–60 nm and 70–90 nm for films of CdS and ZnS, respectively. Visually, the sample has a surface which contains terrain drops: the pronounced depression and localized point of the hill. The microheterogeneity of the surface topography of films of $\mathrm{Cd}_x\mathrm{Zn}_{1-x}\mathrm{S}$ ($0.5\leq x \leq1$) is smooth, and the layers are smoother. With increased zinc sulfide content in the studied samples there is a change of the microrelief of their surface by consolidation of the particles. The thickness of the layers that was determined by SEM to be 500–1000 nm.

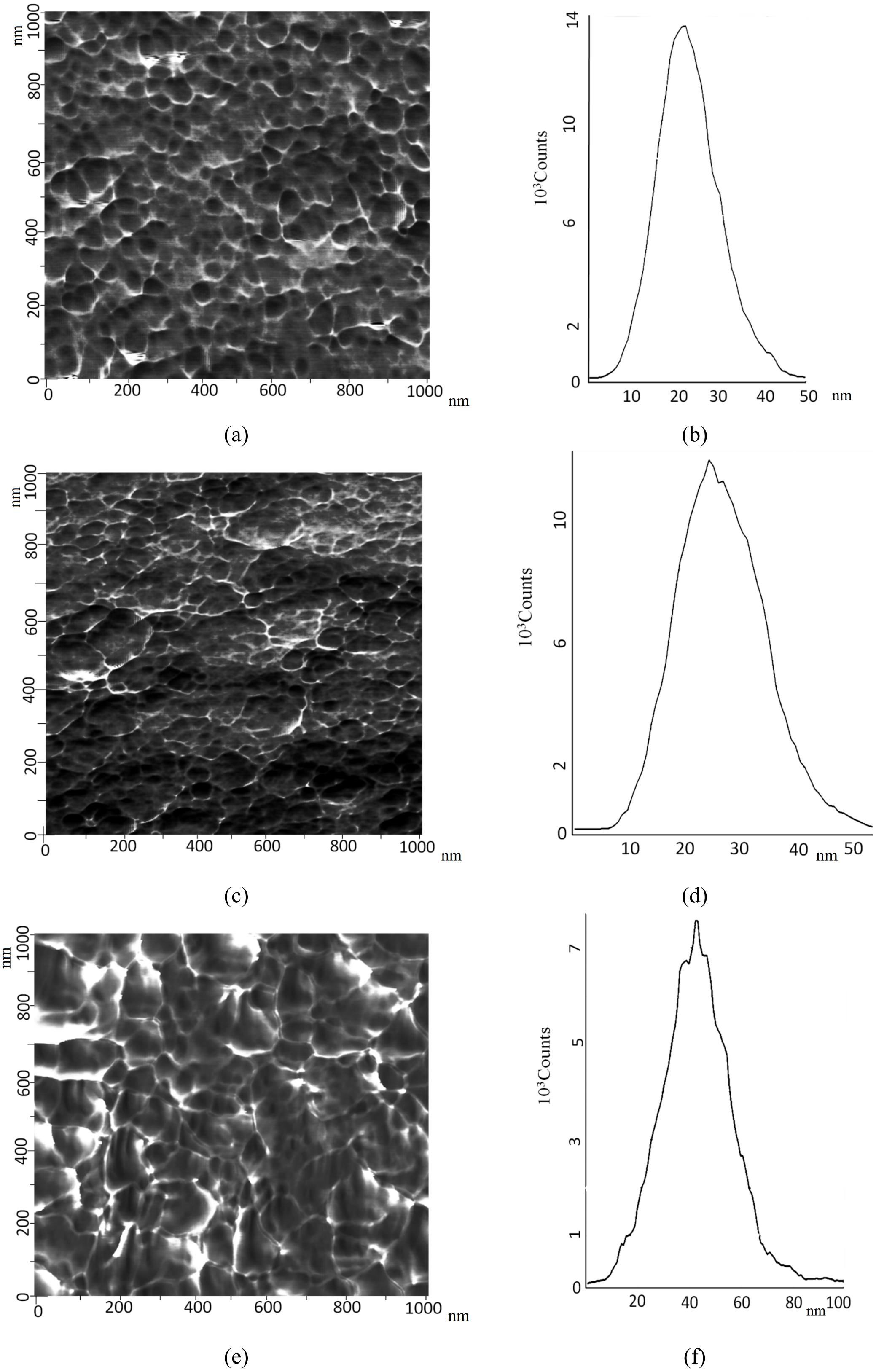

(a) (b)

(c) (d)

(e) (f)

FIG. 1. AFM scans of the surface mode of phase contrast (a,c,e) and density histograms of distribution of values of surface elevation (b,d,f) films of CdS (a,b), $Cd_{0.5}Zn_{0.5}S$ (c,d) and ZnS (e,f)

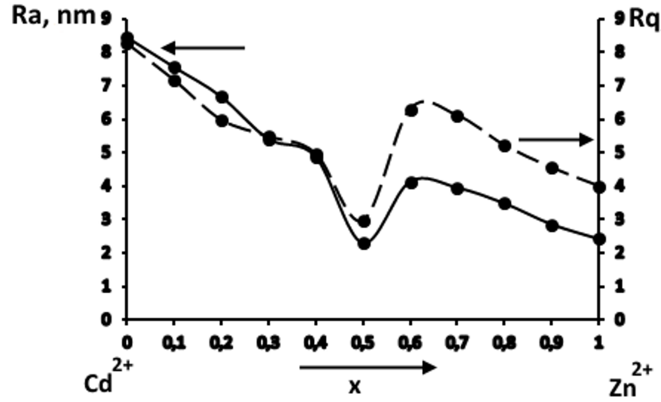

FIG. 2. The average and quadratic mean roughness, depending on the quantitative composition of the $Cd_xZn_{1-x}S$ films

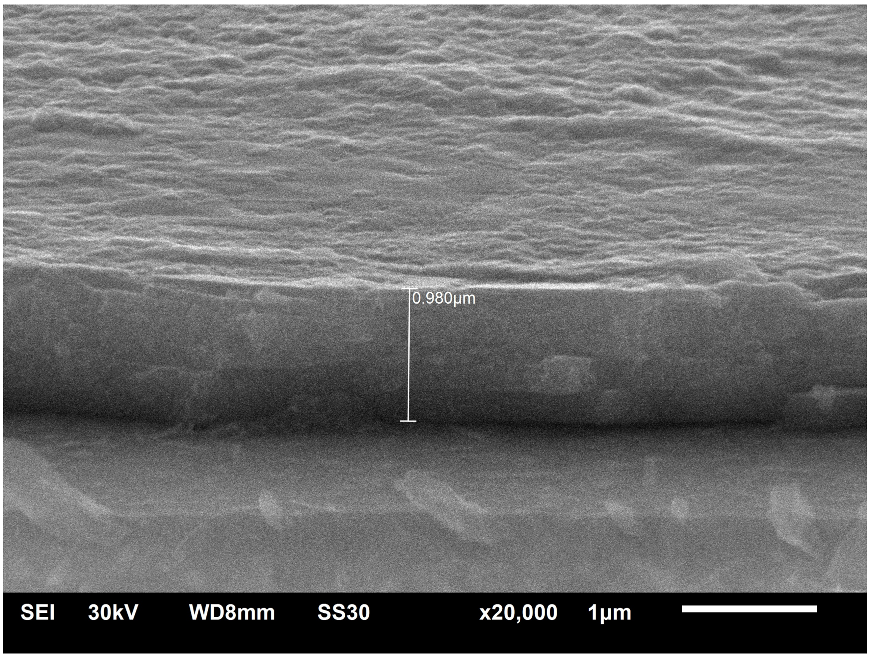

FIG. 3. Micrograph of the surface of the films of CdS

Acknowledgments

The authors wish to thank the Center for Collective Use of Voronezh State University for providing analytical equipment.

References

[1] Klyuev V.G. Pham Thi Han Mien, Bezdetko Yu. S. Nature of the luminescence centers of CdS nanocrystals. *Condensed matter and interphases*, 2014, **16**(1), P. 27–31.

[2] Lazarev V.B., Shevchenko V.I., Marenkin S.F. Some problems of physical chemistry and materials science of new semiconductor materials. *Physical methods of investigation of inorganic materials*, Moscow, 1981, P. 19–32.

[3] Trukhan V.M., Sheleg A.U., Fekeshgazi I.F. Cadmium diphosphide and zinc diarsenide single crystals – promising materials for electronic engineering. *Photoelectronics*, 2004, **13**, P. 41–45.

[4] Samofalova T.V., Meteleva Yu.V., Naumov A.V., Semenov V.N., Novikov G.F. Properties of films of the system CdS-ZnS deposited from mixed thiourea of coordination compounds. *Condensed matter and interphases*, 2007, **9**(2), P. 152–155.

[5] Samofalova T.V., Ovechkina N.M., Kharin A.N. Semenov V.N. Surface microstructure of pyrolytic lead sulfide films. *Condensed matter and interphases*, 2013, **15**(3), P. 332–336.

[6] Mironov V.L. *Basics of scanning probe microscopy: a textbook for senior students of higher educational institutions*. Nizhny Novgorod, 2004, 110 pp.

[7] Samofalova T.V., Semenov V.N. Films based on solid solutions of the ZnS-CdS system from thiourea coordination compounds and their properties. *Journal of Applied Chemistry*, 2013, **86**(12), P. 1863–1871.

[8] Naumov A.V., Samofalova T.V., Semenov V.N., Nechaev I.V. Thiocarbamide coordination compounds in the synthesis of solid solutions $\mathrm{Cd}_x\mathrm{Zn}_{1-x}\mathrm{S}$. *Journal of Inorganic Chemistry*, 2011, **46**(4), P. 666–672.

[9] Naumov A.V., Semenov V.N. Processes of directed synthesis of films of metal sulphides from thiocarbamide coordination compounds. *Proceeding of Voronezh State University. Series: Chemistry. Biology. Pharmacy*, 2000, **2**, P. 50–55.

[10] Naumov A.V., Semenov V.N., Goncharov E.G. Properties of CdS films obtained from coordination compounds of cadmium with thiourea. *Inorganic Materials*, 2001, **37**(6), P. 647–652.

[11] Semenov V.N., Naumov A.V. Formal kinetics of deposition of a thin layer from the spray solution stream. *Condensed matter and interphases*, 1999, **1**(2), P. 176–180.

[12] Emsley D. *Elements*. The World, Moscow, 1993, 256 pp.

[13] Samofalova T.V., Semenov V.N. Deposition of thin layers of zinc sulfide from thiourea complexes and their properties. *Condensed matter and interphases*, 2016, **18**(2), P. 248–255.

NANOSYSTEMS: PHYSICS, CHEMISTRY, MATHEMATICS, 2017, 8 (4), P. 512–522

Sizes and size distributions of nanoparticles: Causes of differences in results obtained by transmission electron microscopy and small angle X-ray scattering

D. O. Shvedchenko, V. V. Volkov, E. I. Suvorova

A. V. Shubnikov Institute of Crystallography of Russian Academy of Sciences,
Leninsky pr., 59, 119333 Moscow, Russia

dmitrymephi@gmail.com, vvo@ns.crys.ras.ru, suvorova@ns.crys.ras.ru

PACS 61.05cf + 61.46.Df + 68.37.Lp **DOI 10.17586/2220-8054-2017-8-4-512-522**

Comparative size and structure characterization of silver and selenium nanoparticles obtained and stabilized in different polymer solutions was performed by transmission electron microscopy (TEM) and small-angle X-ray scattering (SAXS). Effects of instrumental properties, nature of the samples, data collecting and data processing on accuracy of measurements are highlighted and summarized. Numerical differences in the mode diameter values derived from the TEM and SAXS data were found to have different sources. The SAXS results can be misleading in case of small particles (2–4 nm), for instance, Ag nanoparticles formed and stabilized in some aqueous polymer solutions due to instrumental limits, while TEM can provide sufficient statistics on such nanoparticles. SAXS is efficient in characterization of size distributions for soft Se-polymer composite particles of 20 to 100 nm in diameter. TEM is mandatory for investigating the chemical and phase composition of particles in mixtures, and their formation mechanism.

Keywords: nanoparticles, selenium, silver, transmission electron microscopy, small-angle X-ray scattering, size distribution.

Received: 26 July 2017

Revised: 5 August 2017

1. Introduction

The chemical, physical, bio- and medical properties of different kinds of particle suspensions are strongly dependent on the particle sizes and the shape of their distributions. Transmission electron microscopy (TEM) and small-angle X-ray scattering (SAXS) remain the main techniques for characterizing nanoparticle sizes and their distributions. On this issue, we refer to reviews of Chu & Liu [1] and Pedersen [2] with extensive analysis of principles and applications of different scattering techniques.

The main issue of experimental articles on the nanoparticle sizes and distributions is to show the best agreement between data in the wide range from a few nm to microns obtained by various scattering techniques and TEM. We argue that in general this approach is wrong since first, it does not consider the different ways that incident beams interact with matter. In this connection, it is worthwhile to mention an example of remarkably different size distributions and the mode diameter derived from the small-angle X-ray scattering and small-angle neutron scattering (SANS) curves obtained from the same sample as shown by Pedersen [2]. The explanation was that the neutrons "see" a high-density core while the X-rays "see" a low-density shell. Therefore, the size distribution histograms from SANS and SAXS for particles composed by copolymers with hydrophobic and hydrophilic chains or core-shell structures will describe different components of the same particles.

The fundamental difference of scattering methods like SAXS from TEM is the need of preliminary knowledge or assumption of shape, structure of particles in order to derive the sizes from the scattering curves. TEM is a direct method for imaging the particles and measuring their sizes over a wide range of diameters from 1 nm to a few tens nm with a capability to extract information of the chemical/phase composition of the particles and their crystalline character in polydisperse and multiphase systems. SAXS operates in terms of scattering intensities from objects depending on the scattering angles and thus is an indirect method of measuring sizes. Therefore, analysis of SAXS data contains a comparison with scattering model functions to fit experimental and simulated intensity curves.

In this paper, we show the advantages for a combination of the methods to obtain comprehensive information about particles in solutions, their distributions with high reliability and reveal the sources of inevitable errors in statistical analyses of particles in both mono- and polydisperse systems. Therefore, the goals of the paper are to: (1) highlight and summarize the main origin (instrumental, sampling, data collection and processing) of errors of these two methods, (2) show the ways to minimize the errors of measurements, (3) present the results of the TEM and SAXS investigation for two entirely different polydisperse systems of Ag and Se nanoparticles synthesized and stabilized in polymer solutions. We compare the volume fractions of the smallest particles (below 5 nm in diameter) measured by TEM and SAXS as well as volume fractions of particles with diameters at the large-size tails of distributions. For this purpose, we applied for the first time a new method of particle recognition and size measurement described in [3]. This automatic method based on approximation of the calculated distribution of grey level to the real distribution in (S)TEM images allowed us to increase the number of measured particles in comparison with the manual analysis.

2. Theoretical background

2.1. SAXS

The scattering intensity from the mixture of different particles may be represented as a sum of partial intensities from several non-interacting polydisperse components (polydisperse systems of particles having in the frame of the component the same shape but different sizes) weighted by their volume fractions [4, 5]:

$$I(s) = \sum_{k=1}^{K} V_k I_k(s), \tag{1}$$

where $\mathrm{V}_k(\mathrm{V}_k > 0)$ and I_k(s) are the volume fraction and scattering intensity from the k-th component, respectively, K is the number of components (usually, this number is chosen in the range of 2 to 4), each having its own analytical distribution with parameters to be determined. The characteristics of partial distributions were parameterized and restored along with their volume fractions using a non-linear least squares fitting procedure.

For the given particle shape and known normalized scattering intensity of a particle $i(sR)$ ($s = 0$, $i(0) = 1$), the scattering intensity $I_k(s)$ from the k-th component is determined as:

$$I_k(s) = T_k(s) \cdot \int_0^{\infty} N_k(R) \cdot [v_k(R) \cdot \Delta\rho_k(R)]^2 \cdot i_k(s, R) \cdot T_k(s) \cdot dR, \tag{2}$$

where the scattering vector $s = (4\pi/\lambda)\sin\theta$, ($\lambda$ is the wavelength, and 2θ is the scattering angle), $N_k(R)$ is a function of size distributions, $\Delta\rho_k(R)$, $v_k(R)$ and $i_k(s, R)$ are the contrast (the difference between the average electron density of the particle and average density of the environment), volume and normalized scattering intensity (the square of the form-factor) of the particle of the radius $R(i_{0k}(0, R) = 1)$, $T_k(s)$ is a structure factor describing the interference between particles for the k-th component in the Percus–Yevick approximation [6]. We assume or learn from TEM that the components, i.e. the particles, are mainly spherical and have different sizes. The equation (1) can be written in the normalized form as:

$$I_k(s) = V_k \frac{\int_0^{\infty} D_k(R) v_k(R) [\Delta\rho_k(R)]^2 i_{0k}(s, R) dR}{\int_0^{\infty} D_k(R) dR} \tag{3}$$

if we take the total volume of the components as:

$$V_k = \int_0^{\infty} v_k(R) N_k(R) dR \tag{4}$$

The total volume distribution function $D_k(R) = N_k(R) v_k(R)$ can be normalized to expression

$$\int_0^{\infty} D_k(R) dR = 1.$$

The analytical expression of the $D_k(R)$ is a distribution with the average particle radius R_{0k} and the half-width ΔR_k:

$$D_k(R) = G(R, R_{0k}, \Delta R_k) = \left(\frac{z+1}{R_{0k}}\right)^{z+1} \frac{R^z}{\Gamma(z+1)} \exp\left[-\frac{(z+1)R}{R_{0k}}\right], \quad z = \left(\frac{R_{0k}}{\Delta R_k}\right)^2 - 1. \tag{5}$$

The form factor in this work is the scattering amplitude from spherical particles of radius R because electron microscopy has shown that the particles are spherical.

To determine the volume fractions and other parameters characterizing the mixture, the experimental scattering intensity $I_{exp}(s)$ should be decomposed into the partial functions (3). This can be done by a non-linear minimization based on the squared residual target function:

$$\chi^2 = \sum_{j=1}^{N} \{[\, c\, I(s_j) - I_{\exp}(s_j)]/\sigma(s_j)\}^2 \tag{6}$$

where N is the number of experimental points and σ(s) denotes the statistical error. The use of the scale factor:

$$c = \frac{\sum\limits_{j=1}^{N} I(s_j) I_{\exp}(s_j)/\sigma^2(s_j)}{\sum\limits_{j=1}^{N} (I(s_j)/\sigma(s_j))^2} \tag{7}$$

allows one to fit the experimental data in a relative scale.

In order to fit experimental I_{exp} and simulated I_{mod} intensities, minimization of the non-linear quadratic functional with the V_k, R_{0k}, ΔR_k, and $T_k(s)$ parameters should be performed:

$$\begin{gathered}\min_{V_k, R_{0,k}, \Delta R_k, \Delta\rho_k} \left\{ \frac{\sum\limits_{i=1}^{N} [(I_{\exp}(s_i) - c \cdot I_{\text{mod}}\,(s_i)) \cdot W(s_i)]^2}{\sum\limits_{i=1}^{N} \left[I^2_{\exp}(s_i) \cdot W^2(s_i)\right]} \right\}, \quad k = 1, ..., K, \\ W(s_i) = \left[\tilde{I}_{\exp}(s_i)\right]^p \Big/ \tilde{I}_{\exp}(s_i), \qquad p = 1, -\frac{1}{2}, -\frac{2}{3}, -\frac{3}{4},\end{gathered} \tag{8}$$

where N is a number of experimental points, $W(s)$ is a weighting function calculated from smoothed experimental data and used to provide the optimum intensity range for all experimental s values. In this work, $p = 1/2$ was used as an optimal value obtained from the simulation, c is a fitting factor for $I_{exp}(s)$ and $I_{mod}(s)$ (7) calculated before the minimization of non-linear quadratic functional. The minimization was performed using the multivariant optimization program package OPTIS as it was applied in the program MIXTURE [4].

2.2. TEM

Imaging in TEM is provided through the mass-thickness contrast produced by incoherent (Rutherford) elastic scattering of electrons for both crystalline and non-crystalline materials. The cross-section for elastic scattering is a function of the atomic number (Z), therefore the samples containing elements with higher Z will scatter more electrons than the low-Z samples, besides the electron scattering increases from thicker areas. Therefore, the mass-thickness contrast is a universal mechanism of imaging for crystalline and non-crystalline objects.

The definition of the contrast K is the difference in intensity ΔI between two adjacent areas [7]:

$$K = \frac{I_1 - I_2}{I_2} = \frac{\Delta I}{I_2} = 1 - e^{-Q\Delta t} \cong Q\Delta t = N_0 \sigma \rho \Delta t, \tag{9}$$

where Q is the total cross section for scattering from the sample, N_0 is Avogadro's number, ρ is the density, Δt is a change in thickness, and σ is the single-atom scattering cross section dependent on energy of incident electrons $E_0(keV)$, a scattering angle θ, and proportional to atomic number square Z^2 (if the effects of electron cloud are ignored).

The number of transmitted electrons, n, through the sample with mass-thickness ρt can be approximated by the expression:

$$n = n_0 e^{-N\sigma\rho t}. \tag{10}$$

The latter formula means the decrease in the number of transmitted electrons with sample thickness, that is, the increase in the number of scattered electrons by thick samples.

High angle annular dark-field (HAADF) scanning TEM (STEM) provides a way of imaging mainly Z-contrast by collecting incoherently scattered electrons and thus possesses a strong compositional sensitivity. Diffraction contrast is a feature of crystalline materials to investigate defects, and phase contrast applied in high resolution TEM is well suited to the study of atomic structure of materials. All these types of contrast in (S)TEM are used for particle analysis and provide comprehensive information of their morphology and structure.

2.3. Origin of measurement differences and errors in SAXS and TEM

The fundamental difference between TEM and SAXS is in the nature of beams and their interaction with matter. The electrostatic Coulomb potential is the scattering matter for electron beams while the electric charge density is the scattering matter for X-rays. This difference leads to the different ways of forming intensity distributions when electron beams and X-rays penetrate through the same sample. There is a direct mathematical link between the X-ray and electron scattering through scattering amplitudes.

Using Thomson scattering equations of electromagnetic waves on the electric charge we can obtain the dependence of the amplitude of X-ray scattering $f_X(\vec{s})$ from the electron density $\rho_e(\vec{r})$ and scattering vector $\vec{r}$:

$$f_X(\vec{s}) = r_0 \iiint \frac{\rho_e(\vec{r})}{e} e^{i(\vec{s}\vec{r})} d^3\vec{r}, \tag{11}$$

where $r_0 = \dfrac{1}{4\pi\varepsilon_0} \cdot \dfrac{e^2}{m_0 c^2}$ is electron radius.

Amplitude scattering of electrons in Born approximation can be written as:

$$f_e(\vec{s}) = \left(\frac{2\pi me}{h^2}\right) \iiint \varphi_a t(\vec{r}) e^{i(\vec{s}\vec{r})} d^3\vec{r}. \tag{12}$$

Using Poisson equation $\Delta\varphi_{at} = \dfrac{\rho_{at}}{\varepsilon_0}$, the link between f_p and f_e can be derived. If the atomic charge density $\rho_{at} = \rho_n - \rho_e$, then the nuclear charge density is:

$$\rho_n(\vec{r}) = Ze\delta(\vec{r}) = \frac{1}{(2\pi)^3} \iiint eZe^{-i(\vec{s}\vec{r})} d^3\vec{s}. \tag{13}$$

Fourier transform is used to derive the electron density and atom potential through X-ray scattering and electron amplitudes:

$$\rho_e(\vec{r}) = \frac{1}{(2\pi)^3} \iiint \frac{e}{r_0} f_X(\vec{s}) e^{-i(\vec{s}\vec{r})} d^3\vec{s}, \tag{14}$$

$$\varphi_{at}(\vec{r}) = \frac{1}{(2\pi)^3} \iiint \frac{h^2}{2\pi me} f_e(\vec{s}) e^{-i(\vec{s}\vec{r})} d^3\vec{s}. \tag{15}$$

Using the Poisson equation, we obtain:

$$-s^2 \frac{h^2}{2\pi me} f_e(\vec{s}) = -\frac{1}{\varepsilon_0}\left(eZ - \frac{e}{r_0} f_X(\vec{s})\right). \tag{16}$$

Finally, taking into account that $s = 4\pi\dfrac{\sin\theta}{\lambda}$, the link between the electron and X-ray scattering amplitudes is written as:

$$f_e = \frac{1}{4\pi\varepsilon_0} \cdot \frac{me^2}{2h^2} \cdot \frac{Z - f/r_0}{(\frac{\sin\theta}{\lambda})^2}. \tag{17}$$

This formula shows the linear dependence between the electron and X-ray scattering amplitudes and their ratio is $f_e : f_X = 10^3 : 1$. Direct proportionality between f_e and Z leads to Ag nanoparticles with high Z on/in the carbon (low Z) substrate having a significant contrast in TEM images. While SAXS is able to provide reliable information about small particles of 1 to 1.5 nm in diameter if their concentrations are high enough and this scattering intensity exceeds that by some density fluctuations of solvents and organic material agglomerations.

Difficulties in recognition of the smallest particles from SAXS data in the range of the sizes from 1 to 5 nm in the heterogeneous polymer solutions is strongly dependent upon the distribution profile on the shape of the scattering curve at angles greater than s = 0.5 – 1 nm^{-1}, which is largely dependent on the scattering from other small inhomogeneities in the solution. This may lead to false peak appearance in the size distribution or to its shift to larger or smaller sizes.

In Table 1, we highlight and summarize the causes of errors due to instrumental properties, features of the samples, data collecting and data processing. The main conclusion from Table 1 is that TEM is most efficient for local analysis since it performs imaging and composition/phase identification, while SAXS produces integral information which depends on the initial hypotheses as to the shape, sizes and state of matter.

There is no methodological limitation to reveal polydisperse distributions of the nm-sized particles using modern TEM equipment, and the reliable statistics can be reached by counting the sufficient number of particles using the relevant software, which significantly reduces the time-consuming efforts.

SAXS can be very useful (fast and reliable) for monitoring the monodispersed particles distributions or a narrow polydispersity in industrial laboratories with the possibility of measuring the total surface of samples.

TABLE 1. Summary of origin of errors in sizing particles due to instrumental properties, sample features, and data collecting and processing

	TEM	SAXS
Instrumental	Images as particle projections. Small volume of material under investigation (sample thickness ≤500 nm) Loss of contrast when the fine beam is used.	Divergence of the X-ray beam and the spread of scattering angles. Halo of parasitic radiation around the direct beam. Loss of intensity when the fine beam is used. Parasitic scattering (the need of monochromators)
Sample	Deterioration of particle contrast due to burying in the polymer film. Deterioration of particle contrast due to carbon contamination because of electron irradiation of organic material. Possible deformation of the particle shape due to drying	Widely different particle shapes provide only slightly different scattering curves. Particles with different composition give similar scattering curves. Scattering by large particles (above 300 nm) Double Bragg reflection form crystallites.
Data collecting and processing	Sampling is not random and is often determined by the nice appearance of particles. Great operating skill is required to get properly focused images of nanoparticles especially in STEM images. Time consuming manual measurements or inappropriate software leading to insufficient statistics.	Assumptions about the form of the distribution functions are required. All generalized definitions are derived assuming that all particles in the sample are identical. Similar scattering curves for different diameter distribution functions.

3. Experimental: Materials and Methods

Silver nanoparticles were synthesized by the chemical reduction of 0.3 M silver nitrate in aqueous solutions of 2 wt. % 2-deoxy-2-methacrylamido-D-glucose (MAG)/2-(dimethylamino) ethyl methacrylate (DMAEMA) copolymers or pure DMAEMA and MAG homopolymers at room temperature and pressure. All synthetic details are given elsewhere [8, 9]. Selenium particles were obtained by reduction of selenious acid using ascorbic acid and stabilized by poly(2-acrylamido-2-methylpropane sulfonic acid) (PAMPS) or by polyvynilpyrrolidon (PVP) in aqueous solutions. Details of the process are described elsewhere [10, 11].

TEM-HRTEM-STEM and X-ray energy dispersive spectrometry (chemical miscoanalysis) investigation of Ag nanoparticle samples – polymer water and Se nanoparticle – polymer water suspensions (1.0 – 2.0-μl droplets) lying on carbon films/Cu grids after drying were investigated by transmission (TEM), scanning transmission electron microscopy (STEM) and X-ray energy dispersive spectroscopy in a FEI Tecnai Osiris microscope (200 kV X-FEG field emission gun). The particle diameters were measured using the new method [3] based on approximation of the calculated distribution of grey level to the real distribution in (S)TEM images providing the best accuracy in measurements of the particle diameters in contrast to algorithms based on image thresholding approach.

Small-angle X-ray scattering (SAXS) measurements were carried out on a laboratory diffractometer “AMUR-K” in the Institute of Crystallography, Moscow [12] at the Cu-K$_\alpha$ wavelength $\lambda = 0.154$ nm using the Kratky-type collimation system. The linear position-sensitive proportional detector used provided the range of the scattering vector modulus $0.11 < s < 15$ nm^{-1} ($s = 4\pi \sin\theta/\lambda$, where 2θ is the scattering angle). Solution samples were placed in a 1 mm quartz capillary with 0.01 mm walls. The obtained scattering profiles were preprocessed by the program package PRIMUS [13] to correct the water scattering and instrumental effects [14]. The volume particle distributions were obtained with the MIXTURE program [4, 13] approximating the particles as spheres. The model volume distributions were presented as three superimposed Schulz distributions with different parameters chosen by progressive iterations during fitting the experimental and calculated scattering intensities.

4. Results and Discussion

4.1. Ag particles

(S)TEM images of silver particles obtained in MAG-DMAEMA copolymer solutions with DMAEMA mole fractions 12, 44, and 100 % are shown in Fig. 1(a,b,c) with the experimental scattering curves and data processing.

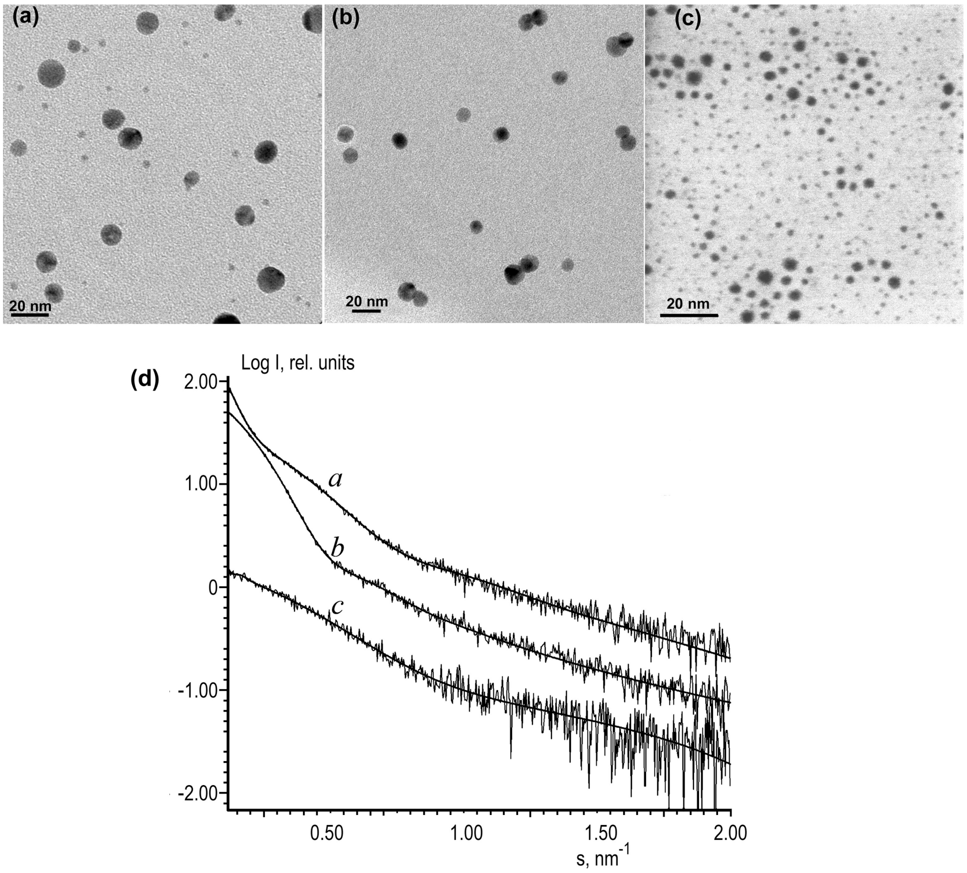

FIG. 1. TEM images (a, b, c) of Ag particles, experimental and approximated (solid lines) SAXS curves (d) obtained from the samples of Ag particles in polymer solutions: MAG–12 % DMAEMA (a), MAG–44 % DMAEMA (b) and pure DMAEMA (c)

The SAXS volume distribution functions and the volume and particle distributions obtained by TEM for Ag particles in three samples with different copolymers are superimposed in Fig. 2.

The mode diameter values of Ag particles measured by SAXS and TEM/STEM with standard deviations are given in Table 2. The absolute difference in these values is 4 nm and the relative can reach 60 %. We can see the shift of the peaks in TEM volume histograms relative to SAXS maximums in volume distribution functions to the side of smaller sizes for the samples with the single mode distributions and to the side of larger diameters for the double mode distributions. The largest difference close to 60 % is observed for the particles in pure DMAEMA homopolymer. We reported earlier [9] that the particles in this sample had the smallest diameters with the mode diameter between 2 and 4 nm, which is the principal limit for SAXS measurements. The difference in mode diameter for two copolymers does not exceed 29 %. The origin of higher value of mode diameter revealed by SAXS for particles in pure DMAEMA and MAG–44 % DMAEMA copolymer can be associated with the formation of a protective polymer shell around particles, which also contributes to small-angle scattering. It is quite probable that a protective shell was formed for particles in MAG–12 % DMAEMA solution, however, the effect of size averaging in polydisperse system with bimodal distribution resulted in some shift of the SAXS volume distribution function peak towards smaller diameters.

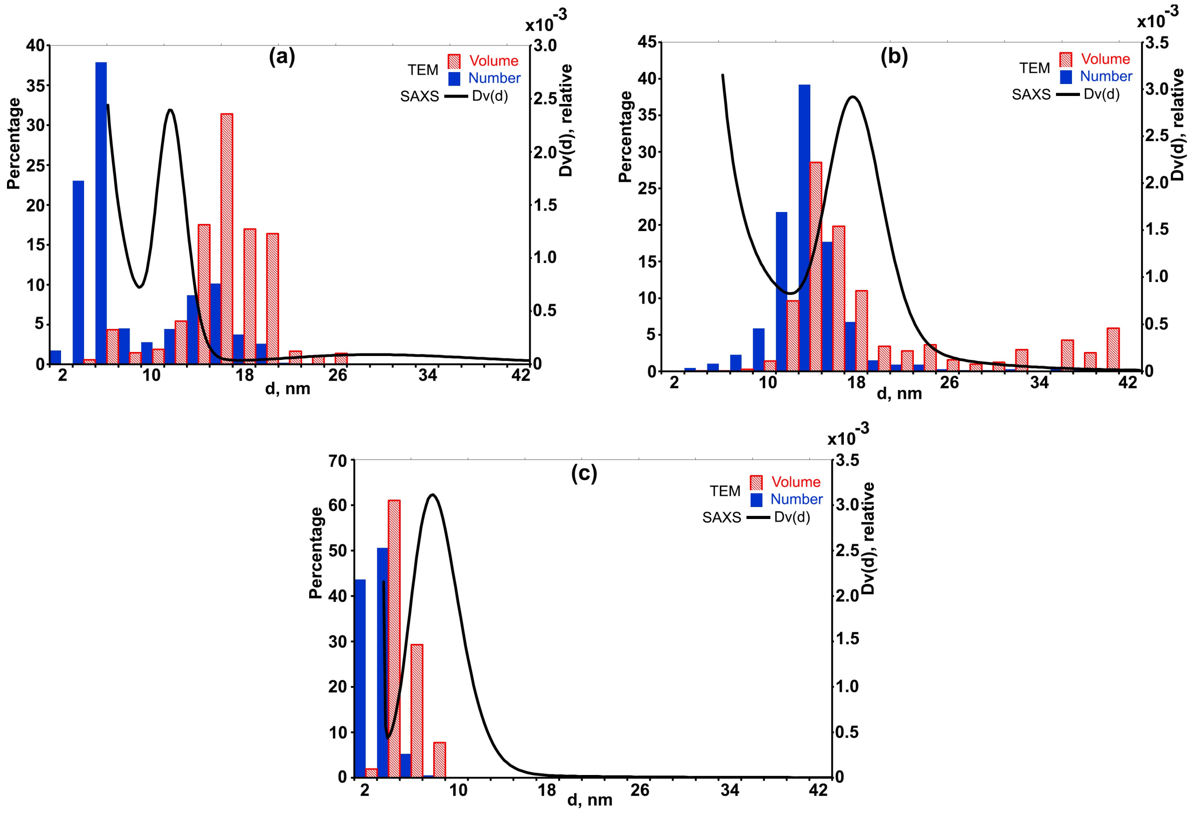

FIG. 2. Volume distribution functions (solid lines) superimposed with histograms of volume and particles distributions vs. particle diameters in two copolymer solutions MAG–12 % DMAEMA (a), MAG–44 % DMAEMA (b), and pure DMAEMA (c)

TABLE 2. Mode diameters of Ag particles in volume distributions obtained by SAXS and TEM/STEM

Sample	Mode diameter, nm	
	TEM	SAXS
Ag in MAG+12 % DMAEMA	17±2	12±2
Ag in MAG+44.5 % DMAEMA	13±2	17±2
Ag in pure DMAEMA	3±2	7±2

4.2. Se particles

TEM images of selenium particles obtained in aqueous PAMS and PVP polymer solutions are shown in Fig. 3(a,b) with their experimental and approximated (solid lines) SAXS intensity curves (Fig. 3(c)). The SAXS volume distribution functions and the volume and particle distributions obtained by TEM for Se particles in PAMS and PVP polymers are superimposed in Fig. 4. The accuracy of distribution parameters for the 3-component models was 2–8 % (in diameter) and 20–40 % for the distribution half-width. The mode diameters of particles measured with TEM and SAXS with standard deviations are listed in Table 3.

TABLE 3. Mode diameters of particles in PVP and PAMS solutions obtained from SAXS scattering

Sample	Mode diameter, nm	
	TEM	SAXS
Se+PVP	53±2	20±3
Se+PAMS	65±2	29±4

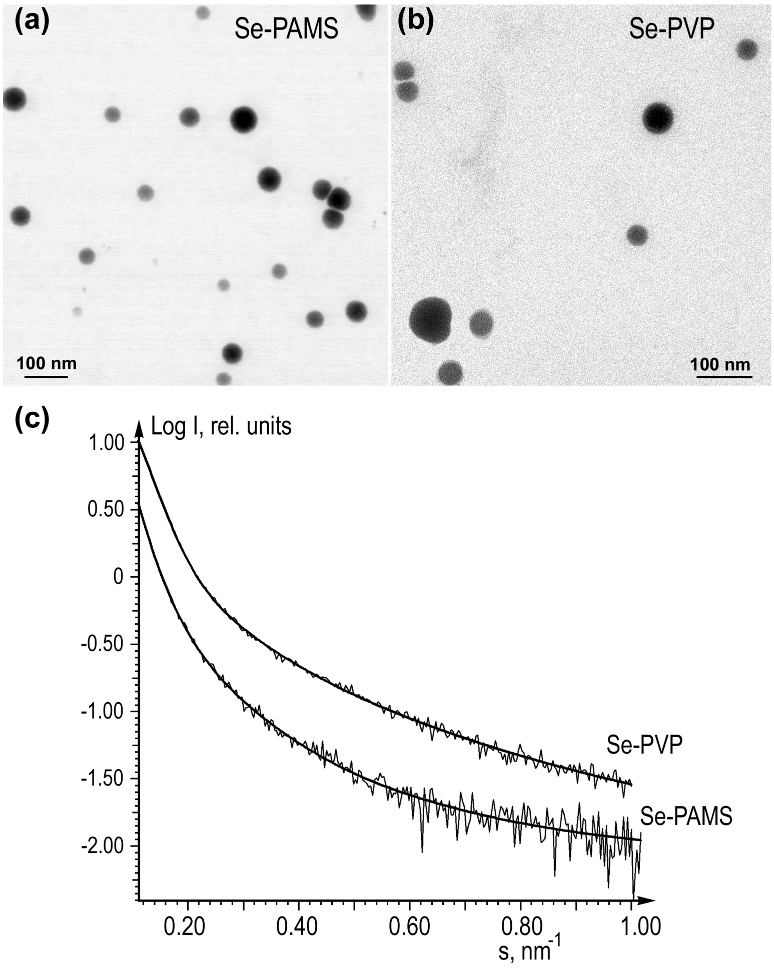

FIG. 3. TEM images of Se particles formed in PAMS (a) and PVP (b) solutions, the experimental and approximated (solid lines) SAXS intensity curves (c)

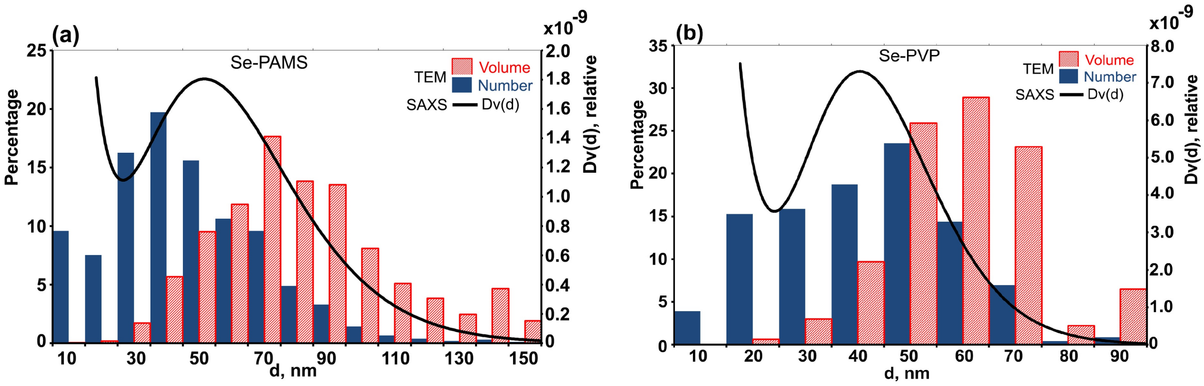

FIG. 4. Volume distribution functions (solid curves) superimposed with histograms of volume and particles distributions vs. particle diameters in Se + PAMS (a), and Se + PVP (b) samples

In contrast to Ag particles, the mode diameters for Se particles differ by more than two-fold in SAXS and TEM measurements. The explanation of this result is in nature of particles. TEM and STEM images (Fig. 5(a,b)) show groups of 2 or 3 deformed particles. The deformation occurred due to surface tension when the TEM sample of water suspension was drying on a carbon film. Obviously, the deformation of particles occurred in the lateral direction when the particles met each other and in the vertical direction under surface tension and gravity, and Se particles became oblate spheroids that are spheroids flattened at the poles. Thus, in the case of soft Se particles, TEM provides only projections of spheroids with larger diameters than those of spherical particles, while SAXS determines the true mode diameters of Se particles.

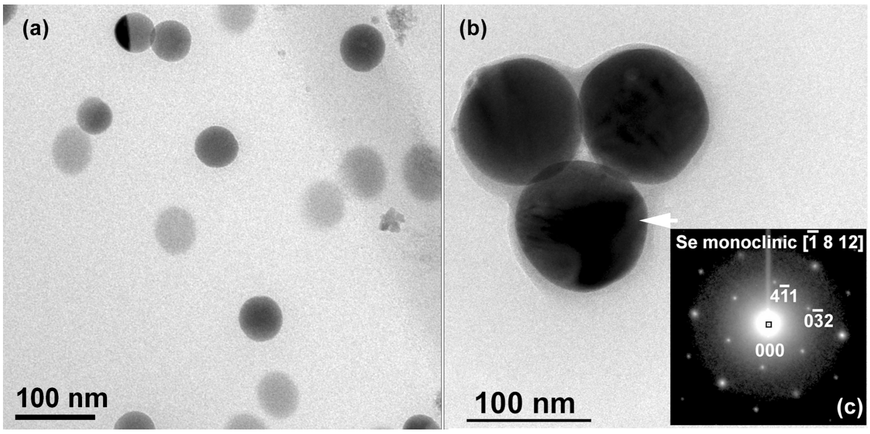

FIG. 5. TEM image of Se particles from the PAMS solution with strong and weak contrast of particles (a), three crystalline Se particles with strong contrast (b), and the corresponding SAED pattern taken from one of the particles (indicated by arrow) along the [−1 8 12] direction in monoclinic Se

Cryogenic TEM can be used to investigate soft Se particles, which can be frozen in a thin water layer, or to image particles located in thin edges of vacuum-dried polymer films. In both cases, the statistics are quite low due to small number of available particles and radiation damage which has a significant effect.

But first, not all grouped Se particles are deformed and second, Se particles in the same sample have different contrast (Fig. 5(a)). Only TEM answers the question as to why Se particles have different structure. They can be crystalline with monoclinic structure, which was discovered by electron diffraction (Fig. 5(b,c)) and these particles are dark in TEM images. They keep the spherical shape and do not deform under surface tension. While other particles do not have crystalline structure, and are not always pure Se particles but Se/polymer composite particles with a different content of polymer inside particles (Fig. 6). X-ray energy dispersive spectrometry (chemical microanalysis) showed different amount of polymer material inside of particle with Se.

Earlier [15], we proposed the mechanism of formation for Se/polymer composite particles and that their rigidity and density differ from the crystalline Se and amorphous Se particles. Also, it was concluded that such differences can influence the biological and medical properties of the particles.

5. Conclusion

In summary, silver and selenium particles obtained and stabilized in different polymer solutions were studied by SAXS and TEM to characterize the size distributions and structure. It was found that numerical difference in the mode diameter values derived from the TEM and SAXS measurements can be caused by various reasons. The SAXS results can be misleading in the case of small particles with the mode diameter of about 2–4 nm (Ag particles in the pure DMAEMA polymer solution) due to instrumental limits and TEM can give unambiguous information on the size distribution with sufficient statistics.

Averaging the sizes in colloid systems with bimodal size distribution by SAXS shifts the maximum into some intermediate position as for Ag particles in MAG–12 % DMAEMA suspension.

Different mode diameter values for nanoparticles coated by the polymer shells measured by X-rays scattering and TEM images can be explained by low contrast of thin polymer shell in TEM images.

SAXS is efficient in characterization of soft particles like Se/polymer composite particles in the range of diameters from 20 to 100 nm. TEM characterization of such soft particle leads to artificial increase of diameters

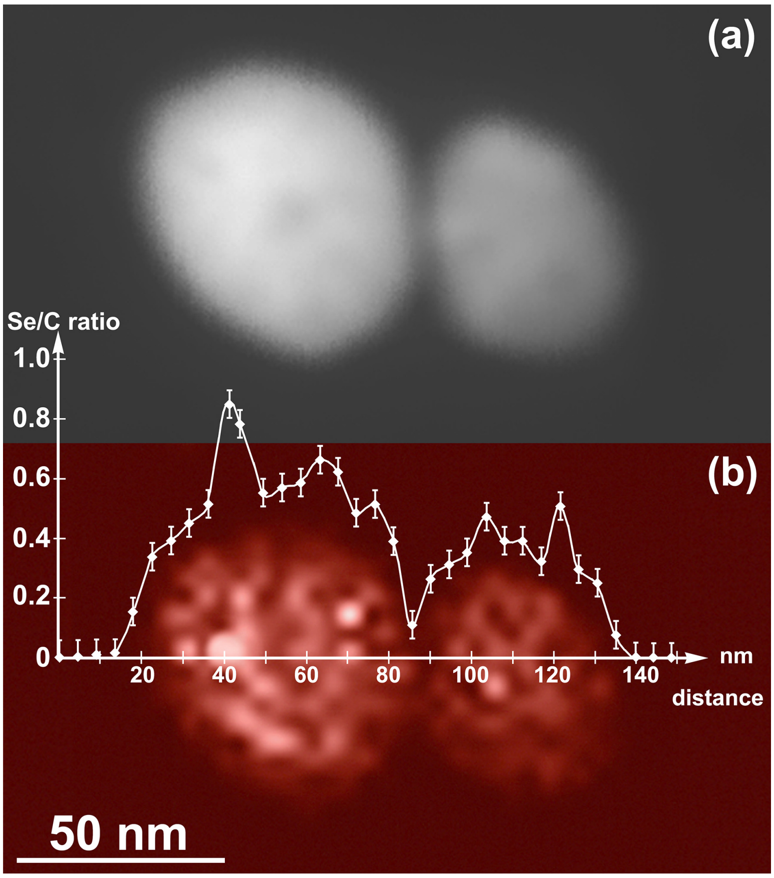

FIG. 6. STEM image and Se/C chemical map with the ratio profile across the Se/PAMS composite particles

due to particle deformation and shape transformation from spherical to oblate spheroids. At the same time TEM study is mandatory to reveal the chemical and structural features of such particles.

Acknowledgments

The authors are thankful to Prof. P. A. Buffat (École Polytecnique Fédéral de Lausanne) for the help in electron microscopy analysis, discussions and comments to the paper.

References

[1] Chu B., Liu T. Characterization of nanoparticles by scattering techniques. *J. Nanopart. Res.*, 2000, **2**, P. 29–41.
[2] Pedersen J.S. Analysis of small-angle scattering data from colloids and polymer solutions: modeling and least-squares fitting. *Adv. Colloid. Interfac.*, 1997, **70**, P. 171–210.
[3] Shvedchenko D.O., Suvorova E.I. A novel method of automated statistical analysis of polymer stabilized metal nanoparticles in electron microscopy images. *Crystallogr. Rep.+*, 2017, **62**(5), P. 802–808.
[4] Svergun D.I., Konarev P.V., Volkov V.V., Koch M.H.J., Sager W.F.C., Smeets J., Blokhuis E.M. A small angle x–ray scattering study of the droplet–cylinder transition in oil–rich sodium bis(2–ethylhexyl) sulfosuccinatemicroemulsions. *J. Chem. Phys.*, 2000, **113**, P. 1651–1665.
[5] Svergun D.I. Small-angle scattering studies of macromolecular solutions. *J. Appl.Cryst.*, 2007, **40**, P. s10–s17.
[6] Percus J.K., Yevick G.J. Analysis of Classical Statistical Mechanics by Means of Collective Coordinates. *Phys. Rev.*, 1958, **110**, P. 1–13.
[7] Williams D.B., Carter C.B. *Transmission Electron Microscopy*. Plenum Press, New York, 1996, 729 pp.
[8] Nekrasova T.N., Zolotova Y.I., Nazarova O.V., Levit M.L., Suvorova E.I., Sirotkin A.K., Baklagina Y.G., Didenko E.V., Pautov V.D.,Panarin E.F. Silver nanocomposites based on (Co)polymers of 2-deoxy-2-methacrylamido-D-glucose, N-vinylamides, and aminoacrylates. *Dokl. Chem.*, 2013, **446**, P. 212–214.
[9] Shvedchenko D.O., Nekrasova T.N., Nazarova O.V., Buffat P.A., Suvorova E.I. Mechanism of formation of silver nanoparticles in MAG–DMAEMA copolymer aqueous solutions. *J. Nanopart. Res.*, 2015, **17**, P. 275.
[10] Valueva S.V., Kopeikin V.V., Kipper A.I., Filippov A.P., Shishkina G.V., Khlebosolova E.N., Rumyantseva N.V., Nazarkina Y.I., Borovikova L.N. Formation of Zero-Valence Selenium Nanoparticles in Polyampholyte Aqueous Solutions in the Presence of Redox Systems. *Polym. Sci. Ser. B+*, 2005, **47**, P. 143–146.

[11] Valueva S.V., Kipper A.I., Kopeikin V.V., Borovikova L.N., Lavrent'ev V.K., Ivanov D.A., Filippov A.P. Formation and Morphological Characteristics of Selenium-Containing Nanostructures Based on Rigid-Chain Cellulose Derivatives. *Polym. Sci. Ser. A+*, 2006, **48**, P. 803–810.

[12] Mogilevsky L.Yu., Dembo A.T., Svergun D.I., Feigin L.A. Small-angle scattering diffractometer with single coordinates detector. *Crystallogr. Rep.+*, 1984, **29**, P. 587–591.

[13] Konarev P.V., Volkov V.V., Sokolova A.V., Koch M.H.J., Svergun, D.I. PRIMUS: a Windows PC-based system for small-angle scattering data analysis. *J. App.Cryst.*, 2003, **36**, P. 1277–1282.

[14] Feigin L.A., Svergun D.I. *Structure Analysis by Small-Angle X-Ray and Neutron Scattering*. Plenum Press, New York, 1987, 335 pp.

[15] Suvorova E.I., Klechkovskaya V.V. Effect of polymer matrix on structure of Se particles formed in aqueous solutions during redox process. *Crystallogr. Rep.+*, 2010, **55**, P. 1116–1121.

NANOSYSTEMS: PHYSICS, CHEMISTRY, MATHEMATICS, 2017, 8 (4), P. 523–530

The XPS investigations of the surface composition of nanoscale films formed by thermal oxidation of V_xO_y/InP heterostructures

B. V. Sladkopevtcev[1], E. V. Zolotukhina[2], E. V. Tomina[1], I. Ya. Mittova[1]

[1]Voronezh State University, Universitetskaya pl., 1, Voronezh, 394018, Russia

[2]Institute of Problems of Chemical Physics of RAS,
Semenov avenue, 1, Chernogolovka, 142432, Russia

dp-kmins@yandex.ru

DOI 10.17586/2220-8054-2017-8-4-523-530

The dependence of oxide films surface layers' compositions on the method of depositing of V_2O_5 on InP and regimes of thermal oxidation of the formed heterostructures was established by the XPS method. Lower indium content near the surface for all samples in comparison with the standard indicates a partial blocking of its diffusion into films during the chemostimulated thermal oxidation of the semiconductor. The presence of vanadium oxides in certain oxidation states and their ratio depends on the method of deposition for the chemostimulator, and on the regime of thermal oxidation. In the case of the electric arc synthesis method, at shorter reaction times, vanadium compounds in the +4 and +5 oxidation states were present in the near-surface layer, which gives evidence for the catalytic mechanism.

Keywords: indium phosphide, XPS, nanoscale films, vanadium pentoxide, thermooxidation.

Received: 30 July 2017

Revised: 5 August 2017

1. Introduction

Oxide films, grown by thermal oxidation of the $A^{III}B^{V}$ semiconductor materials, have poor dielectric properties [1] unlike films, formed by oxidation of elemental semiconductors such as silicon. Inherent to the mechanism of phosphides oxidation formation of component A in the free form [1] with simultaneous evaporation of P_2O_5 leads to a "metallizing" the film and degradation of its surface.

However, indium phosphide, in comparison with silicon, is a direct-gap semiconductor, and therefore it can be used in areas related to the conversion of electromagnetic radiation. Oxidation of InP (thermal, chemical, electrochemical, anodic and plasmic) makes it suitable for the creation of high-frequency field-effect transistors and long-wavelength lasers (based on MIS structures), solar cells (multilayer heterostructure (Indium tin oxide)/InP) etc. [2, 3].

The poor quality of $A^{III}B^{V}$ oxide films grown on clean substrates can be overcome by introducing a system of chemostimulators, altering the mechanism of oxidation, accelerating the growth of films on the surface of a semiconductor with simultaneous modification of their structures and properties.

The introduction of a chemostimulator in the oxidation system is possible in two ways: 1) through the gas phase in the thermal oxidation process; 2) directly on the semiconductor surface in the form of films or nanoscale islands before oxidation [4, 5]. In the latter case, two groups of methods were used: hard (magnetron sputtering, electric explosion), acting on the surface prior to the thermal oxidation; soft (sol-gel processes, low-temperature metalo-organic chemical vapor deposition (MOCVD), etc.), which made little change to the surface during the process of chemostimulator deposition. The unique properties of the V_2O_5 chemostimulator allow the use of both the approaches and the two groups of methods (in one approach) deposition on the surface of InP. A distinctive feature of the vanadium oxides, in particular its pentoxide, is transition mobility $V^{+5} \leftrightarrow V^{+4}$, allowing both the catalytic and transit mechanisms of InP thermal oxidation [4]. In previous studies, the phase composition of the films was constantly monitored by X-ray diffraction, but a detailed examination of the surface layer requires establishing the peculiarities of the effect of the heterostructure synthesis method on the mechanism of their thermal oxidation. The use of X-ray photoelectron spectroscopy (XPS) allows investigating this urgent issue and it was used for the first time for these studies. The goal of this study was establishing the dependence of the composition of the surface of films formed by thermal oxidation of V_xO_y/InP heterostructures upon the method of chemostimulator application and the thermal oxidation regime by the XPS method.

2. Experimental

In this experiment, the polished substrates of monocrystalline indium phosphide FIE-1A (100), with a concentration of majority carriers no lower than $5{\cdot}10^{16}$ /cm^{-3} at 300 K, n-type conductivity (doped by Sn), wafers of 0.5 mm thickness were used.

Before the synthesis of heterostructures, the surfaces of the semiconductors were treated with H_2SO_4 (reagent grade, Russian State Standard GOST 4204-77, 92.80 %) : H_2O_2 (analytical grade, Russian State Standard GOST 177-88, 56 %): H_2O = 2 : 1 : 1 etchant [6] for 10 min and then rinsed repeatedly in doubly-distilled water and air-dried to remove a natural oxide film surface and various contaminants.

The chemostimulator (vanadium pentoxide) was deposited on the surface of the semiconductor by the method of electric explosion of conductor (EEC, hard method) and by method of deposition of V_2O_5 gel via aerosol phase (soft method).

Synthesis by method of electric explosion conductor was performed in a modified vacuum universal post Shimadzu at a chamber pressure of 1.333 Pa. The residual oxygen in the system was sufficient to oxidize the metallic vanadium to vanadium pentoxide. A vanadium wire with the diameter of 0.5 mm and the length (L) of 30 mm (main substance content of 99.99 %) served as the explodable conductor. The voltage was 110 V. The distance (H) between the source and the substrate was 25 mm. Under these conditions, islands of V_2O_5 were deposited on the surface of the InP with an admixture of metallic V, which under thermal oxidation conditions, also transformed into vanadium pentoxide (XRD data [7]). Thus islands of nanoheterostructures (V_2O_5)/InP were formed. According to scanning electron (SEM) and scanning tunneling (STM) microscopy [5, 7] the lateral dimensions of islands ranged from 80–150 nm, their surface concentration – 15–20 mkm^{-2}. The choice of such a regime is justified by numerous experiments [5, 7] and is due to optimization to maximize the rate of thermal oxidation for the nanoisland heterostructures compared with that of pure InP, which has been adopted as the standard.

The second method consisted of using a vanadium pentoxide gel and precipitation of it from the aerosol phase using a compressor disperser, using a detailed previously-described synthetic procedure is described in the study [8]. The freshly prepared V_2O_5 gel was precipitated for 3 min onto a cooled InP substrate. For the removal of the chemically bound water and crystallization of the resulting amorphous layers, the samples were thermally annealed in the flowing quartz reactor of a horizontal resistance heating furnace (MTP-2M-50-500) with temperature accuracy of ±1 °C (OWEN TRM-10) at 200 °C during 60 min. At the same time, layers of nanometer thickness range (20–25 nm) were formed on the semiconductor surface. The specific use of vanadium pentoxide gel leads to a complication in the composition of the layers deposited, vanadium oxides of varying oxidation states are present in them even before the start of the thermal oxidation process (X-ray phase analysis data [XRD] [9]). The composition is also affected by the annealing parameters; therefore, the corresponding thin-film heterostructures were subsequently labeled as V_xO_y/InP.

The samples of heterostructures synthesized by these methods and InP standards without a chemostimulator were thermally oxidized in the same apparatus at temperatures of 500 and 530 °C in a flow of oxygen at a flow rate of 30 l/h (linear velocity 10 cm/min). A method with full oxidation was used. This method includes the termination of the process at certain intervals to control the thickness, followed by thermal oxidation, until the total process time reached a maximum value of 60 min.

The thickness of the growing films was determined by the express ellipsometric method using a single-wavelength laser ellipsometer LEF-754 with a HeNe laser (radiation wavelength was 632.8 nm, the accuracy was ±1 nm) at three surface points with an averaging of the obtained data.

The composition of the films near the outer interface was investigated by X-ray photoelectron spectroscopy (XPS) using the SIA 100 CAMECA-Riber spectrometer (studies were carried out at the University of Burgundy, Carnot Institute, Dijon, France). Despite the fact that the thickness of the investigated films does not exceed 80 nm, this method, due to its nature, gives a representation of the composition of the near-surface layer (2 nm). The processing of the spectra was done using CasaXPS software: smoothing spectra, subtracting the background using a linear function, approximation of the photoelectronic lines was carried out using the Gaussian function. The comparison and identification of compounds was based on data from literature sources and databases [10].

3. Results and discussion

Table 1 shows the characteristics of the samples studied by the XPS method, after thermal oxidation in an oxygen atmosphere.

TABLE 1. Characteristics of studied samples

Sample no.	**Method for the production of heterostructures**	**Thermal oxidation mode**	**Film thickness, nm**
1	InP (reference)	530 °C, 60 min	54
2	(V_2O_5)/InP: electric explosion, wire length 30 mm, distance 25 mm		28
3	(V_2O_5)/InP: electric explosion, wire length 30 mm, distance 25 mm	530 °C, 60 min	80
4	(V_2O_5)/InP: electric explosion, wire length 30 mm, distance 25 mm	500 °C, 60 min	48
5	V_xO_y/InP: precipitation of the gel from the aerosol, annealing at 200 °C, 60 min	500 °C, 60 min	55

It is known that the XPS method is mainly a method of elemental analysis, but based on the magnitude of the chemical shift the binding energy can be related to the corresponding compound [11]. First, let us consider the general patterns obtained from the analysis of X-ray spectroscopy data.

TABLE 2. The quantitative content of elements in the samples (according to XPS data)

Sample no.	**Content of elements, %**			
	O	**P**	**In**	**V**
1	41.3	3.0	22.1	0.0
2	39.0	1.9	17.2	2.9
3	43.2	3.7	16.7	2.5
4	42.5	2.7	18.1	3.8
5	44.1	0.3	0.4	14.2

O 1s level. In all samples, peaks, which can be decomposed into several components corresponding to different binding energies, were found. Peaks with a binding energy of 528.9–530.8 eV were characteristic for oxygen in indium and vanadium oxides [12]. In addition, sample no. 3 revealed an additional peak corresponding to a higher binding energy of 531.6 eV, corre-sponding to the O–P bond in oxides or phosphates [13].

P 2p level. In all samples, a peak corresponding to the binding energy of 132.7 eV (132.6 and 132.8 eV) which is attributed to the P–O bond in the phosphates HPO_4^{2-} was detected [14]. The P–O bond, characteristic for phosphorus oxides P_2O_5 was higher based on energy (135.6 eV [15]). Consequently, during oxidation, indium phosphate compounds and not phosphorus oxides were formed, but their number in all cases was very insignificant. This fact is associated with intensive evaporation of the volatile component – phosphorus in the form of its volatile oxide from the samples, which is especially manifested in nano-island structures with the given oxidation parameters.

In 3d level. In the indium spectra, doublet peaks characteristic for unoxidized indium (443.5 and 451.1 eV) and its oxygen-containing compound In_2O_3 (444.2 and 452.1 eV) were observed [1].

V 2p level. In samples no. 2–5, the doublet peaks $V2p_{1/2}$ (522–523.9 eV) and $V2p_{3/2}$ (515.4–517.2 eV), characteristic for the V–O bond in vanadium oxides of different oxidation states: V_2O_3, VO_2, V_2O_5 [16,17], which correlates, to a certain extent with the XRD data obtained for these samples in earlier studies were detected [5].

For samples 2 and 3, which were nano-island (V_2O_5)/InP heterostructures formed by the EEC method, and were oxidized at the same temperature (530°C) with different durations – 10 minutes. (no. 2) and 60 min (no. 3), the peaks corresponding to the oxygen-element bonds in the oxides were somewhat different in shape (Figs. 1(a,b)); with increasing thermal oxidation time, the peak becomes asymmetric. This was explained by the increased indium oxide content in films, which is one of the main reaction products. Along with the phosphate phases [1] indium oxides were predominant, at the final stages of the process. The peaks that correspond to phos-phorus in the two compared samples correspond to the P–O bonds in the phosphates (HPO_4^{2-} group).

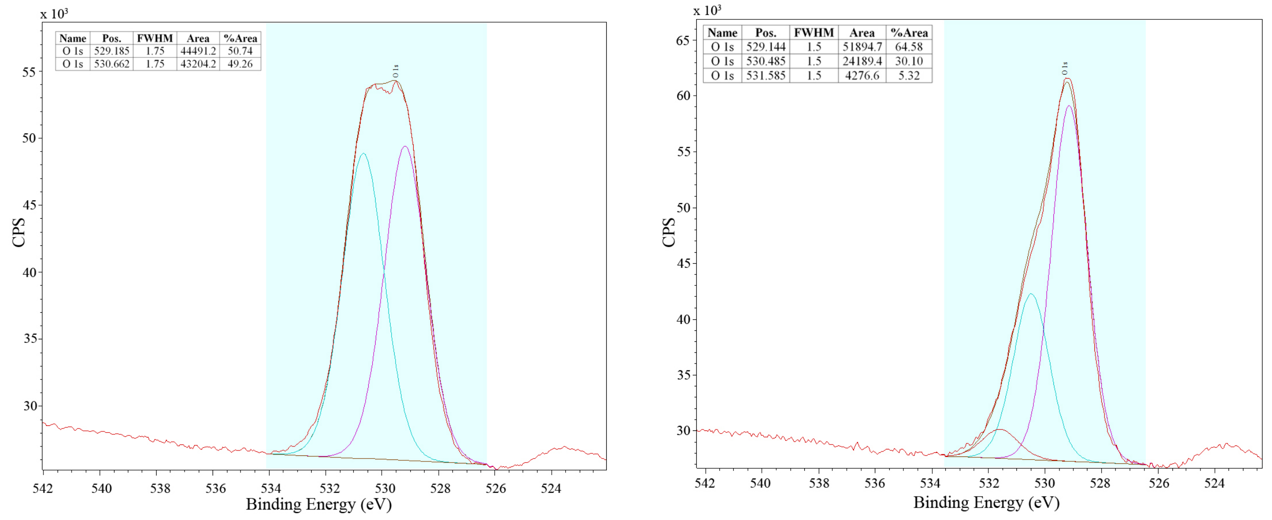

Name	Pos.	FWHM	Area	%Area
O 1s	529.185	1.75	44491.2	50.74
O 1s	530.662	1.75	43204.2	49.26

Name	Pos.	FWHM	Area	%Area
O 1s	529.144	1.5	51894.7	64.58
O 1s	530.485	1.5	24189.4	30.10
O 1s	531.585	1.5	4276.6	5.32

(a) (b)

FIG. 1. XPS for the O1s- region for nano-island (V_2O_5)/InP heterostructures, formed by the EEC method and thermooxidized in oxygen under the following conditions: 530 °C, 10 min (a) and 530 °C, 60 min (b)

Indium in samples no. 2 and 3 was present both in the form of In_2O_3 and in the form of unoxidized In. Thus, correlation with spectral ellipsometry data [18] was detected, indicating absorption near 500 nm, caused by the presence of unoxidized indium in films. For nano-island heterostructures, at short oxidation times, the presence of peaks corresponding to the semiconductor substrate was noted and it was associated with the specificity of these samples themselves - an incomplete initial coating by the surface chemostimulator. At low oxidation times, the surface undergoes extensive overgrowth in the lateral direction, thus nanoscale islands act as active catalytic centers.

The total content of vanadium in samples no. 2 and 3 was different, being somewhat higher in sample no. 2 (Figs. 2(a,b), Table 2). Vanadium was mainly present in the form of oxides (peaks corresponding to V–O bonds), VO_2, V_2O_5 were predominant, and after 60 min of oxidation (sample no. 3), peaks corresponding to V_2O_5 were mainly observed. The presence of vanadium compounds in oxidation states of +4 and +5 at the initial stage of oxidation (the first 10 min) confirms the catalytic mechanism of the process due to the easy transition $V^{+5} \leftrightarrow V^{+4}$ [19]. During the advanced stage of oxidation, the effect of V_2O_5 islands was practically absent; the process is actually the proper oxidation of indium phosphide [5], which was due to the peculiarities of the V_2O_5 presence in a small amount on the surface (islands).

The comparison of the XPS results for the two samples (no. 2 and 3) and the reference (sample no. 1) demonstrated that the intensity of the phosphorus peaks was approximately the same for samples no. 1 (reference) and no. 2 (oxidation for 10 min at 530 °C) and slightly less for sample no. 3 (oxidation for 60 min at 530 °C). In the reference sample, as well as in samples no. 2 and 3, indium is also present in the form of In_2O_3 and In, however, based on the intensity of the corresponding peaks, the content of In is in free form is higher for the reference, which demonstrates partial blockage of the diffusion of indium into the growing film by chemostimulator, even in the case when it present in the form of islands on the surface of the semiconductor (Figs. 3(a–c)).

Comparison of samples of the same type (the same optimal EEC parameters, see Table 1), oxidized for the same time, but at different temperatures (530 °C (no. 3) and 500 °C (no. 4)), allowed detecting the dependence of the surface composition of the films upon the temperature of the oxidation process.

The peaks for oxygen were generally similar in intensity and shape (the difference in temperature was not too significant – 30 degrees, which explains this similarity) and corresponded to oxides, in particular, vanadium pentoxide and indium oxide (Fig. 1(b), Fig. 4(a,b)).

The phosphorus peaks had a similar shape and corresponded to the P–O bonds in phosphates. In both samples, indium predominates in the form of its oxide, but free indium was also present, indicating incomplete blocking of its diffusion into the film during the studied process. Vanadium in both samples was mainly present in the form of V_2O_5 and VO_2, but at a lower temperature, after 60 min of oxidation, vanadium oxide (III) was also found.

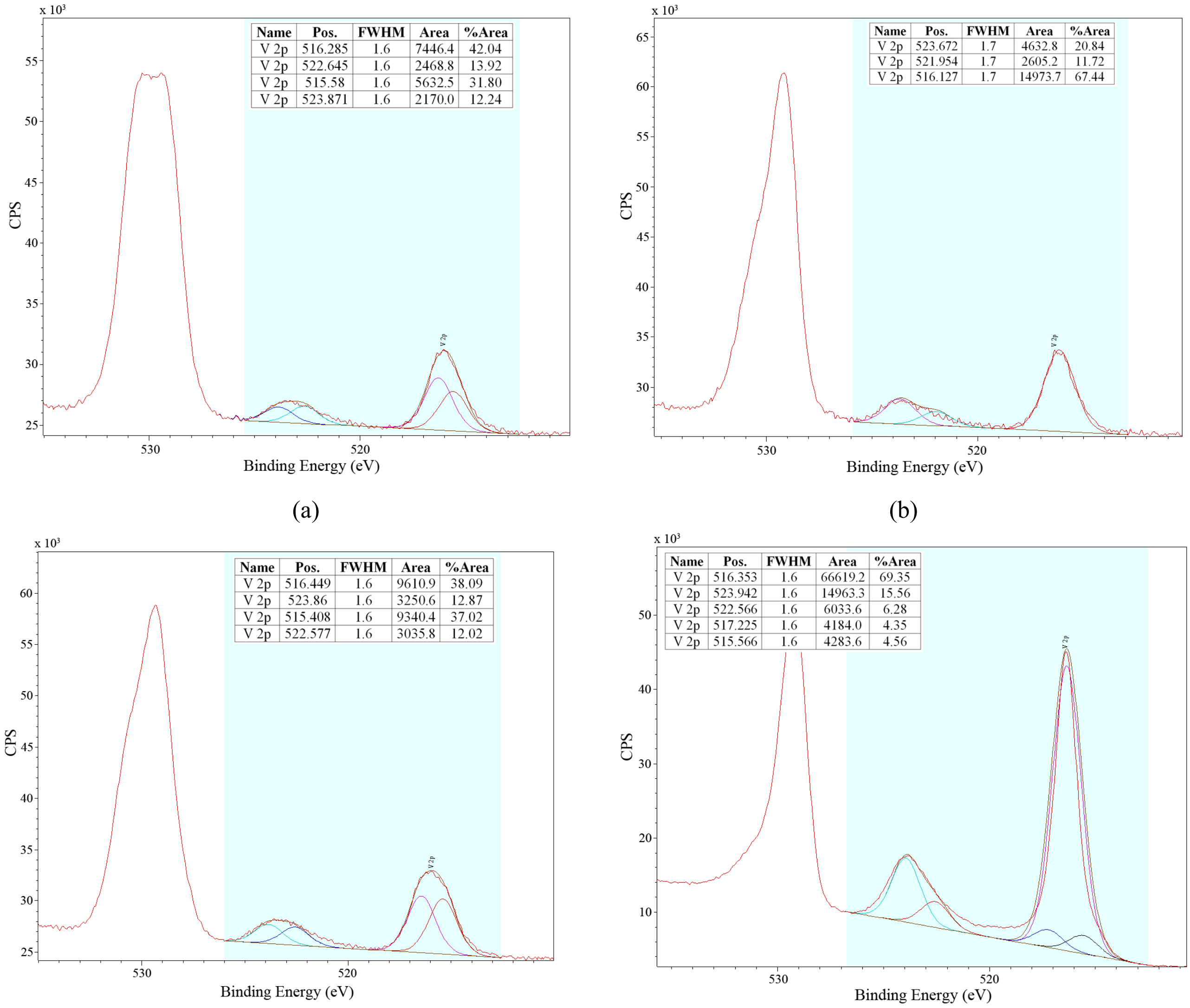

(a)

Name	Pos.	FWHM	Area	%Area
V 2p	516.285	1.6	7446.4	42.04
V 2p	522.645	1.6	2468.8	13.92
V 2p	515.58	1.6	5632.5	31.80
V 2p	523.871	1.6	2170.0	12.24

(b)

Name	Pos.	FWHM	Area	%Area
V 2p	523.672	1.7	4632.8	20.84
V 2p	521.954	1.7	2605.2	11.72
V 2p	516.127	1.7	14973.7	67.44

(c)

Name	Pos.	FWHM	Area	%Area
V 2p	516.449	1.6	9610.9	38.09
V 2p	523.86	1.6	3250.6	12.87
V 2p	515.408	1.6	9340.4	37.02
V 2p	522.577	1.6	3035.8	12.02

(d)

Name	Pos.	FWHM	Area	%Area
V 2p	516.353	1.6	66619.2	69.35
V 2p	523.942	1.6	14963.3	15.56
V 2p	522.566	1.6	6033.6	6.28
V 2p	517.225	1.6	4184.0	4.35
V 2p	515.566	1.6	4283.6	4.56

FIG. 2. XPS spectra for the V2p- region for nano-island heterostructures (V_2O_5)/InP, formed by the EEC method and thermooxidized in oxygen under the following conditions: 530 °C, 10 min (a) 530 °C, 60 min (b), 500 °C, 60 min (c), and a thin film heterostructure V_xO_y/InP (no. 5) formed by precipitating the gel with annealing at 200 °C, 60 min, and thermooxidized with oxygen at 500 °C, 60 min (d)

A more correct comparison of samples no. 4 and 5 (see Table 1 and Table 2), synthesized by hard and soft methods, respectively, but oxidized under the same conditions – 500°C, 60 min. The content of vanadium in them significantly differed: it was much higher in sample no. 5 and it was represented by compounds with lower oxidation states (Figs. 2(c,d), Table 2). The synthesis of the vanadium pentoxide gel, its further precipitation from the aerosol and annealing in air lead to the presence of vanadium in the form of a number of oxides, e. g. films had a complex composition already before oxidation [8], depending on the type of annealing (fast high-energy pulsed photon annealing or long term thermal). The quantitative and qualitative ratio of vanadium oxides was also determined by the duration of annealing in an oxidizing or reducing atmosphere [9]. The low phosphorus content in the surface layer of samples no. 4 and no. 5 was due to the fact that the film formed as a result of thermal oxidation does not prevent the evaporation of volatile component. In this case, a correlation with the Auger electron spectroscopy (AES) data [8] was observed, which indicate a very low amount of phosphorus on the surface of the film and in the volume.

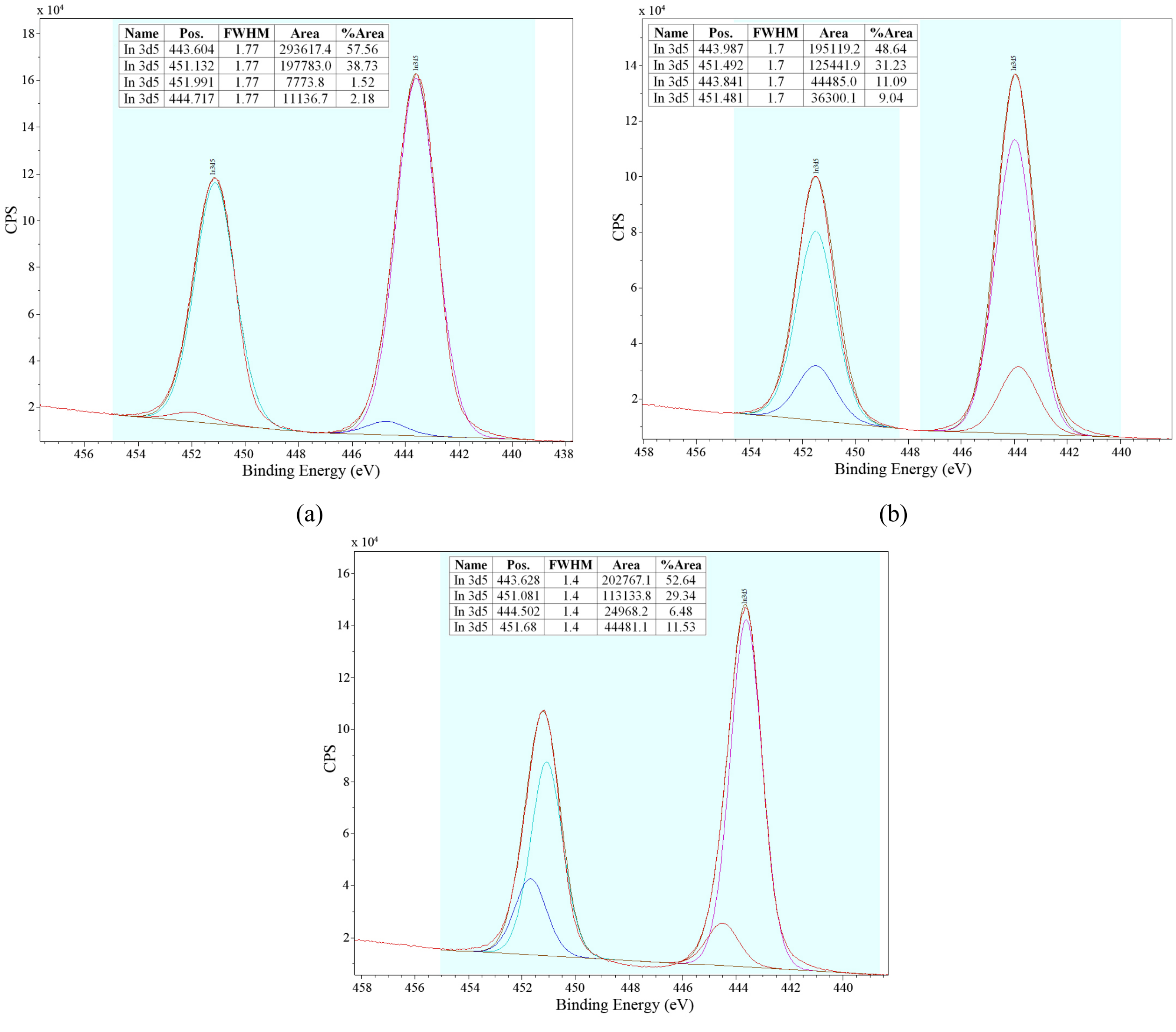

Name	Pos.	FWHM	Area	%Area
In 3d5	443.604	1.77	293617.4	57.56
In 3d5	451.132	1.77	197783.0	38.73
In 3d5	451.991	1.77	7773.8	1.52
In 3d5	444.717	1.77	11136.7	2.18

(a)

Name	Pos.	FWHM	Area	%Area
In 3d5	443.987	1.7	195119.2	48.64
In 3d5	451.492	1.7	125441.9	31.23
In 3d5	443.841	1.7	44485.0	11.09
In 3d5	451.481	1.7	36300.1	9.04

(b)

Name	Pos.	FWHM	Area	%Area
In 3d5	443.628	1.4	202767.1	52.64
In 3d5	451.081	1.4	113133.8	29.34
In 3d5	444.502	1.4	24968.2	6.48
In 3d5	451.68	1.4	44481.1	11.53

(c)

FIG. 3. XPS spectra for the In3d-region in a reference sample, oxidized in the 530 °C regime, 60 min (a), and nano-island heterostructures (V_2O_5)/InP, formed by EEC method and thermooxidized in oxygen under the following conditions: 530 °C, 10 min (b) and 530 °C, 60 min (c)

In samples formed by EEC (for example, no. 3), the shapes of the peaks for oxygen differ from those for samples synthesized by gel dispersion (Figs. 4(a,c), Table 2). In the case when the gel was used, the intensity of the peaks was lower, corresponding to the oxygen bonds in the oxides, however, in the sample no. 3, P–O bonds characteristic for phosphates were also present. The peak corresponding to phosphorus in sample no. 5 was much smaller in comparison with the sample no. 3.

A common feature of the studied processes of oxidation of both nano-islands and thin-film heterostructures is the depletion of the film by the volatile component-phosphorus, which was shown by its minute content both in the near-surface layer and in the volume. At the same time, in the composition of films, it was mainly present in the form of phosphates. Thus, both methods do not fully contribute to the retention of the volatile component and its binding, in contrast, for example, to the hard magnetron method of depositing of vanadium pentoxide films [4].

Another feature is the fact that the XPS method did not reveal peaks, which could be interpreted as corresponding to the bonds in the $InVO_4$ compound, on the surface of the films. The presence of such peaks was established by X-ray diffraction analysis for thin-film heterostructures formed by the soft method [9]. The presence of this compound indicates the binding of vanadium, which causes the absence of its regeneration and the violation of the cyclicity of the process. The formation of $InVO_4$ predominantly at the internal interface confirms the earlier

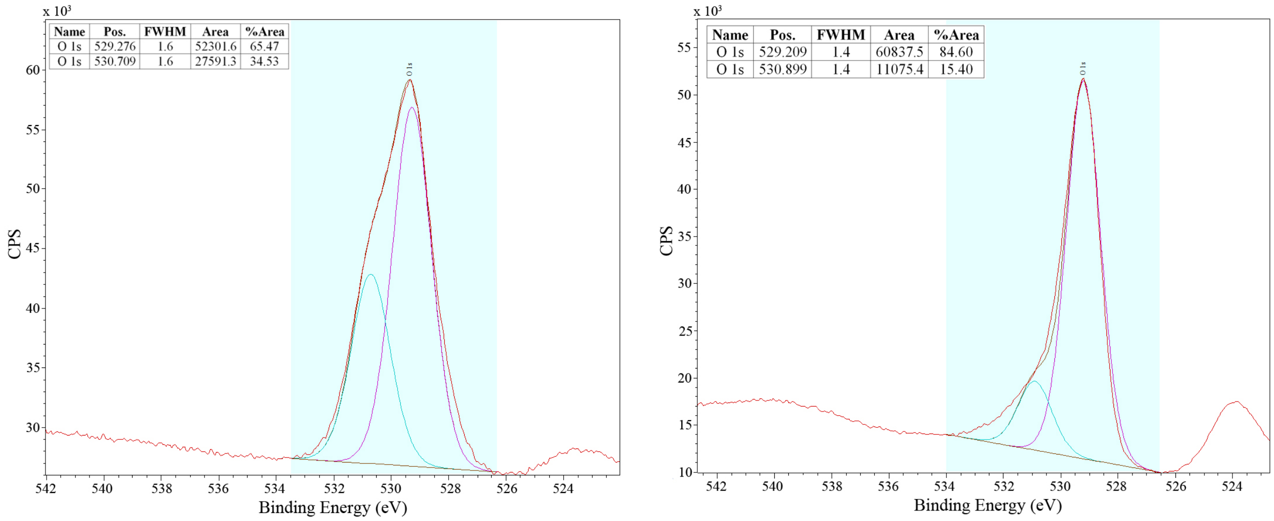

Name	Pos.	FWHM	Area	%Area
O 1s	529.276	1.6	52301.6	65.47
O 1s	530.709	1.6	27591.3	34.53

Name	Pos.	FWHM	Area	%Area
O 1s	529.209	1.4	60837.5	84.60
O 1s	530.899	1.4	11075.4	15.40

(a) (b)

FIG. 4. XPS spectra for the region O1s- for nano-island (V_2O_5)/InP heterostructures, formed by EEC method and thermooxidized in oxygen at 500 °C, 60 min (a), and V_xO_y/InP thin-film heterostructure (no. 5) formed by precipitation of the gel with annealing at 200 °C, 60 min and thermooxidized by oxygen at 500 °C, 60 min (b)

conclusions [19] about the effect of the chemostimulator application method on the mechanism of the oxidation process.

4. Conclusions

The dependence of the composition of oxide films' surface layers on the deposition method of V_2O_5 on InP and the regimes of thermal oxidation for the formed heterostructures was established by the XPS method. The lower indium content near the surface for all samples in comparison with the standard indicates a partial blocking of its diffusion into films during the chemostimulated thermal oxidation of the semiconductor. Phosphorus in the near-surface layers was predominantly in the form of phosphate compounds, but its content in all studied samples was very small, which is associated with the intensive evaporation of volatile phosphorus oxide during thermal oxidation. The presence of vanadium oxides in certain oxidation states and their ratio depends on the method of chemostimulator application, and on the temperature and dura-tion of thermal oxidation. The application of a chemostimulator by a soft method leads to a higher variety of vanadium oxides with differing oxidation states. In the case of the electric arc synthesis method, for short reaction times, vanadium compounds in the +4 and +5 oxidation states were present in the near-surface layer, which provides evidence for the catalytic mechanism.

Acknowledgments

This work was supported by the RFBR grant No. 16-43-360595 p_a.

References

[1] Wager J.F., Wilmsen C.W. Thermal oxidation of InP. *J. Appl. Phys.*, 1980, **51**(1), P. 812–814.

[2] Oktyabrsky S., Ye P.D. *Fundamentals of III-V Semiconductor MOSFETs*. Springer, New York, 2010, 445 pp.

[3] Pakes A., Skeldon P., et al. Composition and growth of anodic and thermal oxides on InP and GaAs. *Surface and Interface Analysis*, 2002, **34**, P. 481–484.

[4] Mittova I.Ya., Tomina E.V., et al. Thermal oxidation of $A^{III}B^{V}$ semiconductors with V_2O_5 nanolayers on the surface. *Glass Physics and Chemistry*, 2011, **37**(2), P. 230–234.

[5] Mittova I.Ya., Sladkopevtsev B.V., et al. Effect of V_2O_5 nanoislands on the surface composition and structure of InP during thermal oxidation. *Inorganic Materials*, 2011, **47**(8), P. 811–815.

[6] Sangwal K. *Etching of Crystals: Theory, Experiment, and Application.* North-Holland Physics Publishing, Amsterdam, 1987, 497 pp.

[7] Mittova I.Ya., Tomina E.V., et al. Synthesis and catalytic performance of V_2O_5 nanoislands produced on the surface of InP crystals by electroexplosion. *Inorganic Materials*, 2010, **46**(4), P. 383–388.

[8] Sladkopevtsev B.V., Mittova I.Ya., et al. Growth of vanadium oxide films on InP under mild conditions and thermal oxidation of the resultant structures. *Inorganic Materials*, 2012, **48**(2), P. 161–168.

[9] Mittova I.Ya., Tomina E.V., et al. Effect of different types of annealing on the thermal oxidation of V_xO_y/InP structures formed by the deposition of vanadium(V) oxide gel on the phase composition and morphology of films. *Journal of surface investigation X-Ray, synchrotron and neutron techniques*, 2014, **9**, P. 91–100.

[10] XPS, AES, UPS and ESCA database (http://www.lasurface.com/accueil/index.php)

[11] Seah M.P., Briggs D. *Practical surface analysis. Auger and X-ray photoelectron spectroscopy*. Wiley & Sons, Chichester, 1996, 674 pp.

[12] Pho Nguyen, Sreeram Vaddiraju, et al. Indium and tin oxide nanowires by vapor-liquid-solid growth technique. *Journal of electronic materials*, 2006, **35**(2), P. 200–206.

[13] Shih P.Y., Yung S.W., et al. Thermal and corrosion behavior of P_2O_5-Na_2O-CuO glasses**.** *Journal of non-cristalline solids*, 1998, **224**, P. 143–152.

[14] Wagner C.D., Moulder J.F., et al. *Handbook of X-ray Photoelectron Spectroscopy*. Perkin–Elmer, Minnesota, 1979, 190 pp.

[15] Yarn K.-F. High sensitive hydrogen sensor by Pd/oxide/InGaP MOS structure. *Modern physics letters B*, 2006, **20**(28), P. 1781–1787.

[16] Suchorski L., Rihko-Struckmann L., et al. Evolution of oxidation states in vanadium-based catalysts under conventional XPS conditions. *Applied Surface Science*, 2005, **249**, P. 231–237.

[17] Benayad A., Martinez H., et al. XPS investigations achieved on the ?rst cycle of V_2O_5 thin films used in lithium microbatteries. *Journal of Electron Spectroscopy and Related Phenomena*, 2006, **150**, P. 1–10.

[18] Mittova I.Ya., Tomina E.V., et al. High-speed determination of the thickness and spectral ellipsometry investigation of films produced by the thermal oxidation of InP and V_xO_y/InP structures. *Inorganic Materials*, 2013, **49**(2), P. 179–184.

[19] Krylov O.V. *Geterogennyi kataliz* (*Heterogeneous Catalysis*). Akademkniga, Moscow, 2004, 679 pp.

NANOSYSTEMS: PHYSICS, CHEMISTRY, MATHEMATICS, 2017, 8 (4), P. 531–534

Antibacterial activity of Amikacin-immobilized detonation nanodiamond

A. S. Solomatin[1,2], R. Yu. Yakovlev[1,2,3], O. V. Efremenkova[4],
I. G. Sumarukova[4], I. I. Kulakova[2], G. V. Lisichkin[2]

[1]Ryazan State Medical University, Ryazan, Russia

[2]Lomonosov Moscow State University, Moscow, Russia

[3]Vernadsky Institute of Geochemistry and Analytical Chemistry of Russian Academ of Sciences,
Moscow, Russia

[4]Gause Institute of New Antibiotics, Moscow, Russia

solo-msu@yandex.ru, yarules@yandex.ru, ovefr@yandex.ru,
noks59@yandex.ru, inna-kulakova@yandex.ru, lisich@petrol.chem.msu.ru

PACS 68.35.-p, 7.85.Tu **DOI 10.17586/2220-8054-2017-8-4-531-534**

Detonation nanodiamonds (NDs) with chlorinated (ND–Cl) and carboxylated (ND–COOH) surfaces were obtained. The broad-spectrum antibiotic Amikacin (Amik) was covalently grafted to the chlorinated surface (ND–Amik) and immobilized by adsorption to carboxylated surface (Amik/ND–COOH). Biological testing *in vitro* showed the presence of antibacterial activity of the obtained samples against *Staphylococcus aureus* FDA P209 and *Escherichia coli* ATCC 25922, close to activity of free amikacin. It was revealed that to maintain antibacterial activity of the samples after their preliminary treatment, important factors such as the use of antioxidants (hydrosulfite and sodium citrate) and lyophilization were necessary.

Keywords: detonation nanodiamond (ND), amikacin (Amik), lyophilization, antioxidants, antibacterial activity.

Received: 27 May 2017

Revised: 3 July 2017

1. Introduction

The development of effective systems of drugs delivery is one of the rapidly developing areas of modern chemistry, pharmacology and medicine [1–3]. Recent research has shown that detonation nanodiamond (ND) is a promising nanocarrier to create delivery systems. It is non-toxic, biocompatible and able to overcome biological barriers, penetrating into the cells [4]. The high concentration of functional groups on its surface allows to use of a wide range of reactions to modify the nanodiamond [5, 6] and immobilize many different biologically active substances (BAS) on it. The adsorption [7] and the covalent grafting [8] are methods commonly used for the immobilization of BAS on ND. A number of studies have shown that the activities of BAS are preserved and their toxicities may be attenuated with immobilization on ND [9, 10]. One of the most effective antibacterial aminoglycosides used for the treatment of various infectious diseases, including tuberculosis, is amikacin. This compound is a broad-spectrum antibiotic and antituberculosis drugs II series [11, 12]. Both ototoxicity and nephrotoxicity are known characteristics of amikacin, as with other aminoglycoside antibiotics [13], however, to a lesser degree [14].

The problem of obtaining of a highly efficient ND-based delivery system for amikacin to reduce its dosage while enhancing the efficiency its action, especially with respect to phthisiopulmonology [11], is highly relevant and challenging. Therefore the goal of this work was to study the antibacterial activity of Amikacin-immobilized detonation nanodiamonds.

2. Experimental

2.1. Materials and methods

Amikacin (Amik) is used in the active pharmaceutical compound "Amikacin sulphate" (JSC "Sintez", Kurgan, Russia), which is a white lyophilized powder for the preparation of injection solutions. Nanodiamond of detonation synthesis (trademark UDA-TAN) were acquired in SKTB "Tekhnolog" (St. Petersburg, Russia). In accordance with the specification, ND contained 0.7 wt.% non-combustible impurities. In order to reduce the impurities content ND was sequentially treated with aq. 0.1 M NaOH solution and concentrated HCl, thoroughly rinsed with water and dried [15].

Reagents with purity "cm. p" and "v. p.": H_2SO_4, HNO_3, HCl, NaOH, $NaHSO_3$, $KMnO_4$, CCl_4, EtOH, N,N-diisopropylethylamine, boric acid, 2,4,6-trinitrobenzenesulfonic acid (TNBS), and sodium citrate were purchased in Sigma. Hydrogen gas of purity 99.99 %; liquid nitrogen; nutrient medium No. 2 gauze for deep cultivation (composition, wt.%: glucose – 1.0, peptone – 0.5, tripton – 0.3, sodium chloride – 0.5, water – 97.7) and with the addition of 3 wt.% agar, exhibiting planting.

The structural characteristics and the size of the primary ND particles were examined by Transmission Electron Microscope JEM-2100 F ("JEOL", Japan). The specific surface area and porosity of the NDs were measured by BET using Gimini 2390 (V1.02 t) (Micromeritics, USA). The ND powder was pre-heated at 120°C and 10^{-3} mm Hg. The accuracy was 5 m^2/g. The analysis of surface functional groups was verified by Fourier Transform Infrared Spectroscopy (FTIR) using Nicolet IR200 (ThermoScientific, USA) with a spectra resolution 2 cm^{-1}. ND (0.8 mg) was mixed with 140 mg of KBr (previously dried at 100°C and 1 mm HG), and then finely ground by the grinding. The chemical composition of NDs surface was analyzed by X-ray photoelectron spectroscopy (XPS) using LAS-3000 (Riber, France) with Al K_α = 1486.6 eV X-rays at the voltage on the tube 12 kV and emission current 20 mA. Photoelectron peaks were calibrated using the line of C 1s-electron of carbon with a binding energy of 285 eV.

2.2. Techniques

The functionalization of ND (chlorination and carboxylation) and the subsequent covalent and adsorption immobilization of amikacin on those functionalized NDs, affording ND–Amik and Amik/ND–COOH, respectively, were performed according to previously described techniques [16]. The ND-Amik conjugate was obtained by covalent grafting of amikacin to the ND-Cl.

2.2.1. Hydrogenation and Chlorination of ND surface. The nanodiamond with hydrogen-containing surface groups (ND–H) was prepared by thermal gaseous hydrogenation, as described previously [16]. A quartz reactor with a sample of purified ND was placed in a tube furnace, heated to 800°C and held for 5 h in a stream of H_2 (at 2-3 liter/h flow rate). The nanodiamond with chlorinated surface (ND–Cl) was prepared from ND–H. Chlorine was generated by reaction of $KMnO_4$ with concentrated HCl; the liberated gas was bubbled through carbon tetrachloride to produce a saturated solution (at 5.6 wt.%). ND-H (500 mg) was added to 40 ml of Cl_2 solution in CCl_4. The resulting mixture was irradiated with an incandescent lamp (500 W) at constant stirring for 24 h. Then the ND–Cl was separated from the solution, rinsed with CCl_4, dried using a rotary evaporator and degassed under vacuum ($<$ 1 bar) for 2 h.

2.2.2. Liquid-phase oxidation of ND surface. The liquid-phase oxidation was carried out in a glass flask equipped with a reflux condenser. ND powder (1 g) was added to 75 ml of HNO_3 and H_2SO_4 (1:3 v/v). The resulting mixture was stirred for 24 hours at 120 °C. Carboxylated ND (ND–COOH) was separated by centrifugation for 10 min at 1000 g. The precipitate was treated with 0.1 M NaOH for 2 hours at 90°C, then with 0.1 M HCl for 2 hours at 90 °C. Such resulting precipitate was separated by centrifugation and repeatedly washed with water. Then, ND–COOH was dried at 60 °C using a rotary evaporator.

2.3. Preparation of ND hydrosols

Hydrosols of ND–COOH and the other samples were prepared according to the procedure described in [17]: 600 mg of nanodiamond powder was placed in a plastic centrifugation tube, and then suspended in 40 ml of water by 1-min sonication. The suspension was then centrifuged at 6000 g for 5 min. This cycle was repeated five times. The amount of ND in supernatant was determined by drying 0.5 ml of hydrosol on the watch glass that was previously adjusted to a constant weight. The watch glass with a hydrosol was placed on a metal grid fixed 2–3 cm above electric hot plates heated at 200°C. ND was dried to a constant weight.

The content of the immobilized amikacin on ND samples was determined by UV spectrophotometry using the preliminary derivatization with TNBS. For this purpose, the test sample hydrosols were diluted to ND concentration of 80 μg/ml. The pre-prepared borate-sodium buffer (pH 9.5) and TNBS (30 mM) were added to the hydrosol to concentrations in the resulting mixture, 0.1 M and 300 μM, respectively. The mixture was stirred on Vortex at 40 °C for 1 h. The optical density of the mixture was determined at a wavelength of 405 nm and the absorption contribution of the ND was subtracted. The content of antibiotic in the investigated hydrosols samples was determined using calibration curves, previously constructed for solutions of free amikacin.

The Amik/ND–COOH hydrosol was divided into two parts. The first part was dried on a rotary evaporator and, prior to testing the antibacterial activity, redispersed in distilled water by ultrasonication (Sample 1a). A solution of antioxidants (sodium hydrosulfite and sodium citrate, pH 4.5) was added to the second aliquot to concentrations of 0.13 and 0.60 wt.% respectively. The mixture was sprayed into liquid nitrogen using a hand sprayer and lyophilized. The lyophilisate was redispersed in distilled water and sterilized using UV irradiation (Sample 1b).

The ND–Amik hydrosol was divided into three parts. The Sample 2b and the Sample 2c were obtained according to the techniques described for Sample 1b, except that Sample 2c was not UV-irradiated. The third part of the ND–Amik hydrosol was treated similarly to the preparation of Sample 2b, but without the addition of antioxidants (Sample 2d). As a reference sample (Control), free amikacin treated similarly to Sample 1b was used.

2.4. Antibacterial activity of Amikacin-immobilized nanodiamonds

The antibacterial activity of the prepared samples was studied by a serial dilution method in medium (deep culture *in vitro*) with respect to *Staphylococcus aureus* FDA P209 and *Escherichia coli* ATCC 25922. The liquid N2 Gause medium was inoculated with test strains at a calculated value of 10^7 bacteria/ml (calculated according to the McFarland turbidity standard). Survival of bacteria was assessed by spots on an agar-agar N2 Gause medium. Preliminarily, the minimum inhibitory concentration (MIC) of the Control was determined in the concentration range 2–16 μg/ml. Then, the same mixture of all investigated samples with the same concentrations of Amikacin were prepared and examined. Conclusions regarding the absence of antibacterial activity were made based on the presence of bacterial colonies on the surfaces of agar-agar media.

3. Results and discussion

Main characteristics of the test samples are shown in Table 1.

TABLE 1. Test samples of ND with immobilized amikacin

Sample	**Method of immobilization of Amik on ND**	**Presence of antioxidants**	**Drying method**	**Amik$_{immob}$ content, wt.%**
1a	Adsorption	–	ordinary	3.1
1b	–”–	+	lyophilization	3.1
2b	Covalent grafting	+	–”–	4.3
2c	–”–	+	–”–	4.3
2d	–”–	–	–”–	4.3

The amount of amikacin immobilized on ND was small, so it is practically below the threshold limit for detection in IR absorption spectra. Therefore, UV-spectroscopy was used as the main method for amikacin determination. Because amikacin has no absorption maxima absorption in the UV range, it was derivatized with TNBS, which forms salts with the amino groups of the antibiotic and allows detection of absorption at 405 nm.

The purpose of antioxidants addition was to verify the assumption of their positive effect on the stability of amikacin. So the mass ratio amikacin/$NaHSO_3$ and amikacin/citrate was equal to 40 and 8, respectively (as in pharmacy amikacin for injection).

The results of the antibacterial activity study for the test samples are summarized in Table 2. From a comparison of the presented data, it follows that the MIC of the Control in relation to *S. Aureus* FDA P209 and *E. coli* ATCC 25922 were 8 and 16 μg/ml, respectively. Sample 1a showed no antibacterial activity in the investigated concentration range for any bacterial strain.

TABLE 2. Influence of the test samples content in a culture medium (Amik concentration) on the growth of *S. aureus* FDA P209 and *E. coli* ATCC 25922: ”–” no growth, ”+” growth. Bacteria incubation with the samples was carried out at 37 °C for 24 h

Sample	***St. aureus* FDA P209**				***E. coli* ATCC 25922**			
	C(Amik), μg/ml				**C(Amik), μg/ml**			
	2	**4**	**8**	**16**	**2**	**4**	**8**	**16**
1a	+	+	+	+	+	+	+	+
1b	+	+	+	–	+	+	+	+
2b	+	+	+	–	+	+	+	–
2c	+	+	+	–	+	+	+	–
2d	+	+	+	+	+	+	+	+
Control	+	+	–	–	+	+	+	–

The antioxidant-containing and lyophilized Amik/ND–COOH (Sample 1b) showed a suppressive effect with respect to *S. aureus* at 16 μg/ml, whereas at the same concentration, it had no noticeable effect with respect to *E. coli*. ND–Amik with antioxidants (Sample 2b) showed antibacterial activity against both strains, and its effect on *E. coli* is comparable to Control. Similar results for Samples 2b and 2c show that irradiation with UV-light (sterilization) has no effect of the biological experiment result, since, on one hand, it does not affect the activity of the sample, and, on the other, the growth of extraneous organisms, which affirms the sterility of the sample and the unnecessariness for additional sterilization. The Sample 2d (lyophilized ND–Amik, but without the addition of antioxidants) showed no antibacterial activity in the studied concentrations range. Thus, lyophilization and the use of antioxidants are important factors in preserving the activity of amikacin immobilized on ND in the delivery system.

4. Conclusions

It has been established that samples of amikacin covalently immobilized on nanodiamonds possess the greatest antibacterial activity. The activity of such samples is close to the activity of free amikacin, which is quite acceptable for delivery systems. It is shown that the biological activity of ND conjugates with amikacin is influenced not only by the method of immobilization, but also by other factors, including, primarily, the presence of antioxidants and lyophilic drying. In turn, the use of these additional factors makes it possible to more fully reveal the potential of the BAS delivery systems based not only on ND, but also on other nanoparticles.

Acknowledgments

This study has been performed with support from the grant of Russian Science Foundation (project 16-08-01156). The equipment used in this study was purchased from the funds of Moscow State University Development Program.

References

[1] *Nanotherapeutics: Drug Delivery Concepts in Nanoscience*. Edited by Lamprecht A. CRC Press, Taylor and Francis Group, Boca Raton, 2008, 292 pp.

[2] Almjasheva O.V., Garabadzhiu A.V., Kozina Yu.V., Litvinchuk L.F., Dobritsa V.P. Biological effect of zirconium dioxidebased nanoparticles. *Nanosystems: physics, chemistry, mathematics*, 2017, **8**(3), P. 391–396.

[3] Popova N.R., Popov A.L., Shcherbakov A.B., Ivanov V.K. Layer-by-layer capsules as smart delivery systems of CeO_2 nanoparticle based theranostic agents. *Nanosystems: physics, chemistry, mathematics*, 2017, **8**(2), P. 282–289.

[4] Zhang X., Hu W., Li J., Tao L., Wei Y. A comparative study of cellular uptake and cytotoxicity of multi-walled carbon nanotubes, graphene oxide, and nanodiamond. *Toxicol. Res.*, 2012, **1**, P. 62–68.

[5] Krueger A. The structure and reactivity of nanoscale diamond. *J. Mater. Chem.*, 2008, **18**, P. 1485–1492.

[6] Shenderova O.A., McGuire G.E. Science and engineering of nanodiamond particle surfaces for biological applications (Review). *Biointerphases*, 2015, **10**(3), P. 030802.

[7] Shugalei I.V., Voznyakovskii A.P., Garabadzhiu A.V., Tselinskii I.V., Sudarikov A.M., Ilyushin M.A. Biological activity of detonation nanodiamond and prospects in its medical and biological applications. *Russ. J. Gen. Chem.*, 2013, **83**(5), P. 851–883.

[8] Liu K.K., Zheng W.W., Wang C.C., Chiu Y.C., Cheng C.L., Lo Y.S., Chen C., Chao J.I. Covalent linkage of nanodiamond-paclitaxel for drug delivery and cancer therapy. *Nanotechnology*, 2010, **21**, P. 1–14.

[9] Chen M., Pierstorff E.D., Lam R., Li S.Y., Huang H., Osawa E., Ho D. Nanodiamond-mediated delivery of water-insoluble therapeutics. *ACS Nano*, 2009, **3**(7), P. 2016–2022.

[10] Chow E.K., Zhang X.Q., Chen M., Lam R., Robinson E., Huang H., Schaffer D., Osawa E., Goga A., Ho D. Nanodiamond therapeutic delivery agents mediated enhanced chemoresistant tumor treatment. *Sci. Tran. Med.*, 2011, **3**(73), P. 73ra21.

[11] Pham D.D., Fattal E., Tsapis N. Pulmonary drug delivery systems for tuberculosis treatment. *Int. J. Pharm.*, 2015, **478**, P. 517–529.

[12] Xie J., Talaska A.E., Schacht J. New developments in aminoglycoside therapy and ototoxicity. *Hear Res.*, 2011, **281**, P. 28–37.

[13] Brummetti R.E., Fox K.E. Aminoglycoside-induced hearing loss in humans. *Antimicrob Agents Chemother.*, 1989, **33**(6), P. 797–800.

[14] Hottendorf G.H., Gordon L.L. Comparative low-dose nephrotoxicities of gentamicin, tobramycin, and amikacin. *Antimicrob. Agents Chemother.*, 1980, **18**(1), P. 176–181.

[15] Method for selective final purification of nanodiamond, Patent. 2506095 Russia: MPK A61 K 47/04, C01 B 31/06, B82 B 3/00, B82 Y 5/00, Jakovlev R.J., Solomatin A.S., Kulakova I.I., Lisichkin G.V., Korolev K.M., Leonidov N.B., N 2012157038/15, 12 pp.

[16] Yakovlev R.Y., Solomatin A.S., Leonidov N.B., Kulakova I.I., Lisichkin G.V. Detonation diamond – a perspective carrier for drug delivery systems. *Rus. J. Gen. Chem.*, 2014, **84**(2), P. 379–390.

[17] Yakovlev R.Y., Osipova A.S., Solomatin A.S., Kulakova I.I., Murav'eva G.P., Avramenko N.V., Leonidov N.B., Lisichkin G.V. An approach to unification of the physicochemical properties of commercial detonation nanodiamonds. *Russ. J. Gen. Chem.*, 2015, **85**(6), P. 1565–1574.

NANOSYSTEMS: PHYSICS, CHEMISTRY, MATHEMATICS, 2017, 8 (4), P. 535–539

Phase transitions in nanostructured $K_{1-x}(NH_4)_{(x)}H_2PO_4$ (x = 0 - 0.15) solid solutions

P. Yu. Vanina[1], A. A. Naberezhnov[2], O. A. Alekseeva[1],
A. A. Sysoeva[2], D. P. Danilovich[3], V. I. Nizhankovskii[4]

[1]Peter the Great Saint Petersburg Polytechnic University,
Polytechnicheskaya, 29, St. Petersburg, 195251, Russia

[2]Ioffe Institute, Polytechnicheskaya, 26, St. Petersburg, 194021, Russia

[3]Engineering center of St. Petersburg State Technological Institute,
Moskovsky prospect, 26, St. Petersburg, 190013, Russia

[4]International Laboratory of High Magnetic Fields and Low Temperatures,
Gajowicka, 95, Wroclaw, 53-421, Poland

p.yu.vanina@gmail.com, alex.nabereznov@mail.ioffe.ru, blackhole2010@yandex.ru,
annasysoeva07@mail.ru, dmitrydanilovich@gmail.com, nizhan@ml.pan.wroc.pl

PACS 77.84.Fa; 68.65.-k; 68.35.Rh; 67.30.ht **DOI 10.17586/2220-8054-2017-8-4-535-539**

Effect of ammonium dihydrogen phosphate admixture on phase transitions in nanostructured solid solutions $(1-x)KH_2PO_4$–$(x)(NH_4)H_2PO_4$ at $x = 0$, 0.05 and 0.15 has been studied by dielectric spectroscopy. The samples have been prepared by embedding of aqueous solutions into porous borosilicate glasses. The X-ray diffraction have shown that the crystal structure at room temperature corresponds to the bulk KDP and the average nanoparticle diameters are 49 (2) nm for the sample with 5 % of $(NH_4)H_2PO_4$ (ADP) and 46 (2) nm for the nanocomposites with 15 % of ADP. Dielectric response data analysis have revealed the shifts of the ferroelectric phase transition temperature as a function of $(NH_4)H_2PO_4$ concentration: at $x = 0$ ΔT_C is equal to ∼6 K, at $x = 0.05$ ΔT_C ∼3 K and at $x = 0.15$ ΔT_C ∼2 K.

Keywords: ferroelectrics, antiferroelectrics, phase transitions, nanocomposite materials.

Received: 17 July 2017

Revised: 6 August 2017

1. Introduction

Studies of size effect (or restricted geometry) in nanostructured systems with different topologies and dimensions in recent years have been significantly stimulated by the intensive development of nanotechnologies. The brightest example of similar systems is nanocomposite materials: polar dielectrics embedded into porous matrices that have a branched network (dendrite-like) through pores. The embedded materials form either a system of isolated particles or a complex dendritic structure, determined by the size and topology of the pores of the host matrix, surface tension, wettability, and so on. [1].

Nanocomposite materials (NCM) based on micro- and macroporous borosilicate glasses have been created at the Ioffe Institute. Pores in these glasses form a through dendritic three-dimensional system, the total porosity (depending on the average pore diameter) can reach 40–50 % of the sample volume. Previously, it has been shown that NCM based on conventional non-magnetic porous matrices containing embedded hydrogen-containing ferroelectrics KH_2PO_4 (KDP) and $(NH_4)H_2PO_4$ (ADP) in a confined geometry, demonstrate the dielectric response anomalies.

Despite the fact that KDP and ADP crystals belong to the same family and have a close chemical composition, at the same time, the baric effect in KDP is stronger than in ADP [2]. On the one hand, the increase of the dielectric constant at low frequencies and the growth of ferroelectric phase transition (PT) temperature have been clearly observed with a decrease in the average pore diameter for KDP [3]. Later, this growth in KDP and ADP nanoparticles has been explained assuming that tensile strains arising from heating due to the difference in the coefficients of thermal expansion for the embedded material and the matrix itself [4].

NCM based on macroporous glasses (PG) with average pore diameter from 20 nm to 60 nm (median value was 45(5) nm), containing embedded $(1-x)$KDP–(x)ADP mixture at $x = 0.05$ and 0.15 have been made for testing the possible phase transition temperature shift, depending on ADP admixture. NCM containing embedded pure KDP has been studied earlier in the paper [5].

2. Experimental part

The studies have been carried out on a capacitance bridge at 1 kHz in the International Laboratory of High Magnetic Fields and Low Temperatures (Wroclaw, Poland). The samples appear to be plates of macroporous glass with KDP-ADP (KADP) mixtures embedded into the pores from aqueous solution with triple recrystallization. The pore filling achieved 35 % for 5 % ADP sample and 38 % for 15 % ADP sample. The temperature dependences of the sample capacitances have been measured at temperatures ranging from 40–200 K, but in Figures for clearance, only the smaller diapasons in the vicinity of the phase transitions are shown. "Cooling-heating" cycles have been repeated twice for every sample during the experiment. The temperature stability was better than 0.1 K.

X-ray diffraction measurements have been performed at the Engineering Center of the St. Petersburg State Technological Institute (technical university) on the Rigaku Smartlab X-rays diffractometer in order to characterize the samples. We have used Cu K_α line, the wavelengths were 1.540593 Å for $K_{\alpha 1}$ and 1.544414 Å for $K_{\alpha 2}$ lines, respectively. The value of the intensity ratio in the doublet was equal to $I_{\alpha 1}/I_{\alpha 2} = 0.497$. X-ray diffraction experiments have been carried out at room temperature with germanium monochromator, the angular diffractometer resolution was of ~0.05 °.

3. Results and discussion

On the first stage we have characterized all our samples using X-ray diffraction at room temperature (RT). In Fig. 1 the diffraction pattern for 0.95KDP+0.05ADP sample at RT and the results of fitting are presented.

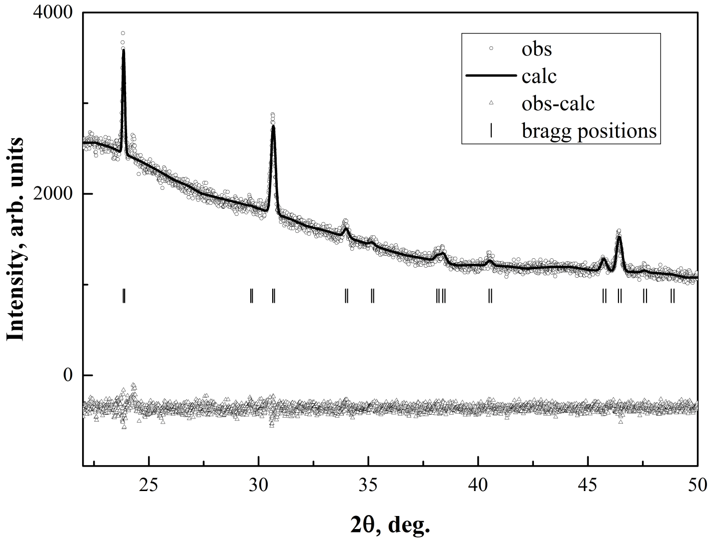

FIG. 1. X-ray diffraction pattern for 0.95KDP+0.05ADP sample at RT. Solid line ("calc") corresponds to profile analysis, open circles ("obs") – experimental data. Vertical bars – Bragg positions, the triangles in the bottom ("obs-calc") part is the difference between experimental data and fitting

The diffraction peak splitting observed in Fig. 1 occurs because of proximity of the $K_{\alpha 1}$ and $K_{\alpha 2}$ lines. Since the embedded materials are the solid solutions of KDP-ADP with a small admixture of ADP, the structures of these nanocomposites have to be close to the structure of KDP and according X-rays diffraction correspond to the spatial group **I-42d**, as well as the bulk KDP at RT, with the unit cell parameters $a = b = 7.459$ and $c = 6.994$ Å. It is also worth noting that the refined unit cell parameters are well correlated with the data obtained earlier for example by the authors [6]: $a = b = 7.448$ and $c = 6.977$ Å. From the broadening of elastic reflections we have estimated the average particle diameters: they are equal to 49 (2) nm for the sample with 5 % of ADP, 46 (2) nm for the sample with 15 % of ADP and 53(5) for NCM with a pure KDP.

Next, the temperature dependences of the capacities of the samples with 5 % and 15 % ADP mole admixture were measured (Fig. 2(b,c)) on cooling and heating. As a reference data, we have used our results related to the capacity of NCM on base of macroporous magnetic glasses with an average pore diameter of 50 nm filled by a pure KDP (Fig. 2(a)) [5].

From the $C(T)$ dependences on Fig. 2(a,b,c) it can be seen that the capacity maxima shift to the lower temperatures at increasing of the ADP admixture both on cooling and heating. It is necessary to note that there are the temperature hysteresis (ΔT_C) between maximum $C(T)$ positions on cooling and on heating decreases with an increase in ADP concentration in the KADP mixture. The positions of maxima in $C(T)$ dependences and the values of ΔT_C for every sample coincide at repetition of "cooling-heating-cooling" cycles and depend only on the ADP concentration.

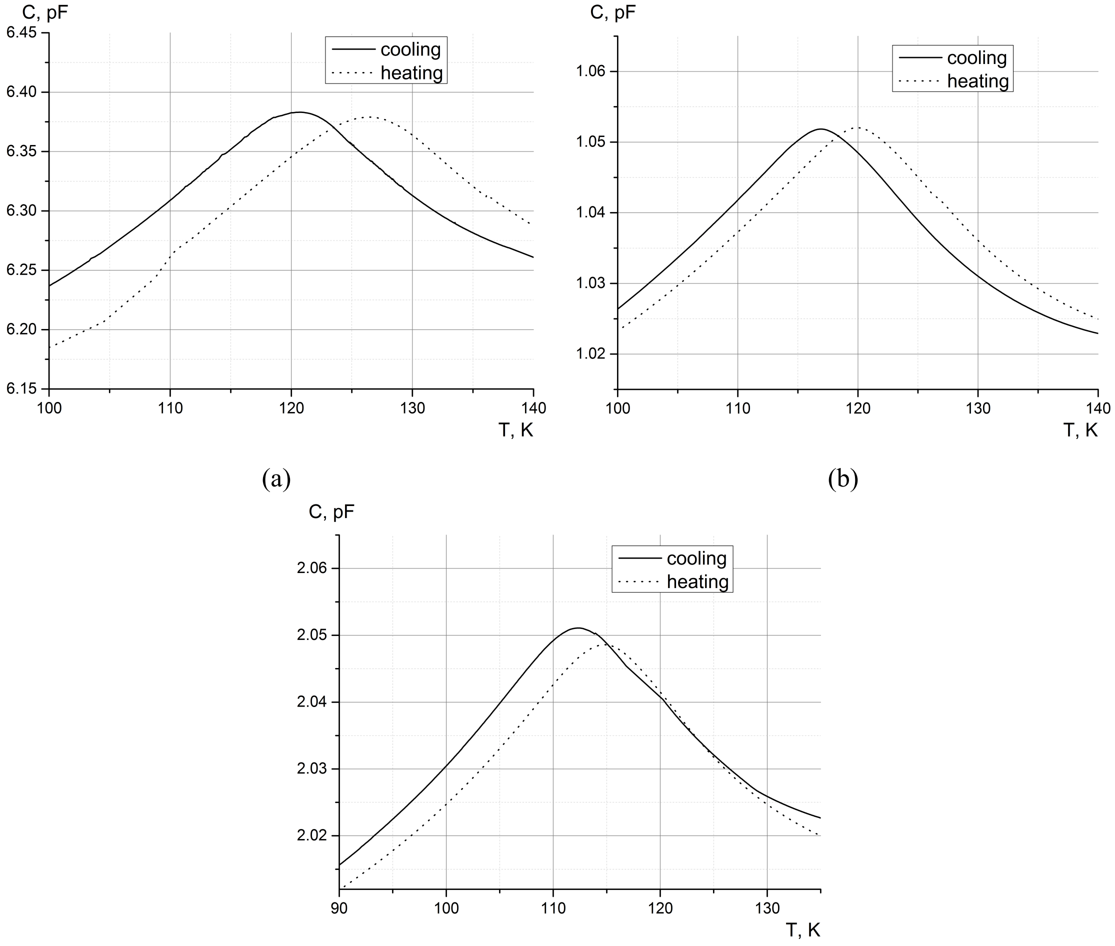

(a) (b)

(c)

FIG. 2. The temperature dependences of the capacity for KADP samples with ADP concentrations 0 % (a) [5], 5 % (b) and 15 % (c) on cooling (solid lines) and heating (dotted lines)

The temperatures of ferroelectric phase transitions have been determined as the position of $C(T)$ maximum after fitting of temperature dependences of sample capacity in a vicinity of PT by the Lorentz function. The errors in determination of $C(T)$ maximum do not exceed 0.05 K.

For the bulk KADP the strong tendency of decreasing of T_C at increasing of APD concentration [9–11] exists, but the detail phase diagram stays ambiguous because the properties of bulk KADP essentially depend on preparation methods [12]. Concerning the thermal hysteresis value ΔT_C in the position of T_C on cooling and on heating, this factor remains unexplored until now.

Figure 3 shows the Curie temperatures T_C in KADP embedded into macroporous glasses as a function of ADP concentration. From these dependences, it is easy to see that the temperatures of phase transition on cooling and on heating shift gradually to lower temperatures, but these shifts are essentially smaller than in the bulk. Simultaneously the temperature hysteresis ΔT_C decreases with increased ADP concentration. The obtained results in comparison with literature data [6–11] for the bulk KADP are presented in Table 1.

4. Conclusion

We have studied the dielectric properties and crystal structure of $K_{(1-x)}(NH_4)_{(x)}H_2PO_4$ (KADP) nanoparticles at $x = 0 - 0.15$ prepared on basis of macroporous glasses by using aqueous solution impregnation. At RT the

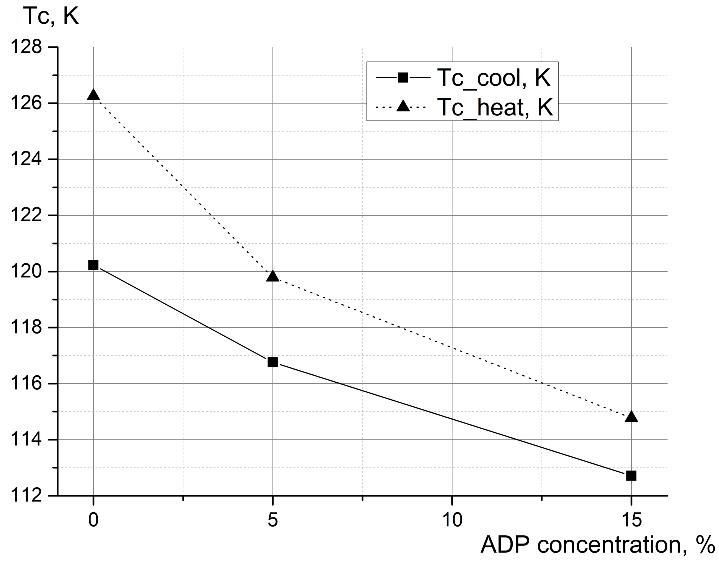

FIG. 3. The concentration dependences of the phase transition temperatures obtained on cooling and heating

TABLE 1. Temperatures of phase transitions in $K_{(1-x)}(NH_4)_{(x)}H_2PO_4$ solid solutions

	Bulk [6–11]	Present work KADP nanoparticles			
	T_C, K	$T_{C(cooling)}$, K	$T_{C(heating)}$, K	$\Delta T_C = T_{C(cooling)} - T_{C(heating)}$, K	Nanoparticle size, nm
$x = 0$	∼122	120.2±0.1 [5]	126.2±0.1	6	53±5
$x = 0.05$	104.2	116.7±0.1	119.8±0.1	3.1	49±2
$x = 0.15$		112.7±0.1	114.8±0.1	2.1	46±2
$x = 0.165$	64.5				

crystal structure of KADP embedded into the pores corresponds to the bulk structure. The average nanoparticle diameters are equal to ∼53(5) nm for the pure KDP nanoparticles, 49(2) nm for the sample with 5 % of ADP and 46(2) nm for 15 % of ADP. Analysis of dielectric response data has revealed the shifts of the ferroelectric phase transition temperature, T_C, as a function of ADP concentration on cooling and heating in comparison to the bulk KH_2PO_4 (KDP), but these shifts are essentially smaller than in the bulk KADP (relatively T_C in KDP) at adequate ADP concentrations. One can note that the increasing of ADP concentration in nanostructured KADP leads to decreasing $T_{C(cooling)}$, $T_{C(heating)}$ and ΔT_C. Most likely the increasing of T_C in NCM in comparison with the bulk materials can be associated with a presence of strains on the “host matrix–embedded materials” interface due to the discrepancy in thermal expansion coefficients.

Acknowledgments

A. A. Sysoeva and A. A. Naberezhnov thank the Russian Foundation for Basic Researches (grant 15-02-01413) for financial support. In Peter the Great Saint Petersburg Polytechnic University the studies were carried out in the framework of the grant of Ministry of Education and Science of Russian Federation, No. 3.1150.2017/4.6. Coauthors thank the Engineering Center of the St. Petersburg State Technological Institute for possibility to carry out the characterization of samples on X-rays diffractometer.

References

[1] Kumzerov Y., Vakhrushev S. Nanostructures within porous material. *Encyclopedia of Nanoscience and Nanotecnology*, 2003, **10**, P. 1-39.

[2] Lines M., Glass. A. *Ferroelectrics and related materials*. Mir, Moscow, 1980, 736 p.

[3] Colla E.V., Fokin A.V., Koroleva E.Yu., Kumzerov Yu.A., Vakhrushev S.B., Savenko B.N. Ferroelectric phase transitions in materials embedded in porous media. *NanoStructured Materials*, 1999, **12**, P. 963–966.

[4] Tarnavich V., Korotkov L., Karaeva O., Naberezhnov A., Rysiakievicz-Pasek E. Effect of restricted geometry on structural phase transitions in $KH_2PO_4$and $NH_4H_2PO_4$ crystals. *Optica Applicata*, 2010, **40**(2), P. 305–309.

[5] Koroleva E., Naberezhnov A., Nizhankovskii V., Vanina P., Sysoeva A. The effect of magnetic field on the ferroelectric phase transition in KH_2PO_4 nanoparticles embedded in magnetic porous glass. *Technical Physics Letters*, 2015, **41**(10), P. 981–983.

[6] Ravi G., Haja Hameed A.S., Ramasamy P. Effect of temperature and deuterium concentration on the growth of deuterated potassium dihydrogen phosphate (DKDP) single crystals. *J. Cryst. Growth*, 1999, **207**, 319 p.

[7] Trybu-la Z., Kaszyński J. Phases Coexistence of Hydrogen-Bonded Mixed Ferroelectric and Antiferroelectric Crystals. *Ferroelectrics*, 2004, **298**, P. 347–351.

[8] Kwon Oh.J., Kim J.-J. Proton glass behavior and phase diagram of the $K_{1-x}(NH_4)_xH_2PO_4$ system. *Physical Review B*, 1993, **48**(9), P. 6639–6642.

[9] Gridnev S.A., Korotkov L.N., Rogova S.P., Shuvalov L.A., Fedosyuk R.M. Dielectric properties and x-T phase diagram of $K_{1-x}(NH_4)_xH_2PO_4$ crystals. Ferroelectrcis Letters, 1991, **13**(3), P. 67–72.

[10] Ono Y., Hikita T., Ikeda T. Phase-transitions in mixed-crystal system $K_{1-x}(NH_4)_xH_2PO_4$. *J. Phys. Soc. Jpn.*, 1987, **56**(2), P. 577–588.

[11] Korotkov L.N., Shuvalov L.A. Transisions to the relaxor and diapole-glass states in mixed crystals of the potassium dihydrogen phosphate family. *Crystallography reports*, 2004, **49**(5), P. 832–842.

[12] Korotkov L.N. *The influence of structural disorder on the physical properties of certain classes of weakly ordered polar dielectrics*. Voronezh State Technical University, Voronezh, 2004, 299 p. (in Russian)

NANOSYSTEMS: PHYSICS, CHEMISTRY, MATHEMATICS, 2017, 8 (4), P. 540–545

Niobium-doped titanium dioxide nanoparticles for electron transport layers in perovskite solar cells

M. F. Vildanova, S. S. Kozlov, A. B. Nikolskaia, O. I. Shevaleevskiy,
N. A. Tsvetkov, O. V. Alexeeva, L. L. Larina

Department of Solar Photovoltaics, Institute of Biochemical Physics,
Russian Academy of Sciences, Kosygin St. 4, Moscow, 119334, Russia

mvildanova@sky.chph.ras.ru

PACS 73.63.Bd **DOI 10.17586/2220-8054-2017-8-4-540-545**

Nb-doped TiO_2 nanoparticles with different doping concentrations, varied from 0 to 2.7 mol.%, were prepared by the sol-gel method followed by thermal treatment. The obtained nanoparticles were used to fabricate a series of electron transport layers for constructing perovskite solar cells (PSCs). The prepared layers were characterized using X-ray diffraction and optical transmission measurements. The effects of Nb doping concentration in TiO_2 layers on the optical absorption behavior, the morphology and charge carrier dynamics were studied. A series of PSCs, based on the developed electron transport layers was fabricated and examined. It was found that PSC fabricated with 2.7 mol.% Nb content TiO_2 electron transport layer have shown up to 19 % improvement of a power conversion efficiency compared to that, based on an undoped TiO_2 layer.

Keywords: nanoparticles, sol-gel method, Nb-doped TiO_2, thin films, semiconductors, solar photovoltaics, perovskite solar cells.

Received: 30 July 2017

Revised: 6 August 2017

1. Introduction

Over the last few decades, nanostructured mesoscopic layers based on metal oxide nanoparticles were successfully used for fabrication the photoelectode materials in dye-sensitized solar cells (DSCs). The same type of photoelectrode materials is also used in a new type of next generation solid-state organic-inorganic lead halide perovskite solar cells (PSCs). In both DSC and PSC photovoltaic devices the photoelectode plays a key role of the electron transport layer, transferring photogenerated charge carriers to the back contact.

In PSCs the active layer, based on perovskite film, such as $CH_3NH_3PbI_3$, absorbs photons with light energy larger than their bandgap and generates the excitons that are separated into electrons and holes. The electrons are then injected into the electron transport layer. The ability of an electron transport layer to effectively transfer the photogenerated electrons diminishes the probability of their direct recombination, charge carrier accumulation at the perovskite/electrode interface and other undesirable effects that may reduce their transport characteristics [1–3].

To find a proper electron transport material for PSCs a number of metal oxides have been examined, including zinc oxide [4, 5], tin oxide [6], aluminum oxide [7] and others [8]. However, the best performance in PSCs was reached using TiO_2 as an electron transport layer [9–11]. Besides that TiO_2 layers show high light radiation stability and perfect electron transfer characteristics [12–14]. A well-known approach to enhance the electron conductivity of a TiO_2 material, including the conductivity of the electron transport layer in PSCs, is doping with metal ions. It was reported that lithium-doped TiO_2 nanoparticles were successfully used in the electron transport layer of a PSC that have shown better conductivity and improved the cell efficiency [15]. Magnesium-doped TiO_2 layers have shown better photoconductivity in comparison with undoped layers, which was explained by a better band alignment at the TiO_2/perovskite interface [16]. Zinc-doped TiO_2 layers have also shown better electrical conductivity than in pristine TiO_2, due to the re-arrangement in the electronic structure of TiO_2 [17, 18]. Finally, a sufficient increase of electron transport parameters was observed in niobium-doped TiO_2 nanorods, used for fabrication of PSCs with improved parameters [19]. The theoretical approach describing the structure of PSCs is discussed in [20].

In our previous papers, we have prepared and examined Nb-doped TiO_2 mesoscopic electrodes for high-efficiency dye-sensitized solar cells [21–23]. It was found that with the increase of Nb doping concentration from 0 to 3 mol.% the conductivity of 10 μm thick TiO_2 mesoscopic layer increases, while a further increase in the doping level resulted in lower conductivity and smaller energy conversion efficiency of DSCs [23].

In the present study, we have prepared Nb-doped TiO_2 layers with different Nb doping concentrations and used them as electron transporting materials for PSCs fabrication. We have examined the crystal structure, optical absorption behavior and the morphology of Nb-doped layers. The photovoltaic performances of perovskite solar cells based on various Nb-doped electron transporting layers are reported. The results address the issues of improving the material properties of Nb-doped layer for the fabrication of more efficient perovskite solar cells.

2. Experimental

2.1. Materials and samples preparation

Nb-doped TiO_2 particles were grown using hydrothermal method. Precursor solutions were prepared following the procedure described in [22] and the co-hydrolysis was carried out at 210 °C for 48 h in an autoclave. We have prepared TiO_2 nanoparticles with the following Nb concentrations: 0.7, 1.7 and 2.7 mol.%. Thick pastes from each of Nb-doped TiO_2 powders were fabricated according to the method reported in [24]. The pre-cleaned FTO glass substrates were first covered with 0.15 M titanium diisopropoxide bis(ethyl acetoacetatonate) solution in 1-butanol, spin-coated at 2000 rpm for 30 s and heated at 125 °C for 5 min to form a blocking layer. Then the prepared nanocrystalline TiO_2 pastes were diluted in ethanol in a mass ratio of 1:3 and deposited on the substrate surface using spin-coating method at 2000 rpm for 1 min, followed by sintering at 500 °C for 1 h. After cooling, the photoelectrodes were treated in aqueous 20 mM $TiCl_4$ at 90 °C for 10 min. The perovskite $CH_3NH_3PbI_3$ layer was formed on the TiO_2 surface under ambient atmosphere conditions by spin-coating the solution-processed single precursor [25] for 30 s at 4000 rpm and then dried at 100 °C for 10 min. The solar cell architecture was completed by depositing a commercial conductive carbon paste on the top of the perovskite film, followed by heat treatment at 100 °C for 30 min, for preparation of the counter electrode. The active area of the photoelectrodes was 0.2 cm^2.

2.2. Characterization Studies

X-ray diffraction (XRD) spectra of the nanocrystalline Nb-doped TiO_2 films were obtained using DRON-3M (Burevestnik, Russia) diffractometer (Cu K_α radiation, 35 kV) in the 13–65 ° range. Optical transmittance spectra of the TiO_2-based layers were recorded using a double-beam Shimadzu UV-3600 spectrophotometer with an integrating sphere ISR-3100 (Shimadzu, Japan) over a wavelength range 250–850 nm. The morphology of the films was investigated using dual-beam scanning electron microscope (SEM) Helios NanoLab 660 (FEI, USA).

The solar cells performance was evaluated by the incident photon-to-current conversion efficiency (IPCE) using QEX10 Solar Cell Quantum Efficiency Measurement System (PV Measurements, USA) and J–V measurements performed under AM1.5 incident light illumination intensity (100 mW/cm^2) using Abet Technologies Solar Simulator (Abet, USA) and Semiconductor Characterization System 4200-SCS (Keithley, USA). The power conversion efficiency (η) of PSC was calculated according to the following equation [26]:

$$\eta(\%) = \frac{V_{oc} \times J_{sc} \times FF}{P_{IN}} \times 100\%, \tag{1}$$

where V_{oc} is open circuit voltage, J_{sc} is short circuit current density, FF is fill factor obtained from the J–V curves and P_{IN} is the incident light intensity. FF was calculated as follows:

$$FF = \frac{V_{max} \times J_{max}}{V_{oc} \times J_{sc}} \tag{2}$$

where V_{max} and J_{max} are the voltage and the current density at the point of maximum power output in the J-V curves, respectively.

3. Results and discussion

The Nb contents of the prepared TiO_2 nanoparticles coincide with the doping levels. Fig. 1 shows XRD patterns of undoped and Nb-doped TiO_2 nanoparticles. It is seen that only the anatase phases of TiO_2 with a (101) preferred orientation can be observed. The differences between the XRD patterns of the samples with various doping levels have not been distinguished.

The transmittance spectra of Nb-doped TiO_2 layers, given in Fig. 2, show a slight blue-shift, increasing with doping concentration. This shift denotes the increase of the TiO_2 bandgap with doping from 3.0 eV in a pristine sample to around 3.2 eV in 2.7 mol.% Nb-doped TiO_2 as it was confirmed in [22]. The bandgap in Nb-doped TiO_2 layers is known to increase with increased Nb doping concentration because of a slight deviation in a TiO_2 lattice parameter [22]. Additionally, the position of a TiO_2 conduction band-edge is increased with Nb doping and the conduction band position at the TiO_2/perovskite interface increases the probability of electron transfer from the photoexcited levels of perovskite to the TiO_2 conduction band.

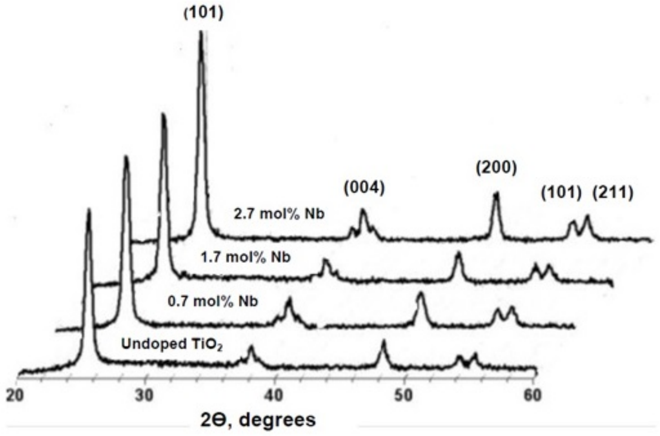

FIG. 1. XRD patterns for Nb-doped TiO_2 nanoparticles with a varied Nb content

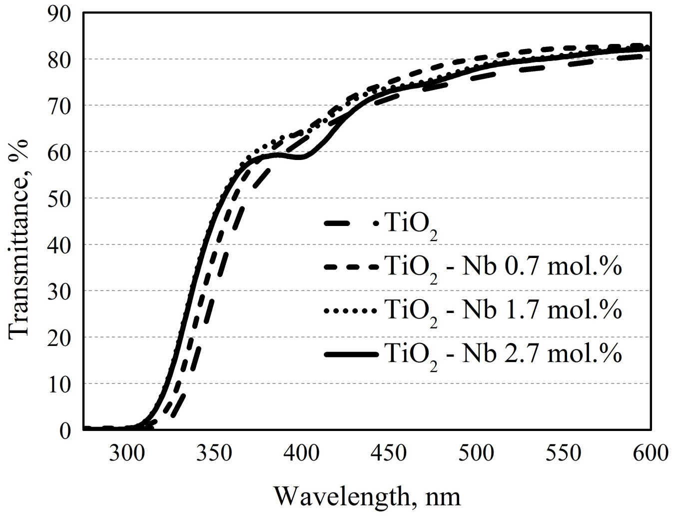

FIG. 2. Optical transmittance of Nb-doped TiO_2 layers with a varied Nb content

The cross-sectional SEM image, demonstrating the interfaces of the Nb-doped electron transport layer deposited on FTO glass substrate and spin-coated $CH_3NH_3PbI_3$ layer for fabrication of a perovskite solar cell, is illustrated in Fig. 3. It is seen that Nb-doped TiO_2 electron transport layer with a thickness of 160 nm has an average grain size of around 20–40 nm that coincides with that of doped TiO_2 nanoparticles prepared. The layer of perovskite material, with a grain size of around 300–500 nm and a thickness of 380 nm, shows good adhesion to the TiO_2 layer.

Using the spin-coating method for fabrication of Nb-doped TiO_2 electron transport layers with different Nb-content, we have prepared a series of PSCs with the following configuration: FTO-glass electrode/Nb-doped TiO_2/$CH_3NH_3PbI_3$/carbon counter electrode (FTO/TiO_2(Nb)/$CH_3NH_3PbI_3$/carbon). The appropriate schematic diagram of prepared perovskite solar cells is shown in Fig. 4.

The current-voltage measurements of the perovskite solar cells were performed under simulated AM1.5G solar radiation. Fig. 5 shows a comparative view of photocurrent density-voltage (J–V) characteristics of TiO_2(Nb)/$CH_3NH_3PbI_3$/carbon heterojunction solar cells fabricated under ambient atmosphere conditions with pristine and 2.7 mol.% Nb-doped TiO_2 electron transport layers. The highest efficiency of 5.8 % (J_{sc} = 15.07 mA/cm^2, V_{oc} = 0.82 V, FF = 0.47) was observed for the PSC with 2.7 mol.% Nb-doped TiO_2. For the PSC based on pristine TiO_2 photoelectrode, the efficiency was 4.86 % (J_{sc} = 13.52 mA/cm^2, V_{oc} = 0.765 V, FF =0.47). The results indicate that the best power conversion efficiency (PCE) belongs to the PSC with the above mentioned type of Nb-doped TiO_2 electron transport layer. Thus, the observed PCE value was found to be up to 19 % higher, than that for the PSC based on pristine TiO_2 electron transport layer. Note that our experiments with a further increase

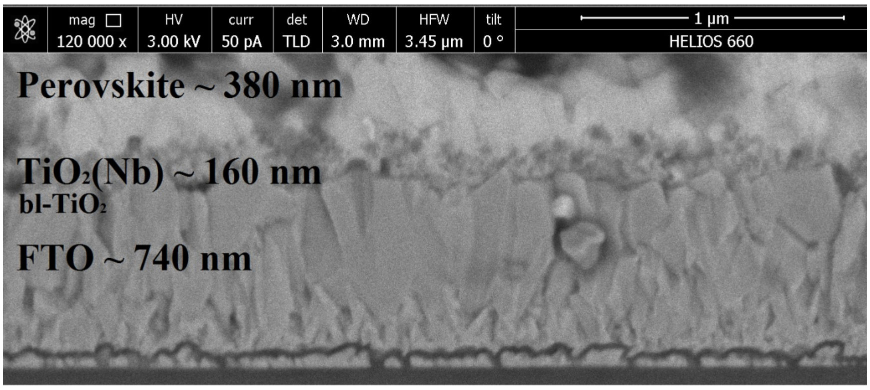

FIG. 3. Cross-sectional SEM micrograph of FTO/Nb-doped $TiO_2/CH_3NH_3PbI_3$ layers for perovskite solar cell fabrication

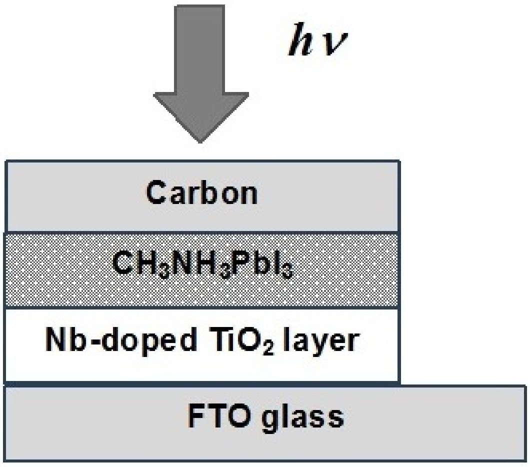

FIG. 4. The schematic diagram of a PSC structure with Nb-doped TiO_2 electron transport layer

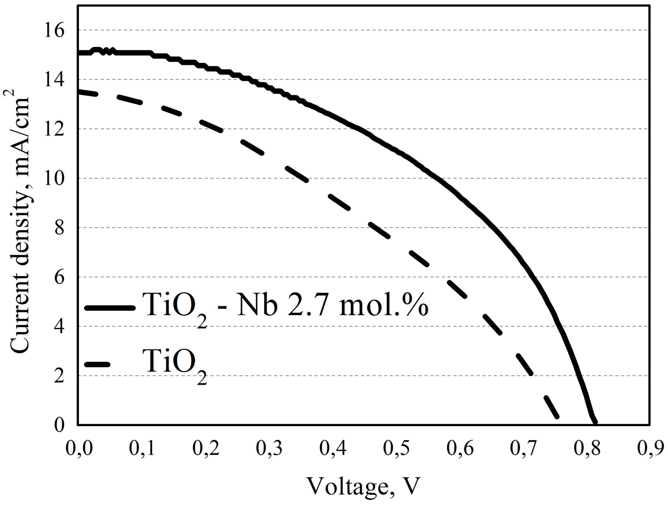

FIG. 5. J–V characteristics of the PSCs based on undoped TiO_2 and a 2.7 mol.% Nb-doped TiO_2 layer

of Nb doping concentration in TiO_2 electron transport layers resulted in decrease of photovoltaic parameters and PCE values in the PSCs fabricated.

Figure 6 shows the IPCE spectrum for the highest performing PSC photovoltaic device based on 2.7 mol.% Nb-doped TiO_2 electron transport layer. Spectral response values greater than 50 % are obtained across the entire visible spectrum from 350 to 750 nm.

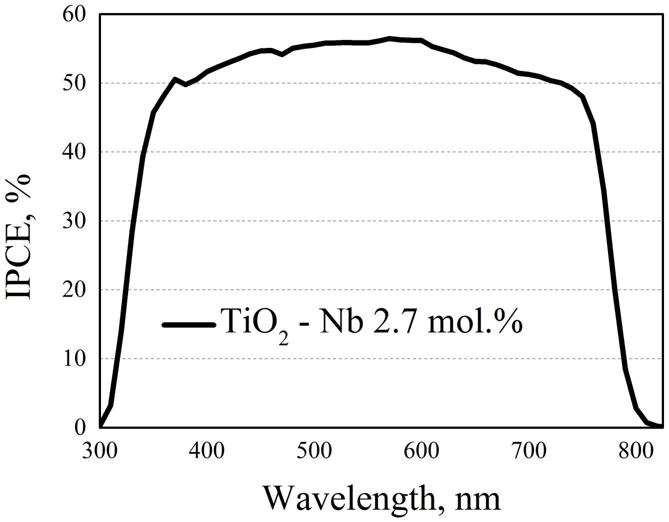

FIG. 6. IPCE spectrum of the PSC based on the 2.7 mol.% Nb-doped TiO_2 electron transport layer

4. Conclusion

Nb-doped TiO_2 nanoparticles with a Nb content varied between 0 and 2.7 mol.% were prepared by co-hydrolysis of Ti and Nb precursors and used for fabrication the electron transport layers in perovskite solar cells. The effects of Nb doping concentration in doped TiO_2 layers on the changes in optical absorption behavior, the morphology and charge carrier dynamics were studied. Using the prepared layers a series of PSCs was fabricated and examined. It was found that the PSC based on TiO_2 electron transport layer with a Nb content of 2.7 mol.% have shown up to 19 % improvement of a power conversion efficiency compared to that, based on an undoped TiO_2 layer. Further increase in the doping concentration resulted in diminishing of the PSC power conversion parameters.

Acknowledgments

This work was supported by the Russian Science Foundation, grant No. 17-19-01776.

References

[1] Yamada Y., Nakamura T., Endo M., Wakamiya A., Kanemitsu Y. Photocarrier recombination dynamics in perovskite $CH_3NH_3PbI_3$ for solar cell applications. *Journal of the American Chemical Society*, 2014, **136**(33), P. 11610–11613.

[2] Marinova N., Tress W., Humphry-Baker R., Dar M.I., Bojinov V., Zakeeruddin S.M., Nazeeruddin M.K., Grätzel M. Light harvesting and charge recombination in $CH_3NH_3PbI_3$ perovskite solar cells studied by hole transport layer thickness variation. *ACS nano*, 2015, **9**(4), P. 4200–4209.

[3] Han G.S., Chung H.S., Kim B.J., Kim D.H., Lee J.W., Swain B.S., Mahmood K., Yoo J.S., Park N.G., Lee J.H., Jung H.S. Retarding charge recombination in perovskite solar cells using ultrathin MgO-coated TiO_2 nanoparticulate films. *Journal of Materials Chemistry A*, 2015, **3**(17), P. 9160–9164.

[4] Son D.Y., Im J.H., Kim H.S., Park N.G. 11 % efficient perovskite solar cell based on ZnO nanorods: an effective charge collection system. *The Journal of Physical Chemistry C*, 2014, **118**(30), P. 16567–16573.

[5] Ajin Sundar S., Joseph John N., Synthesis and studies on structural and optical properties of zinc oxide and manganese-doped zinc oxide nanoparticles. *Nanosystems: Physics, Chemistry, Mathematics*, 2016, **7**(6), P. 1024–1030.

[6] Correa Baena J.P.C., Steier L., Tress W., Saliba M., Neutzner S., Matsui T., Giordano F., Jacobsson T.J., Srimath Kandala A.R., Zakeeruddin S.M., Petrozza A., Abate A., Nazeeruddin M.K., Grätzel M., Hagfeldt A. Highly efficient planar perovskite solar cells through band alignment engineering. *Energy and Environmental Science*, 2015, **8**(10), P. 2928–2934.

[7] Lee M.M., Teuscher J., Miyasaka T., Murakami T.N., Snaith H.J. Efficient hybrid solar cells based on meso-superstructured organometal halide perovskites. *Science*, 2012, **338**(6107), P. 643–647.

[8] Bi D., Moon S. J., Häggman L., Boschloo G., Yang L., Johansson E.M., Nazeeruddin M.K., Grätzel M., Hagfeldt A. Using a two-step deposition technique to prepare perovskite ($CH_3NH_3PbI_3$) for thin film solar cells based on ZrO_2 and TiO_2 mesostructures. *Rsc Advances*, 2013, **3**(41), P. 18762–18766.

[9] Su T.S., Hsieh T.Y., Hong C.Y., Wei T.C. Electrodeposited ultrathin TiO_2 blocking layers for efficient perovskite solar cells. *Scientific reports*, 2015, **5**.

[10] Murugadoss G., Mizuta G., Tanaka S., Nishino H., Umeyama T., Imahori H., Ito S. Double functions of porous TiO_2 electrodes on $CH_3NH_3PbI_3$ perovskite solar cells: Enhancement of perovskite crystal transformation and prohibition of short circuiting. *APL Materials*, 2014, **2**(8), P. 081511.

[11] Lindblad R., Bi D., Park B.W., Oscarsson J., Gorgoi M., Siegbahn H., Odelius M., Johansson E. M. J., Rensmo H. Electronic structure of $TiO_2/CH_3NH_3PbI_3$ perovskite solar cell interfaces. *The journal of physical chemistry letters*, 2014, **5**(4), P. 648–653.

[12] Zhu T., Gao S.P. The stability, electronic structure, and optical property of TiO_2 polymorphs. *The Journal of Physical Chemistry C*, 2014, **118**(21), P. 11385–11396.

[13] Yu H., Zhang S., Zhao H., Will G., Liu P. An efficient and low-cost TiO_2 compact layer for performance improvement of dye-sensitized solar cells. *Electrochimica Acta*, 2009, **54**(4), P. 1319–1324.

[14] Van de Lagemaat J., Park N.G., Frank A.J. Influence of electrical potential distribution, charge transport, and recombination on the photopotential and photocurrent conversion efficiency of dye-sensitized nanocrystalline TiO_2 solar cells: a study by electrical impedance and optical modulation techniques. *The Journal of Physical Chemistry B*, 2000, **104**(9), P. 2044–2052.

[15] Heo J.H., You M.S., Chang M.H., Yin W., Ahn T.K., Lee S.J., Sung S.J., Kim D.H., Im S.H. Hysteresis-less mesoscopic $CH_3NH_3PbI_3$ perovskite hybrid solar cells by introduction of Li-treated TiO_2 electrode. *Nano Energy*, 2015, **15**, P. 530–539.

[16] Wang J., Qin M., Tao H., Ke W., Chen Z., Wan J., Qin P., Xiong L., Lei H., Yu H., Fang, G. Performance enhancement of perovskite solar cells with Mg-doped TiO_2 compact film as the hole-blocking layer. *Applied Physics Letters*, 2015, **106**(12), P. 121104.

[17] Niaki A.G., Bakhshayesh A.M., Mohammadi M.R. Double-layer dye-sensitized solar cells based on Zn-doped TiO_2 transparent and light scattering layers: improving electron injection and light scattering effect. *Solar Energy*, 2014, **103**, P. 210–222.

[18] Zhu F., Zhang P., Wu X., Fu L., Zhang J., Xu D. The Origin of Higher Open-Circuit Voltage in Zn-Doped TiO_2 Nanoparticle-Based Dye-Sensitized Solar Cells. *ChemPhysChem*, 2012, **13**(16), P. 3731–3737.

[19] Yang M., Guo R., Kadel K., Liu Y., O'Shea K., Bone R., Wang X., He J., Li W. Improved charge transport of Nb-doped TiO_2 nanorods in methylammonium lead iodide bromide perovskite solar cells. *Journal of Materials Chemistry A*, 2014, **2**(46), P. 19616–19622.

[20] Oksengendler B.L., Ashurov N.R., Maksimov S E., Uralov I.Z., Karpova O.V. Fractal structures in perovskitebased solar cells. *Nanosystems: Physics, Chemistry, Mathematics*, 2017, **8**(1), P. 92–98.

[21] Kozlov S., Nikolskaia A., Larina L., Vildanova M., Vishnev A., Shevaleevskiy O. Rare-earth and Nb doping of TiO_2 nanocrystalline mesoscopic layers for high-efficiency dye-sensitized solar cells. *Physica status solidi A*, 2016, **213**(7), P. 1801–1806.

[22] Tsvetkov N., Larina L., Shevaleevskiy O., Ahn B.T. Electronic structure study of lightly Nb-doped TiO_2 electrode for dye-sensitized solar cells. *Energy and Environmental Science*, 2011, **4**(4), P. 1480–1486.

[23] Tsvetkov N.A., Larina L.L., Shevaleevskiy O., Al-Ammar E.A., Ahn B.T. Design of conduction band structure of TiO_2 electrode using Nb doping for highly efficient dye-sensitized solar cells. *Progress in Photovoltaics: Research and Applications*, 2012, **20**(7), P. 904–911.

[24] Ito S., Chen P., Comte P., Nazeeruddin M.K., Liska P., Péchy P., Grätzel M. Fabrication of screen-printing pastes from TiO_2 powders for dye-sensitised solar cells. *Progress in photovoltaics: research and applications*, 2007, **15**(7), P. 603–612.

[25] Park N.G. Methodologies for high efficiency perovskite solar cells. *Nano convergence*, 2016, **3**(1), P. 1–13.

[26] McEvoy A., Markvart T., Castañer L. *Practical handbook of photovoltaics: fundamentals and applications*. Elsevier, 2003.

NANOSYSTEMS:

PHYSICS, CHEMISTRY, MATHEMATICS

INFORMATION FOR AUTHORS

The journal publishes research articles and reviews, and also short scientific papers (letters) which are unpublished and have not been accepted for publication in other magazines. Articles should be submitted in English. All articles are reviewed, then if necessary come back to the author to completion.

The journal is indexed in Web of Science Core Collection (Emerging Sources Citation Index), Chemical Abstract Service of the American Chemical Society, Zentralblatt MATH and in Russian Scientific Citation Index.

Author should submit the following materials:

1. Article file in English, containing article title, the initials and the surname of the authors, Institute (University), postal address, the electronic address, the summary, keywords, MSC or PACS index, article text, the list of references.
2. Files with illustrations, files with tables.
3. The covering letter in English containing the article information (article name, MSC or PACS index, keywords, the summary, the literature) and about all authors (the surname, names, the full name of places of work, the mailing address with the postal code, contact phone number with a city code, the electronic address).
4. The expert judgement on possibility of publication of the article in open press (for authors from Russia).

Authors can submit a paper and the corresponding files to the following addresses: nanojournal.ifmo@gmail.com, popov1955@gmail.com.

Text requirements

Articles should be prepared with using of text editors MS Word or LaTex (preferable). It is necessary to submit source file (LaTex) and a pdf copy. In the name of files the English alphabet is used. The recommended size of short communications (letters) is 4-6 pages, research articles– 6-15 pages, reviews – 30 pages.

<u>Recommendations for text in MS Word</u>:

Formulas should be written using Math Type. Figures and tables with captions should be inserted in the text. Additionally, authors present separate files for all figures and Word files of tables.

Recommendations for text in LaTex:

Please, use standard LaTex without macros and additional style files. The list of references should be included in the main LaTex file. Source LaTex file of the paper with the corresponding pdf file and files of figures should be submitted.

References in the article text are given in square brackets. The list of references should be prepared in accordance with the following samples:

[1] Surname N. *Book Title*. Nauka Publishing House, Saint Petersburg, 2000, 281 pp.
[2] Surname N., Surname N. Paper title. *Journal Name*, 2010, **1** (5), P. 17-23.
[3] Surname N., Surname N. Lecture title. In: Abstracts/Proceedings of the Conference, Place and Date, 2000, P. 17-23.
[4] Surname N., Surname N. Paper title, 2000, URL: http://books.ifmo.ru/ntv.
[5] Surname N., Surname N. Patent Name. Patent No. 11111, 2010, Bul. No. 33, 5 pp.
[6] Surname N., Surname N. Thesis Title. Thesis for full doctor degree in math. and physics, Saint Petersburg, 2000, 105 pp.

Requirements to illustrations

Illustrations should be submitted as separate black-and-white files. Formats of files – jpeg, eps, tiff.

NANOSYSTEMS:

PHYSICS, CHEMISTRY, MATHEMATICS

Журнал зарегистрирован
Федеральной службой по надзору в сфере связи, информационных технологий и массовых коммуникаций
(свидетельство ПИ № ФС 77 - 49048 от 22.03.2012 г.)
ISSN 2220-8054

Учредитель: федеральное государственное автономное образовательное учреждение высшего образования
«Санкт-Петербургский национальный исследовательский университет информационных технологий, механики и оптики»

Издатель: федеральное государственное автономное образовательное учреждение высшего образования
«Санкт-Петербургский национальный исследовательский университет информационных технологий, механики и оптики»

Отпечатано в Учреждении «Университетские телекоммуникации»
Адрес: 197101, Санкт-Петербург, Кронверкский пр., 49

Подписка на журнал НФХМ
На первое полугодие 2018 года подписка осуществляется через
ОАО Агентство «Роспечать»
Подписной индекс 57385 в каталоге «Издания органов научно-технической информации»